

Measurements of the leading neutron production in polarized pp collision at $\sqrt{s}=200$ GeV

Manabu Togawa



A Dissertation Submitted in Partial Fulfillment of
the Requirement for the Degree of

Doctor of Science

Department of Physics
Kyoto University

January, 2008

Abstract

In the 2001–2002 run period at Relativistic Heavy Ion Collider (RHIC), polarized protons were accelerated to 100 GeV for the first time, with collisions at $\sqrt{s}=200$ GeV. We performed a pilot experiment at IP12 to search for non-zero single transverse asymmetry, A_N , in π^0 production at very forward angles based on the observation of large asymmetries in large x_F in $\sqrt{s} = 19.4$ GeV at Fermilab. The experiment was primary designed to detect photons from π^0 s but was also capable to detect neutrons in the forward angle, ± 2.8 mrad. The detector for neutral particles was placed downstream of the RHIC DX dipole magnets, which bent out a proton beam and other charged particles.

Observed asymmetries for photons and π^0 s were consistent with zero within the errors, whereas a significant asymmetry was observed for neutrons. The value of the asymmetry is $A_N = (-0.090 \pm 0.006 \pm 0.009) \times (1.0_{-0.25}^{+0.52})$, where the errors are statistical, systematic and the scale error is from the beam polarization uncertainty. This discovery enabled to monitor the beam polarization at the collision points at RHIC.

For further investigation about this large asymmetry in the leading neutron production and its origin, we have measured the x_F dependence of A_N and cross section with the PHENIX detector in the similar kinematics region at $\sqrt{s}=200$ GeV. The observed asymmetries are consistent with the IP12 result within the errors and show almost no x_F dependence. The measured cross sections are consistent with the x_F scaling claimed by the ISR experiment which measured the neutron production in pp collisions at $\sqrt{s}=30.6$ – 62.7 GeV. These cross sections for large x_F neutron production, as well as those in ep collisions by ZEUS, are mainly reproduced by a pion exchange. Therefore, the observed large asymmetry for the neutron production is considered to come from the interference between a spin-flip amplitude due to the pion exchange and non-flip amplitudes from other Reggeon exchange.

Contents

1	Introduction	5
1.1	A_N for inclusive productions in the forward kinematics	6
1.2	Leading neutron production	7
1.2.1	Definition of kinematics for the leading neutron production	7
1.2.2	ISR experiment at CERN	9
1.2.3	H1 and ZEUS experiments at HERA	11
1.2.4	Regge theory	11
1.2.5	Meson-Cloud Model	15
I	IP12 experiment	17
2	IP12 experiment	18
2.1	Overview	18
2.2	RHIC-AGS complex for the Polarized Proton Collider	19
2.2.1	Polarized ion source	21
2.2.2	Depolarization resonance	23
2.2.3	Partial snakes in AGS	24
2.2.4	Siberian snake and Spin rotator in RHIC	24
2.2.5	pC - and pp -CNI polarimeters	25
2.3	Experimental setup	25
2.3.1	Hodoscopes for beam-beam counters	28
2.3.2	East detector : Electromagnetic Calorimeter	28
2.3.3	West detector : Hadron Calorimeter	30
2.3.4	Data taking	30
3	Analysis	36
3.1	Selection of the collision event	36
3.2	Particle identification	37
3.3	π^0 mass spectrum	40
3.4	Asymmetry calculation	40
3.5	A_N decomposition	44

3.6	Neutron asymmetry measured with the HCal	45
3.7	Multiplicity of hodoscopes associated with neutron sample	46
4	Results of the IP12 experiment	48
II	PHENIX experiment	49
5	PHENIX experiment	50
5.1	Overview	50
5.2	Experimental setup	51
5.2.1	Zero Degree Calorimeter (Shower Max Detector, Charge veto counter)	51
5.2.2	Beam Beam Counters	53
5.2.3	PHENIX data acquisition system	56
5.2.4	Data taking for the leading neutron sample	56
6	Simulation study	59
6.1	Study of the ZDC and SMD responses	59
6.1.1	Energy linearity and resolution for the ZDC	61
6.1.2	Energy response in the detector edge	61
6.1.3	Position resolution in the center region	62
6.1.4	Position response in the detector edge	66
6.1.5	Systematics for the position measurement	67
6.2	Study of the neutron identification by PYTHIA event generator	69
6.2.1	Event structure	69
6.2.2	Neutron identification	74
6.2.3	Background contamination after the neutron identification	77
7	Analysis for the cross section	80
7.1	Cross section calculation	80
7.1.1	Cross section at the PHENIX experiment	80
7.1.2	Cross section at the ISR experiment	80
7.2	Energy distribution in the very forward kinematics	80
7.3	Stability	81
7.3.1	Energy gain	81
7.3.2	Neutron yield	81
7.4	Study of the beam gas background	82
7.5	Relative efficiency to the SMD cut between the real and simulation data	82
7.6	Energy Unfolding	83
7.6.1	Unfolding method	83
7.6.2	Unfolding the data	85

7.7	Estimation of the efficiency for the experimental cut	87
7.8	Result	87
7.9	Systematic errors	89
7.9.1	Scaling errors	89
7.9.2	Systematics for the energy linearity	90
7.9.3	Systematics for the determination of the beam axis on the ZDC geometry	91
8	Analysis for the single transverse spin asymmetry	94
8.1	The study of the beam axis on the detector geometry	94
8.2	Azimuthal angle dependence of A_N	98
8.2.1	Asymmetry calculation	98
8.2.2	Preparation of the simulation sets for each trigger	98
8.2.3	Estimation of the smearing effect	100
8.2.4	Systematic errors	102
8.3	x_F dependence of A_N	110
8.3.1	Asymmetry calculation	110
8.3.2	Estimation of the smearing effect	111
8.3.3	Estimation of the mean x_F in each bin	111
8.3.4	Systematic errors	114
9	Results of the PHENIX experiment	118
9.1	Cross section	118
9.2	Azimuthal angle dependence of A_N	119
9.3	x_F dependence of A_N	119
10	Discussion	124
11	Conclusion	126
A	Definition of the single transverse spin asymmetry	130
A.1	Necessity to be finite A_N	130
A.2	Square root formula	131
A.2.1	Physics asymmetry	132
A.2.2	Detector asymmetry	132
A.2.3	Luminosity asymmetry	133
A.3	Luminosity formula	133
A.4	Background contamination	134
B	Local Polarimeter	135
B.1	Introduction	135
B.2	Procedure	137

B.3	Measurement	137
B.3.1	$A_N^{Transverse}$	137
B.3.2	$A_{LR}^{Longitudinal}$ and $A_{UD}^{Longitudinal}$	138
B.4	Estimation of P_L/P	138
B.5	Summary table	142
C	Uncertainty in bunch shuffling	143
C.1	Uncertainty from the bunch number	143
C.2	Residual asymmetry in bunch shuffling	144
C.2.1	Expected $A^{shuffle}$ values for ϕ -dependence asymmetry	147
D	Charged particles at BBC associated with leading neutron	148
D.1	Multiplicity distribution	148
D.2	Single transverse spin asymmetry	148
E	Leading neutron asymmetries at various center of mass energies	150
F	Polarization of inclusive Λ^0 production	152

Chapter 1

Introduction

The property of the nucleon which comprises the real world is one of the most important interests in physics. In the 1970s, experiments of electron-proton Deep Inelastic Scattering (DIS) found the intrinsic structure that we currently consider as elementary particles namely quarks and gluons (partons) in the nucleon. DIS efforts have allowed to extract important information on the partonic structure of the nucleon to a high accuracy. The Quantum Chromo Dynamics (QCD) parton model has been shown to be very reliable in the perturbative region.

On the other hand, small momentum transfer reactions which can not be described by the perturbative QCD are still less explored. They can improve our knowledge on the inner hadronic reaction. The prominent effects are the consequence of the strong correlation between sea-quark and sea-antiquark with the quantum number of the meson [1], for example, a pion exchange via $p \rightarrow n\pi$ and $p \rightarrow \Delta\pi$. The measurements of the neutron in the very forward kinematics, which is called a leading neutron, in ISR at CERN [2, 3] and, H1 and ZEUS at HERA [4]-[9] are successfully described by a model based on an One Pion Exchange (OPE) in Regge calculus [10]-[15] with the absorptive correction [14]. Moreover, there is a meson-cloud model which deals with the quantum number of the meson as a hadronic structure. This model also describe the leading neutron production in the ISR experiment by the $n\pi$ state in the proton (a pion-cloud) [16].

Such works are especially important for nuclear physics, as one wants to know what amount of the nucleon-nucleon interaction is describable in terms of meson exchange forces. Therefore, detailed investigations for the leading neutron are necessary.

Leading neutron from polarized pp collision has one more interesting behavior, single transverse spin asymmetry (A_N) which is defined as

$$A_N \equiv \frac{d\sigma^{\uparrow 0} - d\sigma^{\downarrow 0}}{d\sigma^{\uparrow 0} + d\sigma^{\downarrow 0}}, \quad (1.1)$$

where superscripts of \uparrow and \downarrow indicate spin up and down of proton beams, respectively. “0” denotes the unpolarized state. We discovered finite A_N for leading neutron productions at a 12 o’clock interaction point (IP12) experiment at Relativistic Heavy Ion Collider (RHIC) and report on this thesis.

The IP12 experiment was initially motivated to search for sizable A_N of production particles in very forward region, 0 ± 2.8 mrad, in polarized pp collision at $\sqrt{s}=200$ GeV for monitoring the beam polarization at the collision point in RHIC. The A_N for π^0 production was one candidate based on the observation of large asymmetries in large x_F at $\sqrt{s} = 19.4$ GeV (section 1.1). Thus, the detector was primary designed to detect photons from π^0 s, but was also capable to detect neutrons. We did not observe finite A_N for photons and π^0 s, whereas we discovered large A_N for leading neutron productions.

For further investigation, we have measured the x_F dependence of A_N and cross section of leading neutrons with the PHENIX detector in similar kinematics and energy regions. The observed asymmetries are consistent with the IP12 result within the errors and show almost no x_F dependence. The measured cross sections are consistent with the x_F scaling claimed by the ISR experiment. These cross sections for large x_F neutron production, as well as those in ep collisions, are mainly reproduced by the OPE model in the Regge framework. Therefore, the observed large asymmetry for neutron productions is considered to come from the interference between a spin-flip amplitude due to the pion exchange and non-flip amplitudes from other Reggeon exchange (Appendix A.1). Remarkably, the OPE model successfully describe one of polarized phenomena of inclusive hadron production; a polarization of inclusive Λ production in pp collision (Appendix F). Moreover, the meson-cloud model also describes the cross section of leading neutron productions. (section 1.2)

Before introducing the measurements of leading neutrons in RHIC, extensive experimental and theoretical reviews are described.

1.1 A_N for inclusive productions in the forward kinematics

A_N for inclusive productions, for example in pp or DIS, has been thought to be originated from a transversity distribution, δq , of polarized Parton Distribution Function (PDF). δq is defined as,

$$\delta q \equiv q_{\uparrow}^{\uparrow}(x_B) - q_{\uparrow}^{\downarrow}(x_B), \quad (1.2)$$

where $q_{\uparrow}^{\uparrow(\downarrow)}$ is the probability of (anti-)parallel spin state for the parton to the nucleon. x_B is a Bjorken- x which is defined as a fraction of longitudinal momentum of the parton to that of the nucleon. According to the expectation from the leading-twist pQCD, A_N should be suppressed as $\alpha_s m_q / \sqrt{s}$, where m_q is the quark mass [17]. Therefore, the experimental observation of large A_N at high center of mass energy of 19.4 GeV in pp collision at Fermilab, shown in next section, was initially a surprise and this asymmetry remains to the RHIC energy at $\sqrt{s}=200$ GeV [18, 19, 20].

Recently three different mechanisms, Sivers effect¹[21], Collins effect [23] and Higher-twist effect [24, 25], have been studied extensively as the possible origin of A_N in high energy collision.

¹The Sivers PDF has suggested the relation of orbital angular momentum of partons in the nucleon [22].

However, these theories would not be applicable to our measurements since kinematics is in non-perturbative region; p_T coverage is approximately below 0.2 GeV/ c due to the acceptance limit. We do not discuss them in this thesis.

A_N of pion productions at FNAL E704

The experiment E704 was carried out at Fermi National Accelerator Laboratory (FNAL) for the study of polarization effects using 200 GeV/ c (anti-)proton beam incident on a 1.0 m liquid hydrogen target ($\sqrt{s}=19.4$ GeV). Significant A_N were observed in this experiment for the fragmentation region of polarized proton beams [26]–[29].

Figure 1.1 shows A_N for inclusive pion productions *vs.* x_F in the region of $0.7 < p_T < 2.0$ GeV/ c , where x_F is Feynman- x which is defined as a fraction of the incident proton momentum carried by the pion in initial direction of the proton. The observed A_N are strikingly large, increasing with x_F and reaching a magnitude of 40% for charged pions around $x_F=0.8$. There is a clear sign dependence of the pion charge, with $A_N^{\pi^+} > 0$ and $A_N^{\pi^-} < 0$, and magnitudes and the x_F dependence are approximately same. The π^0 asymmetry is positive but magnitude is about a half of charged pions.

Pion asymmetries have not only the x_F but also p_T dependence. Figure 1.2 includes A_N values in lower p_T region, $0.2 < p_T < 0.7$ GeV/ c , in case of π^\pm . The magnitudes are smaller in the low p_T region and it indicates that A_N increases dramatically in p_T above 0.7 GeV/ c . Figure 1.3 shows the p_T dependence of $A_N^{\pi^0}$ in the region of $0.5 < x_F < 0.8$. It also indicates same behavior as π^\pm , increasing with p_T .

Our experiment was initially motivated by this π^0 asymmetry; we needed to find significant A_N to monitor spin directions of proton beams at the PHENIX interaction point (Local Polarimeter; Appendix B). Even if the extrapolation of $A_N^{\pi^0}$ to p_T below 0.2 GeV/ c , which is our experimental coverage, seems to be small or zero, A_N for photons decayed from π^0 with higher p_T has a possibility to be measured.

1.2 Leading neutron production

1.2.1 Definition of kinematics for the leading neutron production

Kinematics of the leading neutron production for $pa \rightarrow nX$ reaction based on the Reggeon (meson) exchange model is shown in Figure 1.4. x_F and p_T of the leading neutron are defined as,

$$x_F = p_L/p_{L(max)} = E_n \cos \theta_n / E_p \sim E_n / E_p, \quad (1.3)$$

$$p_T = E_n \sin \theta_n \sim x_F E_p \theta_n. \quad (1.4)$$

From these variables, the momentum transfer squared from the proton can be described as,

$$t \sim -\frac{p_T^2}{x_F} - t_0 \quad \text{where,} \quad t_0 \equiv \frac{1-x_F}{x_F}(m_n^2 - x_F m_p^2). \quad (1.5)$$

In ep collision, we can evaluate $-Q^2$ by measuring the recoil electron.

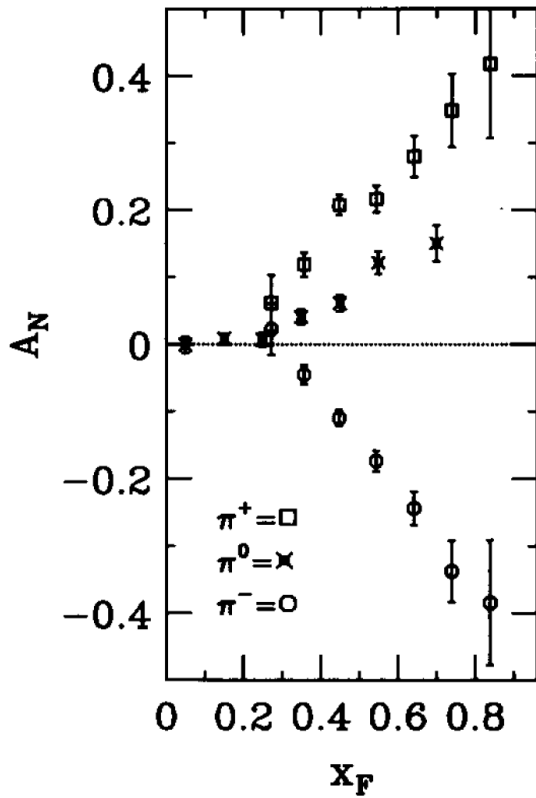


Figure 1.1: A_N for inclusive π^+ , π^- and π^0 productions from polarized pp scattering in $\sqrt{s}=19.4$ GeV at FNAL E704. They are plotted as a function of x_F in $0.7 < p_T < 2.0$ GeV/c. [27]

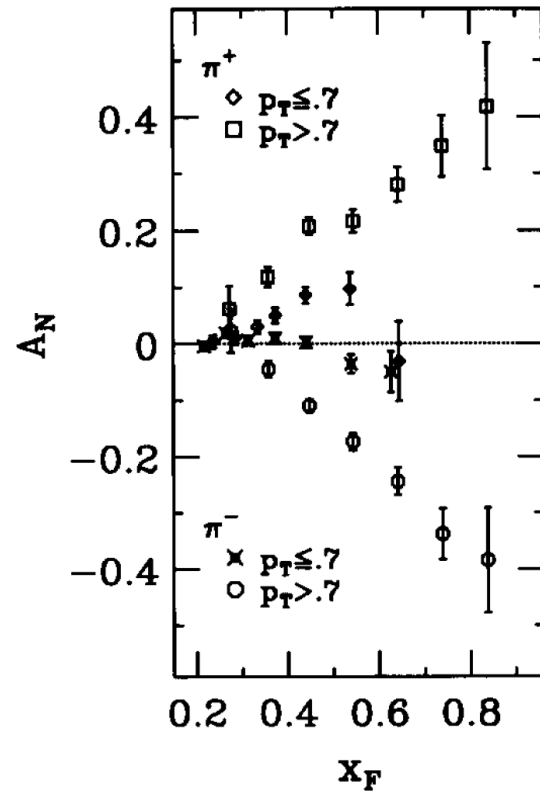


Figure 1.2: A_N vs. x_F for inclusive π^+ and π^- from polarized pp scattering in $\sqrt{s}=19.4$ GeV in two p_T ranges, $0.2 < p_T < 0.7$ GeV/c and $0.7 < p_T < 2.0$ GeV/c. [27]

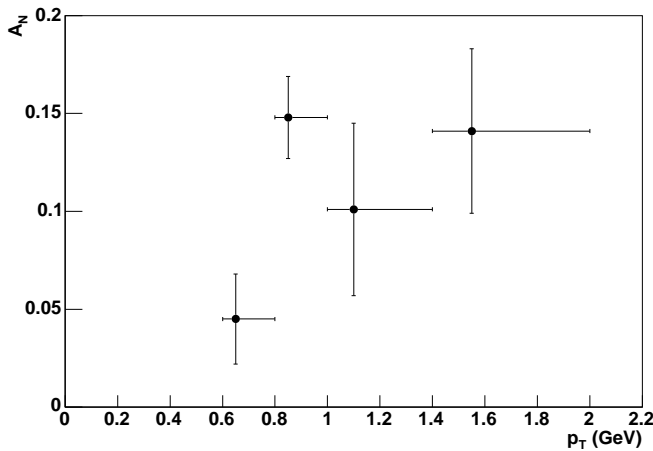


Figure 1.3: A_N vs. p_T for inclusive π^0 productions from polarized pp scattering in $\sqrt{s}=19.4$ GeV. The data is shown for $0.5 < x_F < 0.8$. [26]

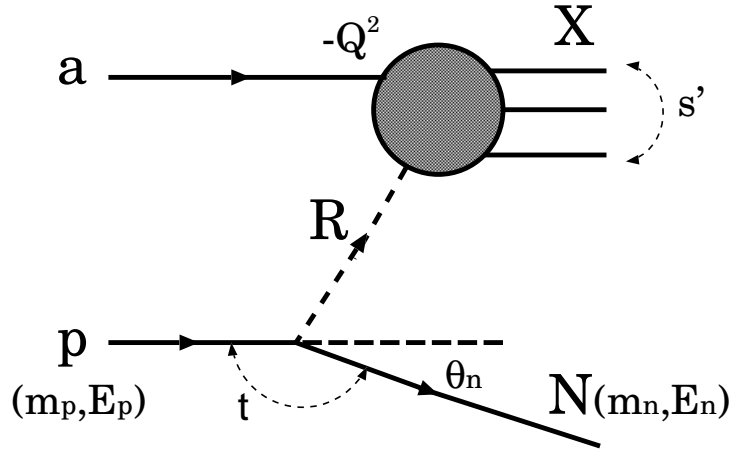


Figure 1.4: A schematic diagram of the leading neutron production, $pa \rightarrow nX$, on the Reggeon exchange model showing with Lorentz invariant variables s' , Q^2 and t . a is proton or positron for pp or e^+p reactions. R indicates a Regge trajectory with isospin odd such as π , ρ , a_2 and Pomeron- π in the Regge theory. In case of the pion exchange model, R means π .

1.2.2 ISR experiment at CERN

The ISR experiments at CERN measured leading neutrons in pp collisions at $\sqrt{s}=30.6, 44.9, 52.8$ and 62.7 GeV [2, 3]. Neutrons were detected in a Sampling Total Absorption Counter (STAC) with the energy resolutions of 26% and 19% for 20 GeV and 30 GeV neutrons, respectively. They were placed for covering $20\pm 4, 66\pm 11$ and 119 ± 11 mrad (finite angle) and 0 ± 1 mrad (zero degree) for the measurement of very forward kinematics.

Invariant cross sections as a function of x_F for various p_T , which can be evaluated by equation 1.4 using the combination of three finite angles (θ_n) and four proton energies (E_p), are shown in Figure 1.5. Only in the zero degree measurement ($p_T \approx 0$ GeV/c), large cross section is shown around $x_F=0.8$. Invariant cross sections at $p_T \approx 0$ GeV/c for various center of mass energies are plotted in Figure 1.6 and they are well scaled by x_F , not by the center of mass energy. These interesting behaviors are well described by the pion exchange model (section 1.2.4).

There is one more evidence of the pion exchange based on the Regge phenomenology as Figure 1.7. Invariant cross sections are plotted as a function of $(1-x_F)$ for $x_F \geq 0.88$ and fitted by straight line. In the Regge theory, cross section is described with a Regge trajectory $\alpha(t)$ as

$$\pi E \frac{d^3\sigma}{dp^3} \sim -\frac{d^2\sigma}{dt dx_F} \propto (1-x_F)^{1-2\alpha(t)} \sigma_{tot}^{aR}(s', t), \quad (1.6)$$

where $\sigma_{tot}^{aR}(s', t)$ is total cross section for a and R scattering in Figure 1.4. From the slope in Figure 1.7, $\alpha(t)$ can be extracted. As an average all over the energies, it is obtained as $\alpha(0)=0.11\pm 0.15$ and is consistent with the intercept of the pion trajectory, $\alpha_\pi(0) = 0$.²

²In case of Pomeron trajectory, $\alpha_P(t=0)=1.08$.

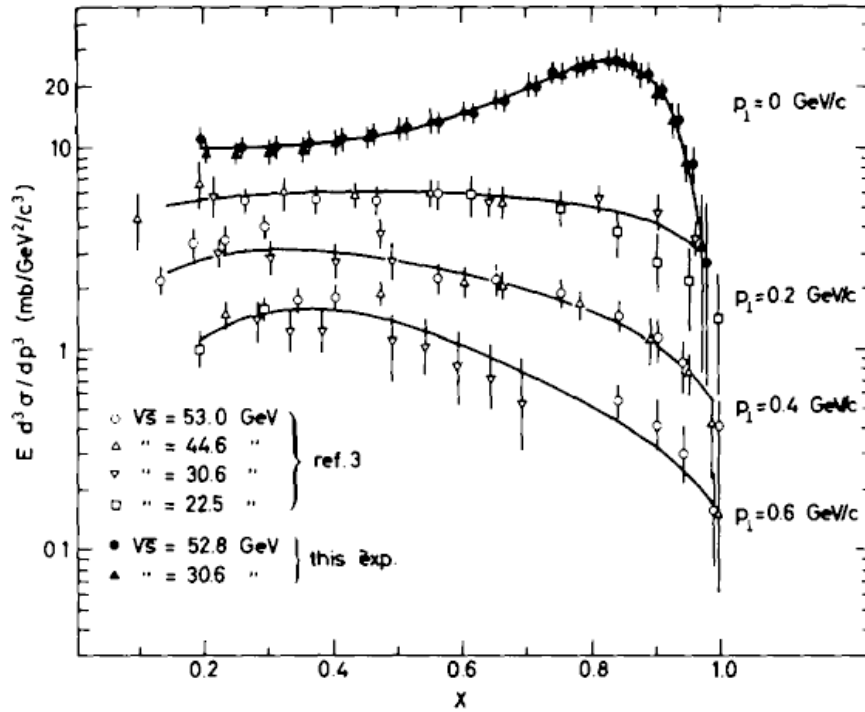


Figure 1.5: Invariant cross sections of neutron productions *vs.* x_F for various p_T in pp collisions at ISR. The lines are hand drawn to guide to eye. [2]

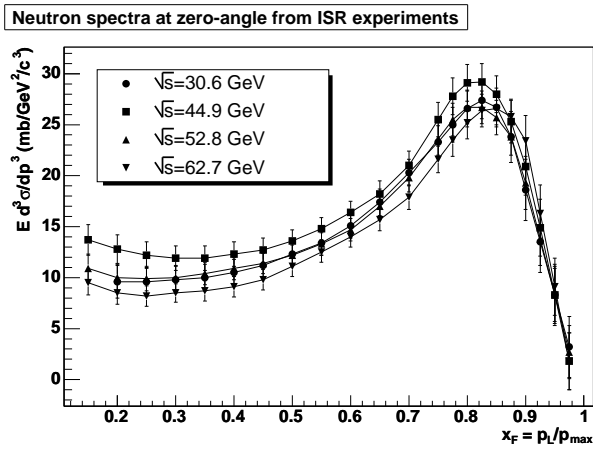


Figure 1.6: Invariant cross sections of leading neutrons *vs.* x_F for various center of mass energies in pp collisions at ISR. [2]

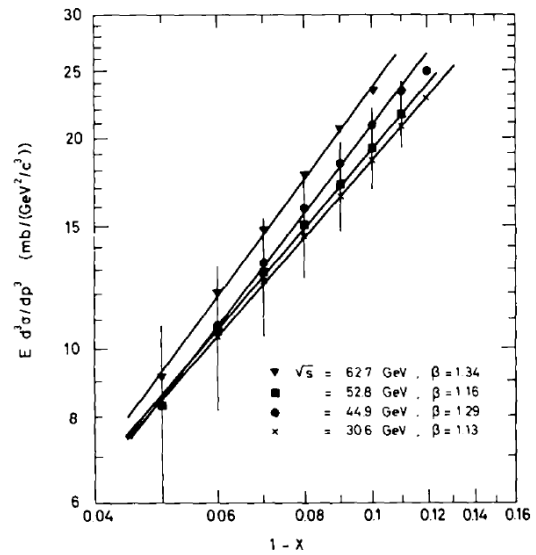


Figure 1.7: Invariant cross sections of leading neutrons as a function of $s'/s \sim 1 - x_F$ at the momentum transfer squared $t \approx 0$. [2]

1.2.3 H1 and ZEUS experiments at HERA

H1 and ZEUS experiments at HERA measured leading neutrons in ep collision at $\sqrt{s}\sim 300$ GeV [4]~[9]. We show a part of ZEUS results in this section. At the ZEUS experiment, a Forward Neutron Calorimeter (FNC) detected leading neutrons with the energy resolution of $\sigma/E = 65\%/\sqrt{E(\text{GeV})}$, covering 0 ± 0.8 mrad.

Result of the cross section is plotted in Figure 1.8 with the ISR pp result. Neutron production from ep scattering also has a peak structure around $x_F=0.8$ and is consistent with the curve which is calculated by the OPE model for ISR results scaled by 0.41. Moreover, they measured the D meson production associated with the leading neutron. The charm production can be generated via a photon-gluon fusion in ep collision and is sensitive to the gluon in a pion if the pion is exchanged. Result is shown in Figure 1.9. The data can be reproduced by the RAPGAP[30]+OPE model only.

According to the results, they also tried to extract a structure function of pion, $F_2^\pi(x_\pi, Q^2)$ where $x_\pi = x_B/(1 - x_F)$ in the framework of the OPE model [5]. $F_2^\pi(x_\pi, Q^2)$ is expected to be evaluated by the measurement of a neutron-tagged structure function, $F_2^{LN}(x_B, Q^2, x_F)$, with the following relationship,

$$F_2^\pi(x_\pi, Q^2) = \Gamma(Q^2, x_F) F_2^{LN}(x_B, Q^2, x_F), \quad (1.7)$$

where $\Gamma(Q^2, x_F)$ is the inverse of the pion flux factor integrated over the measured t region and corrected for the t -averaged absorption effect. Obtained F_2^π are shown in Figure 1.10 with the curve for the $F_2(x_B, Q^2)$ of the proton scaled by 0.36 and the calculation from GRV parameterization [31]. It has approximately the same x_B and Q^2 dependence as F_2 of the proton. The data provide new constraints on the shape of the pion structure function for $x_\pi < 10^{-2}$.

1.2.4 Regge theory

In 1935, Yukawa predicted that there must be a particle, now known as the pion, which would carry the strong interaction [32]. However, we now know that although the pion exchange is an important component of the static force in high energy scattering, exchange of a very large number of particles is involved. Regge theory [33] provides a simple quantitative description of the combined effect of all these particle exchanges.

Regge theory is the framework based on the analytic property of scattering amplitudes and it has been studied before the establishment of QCD. Unlike QCD which is starting from the first principle, Lagrangian, it is difficult to obtain a comprehensive assessment for the particle interaction. However, its technique is extremely useful even now, especially in the non-perturbation frame.

Cross section for inclusive scattering in the region of small momentum transfer

The cross section for an inclusive reaction, $ab \rightarrow cX$, in the region of small momentum transfer is described by a diagram of Figure 1.11. Rb scattering term, total cross section Rb , can be

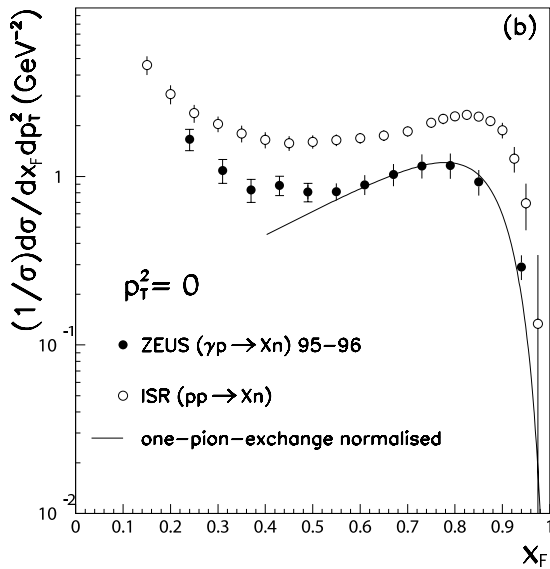


Figure 1.8: Differential cross sections normalized by $\sigma_{tot}^{\gamma p \rightarrow nX}$ of the leading neutron *vs.* x_F at $p_T \approx 0$ GeV/c. Closed and open circles show $ep \rightarrow nX$ at ZEUS and $pp \rightarrow nX$ at ISR, respectively. The curve is the expectation of the OPE model for ISR data scaled by 0.41. [5]

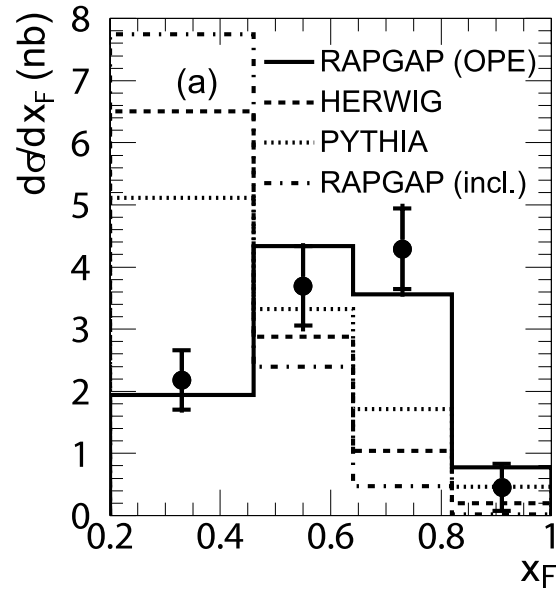


Figure 1.9: Differential cross sections for neutron-tagged $D^{*\pm}$ *vs.* neutron x_F from ep collisions at ZEUS. $D^{*\pm}$ was detected in the Central Tracking Detector (CTD) covering $|\eta| < 1.5$. Only RAPGAP+OPE model can reproduce the data. [7]

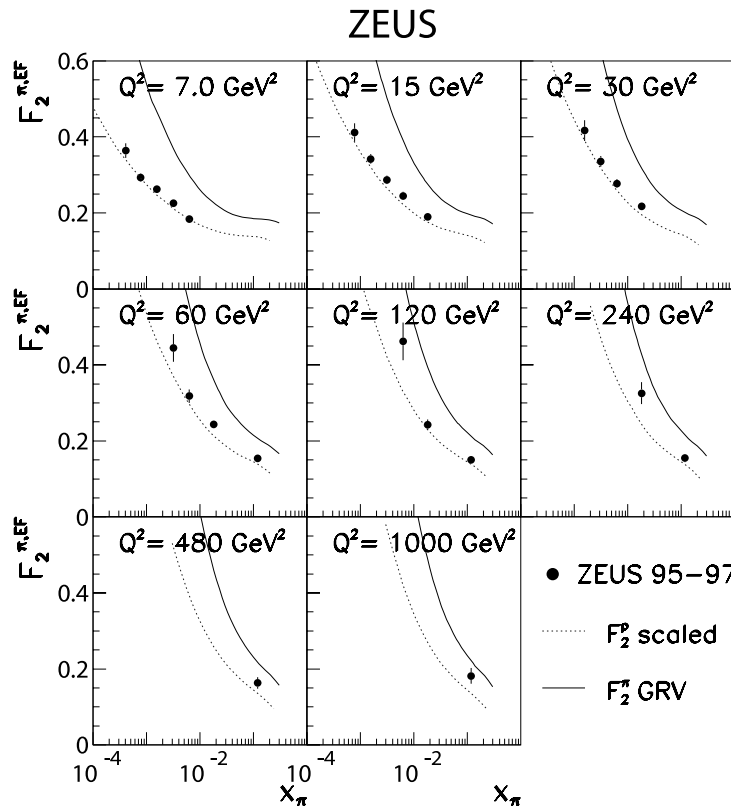


Figure 1.10: F_2^π as a function of x_π for the pion in bins of Q^2 determined for $0.64 < x_F < 0.82$. The pion flux used to determine F_2^π is the effective OPE flux (EF) used in hadron-hadron reaction. Only statistical uncertainties are shown. The dotted lines are the $F_2(x_B, Q^2)$ of the proton, scaled by 0.361. The solid curves are F_2^π obtained from the GRV parameterization. [5]

replaced as Figure 1.12 by an optical theorem with new Reggeon R_k (Triple-Regge diagram). A term Figure 1.12 contributes to the cross section, $d^2\sigma/dtdx_F$, as

$$g_{acR_i}(t)g_{acR_j}(t)G_k^{ij}(t)e^{i(\phi(\alpha_1(t))-\phi(\alpha_2(t)))}(1-x_F)^{1-\alpha_1(t)-\alpha_2(t)}\sigma_{tot}^{bR}(s'), \quad (1.8)$$

where, $g_{acR_i}(t)$ and $g_{acR_j}(t)$ are the couplings of Reggeon R_i and R_j to the hadron ac , respectively. $G_k^{ij}(t)$ is the triple-Reggeon vertex and $\phi(\alpha(t))$ is the phase arising from the signature factor, $1 \pm e^{-i\pi\alpha(t)}$. All contributions of Reggeon for $R_{i,j,k}$ should be considered to obtain the result. For the $\sigma_{tot}^{bR}(s')$, convenient database provided by Particle Data Group (PDG) [34]. If s' is bigger, $\sigma_{tot}^{bR}(s')$ can be described by the Pomeron exchange (R_k =Pomeron).

The leading neutron production in pp scattering, $pp \rightarrow nX$, has been obtained by exchanges of π , ρ and a_2 mesons. In case of the pion exchange, the cross section is described as follows [10].

$$\left. \frac{d\sigma_{pp \rightarrow nX}}{dtdx_F} \right|_{\pi} = \frac{1}{4\pi} \frac{2g_{pn\pi}^2}{4\pi} \frac{-t}{(t-m_{\pi}^2)^2} (1-x_F)^{1-2\alpha_{\pi}(t)} [F(x_F, t)]^2 \sigma_{tot}^{p\pi}(s'), \quad (1.9)$$

where $g_{pn\pi}^2/4\pi = 27.5$ [35] is the $pn\pi$ coupling constant and $\alpha_{\pi}(t)$ is approximately $\alpha't$ with $\alpha' = 1 \text{ GeV}^{-2}$ for the pion trajectory. $F(x_F, t)$ is the form factor included the effect of the final state re-scattering of the neutron. For the hadronic charge exchange experiments, a good description of most of the $pn \rightarrow pX$ data [36] is obtained using Bishari flux [37], which corresponds to equation 1.9 with $F(x_F, t)=1$.

Equation 1.9 can be represented by a Regge factorization with the pion flux factor, $f_{\pi/p}(x_F, t)$, simply ³.

$$\left. \frac{d\sigma_{pp \rightarrow nX}}{dtdx_F} \right|_{\pi} = f_{\pi/p}(x_F, t) \sigma_{tot}^{p\pi}(s'). \quad (1.10)$$

Invariant cross section is obtained as $Ed^3\sigma/dp^3 \approx -(1/\pi) \cdot d^2\sigma/dtdx_F$ (Equation 1.6) and calculation results are plotted with ISR data in Figure 1.14. Here, cross sections were calculated by not only the pion exchange but also ρ, a_2 exchanges. Two step process, $p \rightarrow \Delta \rightarrow n$ were also considered. Regge theory well describes the leading neutron production and shows remarkable component is from the pion exchange. As a result for the leading neutron production in high s' , triple-Regge diagram $\pi\pi P$ as Figure 1.13 is considered to be dominant.

³Recently novel theoretical tools including leading neutron production based on standard pQCD have been developed with a non-perturbative distribution (fracture function) which allow to absorb collinear singularities at leading order in the QCD coupling constant.

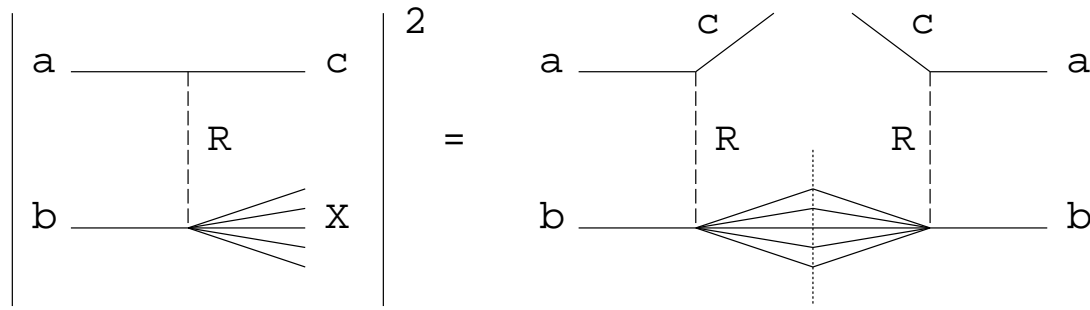


Figure 1.11: Left : Amplitude for $ab \rightarrow cX$ via Reggeon exchange. It is same as right diagram.

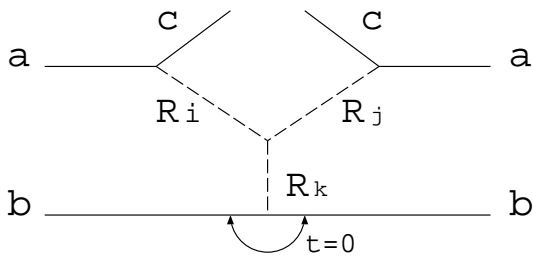


Figure 1.12: Triple Regge diagram for inclusive scattering amplitude. It is same as Figure 1.11 using an optical theorem for Rb scattering with new Reggeon R_k .

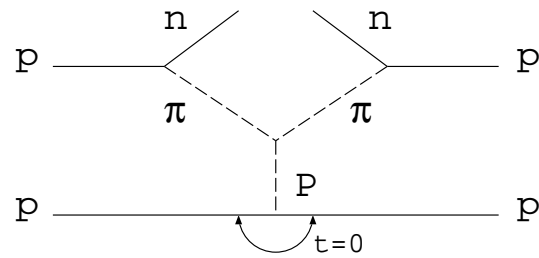


Figure 1.13: Dominant process for the leading neutron production in high s' .

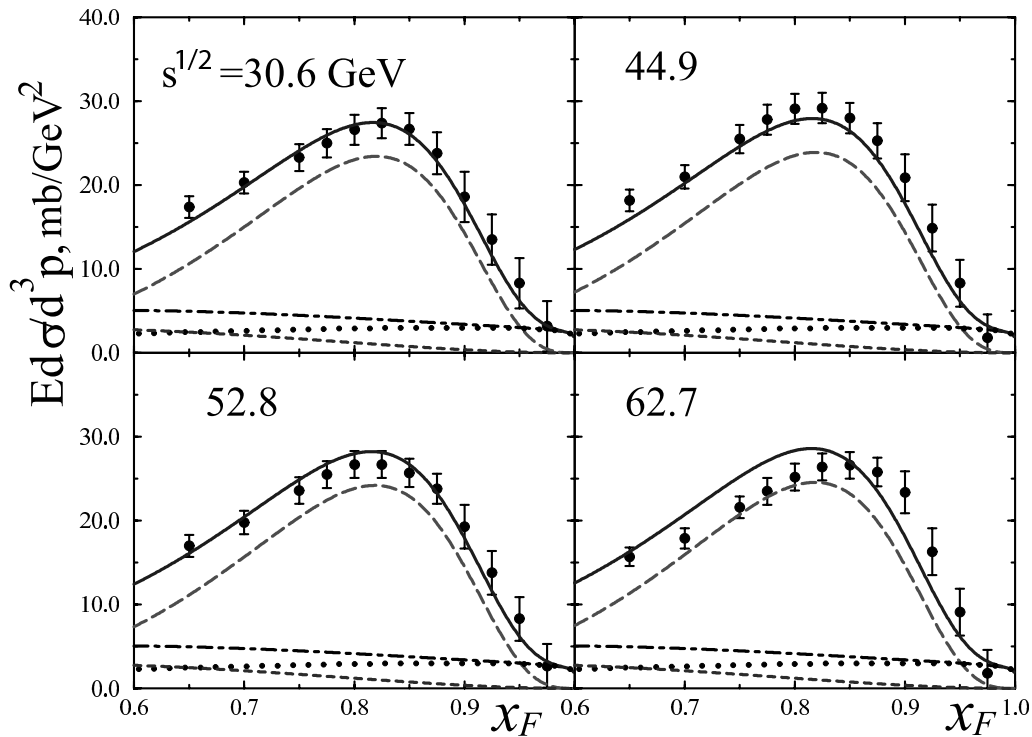


Figure 1.14: Invariant cross sections for inclusive neutron productions, $pp \rightarrow nX$, as a function of x_F for $p_T^2=0$ (GeV/c)². The long dashed curve shows the contribution from the pion exchange. The dotted curve is the ρ, a_2 -exchange contribution, the dashed curve shows the contribution from the two-step process $p \rightarrow \Delta \rightarrow n$ and the dot-dashed line is sum of them. The solid curve represents the sum of all components. The experimental data are from ISR. [10, 15]

1.2.5 Meson-Cloud Model

The meson-cloud model deals with the proton as a bare baryon surrounded by a virtual meson cloud, such as $p \rightarrow n\pi$ and $p \rightarrow \Delta\pi$ states⁴. This model gives a best description for the recent interesting result from the Drell-Yan experiment at FNAL E866, there is an excess of the \bar{d} quark relative to the \bar{u} quark in the nucleon sea [41], via the \bar{d} quark in the π^+ of a pion-cloud ($p \rightarrow n\pi^+$). D'Alesio and Pirner applied to the meson-cloud model to leading neutron productions in the ISR experiment and successfully describe by the pion-cloud model [16].

Cross section for the leading neutron production

A schematic view of the leading neutron production based on the pion-cloud model is shown in Figure 1.15. The pion is stripped from one proton and scattering with other proton. The remaining neutron runs forward on the proton axis roughly. This process is basically same as the pion exchange shown as Figure 1.4. Thus, the differential cross section is given by the pion flux factor times the total p - π cross section in the same way of the Regge calculation as,⁵

$$\left. \frac{d\sigma_{pp \rightarrow nX}}{dx_F dp_T^2} \right|_{\pi} = F_{n\pi}(x_F, p_T) \sigma_{tot}^{p\pi}(s'), \quad (1.11)$$

where the flux factor $F_{n\pi}(x_F, p_T)$ gives the probability for the splitting of a proton to the neutron-pion system and is calculated based on the meson-cloud model.

On the meson-cloud framework, proton is described as,

$$\begin{aligned} |p \uparrow\rangle &= \sqrt{S} \left\{ |p_0 \uparrow\rangle + \sum_{\lambda\lambda'} \sum_{BM} \int dx_F dp_T^2 \phi_{BM}^{\lambda\lambda'}(x_F, p_T) |B, M; x_F, p_T\rangle \right\} \\ &= \sqrt{S} \left\{ |p_0 \uparrow\rangle + \sum_{\lambda\lambda'} \int dx_F dp_T^2 \phi_{N\pi}^{\lambda\lambda'}(x_F, p_T) \right. \\ &\quad \left. \times \left[\sqrt{\frac{1}{3}} |p, \pi^0; x_F, p_T\rangle + \sqrt{\frac{2}{3}} |n, \pi^+; x_F, p_T\rangle + \dots \right] \right\}, \quad (1.12) \end{aligned}$$

where, $\phi_{BM}^{\lambda\lambda'}(x_F, p_T)$ is the probability amplitude to find a baryon B with longitudinal momentum fraction x_F , transverse momentum p_T and helicity λ and a meson M with longitudinal momentum fraction $(1 - x_F)$, transverse momentum $-p_T$ and helicity λ' inside a proton with spin up. \sqrt{S} is the renormalization constant, which is fixed by $\langle p|p\rangle = 1$ and gives the amplitude for the bare proton. The pion flux in equation 1.11 is calculated as,

$$F_{n\pi}(x_F, p_T) = \frac{2}{3}\pi \sum_{\lambda\lambda'} \left| \phi_{N\pi}^{\lambda\lambda'}(x_F, p_T) \right|^2. \quad (1.13)$$

The light-cone, covariant Regge and Skyrme-type model approaches [42, 43] were performed to calculate the pion flux factor. In addition, if an impact parameter b in Figure 1.15 is small, the

⁴A similar fluctuation for intrinsic strange and charm in proton, such as $p \rightarrow K^+\Lambda$ and $D\Lambda_c$, can be possible. However they are less strong because they are higher excitation states. [38, 39]

⁵We use $dp_T^2 = -x_F dt$ from equation 1.5. Negative sign is ignored in this discussion.

projectile proton and the neutron are re-scattering which is called the absorption effect. The absorption correction is also discussed in [16].

Invariant cross section is obtained as $E d^3\sigma/dp^3 \sim -(x_F/\pi) \cdot d^2\sigma/dx_F dp_T^2$ and shown in Figure 1.16. Calculated lines are scaled by a factor of 1.2 for the normalization of other contributions, for example ρ exchange and $\Delta \rightarrow n$, estimated to be 20%. Data points show the cross sections in pp collision at $\sqrt{s} = 53$ GeV from the ISR experiment. All models describe well the cross section of the leading neutron production.

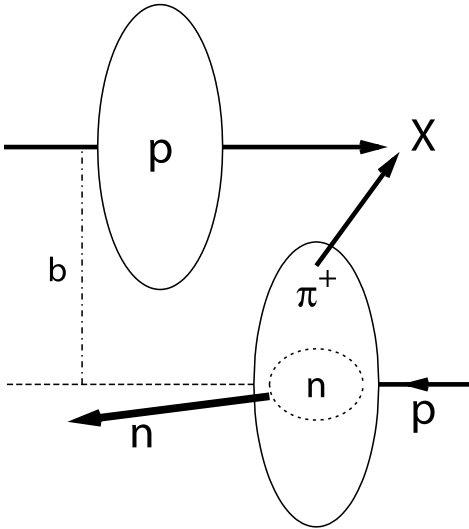


Figure 1.15: A schematic view of the inclusive neutron production based on the pion-cloud model. If an impact parameter b is small, the projectile proton and the neutron are re-scattering (absorption effect). [16]

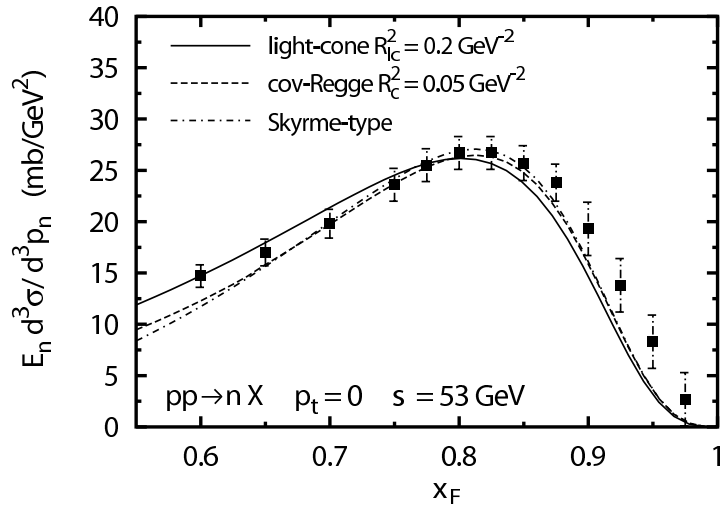


Figure 1.16: Invariant cross sections for the inclusive neutron production in pp collision as a function of x_F at $p_T=0$ (GeV/c) calculated by three different models based on the pion-cloud model. Data points show the cross sections at $\sqrt{s} = 53$ GeV from the ISR experiment. [16]

In this thesis, we report measurements of leading neutron productions in polarized pp collision at $\sqrt{s}=200$ GeV from the IP12 experiment (Part I; Chapter 2–4) and the PHENIX experiment (Part II; Chapter 5–9). For the IP12 experiment, the experimental overview is described in Chapter 2. The analysis for the asymmetry calculation is discussed in Chapter 3 and the results are presented in Chapter 4. For the PHENIX experiment, the experimental overview is described in Chapter 5. The simulation study for the leading neutron detection are described in Chapter 6. The analyses for the cross section and the asymmetries are discussed in Chapter 7 and 8, respectively. Chapter 9 shows the results of the PHENIX experiment. We present the discussion in Chapter 10 and the conclusion in Chapter 11.

Part I

IP12 experiment

Chapter 2

IP12 experiment

2.1 Overview

Extracting the spin state of partons in the nucleon is one of main physics objects at RHIC which has the capability of colliding polarized protons [44]¹. Most of spin related analyses for inelastic scattering will extract the spin information of partons through the spin asymmetries, which are defined as differences of cross sections with the different spin combinations of beams as,

- Longitudinally polarized combinations : $A_L \equiv -\frac{\sigma^{+0}-\sigma^{-0}}{\sigma^{+0}+\sigma^{-0}}$, $A_{LL} \equiv \frac{\sigma^{++}-\sigma^{+-}}{\sigma^{++}+\sigma^{+-}}$
- Transversely polarized combinations : $A_N \equiv \frac{\sigma^{\uparrow 0}-\sigma^{\downarrow 0}}{\sigma^{\uparrow 0}+\sigma^{\downarrow 0}}$, $A_{NN} \equiv \frac{\sigma^{\uparrow\uparrow}-\sigma^{\uparrow\downarrow}}{\sigma^{\uparrow\uparrow}+\sigma^{\uparrow\downarrow}}$ ²

where superscripts $+(-)$ indicates the helicity state of beams.

A layout of the RHIC facility is shown in Figure 2.1. In the RHIC ring, proton beams, which are called Blue and Yellow beams, preserve their polarizations (section 2.2.1) by a Siberian snake (section 2.2.4) as the vertically transverse direction and polarizations have been measured by the pC -CNI polarimeters (section 2.2.5). We can study the physics which are related to the transverse spin by colliding them directly (Transverse run period). For the study of the parton helicity distribution, which will appear as A_{LL} , it is necessary to rotate spin directions of protons to the longitudinal. The spin rotator magnets (section 2.2.4), which have been installed up- and down-streams of the collision points at PHENIX and STAR, enable us to take longitudinal beams by rotating protons (Longitudinal run period).

For the confirmation of the longitudinal polarization at collision point, we need to develop a new polarimeter which can evaluate the spin direction by a production process with a sizable asymmetry in pp collision (Local Polarimeter : details at Appendix B). To establish the local polarimeter system, we searched for a single transverse spin asymmetry, A_N , at 12 o'clock interaction point (IP12 experiment) in 2001-2002. Neutral particle detection in the very forward kinematics, ± 2.8 mrad, was chosen due to accessibility with the existing PHENIX detectors [46].

¹Other is the searching for Quark Gluon Plasma (QGP) state by colliding heavy ions as RHIC's name indicates [45].

²In some literature, A_{NN} is denoted as A_{TT} .

The IP12 experiment was originally designed by a ElectroMagnetic Calorimeter (EMCal) to detect the photon from π^0 s based on the observation of a large pion asymmetry at $\sqrt{s}=19.4$ GeV (section 1.1). The detector consisted of a scintillation counter as a charged particle veto, a preshower EMCAL, a 60 (5×12)-element array of PbWO_4 EMCAL and the two scintillation counters with an iron block in between to distinguish neutrons. The energy resolution was $\Delta E/E \simeq 10\%/\sqrt{E(\text{GeV})}$ and the position resolution was about 1 mm. We also installed a Hadron Calorimeter (HCal) to measure only neutrons in the opposite side. The setup included a photon veto, consisted of a 5 cm thick lead block followed by a scintillator, the HCal made of tungsten plates with optical fiber readout planes and five PbWO_4 crystals for the reconstruction of neutron position. For the neutron measurement with the HCal, the energy resolution was estimated to be 40–50% and the position resolution evaluated to be 3–4 cm studied by the simulation which was prepared based on the test beam result.

For the data taking, pp collision was triggered by the scintillator hodoscopes located ± 1.85 m from the collision point covering $|\eta| = 2.2$ to 3.9 and we also required some energy deposit in each calorimeter. Average polarization for the Blue and Yellow beams were 12 and 17 %, respectively.

2.2 RHIC-AGS complex for the Polarized Proton Collider

The study of high energy polarized proton beams has been a long term program at BNL with the development of polarized beams in a Booster and an Alternating Gradient Synchrotron (AGS) rings for the fixed target experiments. The capability of polarized proton beams has been extended to the RHIC machine. The first collision at RHIC was in 2000 and the performance has been improved every year. The main components used for the acceleration of proton beams at RHIC are shown in Figure 2.1.

We will describe the overview of the RHIC as a polarized proton collider. More details are found in references [47, 48]. Polarized proton injection uses an optically-pumped polarized H ion source (section 2.2.1). It produces 500 μA in a single 300–400 μs pulse, which corresponds to $9\text{--}12\times 10^{11}$ polarized H. The polarization have reached 80% or more at the source. There are several steps from polarized H pulse to a bunched polarized proton beam; the LINAC, the Booster, the AGS then the RHIC.

A pulse of polarized H ions are accelerated to 200 MeV kinetic energy in the 200 MHz LINAC. The pulse of H ions is strip-injected and captured into a single bunch as polarized protons in the Booster. The single bunch of polarized proton is accelerated in the Booster to 1.5 GeV kinetic energy and then transferred to the AGS, where it is accelerated to 24.3 GeV (RHIC 100 GeV run parameter). Then, the polarized protons are transferred to the RHIC. The AGS to RHIC transfer line has been designed to transport proton beams in the energy range, from 20.6 GeV to 28.3 GeV. Each of RHIC rings can be filled with up to 120 polarized proton bunches from the AGS, in which case the time between bunch crossing at Interaction Points

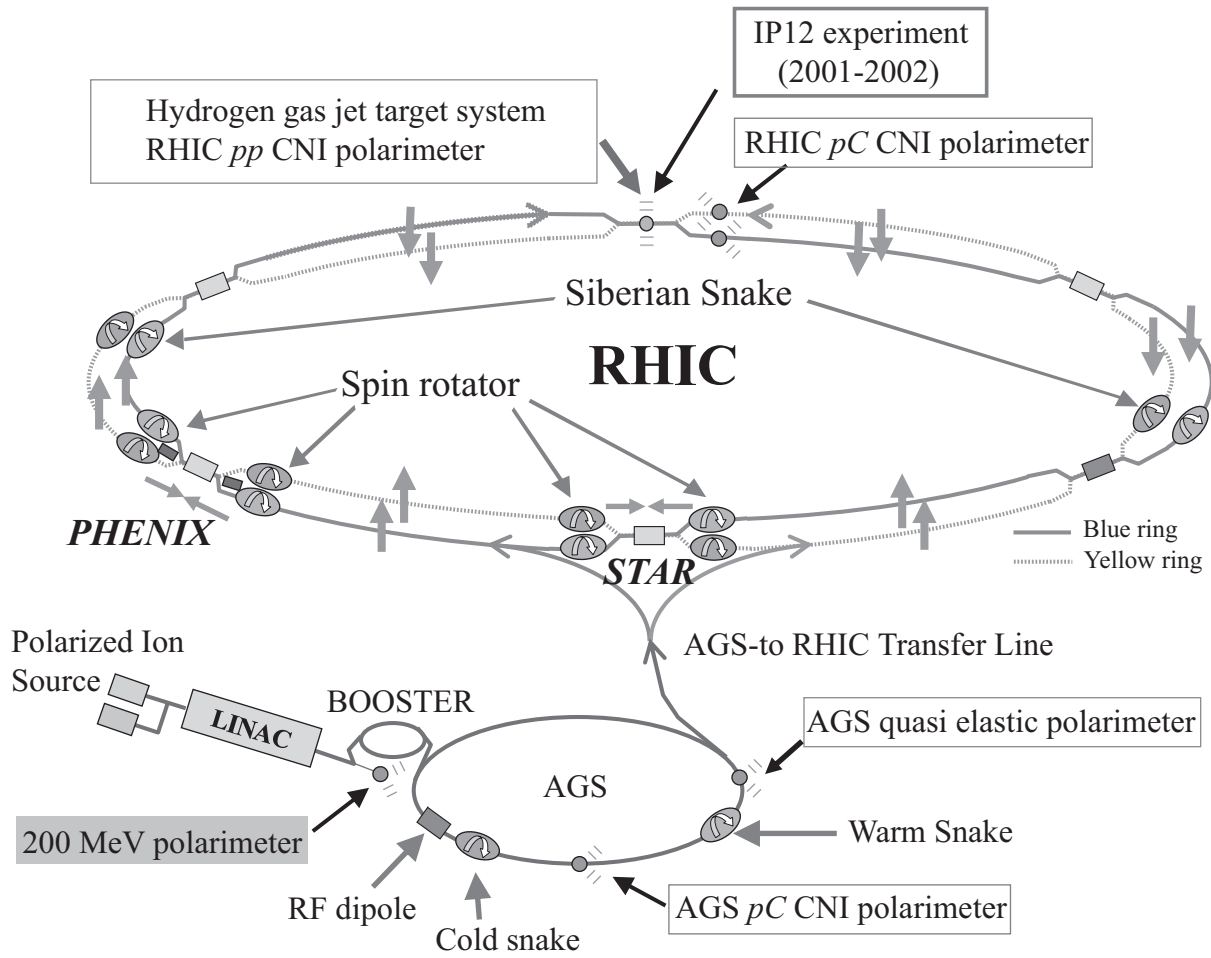


Figure 2.1: A layout of the RHIC facility. Polarized protons are accelerated from the source through a LINAC, a Booster synchrotron, and the AGS before being injected to the RHIC rings. Several of the components used to maintain polarization throughout the acceleration stages are shown. Location of polarimeters are also noted. The places of IP12 and PHENIX experiments are 12 o'clock and 8 o'clock points as a clock.

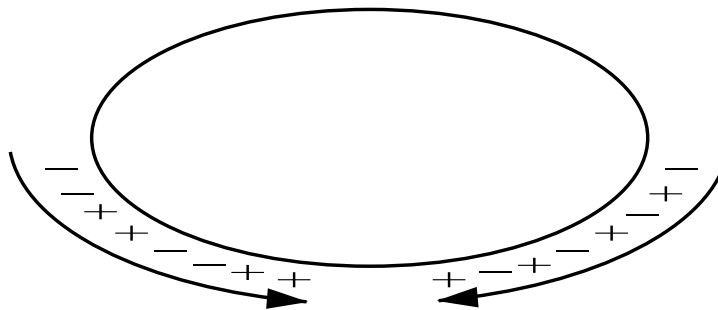


Figure 2.2: The pattern of the polarization signs of the bunches in the two counter-rotating beams in RHIC. It is typically desirable to collide equal numbers of $(++,+-,-+,-)$ bunches at each experiment, where $+-$ represents a bunch in one beam with polarization up colliding with a bunch in the other beam with polarization down in transverse pp mode.

(IPs) is 106 nsec.

In the RHIC operation, for example 2005 year run, rings were filled with 111 polarized proton bunches and 9 abort bunches to estimate a beam gas background. The same pairs of bunches interact at each intersection region but spin directions of pairs are different in each interaction. It is typically desirable to collide equal numbers of $(++,+,-,-+,-,-)$ bunches at each experiment, where $+,-$ represents a bunch in one beam with polarization up colliding with a bunch in the other beam with polarization down. One solution which would satisfy all the intersections is to load the bunches of one ring $(++--)$, etc.), and load the bunches of the other ring with $(+-+-)$, etc.) as shown in Figure 2.2. The polarization sign of each bunch is decided at the exit of H ion source where polarization direction is aligned in transverse. This is very useful for the asymmetry analysis since any common systematic errors, for example detector asymmetry, are canceled out by using those spin combinations (see Appendix A). After filling of both rings is complete, the beams are accelerated to the flat-top energy.

Polarized proton beams have been accelerated, stored and collided in the RHIC rings at center-of-mass energies of 62.4, 200 and 410 GeV so far. The acceleration of polarized beam in circular acceleration is complicated by the presence of numerous depolarization resonances. During acceleration, the polarization may be lost when the spin precession frequency passes through depolarizing resonances (section 2.2.2). Therefore the polarization is maintained by the use of two partial Siberian snakes in the AGS (section 2.2.3) and two full Siberian snakes [49]–[51] in each RHIC ring (section 2.2.4). Besides constant polarized beam deliveries to the experiments (PHENIX, STAR, *etc.*), the beam-development has also been continued. In FY2006, polarization and intensity for the average store in RHIC reached 60% and 1.5×10^{11} protons/bunch, respectively. Polarized protons were first accelerated to the highest beam energy of 205 GeV in RHIC with a significant polarization measured at top energy in FY2005 [52] and further high-energy beam commissioning has been continued in FY2006 towards the maximum beam energy of 250 GeV.

The brief history of the RHIC facility, which is focused on the polarized proton beam acceleration, is summarized in Table 2.1.

2.2.1 Polarized ion source

The polarized H^- has been generated by Optically Pumped Polarized Ion Source (OPPIS) [53] was constructed at TRIUMF from the KEK OPPIS source (Figure 2.3). H^+ ions are extracted from the 29 GHz Electric Cyclotron Resonance (ECR) proton source and enter the rubidium cell, which has polarized rubidium vapor by optically pumped using 795 nm laser and its polarization is kept by 2.5 T solenoid magnet. H^+ capture a polarized electron by H^+-Rb interaction and become hydrogen atom. Then, the hydrogen pass through a Sona region where the polarization is transferred from electron spin to H nucleus spin by the Sona transition [54]. H capture un-polarized electron from sodium vapor and become polarized H^- ions. It achieved 85% polarization for 10×10^{11} protons per pulse at FY2006.

FY2001 (2001–2)	Polarized proton acceleration was commissioned in one RHIC ring (Blue ring) with two snakes and one pC polarimeter.
FY2002 (2001–2)	All snakes and pC polarimeters in both RHIC rings were commissioned and operational. First transverse-spin polarized proton collisions were achieved.
FY2003 (2002–3)	Spin rotators at RHIC and pC polarimeter at AGS were commissioned and operational. First longitudinal-spin polarized proton collisions were achieved.
FY2004 (2003–4)	AGS warm snake was commissioned. Hydrogen gas jet target was commissioned and operated for the measurement of absolute polarization.
FY2005 (2004–5)	The calibration for pC polarimeters (in the blue-ring and yellow-ring) were completed.
FY2006 (2005–6)	AGS cold snake was commissioned.

Table 2.1: Summary of the history focused on the polarized proton acceleration in RHIC.

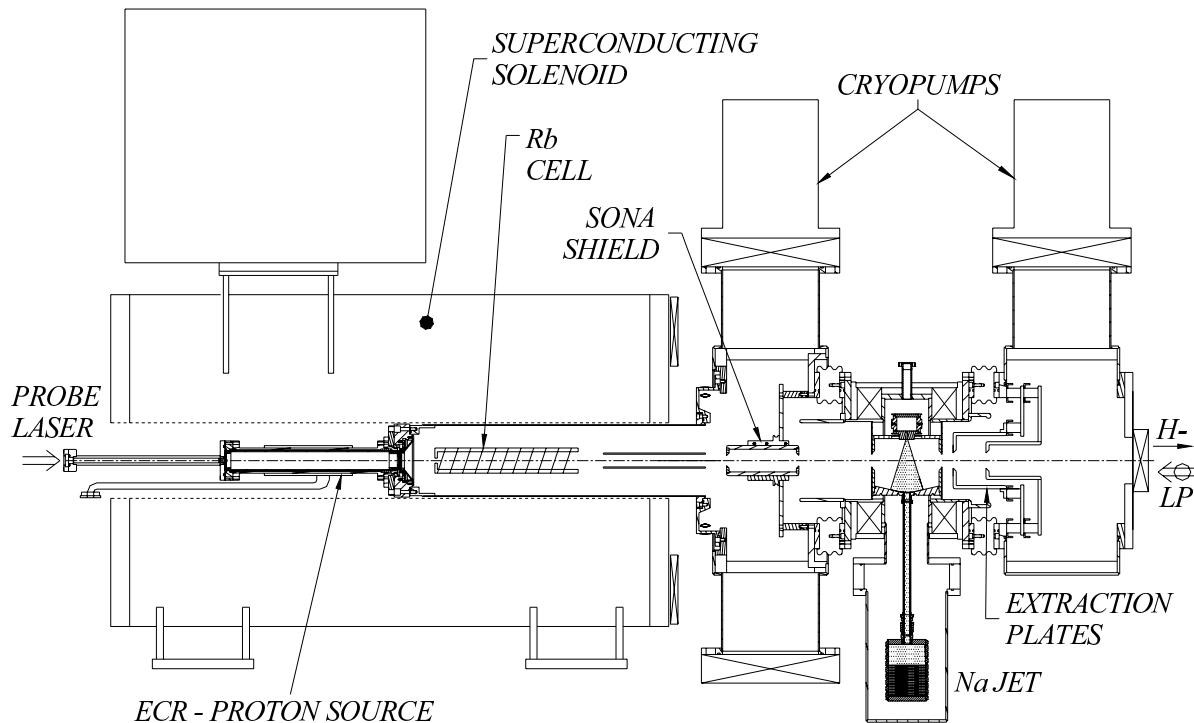


Figure 2.3: A schematic view of BNL OPPIS.

2.2.2 Depolarization resonance

Beam polarization during acceleration can be compromised by depolarization mechanisms driven by magnetic field. The evolution of the spin direction of polarized protons in external magnetic field is governed by the Thomas-BMT equation [55],

$$\frac{d\vec{P}}{dt} = - \left(\frac{e}{\gamma m} \right) \left[G\gamma\vec{B}_\perp + (1 + G)\vec{B}_\parallel \right] \times \vec{P}, \quad (2.1)$$

where the polarization vector \vec{P} is expressed in the frame that moves with the particle. γ is Lorentz factor, $\gamma = E/m$, and $G=1.793$ is the proton anomalous magnetic momentum. \vec{B}_\perp and \vec{B}_\parallel are perpendicular and parallel magnetic fields to the beam direction, respectively. This simple precession equation is very similar to the Lorentz force equation which governs the evolution of the orbital motion in an external magnetic field,

$$\frac{d\vec{v}}{dt} = - \left(\frac{e}{\gamma m} \right) \vec{B}_\perp \times \vec{v}. \quad (2.2)$$

From comparing these two equations, it can readily be seen that, in a pure vertical field, the spin precessed $G\gamma$ times orbital revolution; $G\gamma$, which is called spin tune, ν_{sp} , gives the number of spin precession frequency. The Thomas-BMT equation also shows that at low energies ($\gamma \sim 1$) longitudinal fields \vec{B}_\parallel can be quite effective to the spin motion, but at high energies, transverse fields \vec{B}_\perp is dominated.

There are two main types of depolarizing resonances.

- Imperfection resonances : It is driven by magnet errors and misalignment. It arises when $\nu_{sp} = G\gamma = n$, where n is an integer. Therefore, these are separated 523 MeV steps.
- Intrinsic resonances : It is driven by the focusing fields and arises when $\nu_{sp} = G\gamma = kP \pm Q_y$, where k is an integer, Q_y is a vertical betatron tune and P is a superperiodicity.

The superperiodicity is the number of repeated section of bending and focusing magnets. The betatron tune indicates a betatron frequency around ring. For example, $P=12$ and $Q_y \sim 8.8$ at the Brookhaven AGS. For most of the time during the acceleration cycle, stable spin direction coincides with the main vertical magnetic field. Close to a resonance, the stable spin direction is perturbed away from the vertical direction by the resonance driving fields. When a polarized beam is accelerated through an isolated resonance, the final polarization can be calculated analytically and is given by the Froissart-Stora equation [56],

$$P_f = \left(2e^{-\pi|\epsilon|^2/2\alpha} - 1 \right) P_i, \quad (2.3)$$

where P_i and P_f are the polarizations before and after crossing resonances. ϵ is the resonance strength and α is the rate of resonance crossing, $\alpha = d(G\gamma)/d\theta$. When the beam is slowly ($\alpha \ll |\epsilon|^2$), accelerated through the resonance, the spin vector will adiabatically follow the stable spin direction resulting in spin flip. However, for a faster acceleration rate partial depolarization

or partial spin flip will occur. Traditionally, the intrinsic resonances are overcome by using a betatron tune jump, which effectively makes α large, and the imperfection resonances are overcome with the harmonic corrections of the vertical orbit to reduce the resonance strength. At high energy, these traditional methods become difficult and tedious because the strength of imperfection resonances generally increase linearly with the beam energy. The calculated strength of imperfection and intrinsic resonances for AGS and RHIC are shown in Figure 2.4–2.6. To avoid these resonances, proton beams have been accelerated with rotating spin direction by snake magnets; partial snakes in AGS (section 2.2.3) and Siberian snake in RHIC (section 2.2.4).

2.2.3 Partial snakes in AGS

We used a warm and a cold snakes to preserve beam polarizations in the AGS acceleration. The warm snake is composed of a normal helical dipole magnet and has been used with a 5% snake strength ($s=0.05$, corresponds to 9 degrees) of original Siberian snake (section 2.2.4). As a result, spin tune obeys,

$$\cos(\pi\nu_{sp}) = \cos\left(\frac{s}{2}\right) \cos(\pi G\gamma), \quad (2.4)$$

which does not satisfy the imperfection resonance conditions. However, it can not overcome strong intrinsic resonances. It has been treated by the spin resonance excitation using a RF dipole [57]. A stronger Siberian snake could also be more effective to overcome strong intrinsic resonances in AGS. A superconducting helical dipole magnet as a 15% partial Siberian snake, the cold snake, is developed and in use.

2.2.4 Siberian snake and Spin rotator in RHIC

To preserve beam polarization in RHIC acceleration, we used Siberian snake which is composed of four superconducting helical dipole magnets, producing a central field of up to 4 T. It rotates the spin direction by 180 degrees without a net orbital distortion in each cycle. Spin motion image is shown in Figure 2.7 (Left). As a result, spin tune is change from $\nu_{sp} = G\gamma$ to $1/2$, independent of the beam energy. Therefore, neither imperfection nor intrinsic resonance conditions can ever be met as long as the betatron tune is different from a half-integer. With one or two Snakes all depolarizing resonances should be avoided. However, if the spin disturbance from small horizontal fields is adding up sufficiently between the Snakes, depolarization can still occur. This is most pronounced when the spin rotations from all the focusing fields add up coherently which is the case at the strongest intrinsic resonances. At RHIC, two Snakes can still cope with the strongest intrinsic resonance. It was successfully demonstrated to preserve the beam polarization at 60% in FY2006.

The Spin rotators, which is basically same composition as Siberian snake, placed around the experiments to rotate the spin direction by 90 degrees again without generating net orbit distortions. Spin motion image is shown in Figure 2.7 (Right). Spin rotators are required at the

intersection points of PHENIX and STAR to allow for the measurements of spin effects with longitudinally polarized protons; The spin rotators rotate the spin direction from the vertical direction into the horizontal plane on one side of the interaction region to provide longitudinal polarization and restore it to the vertical direction on the other side.

Design and construction of the snakes and rotators is discussed in [58, 59].

2.2.5 pC - and pp -CNI polarimeters

The single transverse spin asymmetry with the beam polarization P is expressed by,

$$A_N = \frac{1}{P}\epsilon_N \quad (2.5)$$

where ϵ_N is called raw asymmetry which is calculated by the production yields (section A.2.1 and A.3). We can extract P by measuring ϵ_N of the physics process which has known A_N .

The proton-carbon Coulomb Nuclear Interference (pC -CNI) polarimeter, which takes advantage of sizable analyzing power, $A_N^{pC} \sim 0.01$ at $-t \sim 0.01-0.02$ GeV², in the elastic scattering of polarized protons with carbon nuclei, serves as a fast feedback tool to tune up the beam acceleration. A_N^{pC} which originates from the interference between electromagnetic force and hadronic force was initially measured by the AGS experiment E950 [60].

The pC -CNI polarimeters are installed in the AGS and RHIC rings. They employed the ultra-thin carbon ribbon target (3.5 g/cm² thick and 5 μ m wide typically), which have been developed at IUCF. Polarimeters regularly collected one million events of recoil carbons from the elastic scattering process within 10 seconds. The pC polarimeter measures beam polarization every a few hours in a store and also measures bunch-by-bunch polarization.

The accuracy of the pC -CNI polarimeter was limited by the uncertainty of A_N^{pC} . The A_N^{pC} was measured at proton beam momentum in 22 GeV/ c and we extrapolates it to 100 GeV/ c using a theoretical calculation [61]. The uncertainty of A_N^{pC} directly affects the beam polarization uncertainty. For example, (1.00 \pm 0.32) scaling uncertainty was applied to 2001-2002 run.

Absolute beam polarization has been measured by a proton-proton (pp)-CNI polarimeter with a well calibrated polarized proton target; since it utilizes pp elastic scattering for beam and target protons, we can extract the beam polarization in high accuracy from the well known target polarization. The accuracy of absolute beam polarization, $\Delta P_b/P_b$ has reached to 0.06 [62, 63].

2.3 Experimental setup

A plan view of the IP12 experiment is shown in Figure 2.8 and schematic views of each component are shown in Figures 2.9 and 2.10. Detectors placed in very forward directions, centered on a production angle of 0°, behind the RHIC DX dipole magnets, which removed produced charged particles.

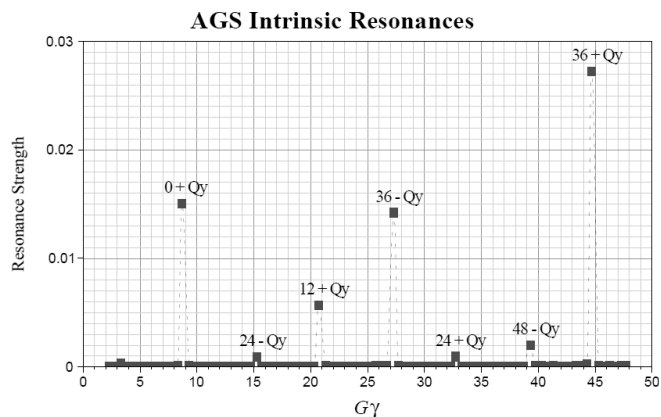


Figure 2.4: The calculated strength of intrinsic spin resonance through the AGS acceleration as a function of $G\gamma \sim 1.9 \times$ beam energy in GeV.

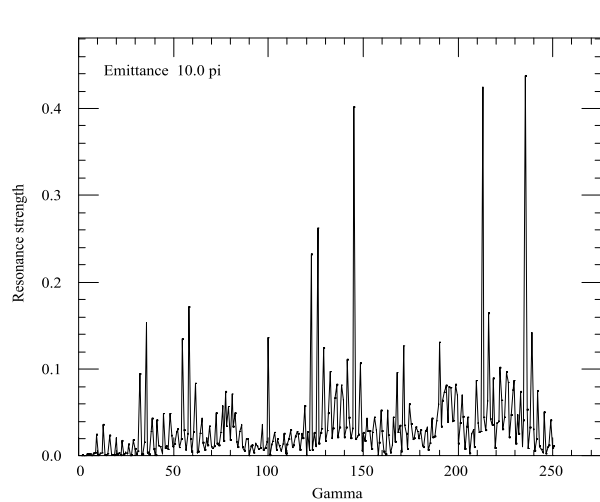


Figure 2.5: The calculated strength of intrinsic spin resonance through the RHIC acceleration as a function of $\gamma = E/m$.

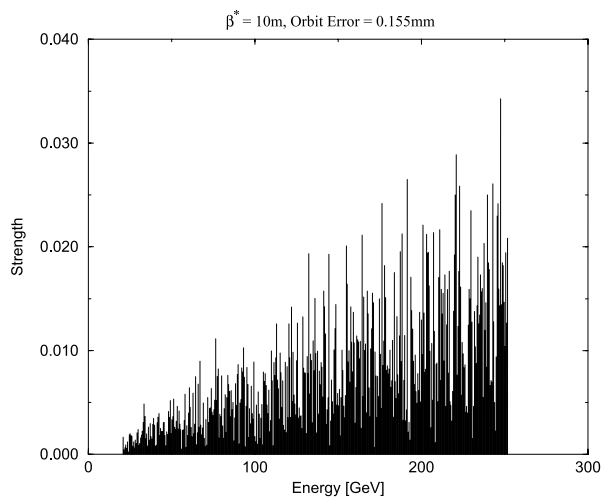


Figure 2.6: The calculated strength of imperfection spin resonance through the RHIC acceleration as a function of proton energy.

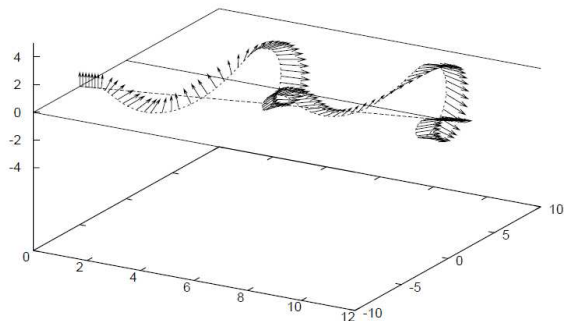
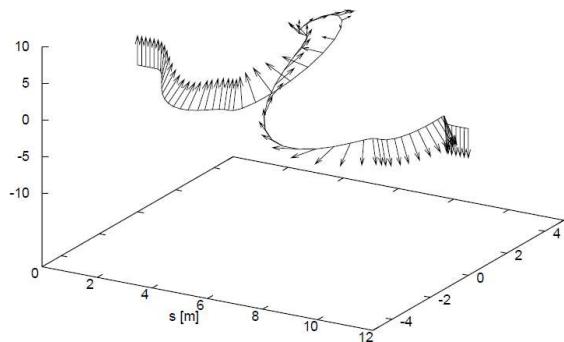


Figure 2.7: Spin motion images through Siberian snake (Left) and spin rotator (Right).

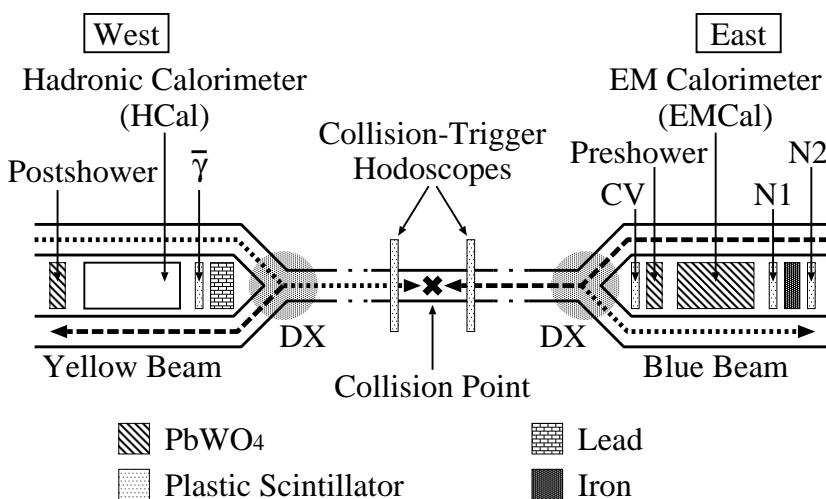


Figure 2.8: A plan view of the IP12 experiment, not to scale. Shown are the principle components of the experiment. Schematic views of the east and west components are shown in Figure 2.9 and 2.10, respectively.

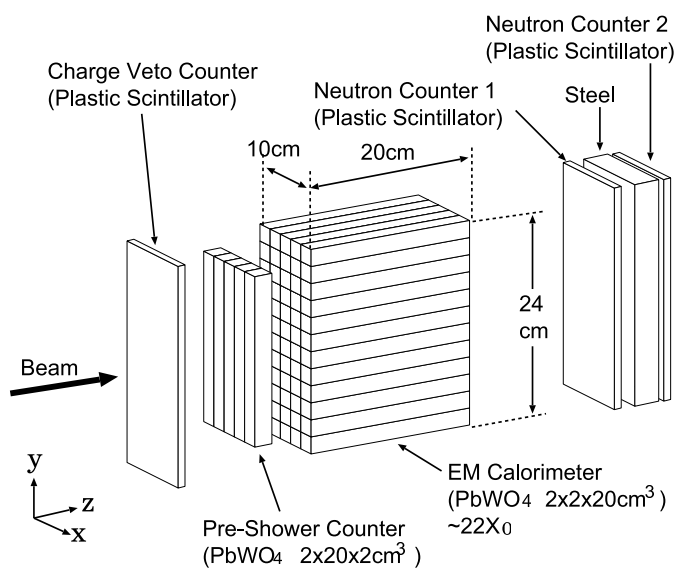


Figure 2.9: A schematic view of the east detector; the EMCal.

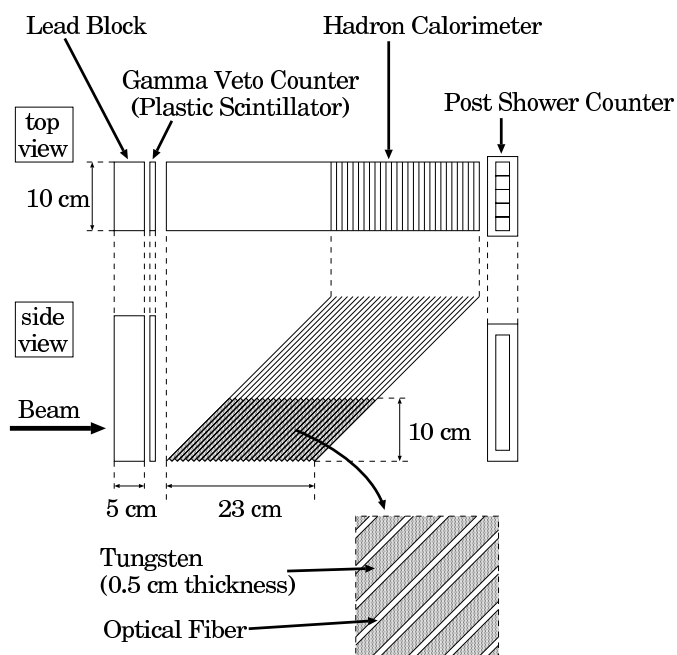


Figure 2.10: A schematic view of the west detector; the HCal.

2.3.1 Hodoscopes for beam-beam counters

The collision-trigger hodoscopes (beam-beam counters) were located ± 1.85 m from the collision point. The hodoscopes were formed with four sets of rectangular scintillators, with full azimuthal coverage, and pseudo rapidity acceptance $|\eta| = 2.2$ to 3.9 in the vertical and horizontal directions (Figure 2.11). The time resolution of the hodoscopes gave a vertex resolution of 23 cm. Details of the selection of collision event are discussed in section 3.2.

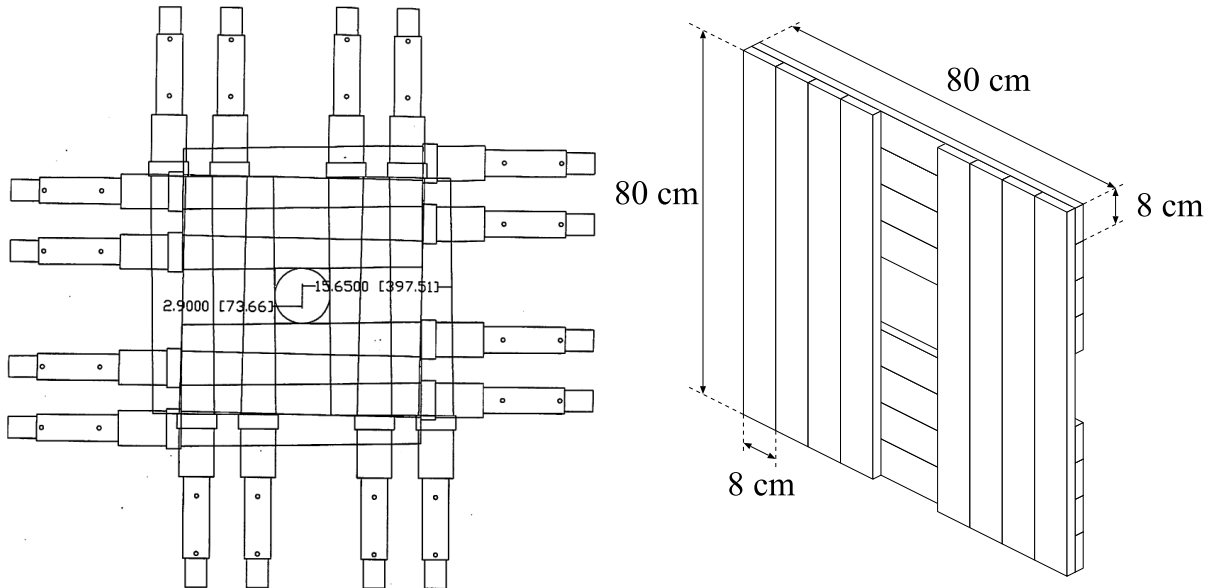


Figure 2.11: A schematic view of hodoscopes. Sensitive areas are shown in the left. A pair was placed ± 1.85 m up- and down-stream of collision point and covered $2.2 < |\eta| < 3.9$ in horizontal and vertical rapidity regions.

2.3.2 East detector : Electromagnetic Calorimeter

The east detector, facing the Blue beam, consisted of a scintillation counter as the charged particle veto (dimensions $10.5 \text{ cm} \times 25 \text{ cm} \times 0.6 \text{ cm}$, CV in Figure 2.8), a preshower electromagnetic calorimeter, and a 60-element array of PbWO_4 crystal electromagnetic calorimeter (EMCal). These were followed by two scintillation counters (dimensions $10 \text{ cm} \times 24 \text{ cm} \times 0.6 \text{ cm}$, N1 and N2 in Figure 2.8) with a 2.8 cm thick iron block between them to observe hadron shower.

The preshower and the EMCal arrays were built from PbWO_4 crystals of $2.0 \times 2.0 \times 20.0 \text{ cm}^3$, coupled to 3/4-inch photomultiplier tubes (HPK R4125) via silicone cookies and filters of 1/10 light reduction. The preshower consisted of five crystals forming a horizontal hodoscope, 10 cm (horizontal) \times 20 cm (vertical) \times 2 cm (deep). The EMCal was a 5 (horizontal) \times 12 (vertical) crystal array, 20 cm (22 radiation length, X_0) deep.

A schematic view is shown in Figure 2.9. Picture of the EMCal and its coordinate are displayed in Figure 2.12 and 2.13.

Test experiment for the EMCal at SLAC

The preshower and the EMCal were calibrated by the electron beam at Final Focus Test Beam (FFTB) Facility at SLAC. The FFTB electron beam was bunched as a few psec in 10 Hz and one bunch has a capability to have several electrons. We requested 10 GeV per electron at the experiment. The EMCal was located on the plate which can be moved less than 1 mm accuracy by electric operation. We corrected the gain tower by tower and evaluated the energy and position resolutions with this experiment.

Figure 2.14 shows the observed energy spectrum which was a sum of all tower energies. We confirmed the EMCal has a good energy linearity up to 100 GeV. In Figure 2.15, the energy resolution was evaluated over the inverse square root energy and it is described as,

$$\frac{\Delta E}{E} \approx \frac{0.11}{\sqrt{E(\text{GeV})}}. \quad (2.6)$$

The reason why the resolution was poor than the typical calorimeter made of PbWO_4 is the filter for light reduction to keep the energy linearity. For the measurement of two photons decayed from π^0 separately, we employed a clustering algorithm; gathering towers which have energy deposit above threshold. In this test, we also evaluated the effect for the energy measurement of the clustering algorithm with 0.1 GeV threshold. Figure 2.16 shows the cluster energies as a function of the incident position for 30, 50 and 70 GeV incident energies. Typically the cluster energy was reduced to 97% from the incident energy. If incident position was in the edge region on the EMCal, for example $y=10\text{--}12$ cm, the cluster energy was more reduced due to the shower leakage. These effects should be corrected based on this result.

The position is reconstructed by a centroid method with the logarithmic weights [64],

$$X = \frac{\sum W_i x_i}{\sum W_i}, \quad W_i = \text{Max} \left[0.0, \ln \left(\frac{E_i}{E_{sum}} \right) + W_0 \right], \quad (2.7)$$

where, x_i and E_i are the position and the deposit energy in each tower above threshold. E_{sum} is the sum of E_i , which is defined as the cluster energy. W_0 is a weight parameter and set to 4 in this analysis. The calculated position as a function of incident one is shown in Figure 2.17. The position was well reconstructed by this method and we obtained position resolutions as 1.4 mm to 1.0 mm for 30 GeV to 70 GeV electrons, respectively. With the simulation study, we consider it was not an intrinsic resolution, dominated by a beam spread (see next section). In the edge region, the response of the position reconstruction was changed due to the shower leakage as well as the energy response. It is corrected based on this result too.

Simulation by GEANT3

At the IP12 experiment, the noise level was worse than the test experiment; it corresponds to 0.4 GeV, and we required 0.5 GeV threshold for the clustering algorithm. For the estimation of the effect to the clustering, for example the energy reduction and the energy resolution etc., we prepared a Monte Carlo simulation for the EMCal detector by GEANT3 [65] and evaluated

its reliability by comparing with the result of SLAC experiment. Responses of the energy and position measurements from the simulation are plotted in Figure 2.16 and 2.17 with the experimental data. They agree well except for the position resolution; that for the simulation is 0.5 mm. It is because of the beam spread of electron beam which was mentioned as a few mm from the accelerator and we concern it was about 1.3 mm by this measurement. The clustering response with the 0.5 GeV threshold was studied by the simulation.

For the neutron measurement, we did not test by known hadron beam. The responses of the energy and position measurements for the neutron were estimated by the simulation, GHEISHA was used for hadron reactions [65], and the energy response is shown in Figure 2.18. The cluster energy fraction for neutrons is $E_{cluster} : E_n \sim 1 : 3$ with a $\sim 100\%$ energy resolution. As the neutron energy, we were using the cluster energy which were calibrated for photons since it is impossible to do the energy correction. The position resolution was estimated to be 5 mm.

2.3.3 West detector : Hadron Calorimeter

Actually we observed finite A_N in the neutron sample detected with the EMCal during run period. To confirm the neutron asymmetry, we installed a hadron calorimeter (HCal) facing the Yellow beam, in west side as shown in Figure 2.8. The setup included a photon veto ($\bar{\gamma}$ in Figure 2.8) which consisted of a 5 cm thick lead block followed by a scintillator, the HCal, and the postshower which was formed by five PbWO_4 crystals as a horizontal hodoscope³, to identify left and right production of the neutron. A schematic view is shown in Figure 2.10.

The HCal was a prototype of the ZDC which have been installed in the RHIC collision points (Details are described in section 5.2.1). The HCal had a transverse dimension of 10 cm \times 10 cm, and 2 interaction lengths, λ_I . The measured energy with the HCal was calibrated by the cosmic-ray data taking after the IP12 experiment and its resolution was expected to be 40–50% for the energy above 20 GeV. The position was reconstructed by the postshower using the centroid method and its resolution at the detector center was estimated to be 3–4 cm. The energy and position resolutions were estimated by the GEANT3 simulation which well reproduce the results of the test beam experiment [66]. The asymmetry was obtained by comparing the left and right scattering only.

2.3.4 Data taking

For the data taking, we required the trigger as a coincidence of following conditions,

- A collision event, with ≥ 1 Minimum Ionizing Particles (MIP) in each hodoscope, within a 5 ns collision window (pp collision event).
- Minimum energy deposit in detectors, more than ~ 5 GeV in the sum of EMCal or ~ 20 GeV in the HCal.

³Construction is same as the preshower in east detector.

We also synchronized it with the RHIC clock which is the same frequency of the beam and sent from the RHIC accelerator. The energies and signal timings of all detectors were recorded by Analog to Digital Converters (ADC; FERA LeCroy 4300B for the EMCAL and LeCroy 2249W for others) and Time to Digital Converters (TDC; LeCroy 2228A). The information of polarization directions (up, down or un-pol.) for both beams were provided by the RHIC accelerator and sorted by Programmable Logic Unit (PLU; LeCroy 4508). They were recorded by the coincidence register (LeCroy 4448). A block diagram of the readout system for the IP12 experiment is shown in Figure 2.19. The trigger rate was 100–300 Hz, and the average live time of the experiment was 75%. We collected 70 million and 8 million events for the EMCAL and HCal samples, respectively.

In this run period, average polarization for Blue and Yellow beams were $(0.116 \pm 0.002 \pm 0.020)$ and $(0.169 \pm 0.002 \pm 0.020)$ respectively, errors show the statistical and systematic natures. In addition, the scaling error, (1.0 ± 0.32) , which was from the calibration of the polarimeter analyzing power should be added (section 2.2.5). For the A_N measurement, we added the systematic errors to the scaling errors by quadratic sum. Total scaling errors were (1.0 ± 0.36) and (1.0 ± 0.34) for Blue and Yellow beams, respectively. Scaling errors should be affected to A_N as $1.0^{+0.57}_{-0.27}$ and $1.0^{+0.52}_{-0.25}$ for Blue and Yellow beams based on a correction of $1/P$ (equation 3.5).

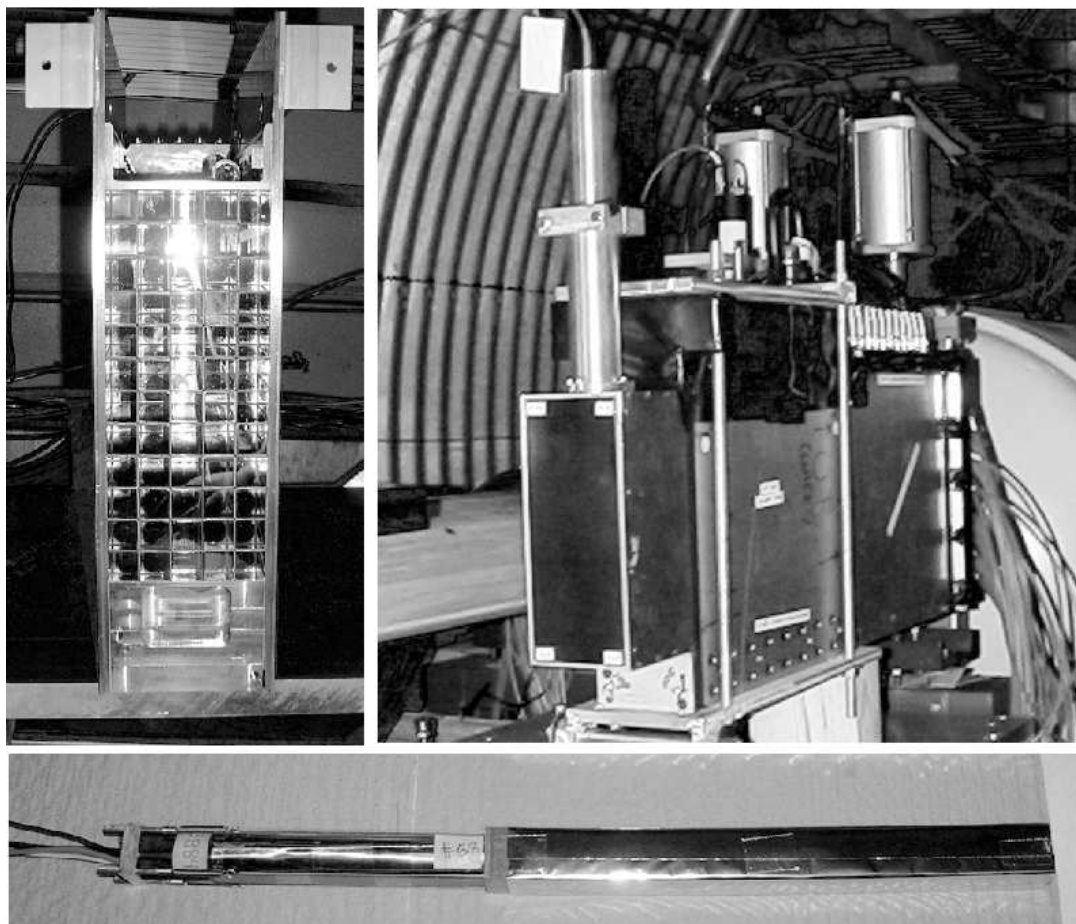


Figure 2.12: Pictures of the EMCAL. Single PbWO_4 crystal is mounted to the photomultiplier as bottom picture. The EMCAL consists of 5 times 12 PbWO_4 crystals as shown in the top left.

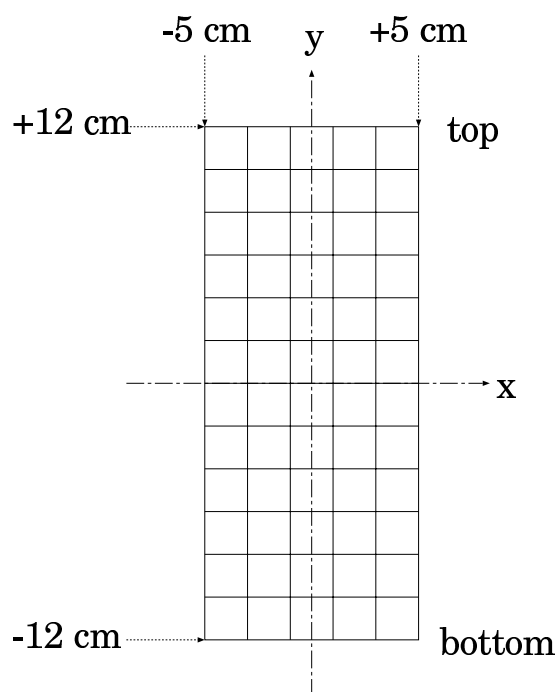


Figure 2.13: The definition of coordinates for the EMCAL.

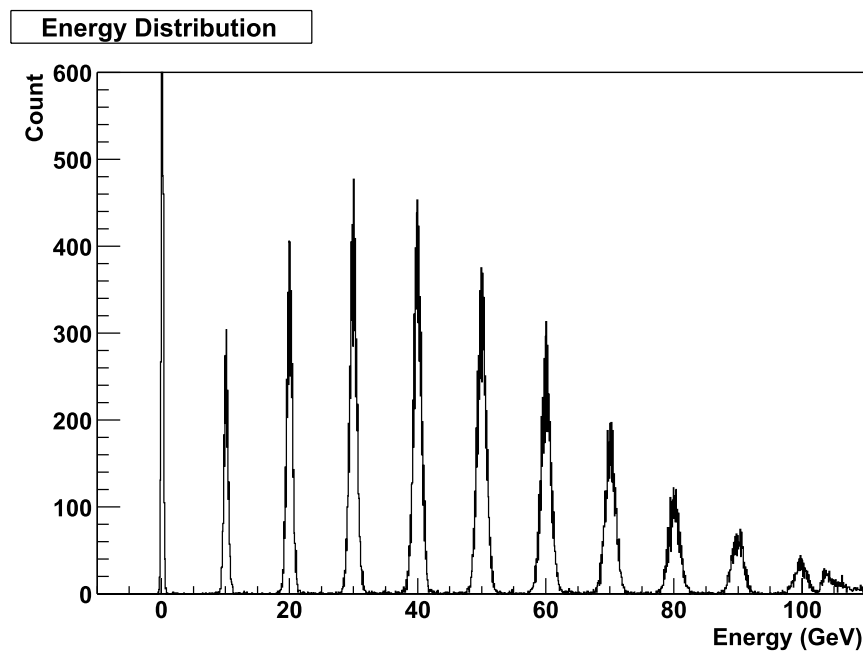


Figure 2.14: The energy spectrum for the electron beam at SLAC.

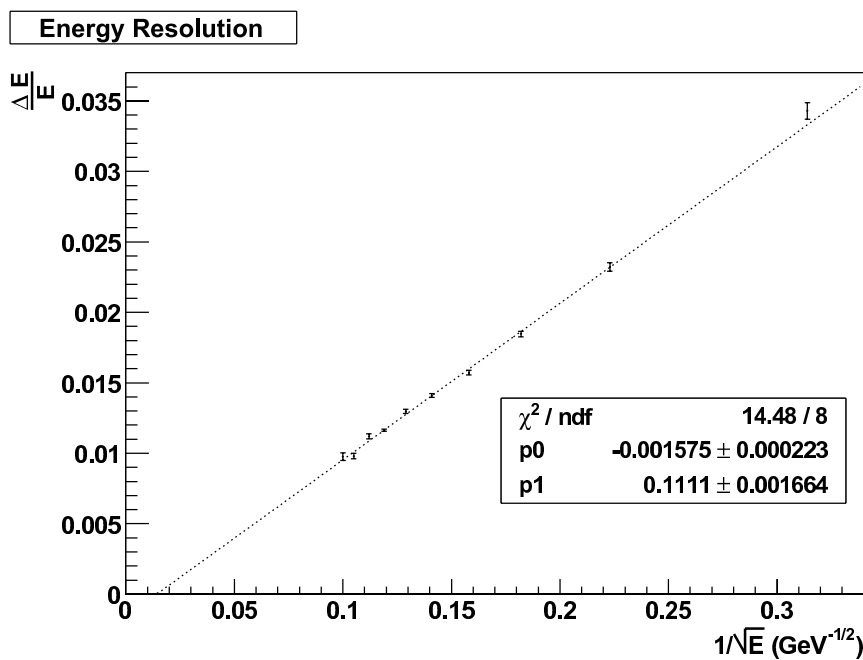


Figure 2.15: The energy resolution of the EMCAL for electrons as a function of the inverse square root energy.

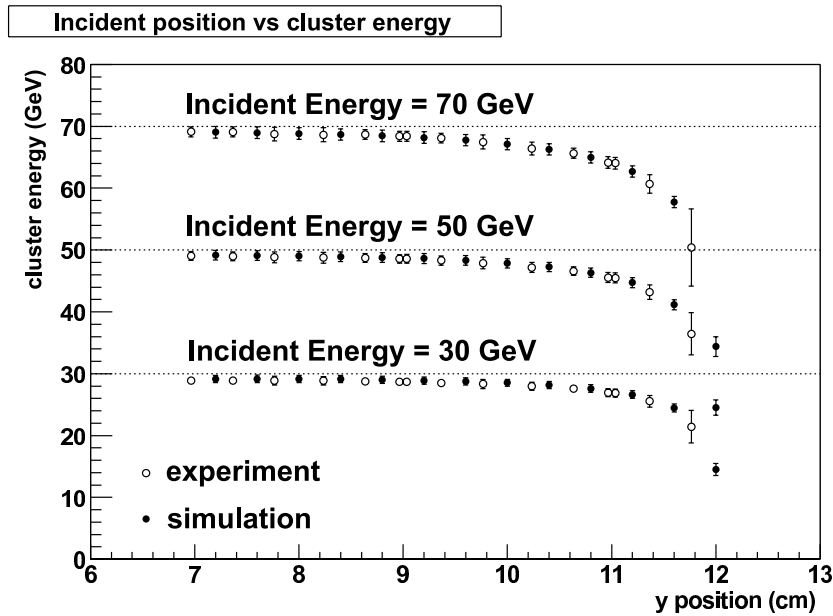


Figure 2.16: The responses of cluster energies for various incident energies as a function of incident y position. Closed and open circles indicate these from the test experiment and the simulation, respectively. The responses was changed in the region of 10–12 cm where is the edge region on the EMCAL (see Figure 2.13).

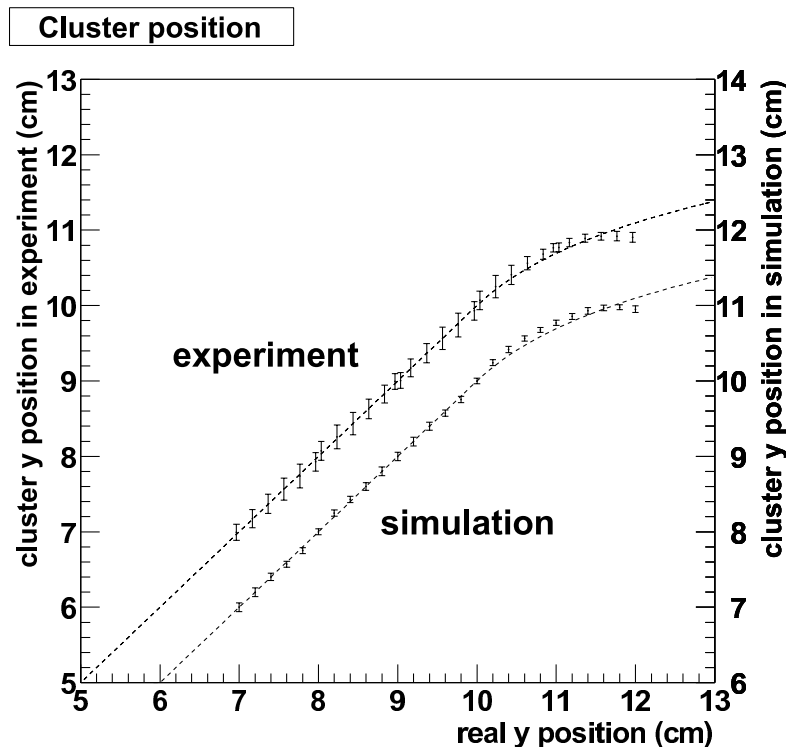


Figure 2.17: The reconstructed position *vs.* incident y position for 30 GeV electrons. Dashed lines are hand draws to guide the eyes. Error bars show the position resolutions which are about 1.4 mm and 0.5 mm for the experimental and the simulation values, respectively. These differences would be caused by the beam spread of electron and we concern it was about 1.3 mm by this measurement. The responses were changed in the edge region as well as the energy response.

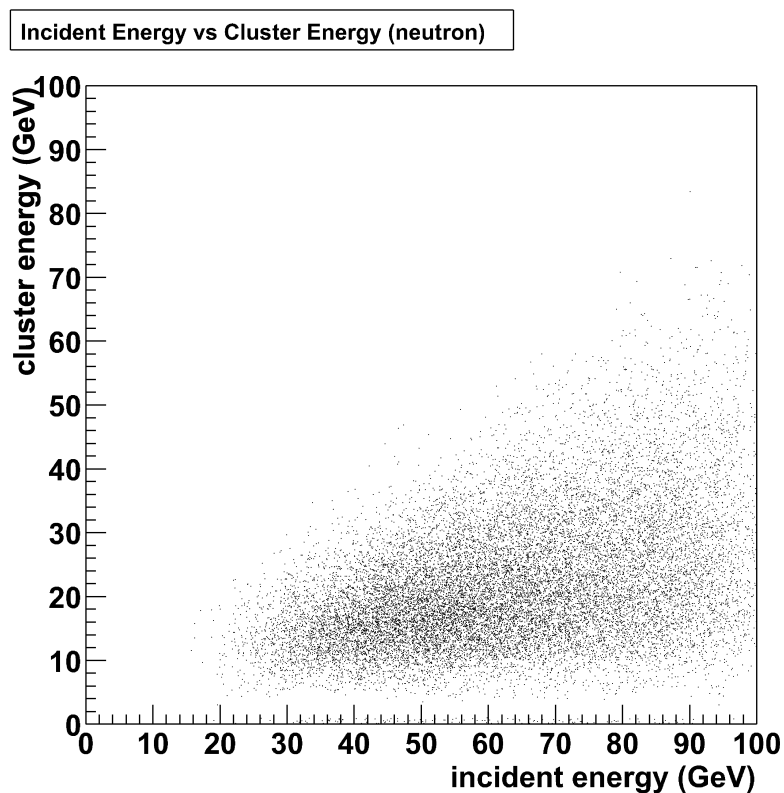


Figure 2.18: The cluster energy in the EMCal as a function of the incident energy in case of neutrons estimated by simulation. The EMCal was calibrated by the electron beams. The response was $E_{cluster} : E_n \sim 1 : 3$ with a $\sim 100\%$ energy resolution.

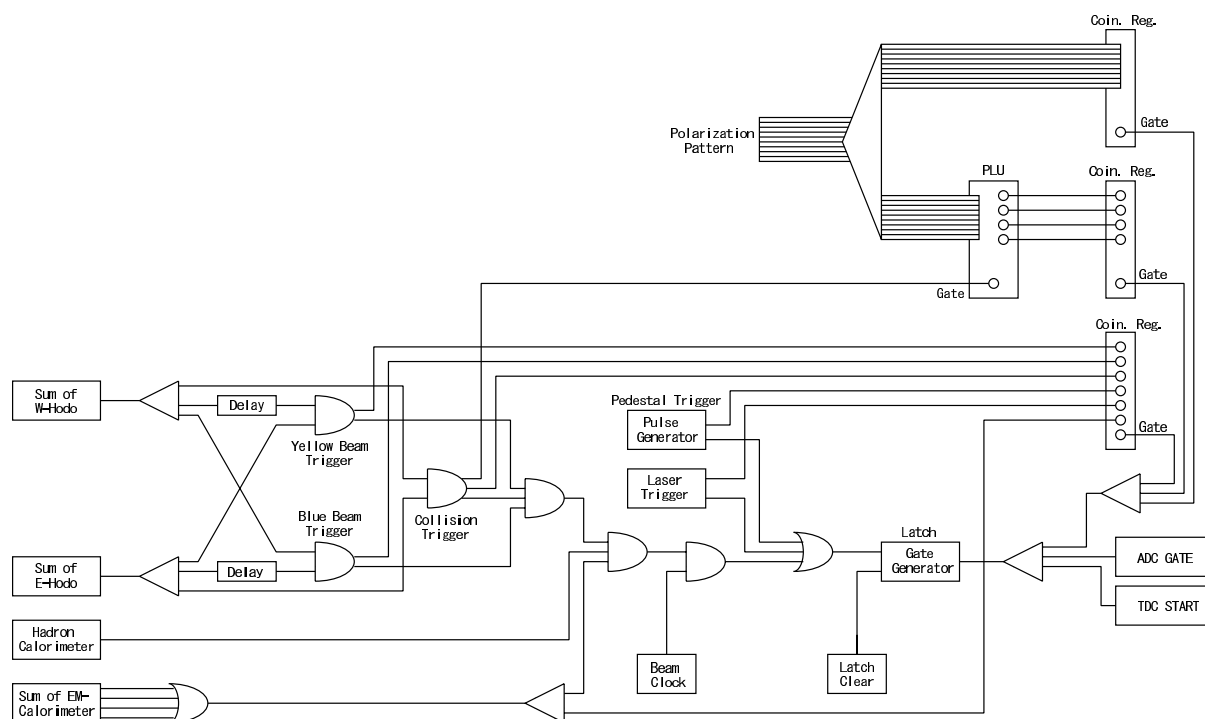


Figure 2.19: A block diagram of the read out system for the RHIC-IP12 experiment.

Chapter 3

Analysis

In this chapter, analysis procedure is introduced by the EMCal analysis. Analysis for the HCal is described in section 3.6.

3.1 Selection of the collision event

The collision was identified by the z -vertex distribution which was reconstructed by the time information of hodoscopes as follows,

$$z\text{-vertex} = (T_{ave.}^{E\text{-Hodo}} - T_{ave.}^{W\text{-Hodo}})c/2, \quad (3.1)$$

where $T_{ave.}^{E\text{-Hodo}}$ and $T_{ave.}^{W\text{-Hodo}}$ are average TDC values, which were truncated means after slewing correction in this analysis, of the east and west hodoscopes, respectively. c is light speed. Figure 3.1 shows a z -vertex distribution and the collision vertex was seen around 0 cm with the width of ~ 50 cm. We found peaks at ± 185 cm and they are called the beam gas events, a particle shower events by the interaction between the beam and particles in the beam pipe. Basically, the width of the beam gas event, ~ 23 cm, is dominated by the vertex resolution of hodoscopes.

For the selection of the collision events with the beam gas as low as possible we used the information of not only the z -vertex but also a TDC sum, which was defined as, $(T_{ave.}^{E\text{-Hodo}} + T_{ave.}^{W\text{-Hodo}})c/2$, and their correlation is shown in Figure 3.2. Since the RHIC clock was used as a common started TDC, the TDC sum of the beam gas should be smaller than the collision event; the beam gas occurred earlier. We selected the collision events by a diamond cut in off-line analysis as shown in Figure 3.2. Maximum contamination of the beam gas were evaluated by mirror images of the diamond cut toward the beam gas peaks on the z -vertex, which are ± 185 cm, at their peaks in the TDC sum, which is 1300 cm. Summary of beam gas contamination are listed in Table 3.1.

The beam gas contamination was studied by the data which were taken without the trigger bias; most of the beam gas events were removed by the hardware trigger at physics data taking (Figure 2.19). As a conservative estimation, the beam gas contamination was increased with the maximum beam intensity based on an assumption of a proportional relation between the

contamination of beam gas and the beam intensity. Normalized values also shown in Table 3.1. Finally, we conclude that the collision were identified with 3% beam gas contamination.

The total number of collision event : 620296

	The number of event in the diamond cut for beam gas	Fraction (%)	Normalized fraction to maximum intensities (%)
Blue beam gas	8977	1.45 ± 0.02	2.41 ± 0.026
Yellow beam gas	4951	0.80 ± 0.01	0.86 ± 0.012
Sum	13928	2.25 ± 0.02	3.27 ± 0.028

Table 3.1: The contamination of the beam gas to the the collision event. Contamination was estimated by the data without trigger bias which removed most of the beam gas events. The fraction of the beam gas was increased with the maximum beam intensity conservatively based on an assumption of a proportional relation between the beam gas contamination and the beam intensity.

3.2 Particle identification

As mentioned in section 2.3, only neutral particles were expected to be detected in the acceptance because any charged particles would be swept away by the DX magnet. The K_L^0 was a possible background for our measurement. At the ISR energies, the K_L^0 fraction to the neutron in a similar kinematical region was estimated to be 3-4 % from observed charged kaon samples [2]. We have included no correction for the K_L^0 background in this analysis and considered that data samples are mixture of photons and neutrons.

The photon and neutron samples were identified according to their behaviors.

- Photon (γ -ID) : Most of them convert in the preshower ($2.2 X_0$), and its shower is expected to be stopped in the EMCal ($22 X_0$). There would be no hit in the post scintillators (N1&N2).
- Neutron (n -ID) : Most of them pass through the preshower ($0.11 \lambda_I$) without interaction. It converts in the EMCal ($1.1 \lambda_I$) and the generated shower hits post scintillators.

As a common cut, we required no charge veto activity to remove unexpected charged particle event.

The purity of the photon and neutron samples were obtained by comparing the event fractions of the photon and neutron samples with and without the preshower activity by 15 MeV threshold. Figure 3.3 shows the energy distributions deposited in the EMCal for (a) the photon sample and (b) the neutron sample. The solid curves were selected the photon and neutron samples using the CV, N1 and N2 except for the preshower, namely γ -PID and n -PID. We define the actual number of photons and neutrons in γ -PID as $N_{\gamma}^{\gamma\text{-PID}}$ and $N_n^{\gamma\text{-PID}}$, respectively, and also define these for n -PID as $N_{\gamma}^{n\text{-PID}}$ and $N_n^{n\text{-PID}}$. In case of the photon sample, it is categorized with (dashed curve) and without (dotted curve) preshower activity; the number

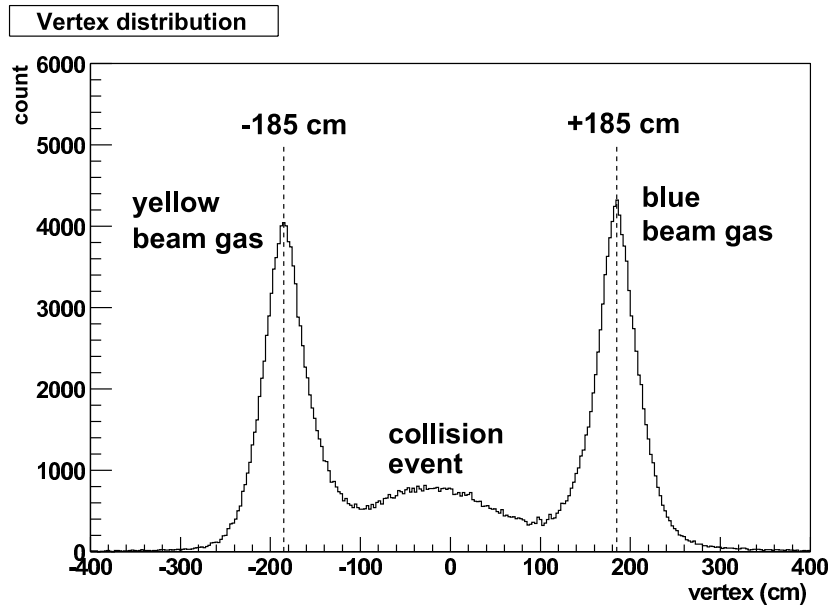


Figure 3.1: The z -vertex reconstructed by the hodoscopes.

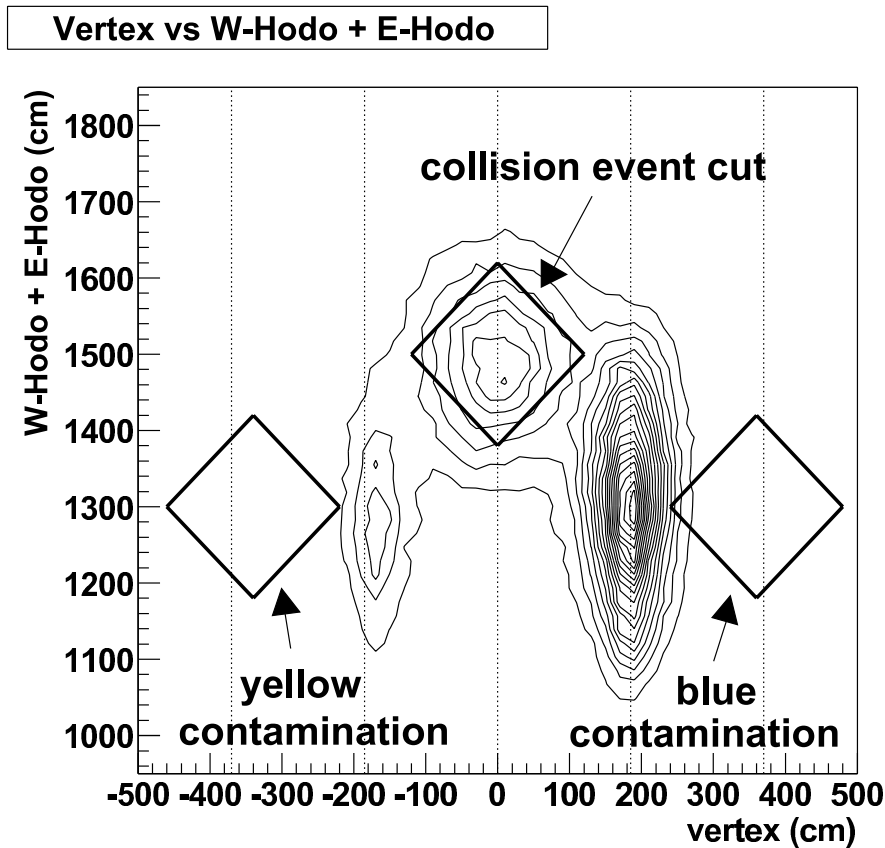


Figure 3.2: $(T_{ave.}^{E-Hodo} + T_{ave.}^{W-Hodo})c/2$ vs. $(T_{ave.}^{E-Hodo} - T_{ave.}^{W-Hodo})c/2 = z$ -vertex. Three islands from the left hand side indicate the yellow beam gas, collision and blue beam gas. The diamond cut, shown in this plane as "collision event cut", was applied to the selection of the collision event. Maximum contamination of the beam gas were evaluated by the mirror images of the diamond cut shown in this Figure.

of events with the preshower, $N^{\gamma\text{-PID } w \text{ Pre}}$, and without the preshower, $N^{\gamma\text{-PID } w/o \text{ Pre}}$ are expressed as follows.

$$\begin{aligned} N^{\gamma\text{-ID}} = N^{\gamma\text{-PID } w \text{ Pre}} &= P_{\gamma}^{\text{Pre}} \cdot N_{\gamma}^{\gamma\text{-PID}} + P_n^{\text{Pre}} \cdot N_n^{\gamma\text{-PID}}, \\ N^{\gamma\text{-PID } w/o \text{ Pre}} &= (1 - P_{\gamma}^{\text{Pre}}) \cdot N_{\gamma}^{\gamma\text{-PID}} + (1 - P_n^{\text{Pre}}) \cdot N_n^{\gamma\text{-PID}}, \end{aligned} \quad (3.2)$$

where P_{γ}^{Pre} and P_n^{Pre} are the conversion probabilities in the preshower for photons and neutrons which can be calculated by radiation length (0.9 cm) and interaction length (18 cm) for PbWO_4 ,

$$\begin{aligned} P_{\gamma}^{\text{Pre}} &= 1 - \exp[-2(\text{cm})/0.9(\text{cm})] \sim 0.892, \\ P_n^{\text{Pre}} &= 1 - \exp[-2(\text{cm})/18(\text{cm})] \sim 0.105. \end{aligned} \quad (3.3)$$

Same description can be used to the neutron identification by changing from γ -PID to n -PID¹ We can obtain actual number of photons and neutrons in each PID samples, $N_{\gamma}^{\gamma\text{-PID}}$, $N_n^{\gamma\text{-PID}}$, $N_{\gamma}^{n\text{-PID}}$ and $N_n^{n\text{-PID}}$, by those formulas. Finally, we obtained the actual number of photons in the photon sample and neutrons in the neutron sample, defined as $P_{\gamma}^{\text{Pre}} \cdot N_{\gamma}^{\gamma\text{-PID}}$ and $(1 - P_n^{\text{Pre}}) \cdot N_n^{n\text{-PID}}$, in equation 3.2.

Possible systematics is from the different efficiencies of the N1 and N2 cut for the hadron showers which are generated at the preshower and EMCAL. Naively, the efficiency for the conversion at upstream of the EMCAL seems to be 100% , and 0% in case of the conversion at down stream. We assumed the efficiency for the conversion at the EMCAL is 50% which is an average of up and downstream cases. Of course, it would be near 100% since the generated shower was boosted toward the N1 and N2. However, we can not estimate it correctly, 50% systematics was added conservatively. This systematics lies in only P_n^{Pre} which are required the N1 and N2 cut².

As a result, purities for the photon and neutron samples in the deposit energy above 20 GeV were 0.82 ± 0.07 and 0.994 ± 0.005 , respectively. Errors show systematic only; statistics are negligibly small. The particle identifications and purities are summarized in Table 3.2.

	Energy cut (GeV)	CV	Pre Shower (MeV)	N1	N2	Purity
Photon ID	>20	×	>15	×	×	0.82 ± 0.07
Neutron ID	>20	×	<15	○	○	0.994 ± 0.005

Table 3.2: The particle identifications for the photon and neutron samples. The energy cut for neutrons was applied to the measured energy calibrated for photons. ○ and × indicate the hit requirements of the scintillators as 1 MIP or more, and below 1 MIP, respectively. The purities are defined as actual numbers of photons and neutrons in the photon and neutron samples, respectively.

¹In this case, $N^{n\text{-ID}} = N^{n\text{-PID } w/o \text{ Pre}}$.

²50% is not directly to P_n^{Pre} . It should be added for relative values with and without the preshower activity, such as $(1 - P_n^{\text{Pre}})/(P_n^{\text{Pre}})$.

3.3 π^0 mass spectrum

π^0 candidates were constructed for all pairs of clusters with the requirements of both cluster energies above 15 GeV. Figure 3.4 shows the invariant mass spectra, $M_{\gamma\gamma}$, in samples with and without the γ -ID. Clear π^0 peak was seen and its width be narrower with the γ -ID. The reason why π^0 peak was shifted by 5 MeV with the γ -ID is the elimination of the events that the photon energy was lost by the conversion in upstream materials due to the requirement of no CV hit. Both mass shift and reduction in number of events are understood from the simulation using the upstream geometry, in particular the conversion in a 2.1 cm thick stainless steel plate just downstream of the DX magnet shown in Figure 2.8.

For the measurement of π^0 A_N , we used a larger data sample, without the γ -ID. The π^0 peak center for events without γ -ID was used for an absolute energy calibration and tower-by-tower for the final calibration. We selected events within ± 20 MeV of the peak center as π^0 sample and the background fraction was estimated using a Gaussian plus polynomial fit, it is $21 \pm 3.8\%$.

3.4 Asymmetry calculation

For the measurement of a left-right asymmetry, it is necessary to eliminate the zero degree region around the beam axis. The acceptance cut was applied as radii 5 – 40 mm from the center of the detector ($5 < r < 40$ mm), or production angles 0.3 – 2.2 mrad. The acceptance area was divided into 20 pieces in a radial pattern (see Figure 3.5). For the asymmetry calculation, we employed a square root formula which cancels other systematics, such as a detector asymmetry until third order by taking average of the number of events in one piece for spin up (N_ϕ^\uparrow) and opposite piece for spin down ($N_{\phi+\pi}^\downarrow$); those measurement should be same physics region due to parity invariance. More details are discussed in Appendix A. The asymmetry was calculated as,

$$\epsilon_N(\phi) = \frac{\sqrt{N_\phi^\uparrow N_{\phi+\pi}^\downarrow} - \sqrt{N_{\phi+\pi}^\uparrow N_\phi^\downarrow}}{\sqrt{N_\phi^\uparrow N_{\phi+\pi}^\downarrow} + \sqrt{N_{\phi+\pi}^\uparrow N_\phi^\downarrow}}. \quad (3.4)$$

It is smeared from the initial $A_N(\phi)$ by a smearing effect; the wrong assignment of the position due to the position resolution. After the correction of the polarization, P , and the smearing effect, $\epsilon_\phi^{smearing}$, we can obtain initial $A_N(\phi)$ as,

$$A_N(\phi) = \frac{1}{P} \frac{1}{\epsilon_\phi^{smearing}} \epsilon_N(\phi). \quad (3.5)$$

The asymmetry was calculated in counterclockwise starting at $\phi = \pi/2$ to check a sine modulation in the azimuthal angle which is characteristic of single transverse spin asymmetry. A_N is defined as an amplitude of the sine modulation as,

$$A_N(\phi) = A_N \sin(\phi - \phi_0), \quad (3.6)$$

where ϕ_0 allows a deviation of the polarization direction.

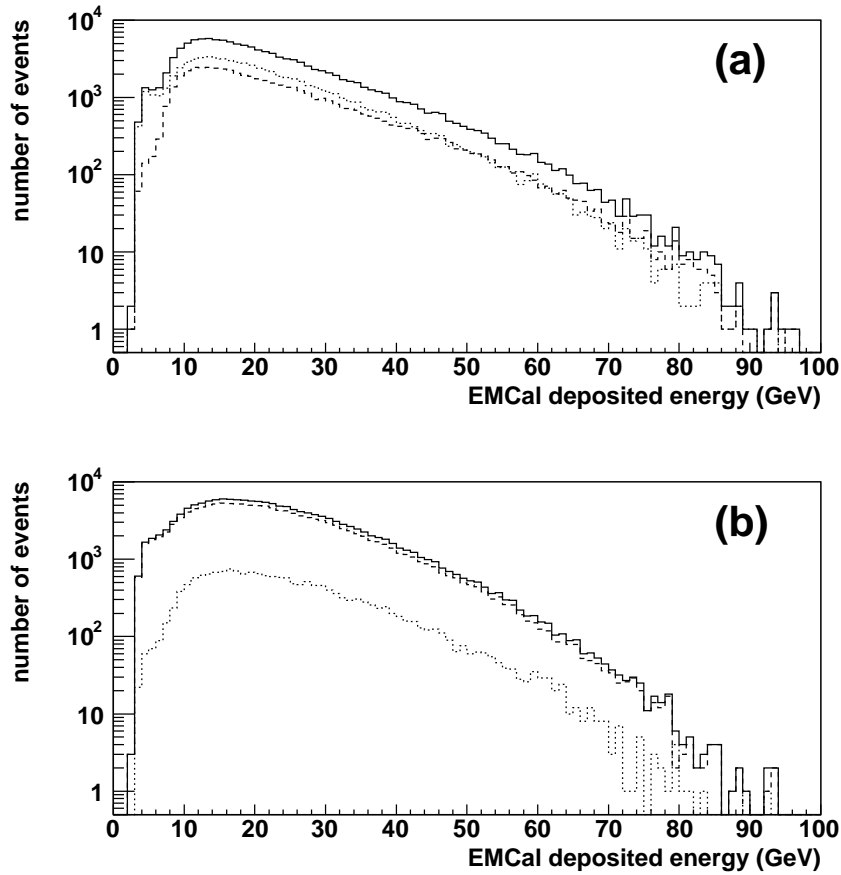


Figure 3.3: Panel (a) shows the deposited energy distribution in the EMCal for events used to select the photon sample required as no CV and no N1&N2. The solid curve displays all events, the dashed curve displays events with preshower energy (this is photo sample), and the dotted curve shows events with no preshower energy. Panel (b) shows the energy distribution for the events used to select neutrons required as no CV and N1&N2 activities. The solid curve is for all events, the dashed curve is for events with no preshower energy (neutron sample), and the dotted curve is for events with preshower energy.

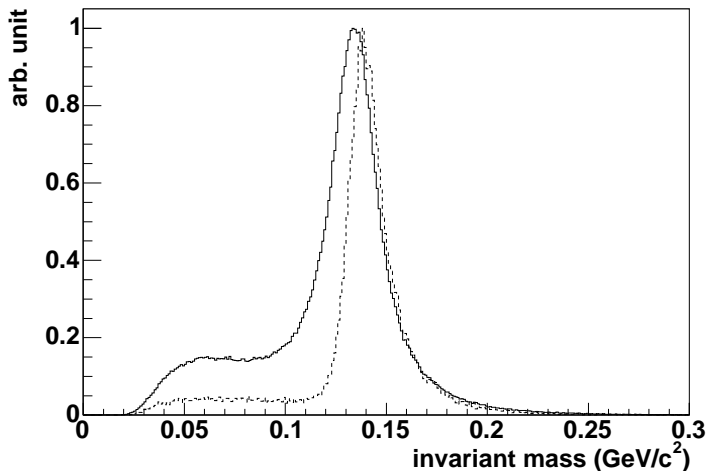


Figure 3.4: Invariant mass of pairs of energy clusters in the EMCal. We required energy above 15 GeV for both clusters. 444K events with no additional selection requirement (Solid) and that for 35K with photon identification (Dashed).

In the RHIC operation, both of the Blue and Yellow beams have been polarized. It enable us to measure the forward and backward asymmetries at the same time. Because the EMCAL was facing the Blue beam, the forward ($x_F > 0$) asymmetry was defined as using polarization patterns of the Blue beam. Similarly the backward ($x_F < 0$) asymmetry was using those of the Yellow beam only.

The $\epsilon_\phi^{Smearing}$ was estimated by the simulation and it was 0.92 for the neutron measurement with the 5 mm position resolution. Error was applied 100%, ± 0.08 , conservatively since that for the hadron reaction was just estimated by the simulation. It should be better in case of photons, with the position resolution ≈ 1 mm. However, we can just separate their particles statistically based on the study of section 3.2. In this analysis, same correction, $\epsilon_\phi^{Smearing} = 0.92 \pm 0.08$, was applied conservatively.

In this chapter, we show the ϵ_N only and the A_N values, after the correction of the polarization and the smearing effect, are shown in next chapter (chapter 4). The asymmetry calculations were performed for the neutron, photon and π^0 samples as shown in Figure 3.6. We could not see significant asymmetries in the photon and π^0 samples, but obvious large negative asymmetry appeared in the forward neutron sample. Line shows the fit result of the sine modulation (equation 3.6) and we obtained the ϕ_0 as -0.148 ± 0.069 . For the final values, we fixed $\phi_0 = -0.148$ for the forward ϵ_N based on this result, and $\phi_0 = 0$ for the backward ϵ_N assuming that the polarization direction of the Yellow beam was transverse completely. After the ϕ_0 was fixed, reduced χ^2 for the forward neutron being 1.47. We attributed a large reduced χ^2 to the scattered beam background observed higher rate in the EMCAL tower near the beam pipe. Whether or not the background has a spin dependence, it affects the azimuthal dependence of equation 3.6. Its contribution to the systematic uncertainty was estimated by the reduced χ^2 , where we have assigned a systematic uncertainty of $\sqrt{0.47} \times \delta A_N$. In case of backward asymmetries, ϵ_N of all samples are consistent with zero. It indicates the forward finite asymmetry is not fake from the measurement as well as the zero backward asymmetry.

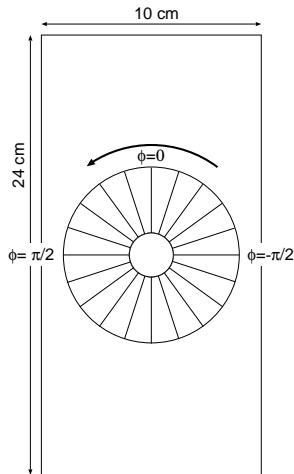


Figure 3.5: The acceptance definition for the azimuthal dependence of A_N .

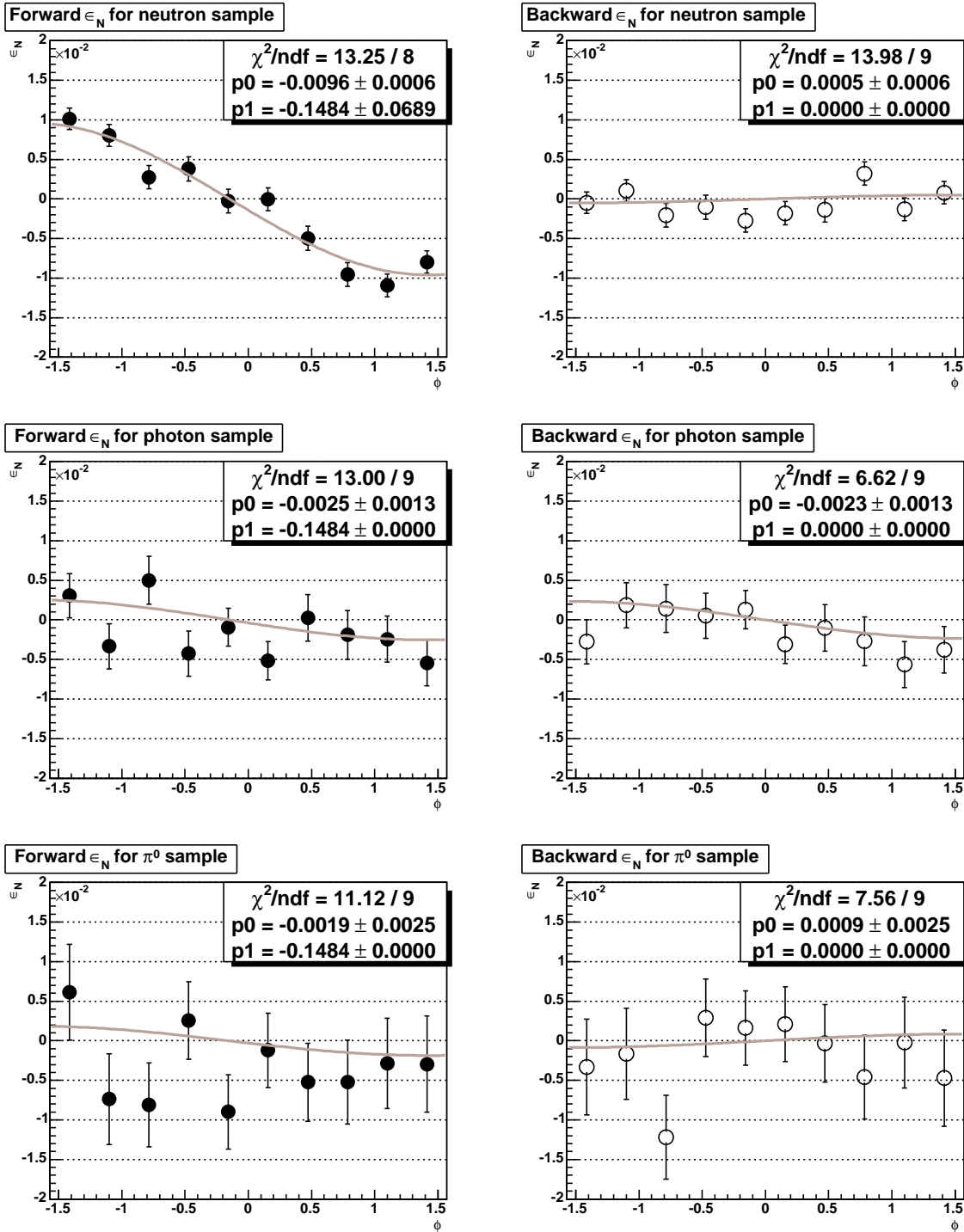


Figure 3.6: The azimuthal angle dependence of ϵ_N for the neutron (Top), photon (Center) and π^0 (Bottom) samples. Closed and open circles show the forward and backward asymmetries, respectively. They were fitted by the sine curve, $f(\phi) = p0 \times \sin(\phi - p1)$ as equation 3.6. $p1$ for the forward and backward were fixed as -0.1484 and 0.000 except for the forward neutron sample.

3.5 A_N decomposition

The asymmetry of neutrons (A_N^n) and photons (A_N^γ) were obtained by the A_N of the neutron (A_N^{n-ID}) and photon ($A_N^{\gamma-ID}$) identified samples through their relation of,

$$\begin{aligned} A_N^{n-ID} &= (1 - P_n) \cdot A_N^\gamma + P_n \cdot A_N^n, \\ A_N^{\gamma-ID} &= (1 - P_\gamma) \cdot A_N^n + P_\gamma \cdot A_N^\gamma, \end{aligned} \quad (3.7)$$

where P_n and P_γ are the purity of neutrons in the neutron sample and photons in the photon sample, respectively (section 3.4). Equation 3.7 is represented as,

$$\begin{aligned} A_N^n &= \frac{1}{P_n + P_\gamma - 1} \left[P_\gamma A_N^{n-ID} - (1 - P_n) A_N^{\gamma-ID} \right], \\ A_N^\gamma &= \frac{1}{P_n + P_\gamma - 1} \left[P_n A_N^{\gamma-ID} - (1 - P_\gamma) A_N^{n-ID} \right]. \end{aligned} \quad (3.8)$$

Statistical errors can be calculated as,

$$\begin{aligned} \delta A_N^n &= \frac{1}{P_n + P_\gamma - 1} \sqrt{(P_\gamma)^2 (\delta A_N^{n-ID})^2 + (1 - P_n)^2 (\delta A_N^{\gamma-ID})^2}, \\ \delta A_N^\gamma &= \frac{1}{P_n + P_\gamma - 1} \sqrt{(P_n)^2 (\delta A_N^{\gamma-ID})^2 + (1 - P_\gamma)^2 (\delta A_N^{n-ID})^2}. \end{aligned} \quad (3.9)$$

Systematic errors for P_n and P_γ are delivered by,

$$\begin{aligned} (\delta A_N^n)_{sys.} &= \frac{|A_N^{n-ID} - A_N^{\gamma-ID}|}{(P_n + P_\gamma - 1)^2} \sqrt{(P_\gamma)^2 (\delta P_n)^2 + (1 - P_n)^2 (\delta P_\gamma)^2}, \\ (\delta A_N^\gamma)_{sys.} &= \frac{|A_N^{n-ID} - A_N^{\gamma-ID}|}{(P_n + P_\gamma - 1)^2} \sqrt{(P_n)^2 (\delta P_\gamma)^2 + (1 - P_\gamma)^2 (\delta P_n)^2}. \end{aligned} \quad (3.10)$$

This decomposition can be applied to ϵ_N with the assumption of the same P and $\epsilon_\phi^{smearing}$ in equation 3.5. The ϵ_N for the neutron and photon after the decomposition are listed in Table 3.3.

In case of π^0 A_N , the dilution from background should be corrected as follows,

$$A_N^{\pi^0} = \frac{A_N^{\pi^0+bg} - r A_N^{bg}}{1 - r}, \quad \delta A_N^{\pi^0} = \frac{\sqrt{(\delta A_N^{\pi^0+bg})^2 + r^2 (\delta A_N^{bg})^2}}{1 - r}, \quad (3.11)$$

where r indicates the background fraction, defined as $r \equiv N^{bg} / (N^{\pi^0} + N^{bg})$. Detail of the dilution effect is explained in Appendix A. In this analysis, we used $r=0.210 \pm 0.038$ which was estimated in section 3.3. The ϵ_N for the background π^0 were estimated by the sample of the combinatorial background dominates in Figure 3.4, where ($|M_{\gamma\gamma} - 0.135| > 0.020$) with assuming that it was same as the background ϵ_N in the π^0 sample ($|M_{\gamma\gamma} - 0.135| < 0.020$). They were consistent with zero as shown in Figure 3.7. Results after the dilution correction are also listed in Table 3.3.

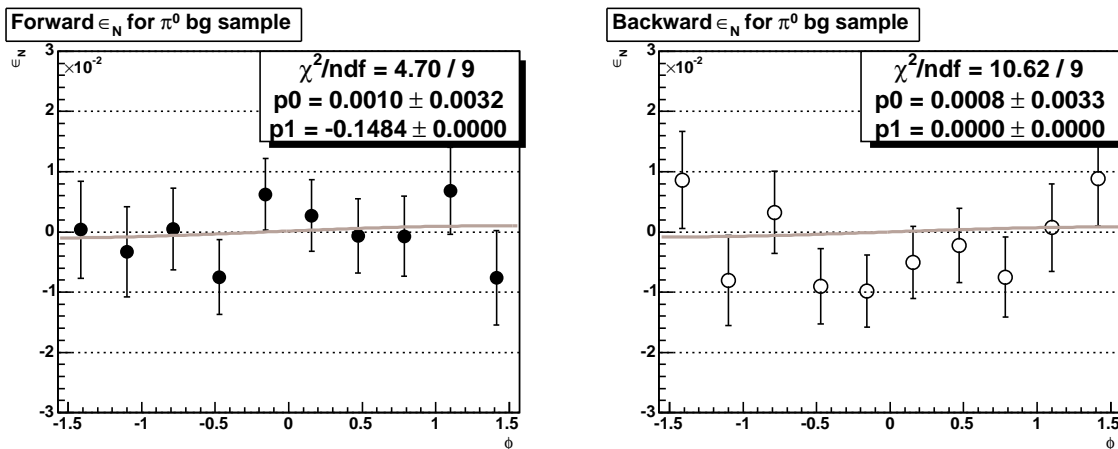


Figure 3.7: The azimuthal angle dependence of ϵ_N for the π^0 background. The definition is same as the π^0 asymmetries in Figure 3.6 but sample was selected the out of π^0 mass range in Figure 3.4, where $|M_{\gamma\gamma} - 0.135| > 0.02$.

$\epsilon_N (\times 10^{-3})$	Forward	Backward
Neutron	$-9.655 \pm 0.641 \pm 0.044$	$0.528 \pm 0.640 \pm 0.018$
Photon	$-0.974 \pm 1.588 \pm 0.742$	$-2.982 \pm 1.590 \pm 0.300$
π^0	$-2.614 \pm 3.300 \pm 0.000$	$0.869 \pm 3.322 \pm 0.000$

Table 3.3: The ϵ_N for the neutron, photon and π^0 after the decomposition. The first and second errors show statistics and systematics, respectively.

3.6 Neutron asymmetry measured with the HCal

To confirm the neutron asymmetry, we added the HCal facing the Yellow beam (section 2.3). With the robust photon veto system, most of photons converts in the 5 cm lead block ($8.9 X_0$)³ and is removed by requiring the gamma veto activity. Sample is expected to be almost neutrons.

Since the HCal can only reconstruct the x -position due to the structure of the postshower, the raw asymmetry was calculated as left-right asymmetry,

$$\epsilon_N = \frac{\sqrt{N_L^\uparrow N_R^\downarrow} - \sqrt{N_R^\uparrow N_L^\downarrow}}{\sqrt{N_L^\uparrow N_R^\downarrow} + \sqrt{N_R^\uparrow N_L^\downarrow}}, \quad (3.12)$$

where $L(R)$ indicates the acceptance of left (right) part which is defined as Figure 3.8. By this acceptance definition, the ϵ_N is reduced according to the $\cos\phi$ dependence as $\epsilon_N = A_N \times \int \cos\phi dS / \int dS$ and it is estimated to be 0.50. The ϵ_N is also smeared by the position resolution, 3–4 cm for the HCal, and total smearing was 0.37 estimated by the simulation. We added 100%

³The conversion ratio is estimated to be 99.99%

systematic error for the smearing effect due to the position resolution, it was $0.50-0.37=0.13$, in the same way of the EMCal analysis (section 3.4). Finally, we obtained the smearing effect, $\epsilon_{HCal}^{Smearing}$, was 0.37 ± 0.13 . In this data taking period (nearly end of 2001-2002 run), polarizations were improved to be 0.160 and 0.181 for the Blue and Yellow beams, respectively. Same systematic and scaling error which are mentioned in section 2.3.4 should be added.

In the EMCal analysis, scattered beam background was suggested by the large χ^2 from the fit result of the neutron asymmetry (section 3.4). In the HCal side, it was estimated by the comparison of events in the left and right acceptances. Figure 3.9 shows the reconstructed position distribution of the sample for A_N calculation and the background ratio was defined as a differences of counts in the left and right, $R_{HCal}^{bg} = (N_L - N_R)/(N_L + N_R) \sim 0.055$. However, the asymmetric distribution in the left and right can rise from other origins, for example, the beam axis was shifted to the HCal center and/or the postshower calibration was insufficient. We just added it as a systematic uncertainty.

Figure 3.10 shows the ϵ_N as a function of the measured energy with the HCal. According to the 40–50% energy resolution, events were distributed above 100 GeV broadly. They were merged in 90 to 100 GeV bin in Figure 3.10 and we used sample in 30–100 GeV for the asymmetry calculation. Significant negative neutron asymmetry was observed in the forward kinematics and not in the backward. Asymmetry does not show any dependence on the neutron energy within the energy resolution and we fitted them by constant to evaluate amplitudes which are written in Figure 3.10. We obtain the A_N after the correction of the polarization and the smearing effect as equation 3.5. The results are shown in the next chapter.

3.7 Multiplicity of hodoscopes associated with neutron sample

In Figure 3.11 we present the uncorrected multiplicity observed by the hodoscope for the neutron sample of the EMCal data with deposited energy above 20 GeV. The vertical and horizontal slats for each hodoscope overlap over 67% of the area, so that a correct estimation of the multiplicity is (uncorrected multiplicity)/1.67.

As seen in the figure, the multiplicity for the forward beam counter, in the direction of the neutron, is low, $\langle \text{multiplicity (forward)} \rangle \sim 2$. The multiplicity in the backward beam counter is large, $\langle \text{multiplicity (backward)} \rangle \sim 7$. Therefore, we observe a clear separation of beam and target fragmentation multiplicity, with a large asymmetry for neutrons produced forward from the polarized beam, in the direction of low multiplicity. This pattern was confirmed with the HCal data, where the forward and backward beam counters are reversed. The low forward multiplicity is consistent with a simple exchange process producing the forward neutron, $p \rightarrow n$.

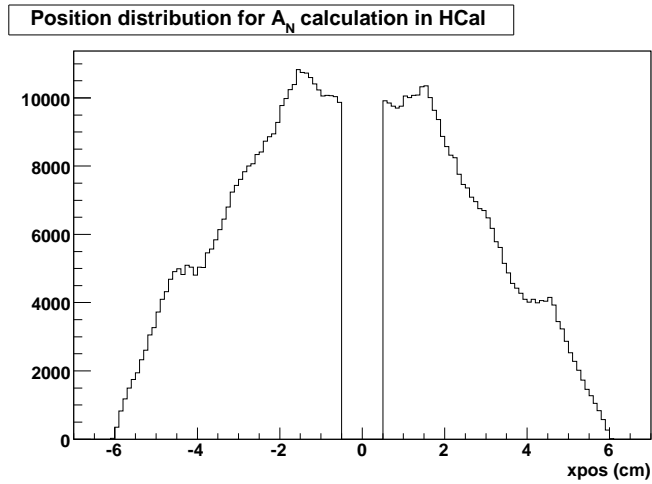
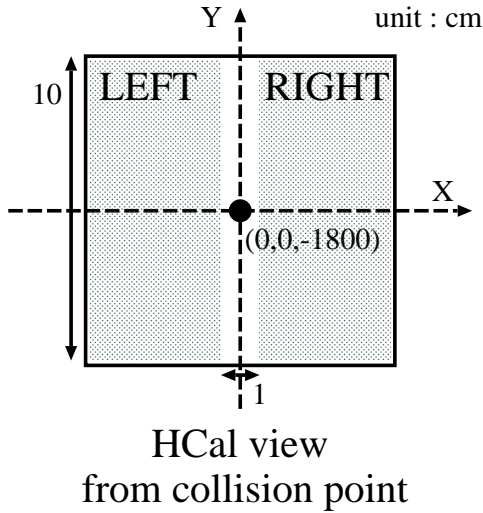


Figure 3.8: Definition of a coordinate for the HCal and the acceptance for the A_N calculation.

Figure 3.9: The reconstructed position distribution by the postshower. Negative and positive x positions were included in the left and right acceptances in Figure 3.8.

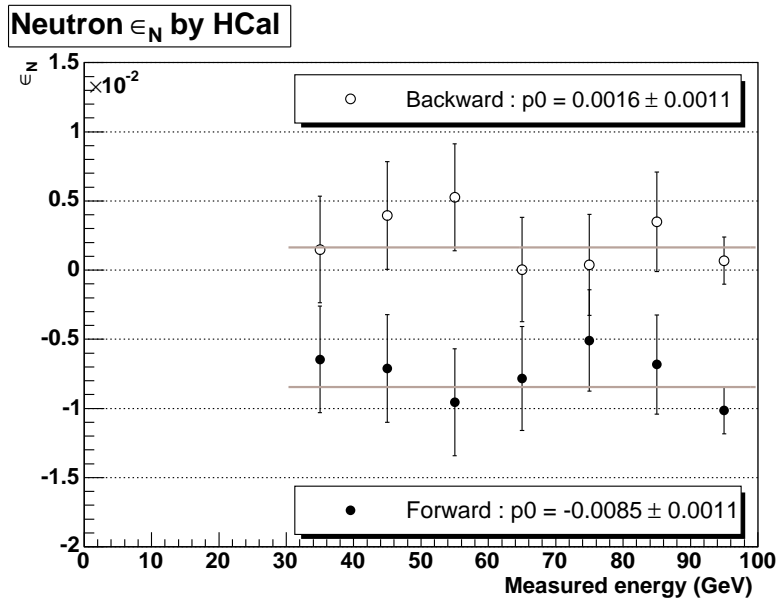


Figure 3.10: The energy dependence of ϵ_N for the neutron productions detected with the HCal. Closed and open circles show the forward and backward asymmetries, respectively. Events which were distributed above 100 GeV were merged in 90-100 GeV bin and we just say about the horizontal axis as the measured energy due to the 40–50% energy resolution.

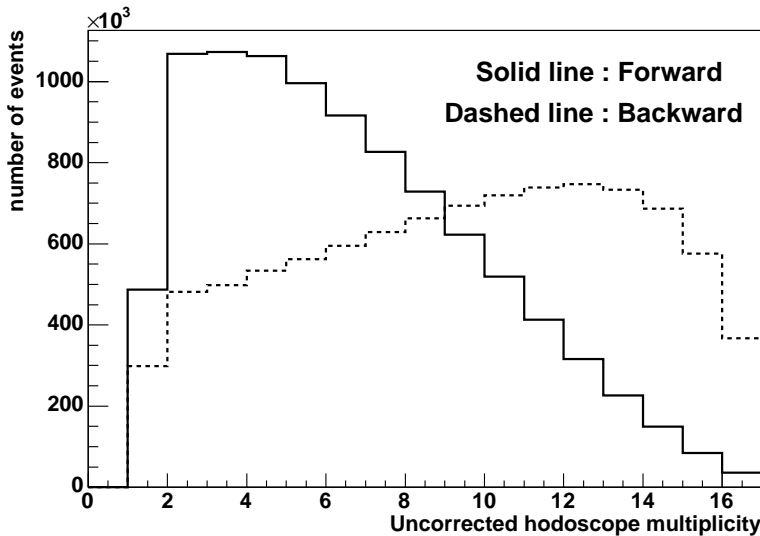


Figure 3.11: Uncorrected multiplicity observed by hodoscopes for the neutron sample of the EMCAL data with deposited energy above 20 GeV. The solid line shows that for the forward counter (east) and the dashed line shows that for the backward counter (west).

Chapter 4

Results of the IP12 experiment

A_N values after corrections of the polarization and smearing effect are summarized in table 4.1. The A_N of photon and π^0 are consistent with zero within the statistics, whereas significant large A_N in the forward neutron production was observed in the EMCal, and it was confirmed by the HCal. The magnitudes and signs are consistent, $A_N \approx -10\%$ with the scaling error $\times 1.00_{-0.25}^{+0.52}$. It was unexpectedly large asymmetry in this low p_T range; the range in p_T for the neutrons can only be estimated from the limits of the acceptance (equation 1.4), which give $p_T < 0.22$ GeV/ c , for the limits $E_n < 100$ GeV and $\theta_n < 2.2$ mrad, since polarization phenomena which has been observed so far seem to vanish in such low p_T (*cf.* pion A_N and Λ polarization, section 1.1).

The measurements of inclusive neutrons in the similar kinematics for unpolarized pp and ep collisions have been studied and these cross sections are consistent with the OPE model predictions (section 1.2). And the OPE model can suggest the finite neutron asymmetry by the spin-flip amplitude due to the pion exchange. It is necessary to check the cross section at the RHIC energy whether the OPE model is applicable or not.

As a further experiment, the PHENIX experiment has measured leading neutrons in similar kinematics with the improved energy measurement. The PHENIX experiment enables us to extract the cross section and the x_F dependence of A_N .

A_N results from EMCal		
	Forward	Backward
Neutron	$-0.090 \pm 0.006 \pm 0.009$	$0.003 \pm 0.004 \pm 0.003$
Photon	$-0.009 \pm 0.015 \pm 0.008$	$-0.019 \pm 0.010 \pm 0.004$
π^0	$-0.024 \pm 0.031 \pm 0.002$	$0.006 \pm 0.021 \pm 0.001$
A_N results from HCal		
Neutron	$-0.126 \pm 0.017 \pm 0.045$	$0.028 \pm 0.019 \pm 0.010$

Table 4.1: The results of A_N obtained at the IP12 experiment. Errors show the statistical and systematic, respectively. Scaling errors from the beam polarization for the EMCal, $1.0_{-0.25}^{+0.52}$ and $1.0_{-0.27}^{+0.57}$ for the forward and backward A_N , respectively, are not included. For the HCal, scaling errors are nearly same for the forward and backward A_N , it is $1.0_{-0.26}^{+0.52}$.

Part II

PHENIX experiment

Chapter 5

PHENIX experiment

We performed the leading neutron measurement at PHENIX as a further measurement of the IP12 experiment. Remarkably, the energy resolution was improved to $\sim 20\%$ at the 100 GeV neutron and it is expected to extract the cross section and the x_F dependence of A_N at $\sqrt{s}=200$ GeV. The data from 2005 run was used for the present thesis and one notable comment is that the beam polarization measurement was dramatically improved with the pp -CNI polarimeter to be $\Delta P/P \approx 0.09$. (*cf.* $\Delta P/P \approx 0.35$ at 2001-2002 run)

5.1 Overview

The RHIC-PHENIX experiment has measured leading neutrons by a Zero-Degree Calorimeter (ZDC) with a position-sensitive Shower-Max Detector (SMD) which cover ± 2.8 mrad of the forward and backward directions [66]. One ZDC module has $1.7 \lambda_I$ and $51 X_0$. It achieves 21% energy resolution for the 100 GeV neutron by locating three ZDCs in series. The SMD is an x - y scintillator strip hodoscopes, 7 for the x -coordinate and 8 for the y -coordinate, inserted between first and second ZDC modules. The neutron position can be obtained by calculating the center of gravity of showers which are generated in the first ZDC module. The position resolution depends on the neutron energy and it was estimated to be ~ 1 mm for the 100 GeV neutron, for example.

Since detectors are located in the same kinematics of the IP12 experiment, downstream of the DX magnet, charged particles from collisions are expected to be removed. A forward scintillation counter has been installed between the DX magnet and the ZDC to remove charged particle backgrounds from other sources in the same way of the IP12.

We prepared two sets of triggers for the neutron measurement. One is the ZDC self trigger and the other is a coincidence with charged particles. Charged particles are detected by a Beam-Beam Counter (BBC) which are placed in up and downstream of the collision point covering with $\pm(3.0-3.9)$ and 2π in η and ϕ spaces, respectively. We collected 6.5 million and 17.6 million events for the ZDC self trigger and that with a BBC coincidence, respectively.

5.2 Experimental setup

A plan view of the experimental setup for the leading neutron measurement at PHENIX is shown in Figure 5.1. Schematic views of whole PHENIX detectors [46] are also shown in Figure 5.2.

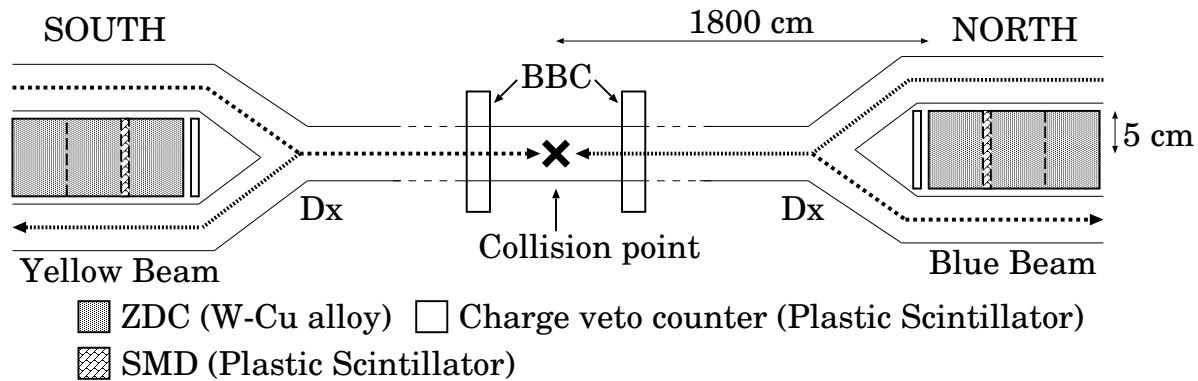


Figure 5.1: A plan view of the experimental setup at PHENIX, not to scale. Shown are the principle components for the leading neutron physics.

5.2.1 Zero Degree Calorimeter (Shower Max Detector, Charge veto counter)

The ZDC is a hadron calorimeter for the measurement of neutrons in very forward kinematics. The response of the ZDC was tested by 100 and 160 GeV proton beams by a prototype ZDC [66]. The prototype was not same as ZDCs which have been installed in RHIC¹. The prototype is composed of tungsten plates with PMMA²-based communication grade optical fibers. One prototype has $2.0 \lambda_I$ and four modules were located in series at the test experiment. On the basis of the test bench, present ZDC was designed.

Present ZDC consists of Cu-W alloy absorbers with PMMA-based communication grade optical fibers and it corresponds to $1.7 \lambda_I$ for one module,. Figure 5.3 shows a design of one ZDC module. A photomultiplier (Hamamatsu R329-2) collects Cherenkov lights from the optical fibers in one module. Three ZDCs are located in series ($5.1 \lambda_I$) at ± 1800 cm away from the collision point within the small acceptance, covering ~ 10 cm in the trasverse plane. It has been calibrated by observing the one neutron from peripheral heavy ion collisions; the 100 GeV neutron, diverged by less than 2 mrad from the beam axis, provides a single neutron peak as shown in Figure 5.6. It achieved 21% energy resolution for the 100 GeV neutron.

The position-sensitive SMD is an x - y scintillator strip hodoscopes inserted between first and second ZDC modules where is the maximum hadronic shower approximately. The x -coordinate (horizontal) is sampled by 7 scintillator strips of 15 mm width, while the y -coordinate (vertical)

¹In the RHIC ring, the ZDC is a global detector. They are installed in all interaction points and used as a luminosity monitor.

²Polymethylmethacrylate (Index 1.49)

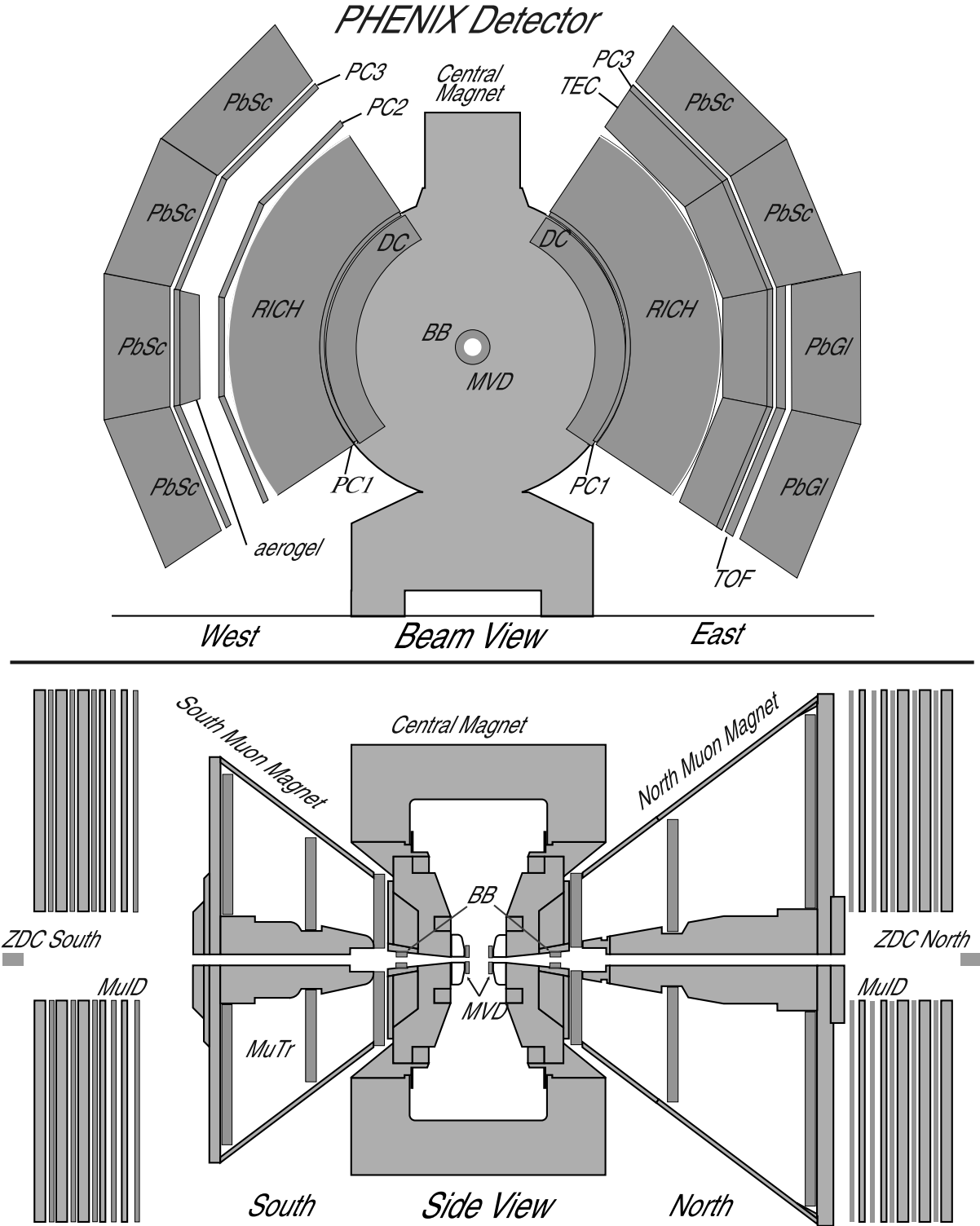


Figure 5.2: Schematic views of whole PHENIX detectors.

is sampled by 8 strips of 20 mm width, tilted by 45 degree (Figure 5.5). The active area in the transverse plane is 105 mm \times 110 mm (horizontal \times vertical). Their signals are collected by a multi-channel photomultiplier (Hamamatsu H6568, M16) through the Wave Length Shifter (WLS) fibers. The neutron position can be reconstructed using the SMD scintillators which have energy deposits above the threshold as follows.

$$x, y = \frac{\sum_i^{N_{multi}^{SMD}} ene(i) \cdot pos(i)}{\sum_i^{N_{multi}^{SMD}} ene(i)}, \quad (5.1)$$

where $ene(i)$ and $pos(i)$ are the pulse height leads to the energy deposit and the position for the i -th scintillator, respectively. The number of scintillators above threshold is shown as N_{multi}^{SMD} and it is defined as a SMD multiplicity. The response of position measurement is studied by the Monte Carlo simulation in chapter 6. SMD scintillators were calibrated relatively by MIP peaks of the cosmic-ray data taken at the beginning of 2003 run. Figure 5.7 shows a raw ADC spectrum of the cosmic sample and we can see a pedestal and MIP peaks around 50 and 100 channels, respectively. Actually the cosmic data was collected by usual CAMAC system which was different gain to the PHENIX data acquisition system. A LED light was used for the gain connection between them. We calibrated the MIP peak about 70 channel after the pedestal subtraction and require a threshold as 40 channel for the centroid method. However there is a large uncertainty for the gain connection by the LED system. It would affect the estimation of the detector efficiency by the simulation in section 7.7. Fortunately, we can estimate the relative SMD efficiency for the real and simulation data by selecting nearly pure neutron samples (section 7.5).

For the charged particle elimination, the 3.3 mm thick plastic scintillator is installed in front of the ZDC. It covers 10 \times 12 cm, it is almost same acceptance as the ZDC. It is calibrated for matching the MIP peak to 100 channel as shown in Figure 5.8. Typically we require the cut by 50 ch for the selection of charged events.

A whole ZDC system is shown in Figure 5.4. In this analysis, we used a SOUTH ZDC detector which is facing Yellow beam only. Its coordinates are defined according to the PHENIX coordinate system as shown in Figure 5.9.

5.2.2 Beam Beam Counters

The BBC consists of 64 one-inch mesh dynode photo multiplier tubes (Hamamatsu R6178) with 3 cm thick quartz radiators as a Cherenkov radiator (Figure 5.10). BBC elements are mounted as the beehive structure around the beam pipe (Figure 5.11) and located ± 144 cm away from the interaction point with the coverage of $3 < |\eta| < 3.9$ and 2π in azimuthal angle.

The BBCs are used to measure the collision vertex point in a direction of the beam axis using hit time informations in NORTH and SOUTH parts. The time resolution of the single BBC element is 52 psec. They are used as the PHENIX minimum bias trigger; they can take about 50% inelastic interaction for pp collision at $\sqrt{s}=200$ GeV (Details are in section 5.2.4).

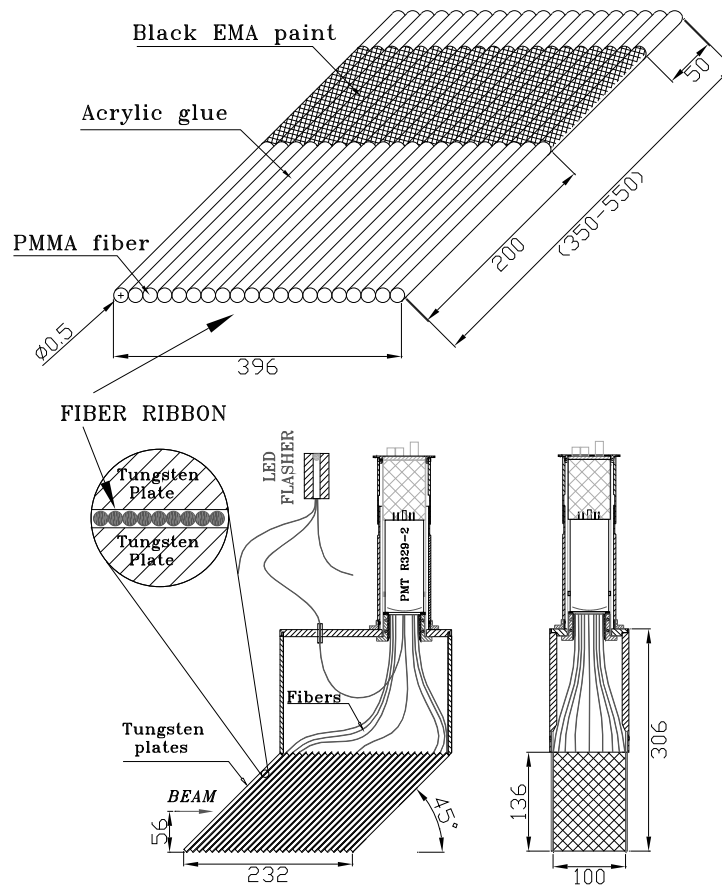


Figure 5.3: A schematic design of the present ZDC module. Units are shown in mm.

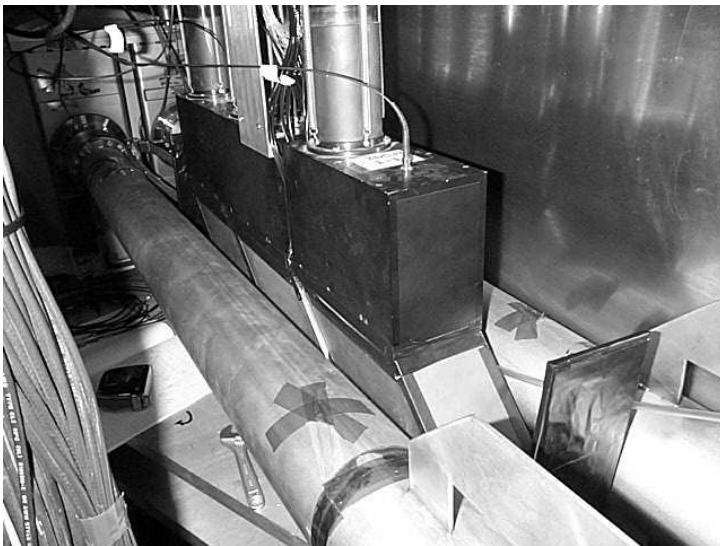


Figure 5.4: A picture of whole ZDC system. Three ZDCs are placed in series and the SMD is installed between first and second ZDC modules. The scintillator as a charge veto counter is placed in front of the ZDC.

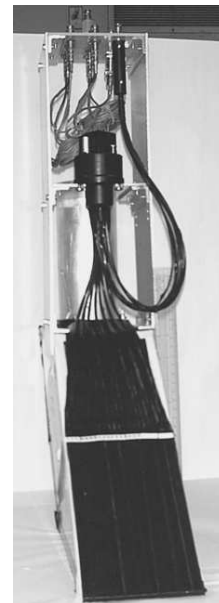


Figure 5.5: A picture of SMD; 7 scintillators for the x -coordinate.

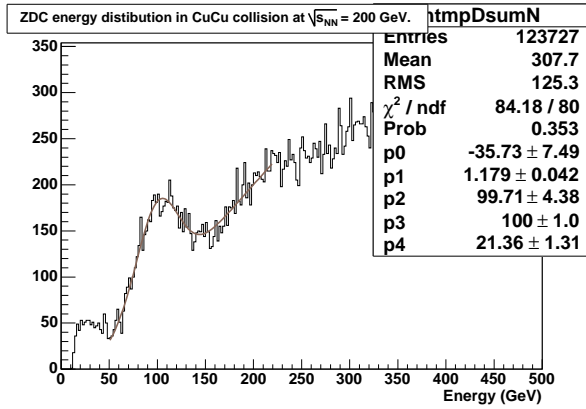


Figure 5.6: The energy distribution with the ZDC in CuCu collision at $\sqrt{s_{NN}} = 200$ GeV. We can see an one neutron peak clearly.

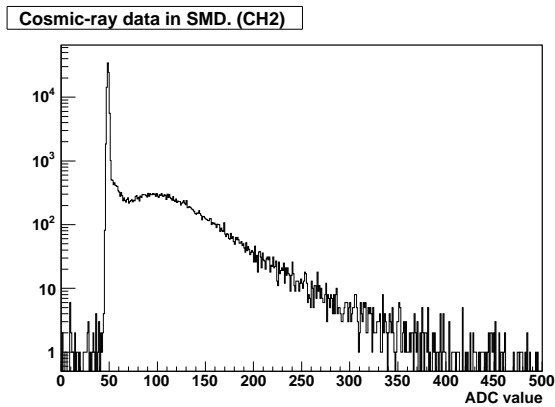


Figure 5.7: The ADC distribution of the SMD for the cosmic-ray data. The pedestal and MIP peaks are shown around 50 and 100 ch, respectively.

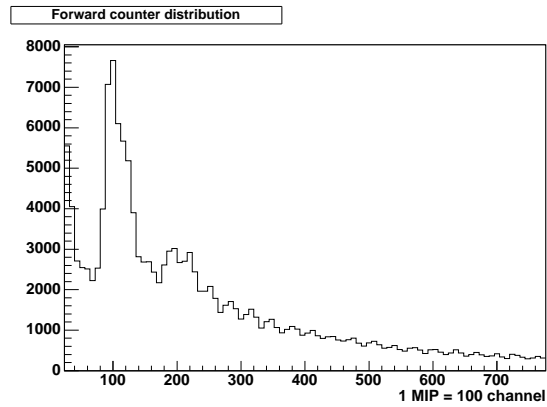


Figure 5.8: The charge distribution of the charge veto counter in pp collision. It is calibrated by the MIP peak to 100 ch.

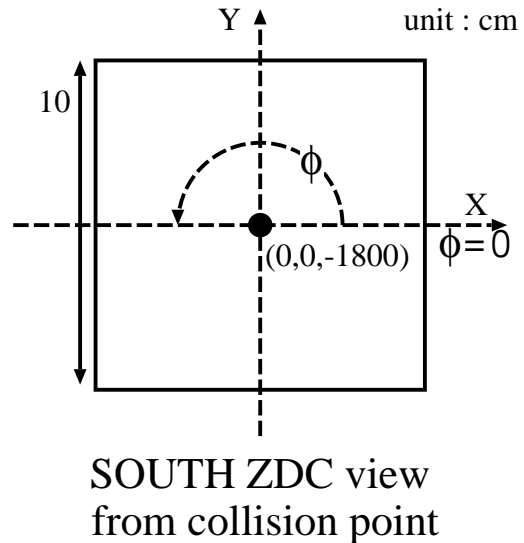
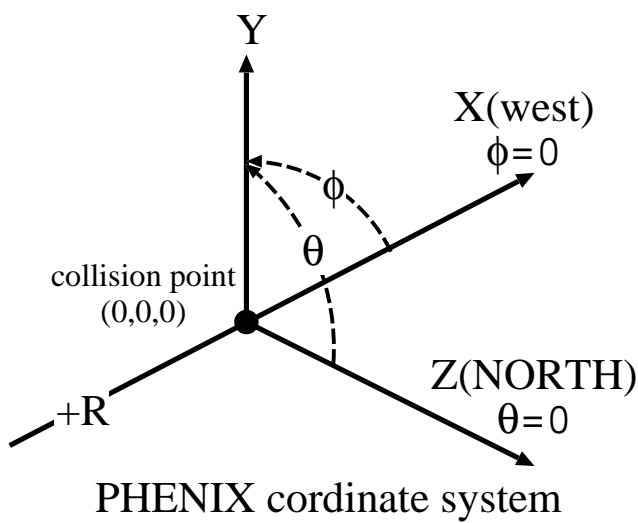


Figure 5.9: The coordinates for the SOUTH ZDC according to the PHENIX coordinate system.

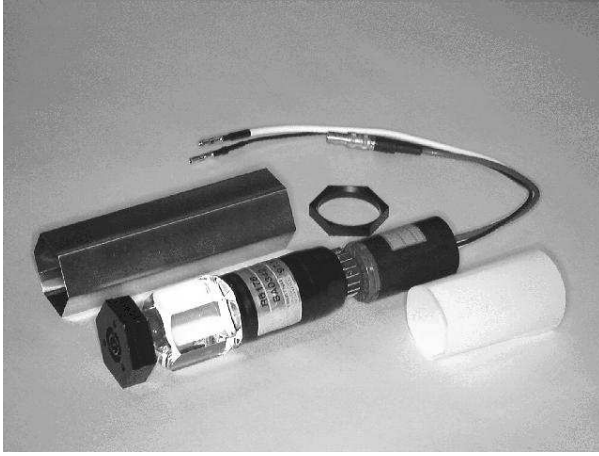


Figure 5.10: A single BBC consists of a one-inch mesh dynode photo-multiplier tube with a 3 cm thick quartz radiator.

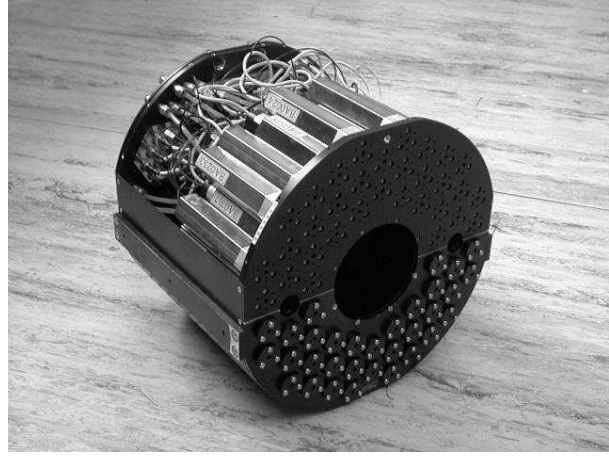


Figure 5.11: A BBC array consists of 64 BBC elements. They are installed ± 144 cm away from the collision point with the coverage of $3 < |\eta| < 3.9$ and 2π in azimuthal angle.

5.2.3 PHENIX data acquisition system

PHENIX detectors are designed to make measurements with high interaction rate; design interaction rates for pp and AuAu are 500 kHz and few kHz, respectively. PHENIX data acquisition (DAQ) system [68, 69] has a capability for such high rate through the pipelined and dead-timeless features implemented to the detector front ends.

The schematic diagram of the PHENIX DAQ is shown in Figure 5.12. Signals from detector are converted to digital information and buffered in Front End Modules (FEM) which include signal amplifiers, shapers and time decisions. Each subsystems such as BBC, ZDC etc. produce a local level-1 trigger (LVL1) for taking physics interest events and send it to Global Level-1 trigger (GL1). Once a trigger is accepted at GL1, Global Timing Module (GTM) requests FEM to send the data to Data Collection Modules (DCM). DCMs perform zero suppression, error checking and data reformatting. Many parallel data streams from DCMs are sent to Sub-Event Buffer (SEB). In the final stage, Assembly Trigger Processor (ATP) fetch the data from SEB and concatenate the event fragments.

The recorded data are sent to the tape device in High Performance Storage System (HPSS) in the RHIC Computing Facility (RCF).

5.2.4 Data taking for the leading neutron sample

Following LVL1 triggers are used to collect the leading neutron sample.

1. Energy deposit in the NORTH or SOUTH ZDC above 5 GeV : **ZDCN|S**
2. One or more hits in 64 photo-multipliers of both NORTH and SOUTH BBC : **BBCLL1(NoVtxCut)**

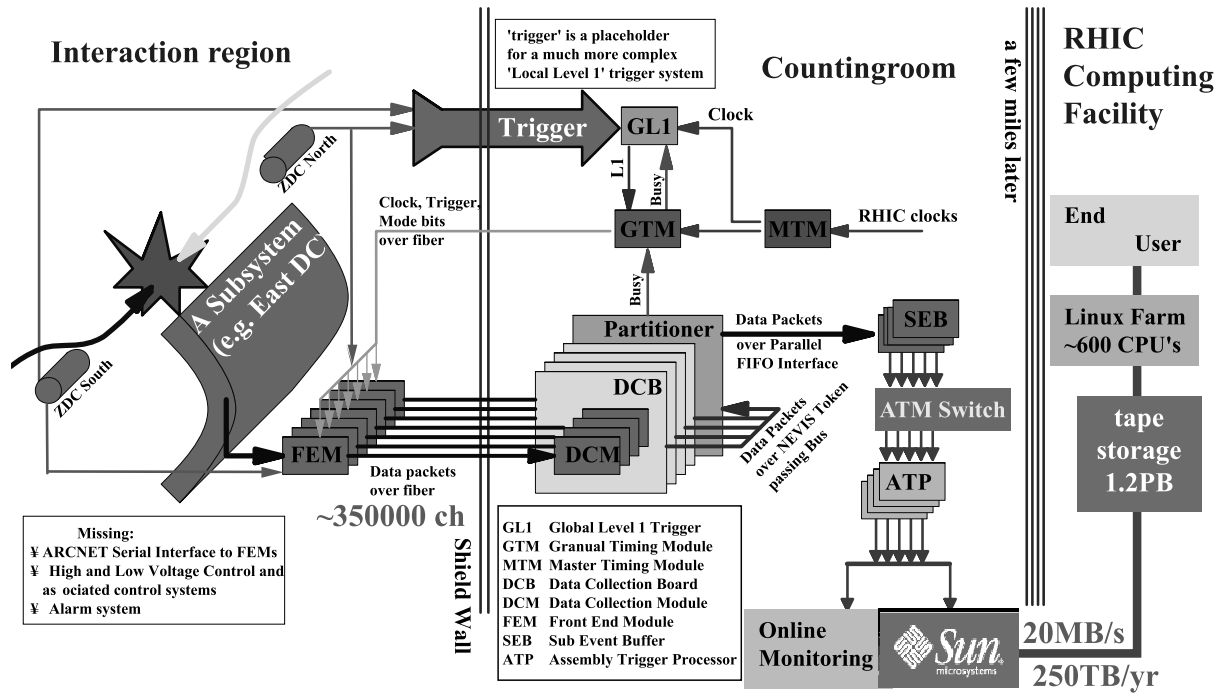


Figure 5.12: A block diagram of the PHENIX data acquisition system.

3. Same as 2, but requiring z -vertex being ± 30 cm (Figure 5.13) : **BBCLL1**
(Defined as a PHENIX minimum bias trigger)

The ZDC self trigger, ZDCN|S, was used for both the cross section and the asymmetry analyses. For the asymmetry analysis, a combination of 1 and 3, namely BBCLL1&(ZDCN|S), was also studied³. Such coincidence study is very interesting since charged particles in the BBC would be generated by a pion-proton scattering in the Regge framework (X in Figure 1.4). The comparison of asymmetries for these two data samples would give us additional information for the neutron production mechanism. Data collections were scaled with the factor of ~ 400 and ~ 25 , correspond to ~ 100 Hz and 200–300 Hz, for ZDCN|S and BBCLL1&(ZDCN|S), respectively due to the DAQ bandwidth⁴.

In transversely polarized pp run at 2005, we collected 6.5 million and 17.6 million events for ZDCN|S and BBCLL1&(ZDCN|S) triggers, respectively. The trigger counts of the BBCLL1(NoVtxCut) were used to the luminosity estimation in this analysis. By the van der Meer/vernier scan analysis, the cross section of BBCLL1(NoVtx) events was 22.9 ± 2.2 mb [70]. Integrated luminosity was calculated for the transverse run period as,

$$\mathcal{L} = \frac{N \text{ of BBCLL1(NoVtxCut)}}{\sigma_{BBC}} = \frac{5536229087}{22.9(\text{mb})} \sim 242 \text{ (nb}^{-1}\text{)}. \quad (5.2)$$

³BBCLL1&(ZDCN|S) trigger has been used to the local polarimeter. Details are shown in Appendix B.

⁴A full PHENIX DAQ bandwidth was achieved 5 kHz at 2005 year run. Most of the bandwidth has been used to other physics triggers.

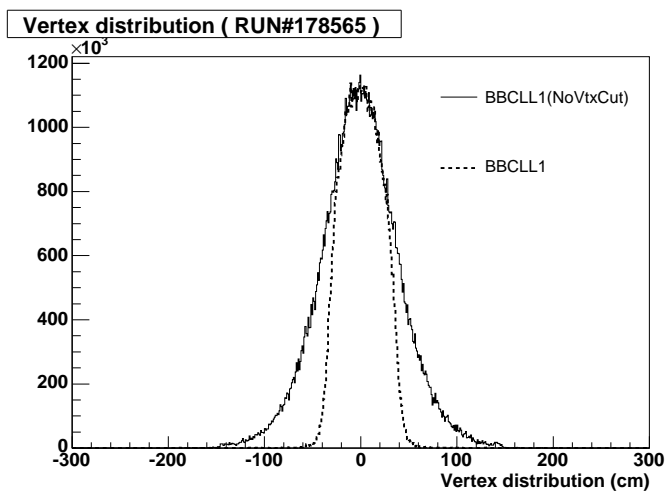


Figure 5.13: z -vertex distributions determined by BBCs. The BBCL1 has been required vertex cut ± 30 cm at online.

Chapter 6

Simulation study

An absolute scale for the energy measurement is determined by the 100 GeV single neutron peak from the heavy ion collision. However, neutrons coming from pp collisions are below 100 GeV. In case of the SMD, it is not tested by any beams. A simulation study is important to evaluate the detector responses for the neutron measurement below 100 GeV and discussed in this chapter. The performance for the neutron identification is also discussed.

The simulation was prepared by GEANT3 with GHEISHA [65] as a hadron interaction (Figure 6.1) which was well reproduce the response of the prototype ZDC. As an event generator, a single neutron event generator and PYTHIA (version 6.220) [71] were prepared. The single event generator creates neutrons as a function of x_F and p_T . The x_F distribution which was used for the simulation input was determined as a differential cross section, $d\sigma/dx_F$, in the cross section analysis (chapter 7). The p_T distribution is difficult to determine by the PHENIX data alone since the position and energy resolutions are insufficient. The p_T distribution from the ISR result, $\exp(-4.8 \pm 0.3 p_T)$, as shown in Figure 6.2 were used to the simulation input, assuming p_T scaling from the ISR to the PHENIX energies. To check a reliability of this assumption, distributions of radius from the detector center, r , for the real and simulation data were compared based on the relation of $p_T \propto r$ as,

$$p_T = E_n \sin \theta_n = E_n \frac{r}{\sqrt{r^2 + d^2}} \sim E_n \frac{r}{d}, \quad (6.1)$$

where d is the distance from the collision point to the detector, corresponding to 1800 cm. The comparison of r distributions with the integration of measured neutron energies 20–120 GeV is shown in Figure 6.3, and they agree well. It means the assumption of p_T scaling is reasonable.

To check the relevance of the simulation, the energy resolution for the 100 GeV neutron was studied as shown in Figure 6.4. The energy resolution is about 22% and consistent with the observed width of one neutron peak from the CuCu data as shown in Figure 5.6.

6.1 Study of the ZDC and SMD responses

The response of the energy measurement at the ZDC is compromised by 1) a non-linearity of photo electron yield to the neutron energy, and 2) a hadron shower leakage at the detector edge

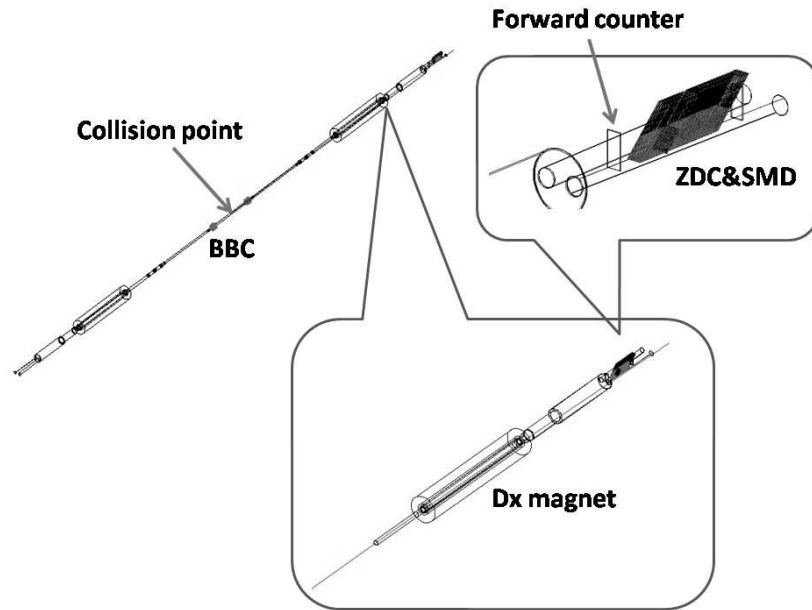


Figure 6.1: A plan view of the simulation setup drawn by GEANT3. the ZDC, BBC, beam pipe and all materials around the ZDC are included.

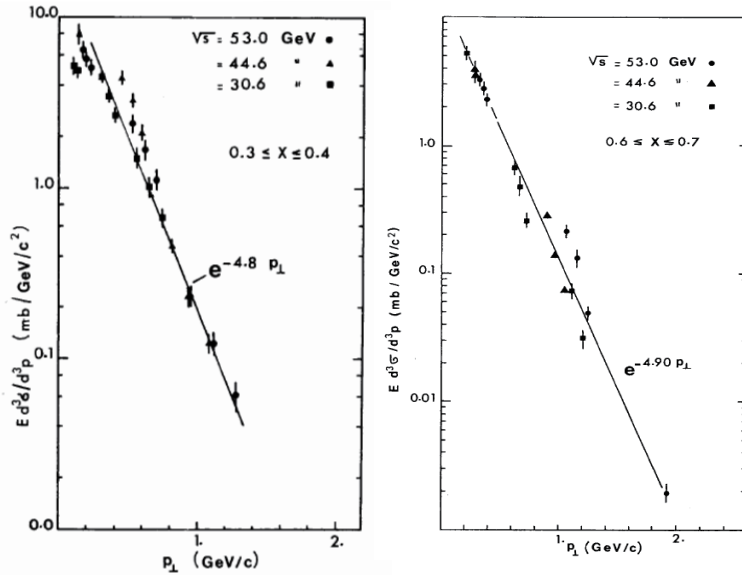


Figure 6.2: p_T distributions of neutron productions for $0.3 < x_F < 0.4$ (left) and $0.4 < x_F < 0.7$ (right) from the ISR experiment. The p_T shape was obtained as $\propto \exp(-4.8 \pm 0.3 p_T)$. [3]

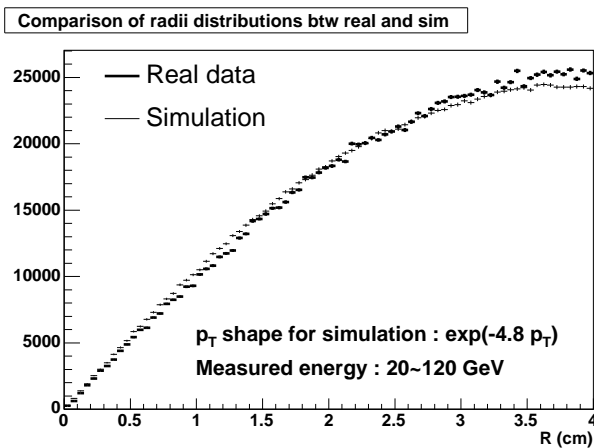


Figure 6.3: r distributions for the real and simulation data with the ISR p_T shape. Distributions are well agree within $r < 4$ cm. The ISR p_T shape is expected to be applicable to our data.

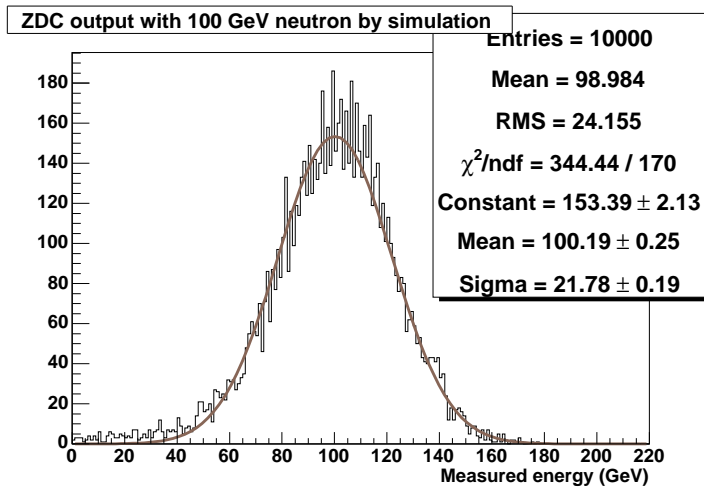


Figure 6.4: The measured energy distribution for 100 GeV neutrons estimated by the simulation and the width is 21.78 ± 0.19 . It is consistent with the width of one neutron peak in heavy ion collision, 21.36 ± 1.31 (Figure 5.6).

(edge effect). The SMD response will be changed by same reasons too. In this section, studies of the ZDC and SMD responses by the simulation with the single neutron event generator are discussed.

6.1.1 Energy linearity and resolution for the ZDC

The energy linearity and resolution were estimated by output responses for various incident energies of neutrons which were from 20 to 100 GeV with 10 GeV intervals in the simulation. Top of Figure 6.5 shows the mean of output energy as a function of the incident energy. Absolute scale was determined by 0 and 100 GeV in the same way of the real data. As a result, ZDC responses of energy measurements below 100 GeV have the non-linearity; output value is 15 GeV for the 20 GeV incident energy, for example. We applied a correction of the non-linearity to the real data based on this result. As a systematic error for this correction, we decided to use the difference between the linear and non-linear cases, conservatively. It is estimated in the analysis part, section 7.9.2, as a variation of the cross section results.

Bottom of Figure 6.5 shows the energy resolution as a function of the inverse square root incident energy. The energy resolution for the 20–100 GeV neutron is described as,

$$\frac{\Delta E}{E} = \frac{64.64}{\sqrt{E} \text{ (GeV)}} + 15.13 \text{ (\%)}. \quad (6.2)$$

6.1.2 Energy response in the detector edge

The edge effect was studied by the prototype ZDC with the 100 GeV proton beam at CERN as shown in Figure 6.6. Plots are the energy response and resolution as a function of incident positions for x and y . Basically the energy response decreases in the edge area, but only in the edge of positive y , it increases. It is caused by the fibers in the top region for the connection to the PMT (Figure 5.3); the leaked shower hits them directly. The simulation which was prepared for the prototype reproduced this effect well.

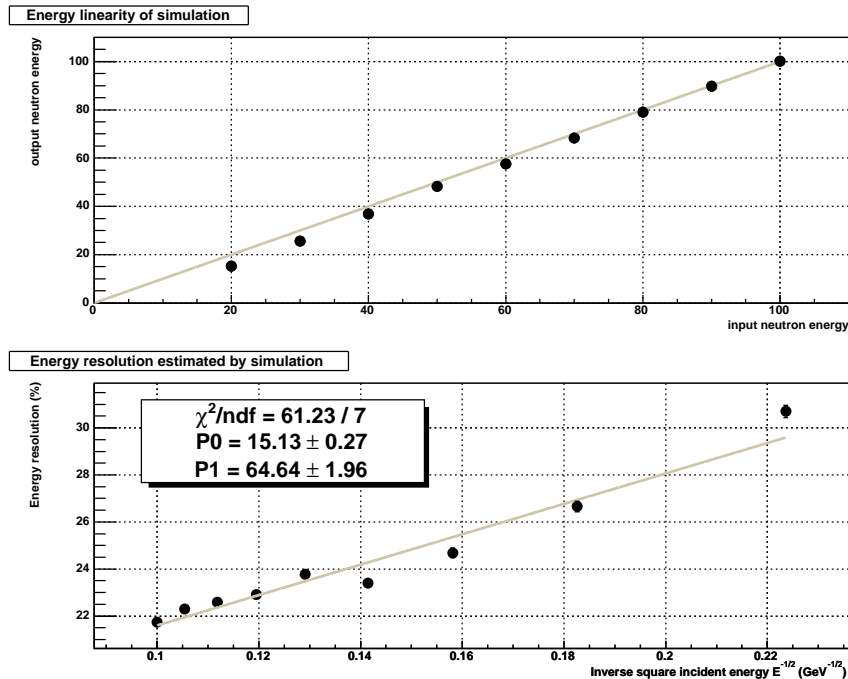


Figure 6.5: Top) The mean of output energy as a function of the incident neutron energy estimated by the simulation. Solid line indicates a linear response. Bottom) The energy resolution as a function of the inverse square root incident energy. Solid line shows the fit result by $\Delta E/E = [P0]/\sqrt{E} + [P1]$.

Figure 6.7 shows the study for the present ZDC estimated by the simulation. The response and resolution in the edge area act a same behavior of the prototype result except for the edge of positive y . It is because of the wide coverage of the absorber plates in positive y region for the present ZDC as an upgrade to reduce the edge effect.

This difference of the edge effects in positive and negative y can be seen in the real data with the SMD position cut. Figure 6.8 shows energy distributions measured at the ZDC for $y > 0$ cm and $y < 0$ cm by the SMD cut. Not only the different response but also the high energy tail in $y > 0$ cm are seen. We should not use the edge area to reduce the edge effect.

According to this study, 95–100% energy response is obtained by selecting $r < 3$ cm as an acceptance cut.

6.1.3 Position resolution in the center region

The neutron position was calculated by the centroid method as equation 5.1. The position resolutions were estimated by the simulation in this section. Figure 6.9 shows the output position distributions and their resolutions as a function of the neutron incident energy for x and y . Since distributions were not be reproduced by gaussian, the resolution was taken as RMS. The position resolution was estimated to be around 1 cm for the neutron energy at 100 GeV. A reliability of this estimation will be discussed in section 6.1.5.

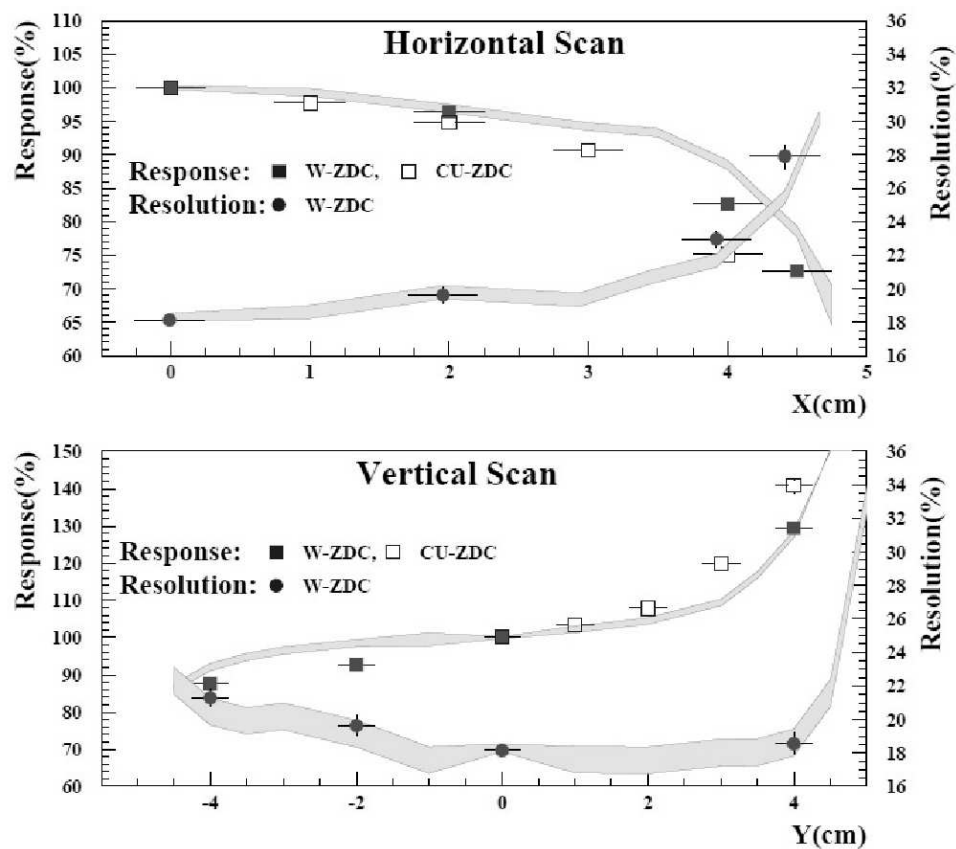


Figure 6.6: The energy response and resolution of the prototype ZDC as a function of the incident neutron position studied by the 100 GeV proton beam at CERN. Gray lines indicate the responses estimated by the simulation and they well reproduced the real data.

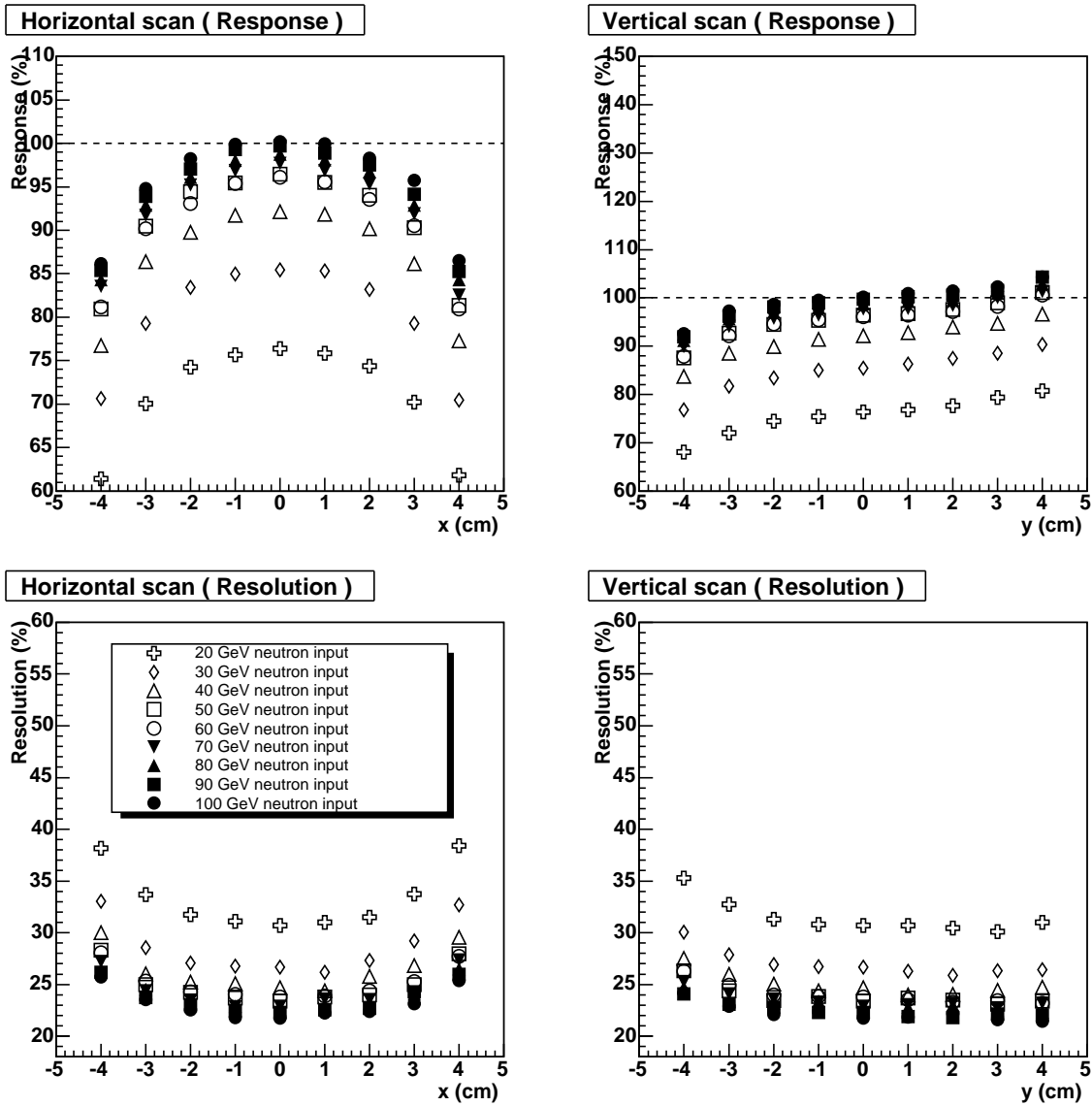


Figure 6.7: The energy response and resolution of the present ZDC as a function of incident neutron position for various incident energies estimated by the simulation.

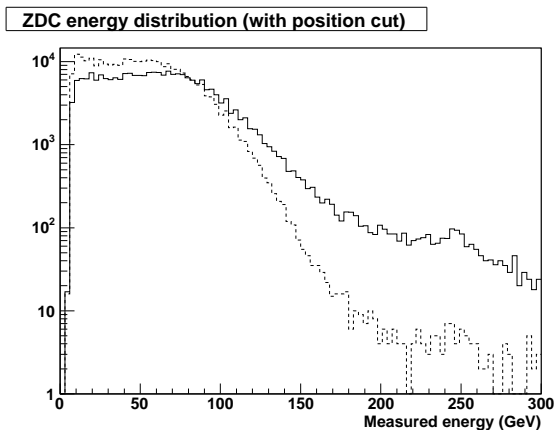


Figure 6.8: Energy distributions measured with the ZDC by the SMD position cut. Solid and dashed distributions indicate the SMD cut with $y > 0$ and $y < 0$, respectively. Not only the different response but also the high energy tail in $y > 0$ cm are seen.

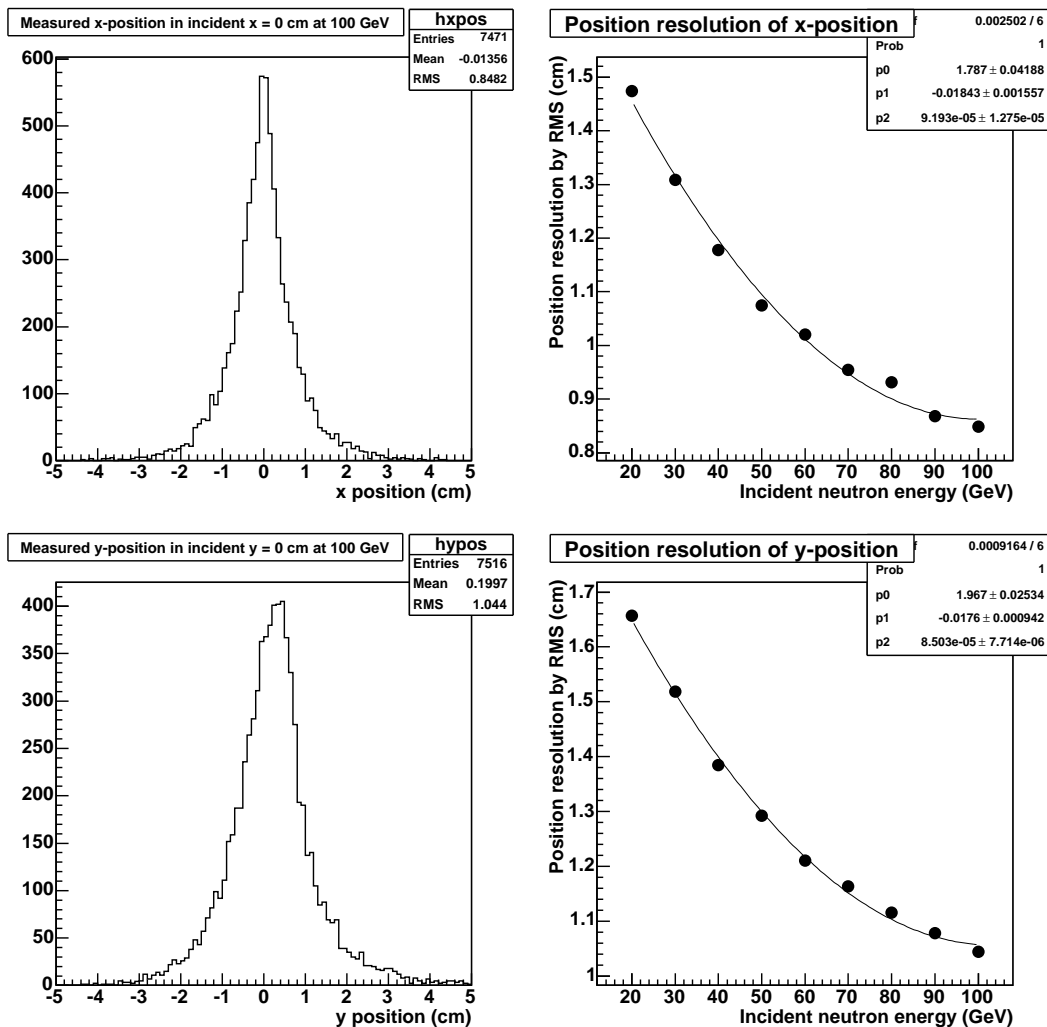


Figure 6.9: Left) Output position distributions of x (top) and y (bottom) for the 100 GeV neutron injected in the ZDC center, $(x,y)=(0,0)$ cm, evaluated by the simulation. The position resolution was obtained as their RMS. Right) The position resolution as a function of the incident neutron energy for x (top) and y (bottom). They were well reproduced by the polynomial 2 fit.

6.1.4 Position response in the detector edge

In the edge area, the position measurement is also affected by the shower leakage. Figure 6.10 shows the output distribution of the x -position for various incident x -positions at the 100 GeV neutron estimated by the simulation. Their peak and RMS values as a function of the incident position for x and y are shown in Figure 6.11. If incident position was in the edge area, the output position was shifted to the detector center caused by the shower leakage. This effect does not depend on the neutron energy. This misalignment caused by the edge effect is corrected based on this result.

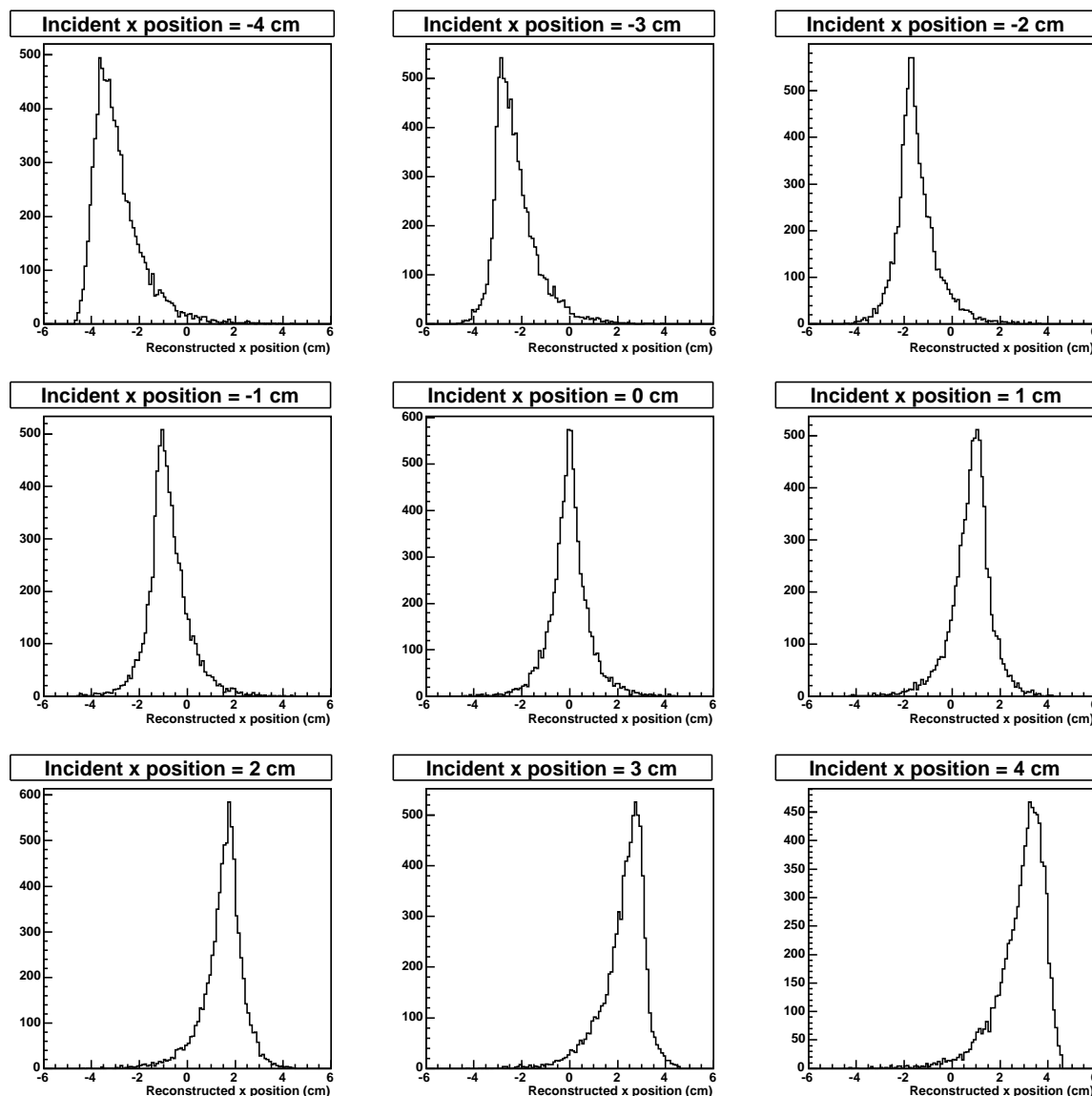


Figure 6.10: The output x -position distributions for 100 GeV neutrons with various incident positions estimated by the simulation. The y -position is basically same behavior as the x -position. (see Figure 6.11)

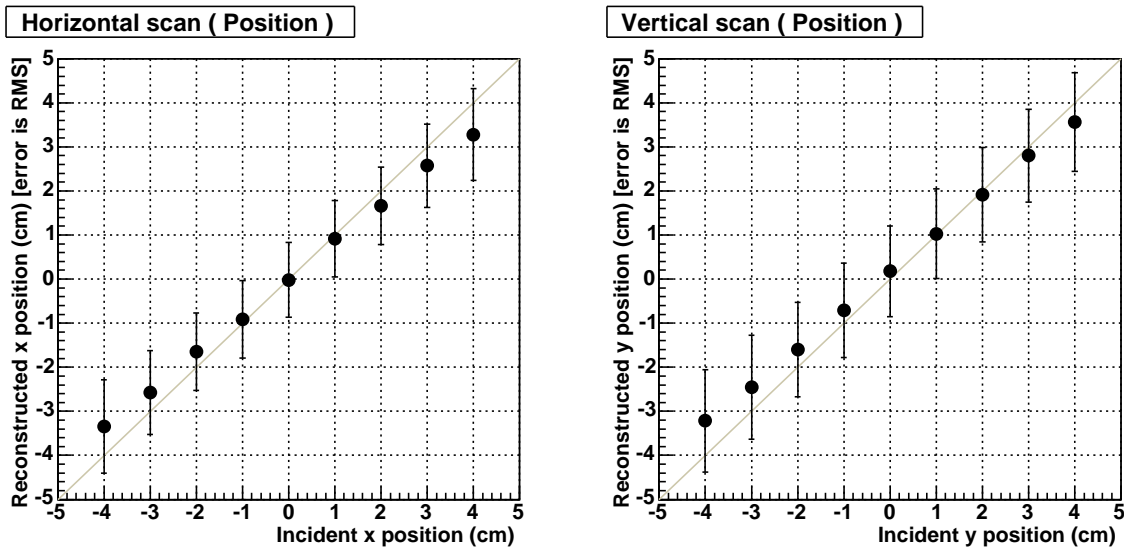


Figure 6.11: The peak value of the output x - (left) and y -position distributions (right) as a function of incident position for 100 GeV neutrons estimated by the simulation. Error bars indicate the RMS of position distributions. Output was not on the gray line which displays a linear response.

6.1.5 Systematics for the position measurement

Responses of position measurements by the SMD were evaluated by the simulation in previous sections, 6.1.3 and 6.1.4. However, the hadron response of GEANT3 simulation has large uncertainty in general.¹ In this section, the reliability of the position measurement is discussed.

The reliability was studied by comparing hadron shower shapes of the real and simulation data. Before the comparison, cut parameters for the neutron identification and the cross section for the simulation input, $d\sigma/dx_F$, were decided. The neutron identification and the analysis for the cross section are described in section 6.2.2 and chapter 7, respectively.

For the discussion of the hadron shower shape, two variables were defined as follows,

- Shower Shape (SS) : Figure 6.12 (left) shows the charge distribution in each SMD in one event. For the definition of the SS, we used the charge in the i -th scintillator above the threshold, C_i , and defined the charge sum, C_{sum} , as $C_{sum} = \sum N_{multi}^{SMD} C_i$, where N_{multi}^{SMD} is the SMD multiplicity. And the charge fraction in each scintillator were defined as $f_i = C_i/C_{sum}$. The SS for one event was defined as Figure 6.12 (Right); the f_i are plotted as a function of $\langle \text{scintillator position} \rangle$ minus $\langle \text{output position calculated by centroid method} \rangle$, which means the shower center is moved to zero. For the statistical evaluation, the SS was calculated event by event and normalized by statistics. From the SS, we can see the profile of the shower width.
- Peak Fraction (PF) : The PF is defined as the highest charge fraction among all scintil-

¹Not only GEANT3 simulation but also any other simulations.

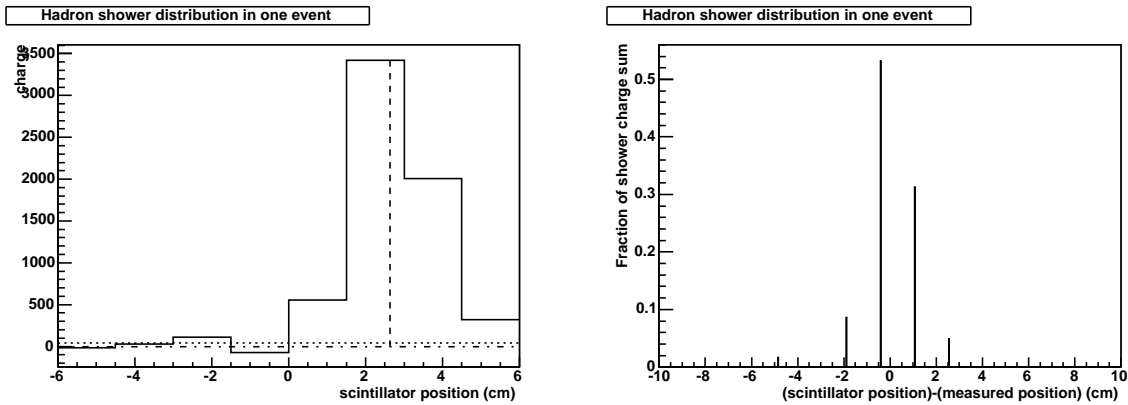


Figure 6.12: A definition of the shower shape (SS) in case of the y position. Left) The SMD charge *vs.* each SMD scintillator in one event. It is expected to be a hadron shower shape at the SMD. The vertical dashed line shows the position calculated by the centroid method and the horizontal dotted line is the threshold for the centroid method (equation 5.1). Right) It is a modified picture of the left one. Horizontal axis indicates $\langle \text{scintillator position} \rangle$ minus $\langle \text{output position calculated by the centroid method} \rangle$ and vertical axis shows a charge fraction in each scintillator to the sum of charges.

lators; $\text{PF} = \text{Max}(f_i)$. In case of Figure 6.12 (Right), the PF is the third scintillator from the right-hand edge and the PF value is about 0.52. The PF distribution is expected to be the reference of a shower height.

These were calculated for x and y independently. We compared these distributions in each SMD multiplicity since the hadron shower shape highly depend on the SMD multiplicity.

The comparison of SS and PF distributions between the real and simulation data are shown in Figure 6.13,6.15 for x and 6.14,6.16 for y , respectively. The shapes for y were reproduced by the simulation well. However these for x were obviously different, especially that of the PF, in a high SMD multiplicity event. Maximum systematic error for the position measurement can be discussed with the matching SS and PF shapes for x in case of the SMD multiplicity = 7, which shows the worst agreement between the real and simulation data.

There was one more disagreement between the real and simulation data as shown in Figure 6.17, displays the SMD charge sum *vs.* each SMD charge for the real and the simulation in top-left and top-right, respectively. In the real data, there was a correlation between them; if the SMD charge sum was larger, the pedestal of SMD moves to higher. We are considering the reason is the cross talk possibly caused by the leakage of photo-electrons in the optical fibers and the multi-anode readout of photomultiplier is also suspicious. It can be reproduced by adding a base offset depending on the charge sum (Smearing by the flat method shown in later).

For the quantitative discussion, SMD charges in the simulation were smeared to match SS and PF shapes to the real data by following 2 methods (Figure 6.18).

- Neighboring method : A fraction ($f_{\text{neighboring}}$) of charge in the i -th scintillator is shared

to neighbor two scintillators (In case of the edge scintillator, the charge is shared to just one side). The $f_{neighboring}$ is the smearing parameter and this sharing is applied to all scintillators. It is expected that shower shape is wider.

- Flat method : A fraction (f_{flat}) of charge in the i -th scintillator is shared to all scintillators. The f_{flat} is the smearing parameter and this sharing is applied to all scintillators². It is expected to reproduce the cross talk which is seen in the correlation between the SMD charge sum and each SMD charge. Shower shape is also expected to be wider.

Both smearing were applied so that the charge sum is conserved.

The behavior considering as the cross talk can be reproduced by the flat method. Bottom-left and bottom-right in Figure 6.17 show the correlations after the flat smearing with the $f_{flat} = 0.05$ and 0.10 , respectively. The distribution with $f_{flat} = 0.05$ looks reasonable to the real data and 0.10 is too much.

For the estimation of systematic error, the flat smearing with $f_{flat} = 0.05$ was applied to the simulation first and the neighboring method was used to match SS and PF shapes. Figure 6.19 show SS and PF shapes for x at the SMD multiplicity = 7 after the smearing of the neighboring and the flat methods with $f_{neighboring} = 0.28$ and $f_{flat} = 0.05$, respectively. Smearing parameter for the neighboring method was determined by minimizing the χ^2 value of the histogram fit for PF shapes between the real and simulation data. After the smearing for matching PF shapes, the SS shape of the simulation also reproduces that of the real data. After the smearing, the position resolution as a function of the incident energy was obtained as Figure 6.20. In the left panel, closed and open circles indicate the position resolutions estimated by the simulation without and with the smearing, respectively. In the right figure, the ratio of them is shown and the position resolution increases 14.1% after the smearing. Finally, we conclude that responses of the position measurements estimated by the simulation are reliable within the 14.1% systematic uncertainty for the position resolution.

6.2 Study of the neutron identification by PYTHIA event generator

The event structure in detector acceptance at pp collision was studied by GEANT3 with PYTHIA event generator. The neutron identification and its reliability are discussed in this section.

6.2.1 Event structure

First, we studied what kind of particles are detected in the ZDC with the 5 GeV energy threshold which was required for the neutron event trigger, ZDCN|S (Figure 6.21). In most of events, about 92%, only one particle is detected with the ZDC in each pp collision. Figure 6.21 left shows a tag-number of the particle which is detected with the ZDC. The tag-number is defined in

²It is same as that a fraction of charge sum is shared to all scintillators.

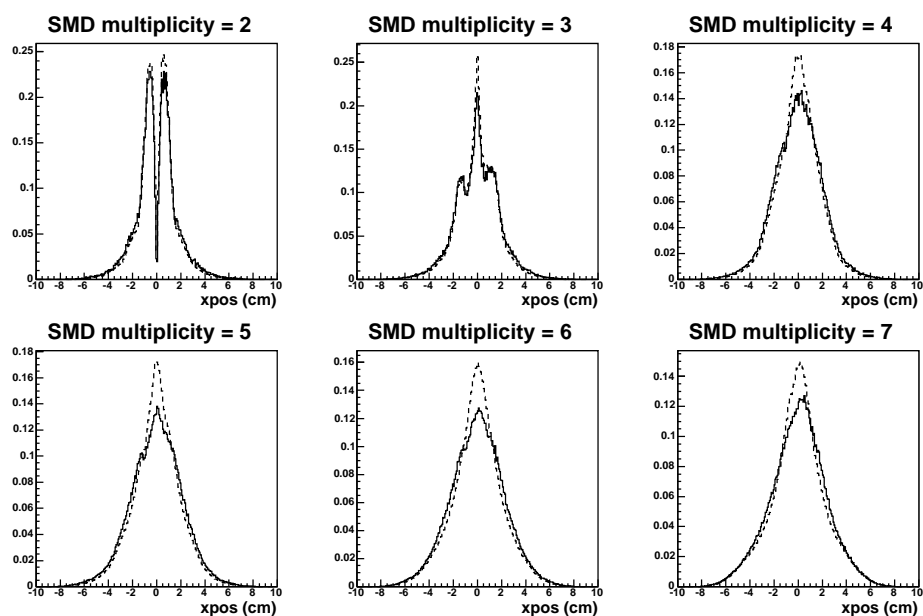


Figure 6.13: The SS shapes for the real (solid line) and simulation (dashed line) data for x -position are plotted in each SMD multiplicity. Vertical scale is normalized by event number.

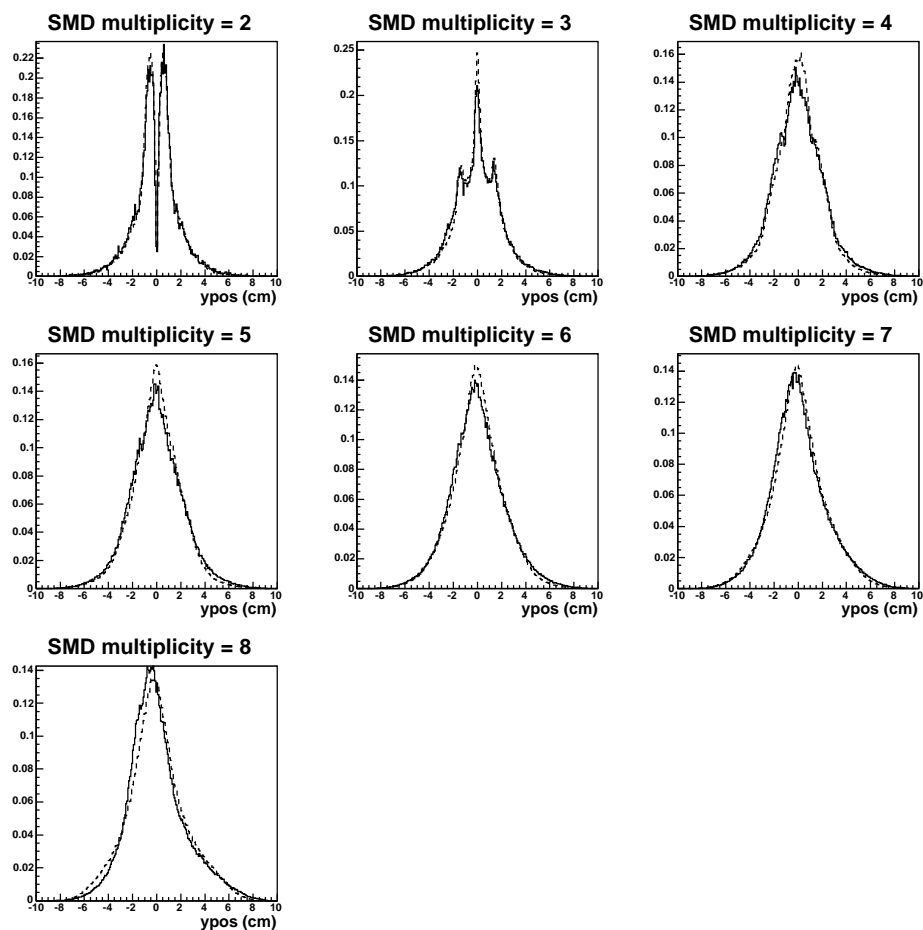


Figure 6.14: The SS shapes for the real (solid line) and simulation (dashed line) data for y -position are plotted in each SMD multiplicity. Vertical scale is normalized by event number.

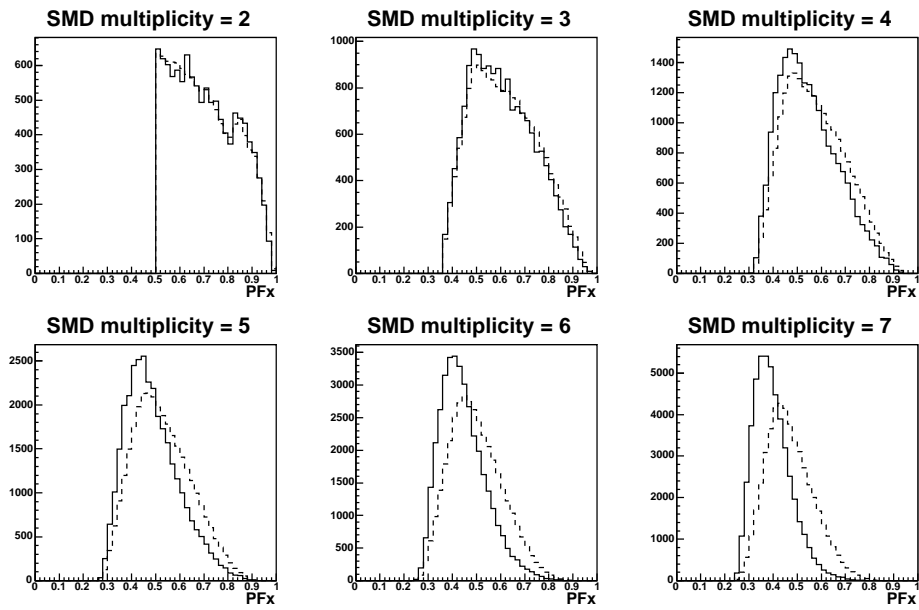


Figure 6.15: The PF distributions for the real (solid line) and simulation (dashed line) data for x -position are plotted in each SMD multiplicity.

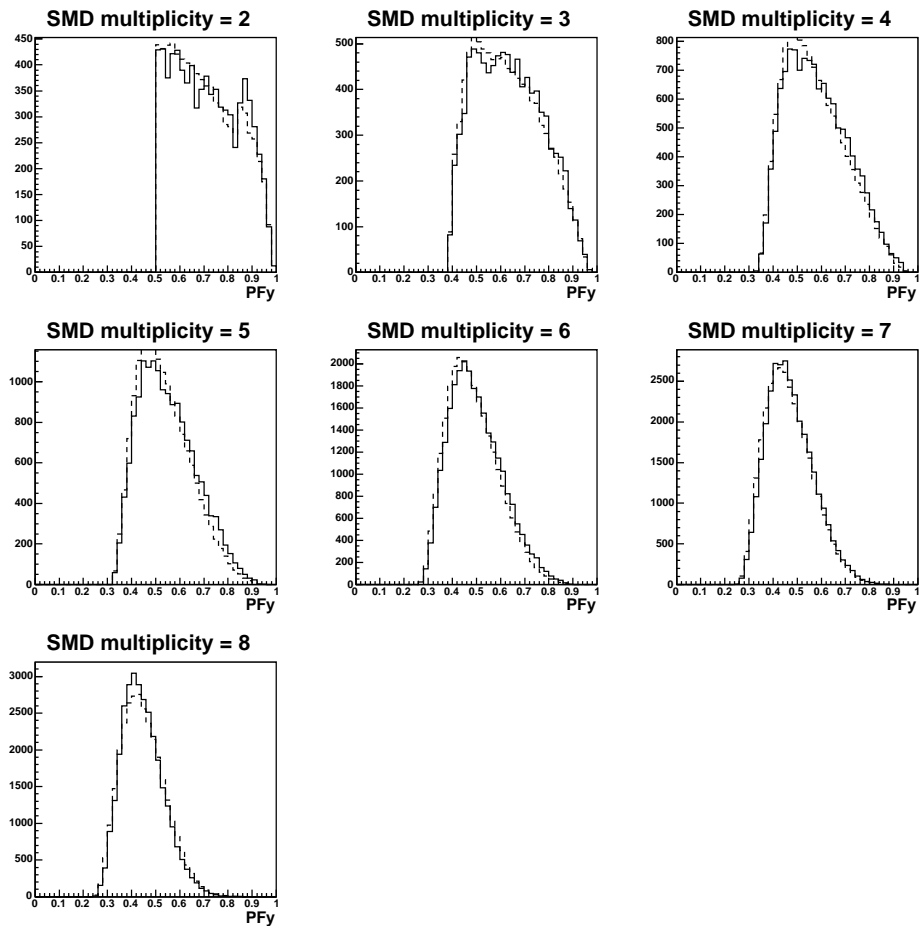


Figure 6.16: The PF distributions for the real (solid line) and simulation (dashed line) data for y -position are plotted in each SMD multiplicity.

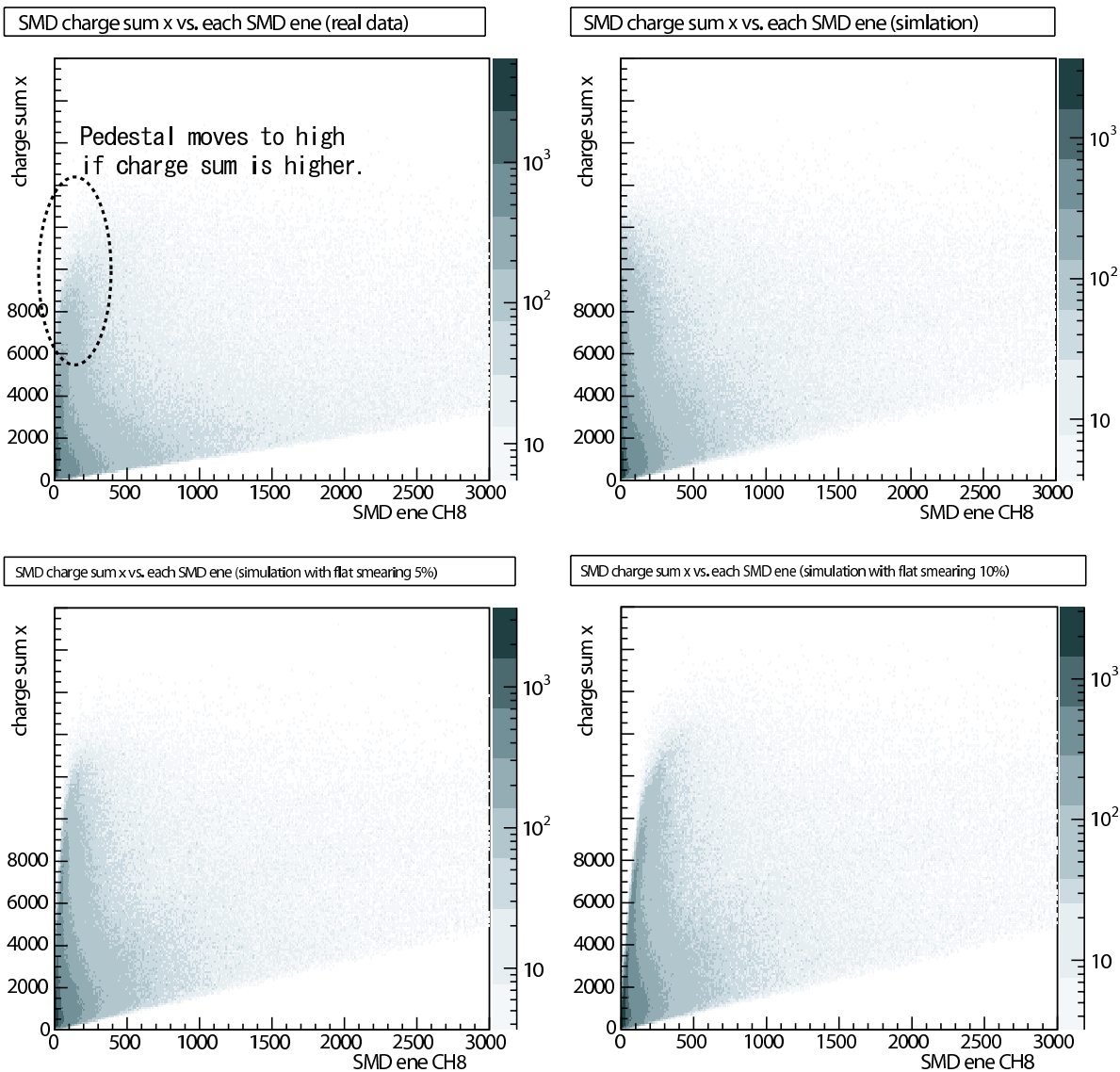


Figure 6.17: The correlation between the SMD charge sum *vs.* SMD charge in one scintillator for x position. The correlations for the real (top-left) and simulation (top-right) are plotted. Here, we show the charge for the scintillator ID number 8 as a horizontal axis, for example. In the real data, we can see the correlation between them; if the SMD charge sum is larger, the pedestal of one SMD moves to higher. This behavior is not reproduced by the simulation. The correlations after the flat smearing with $f_{flat}=5\%$ (bottom-left) and 10% (bottom-right) in the simulation are shown. The correlation is reproduced reasonably by the flat smearing with $f_{flat}=5\%$.

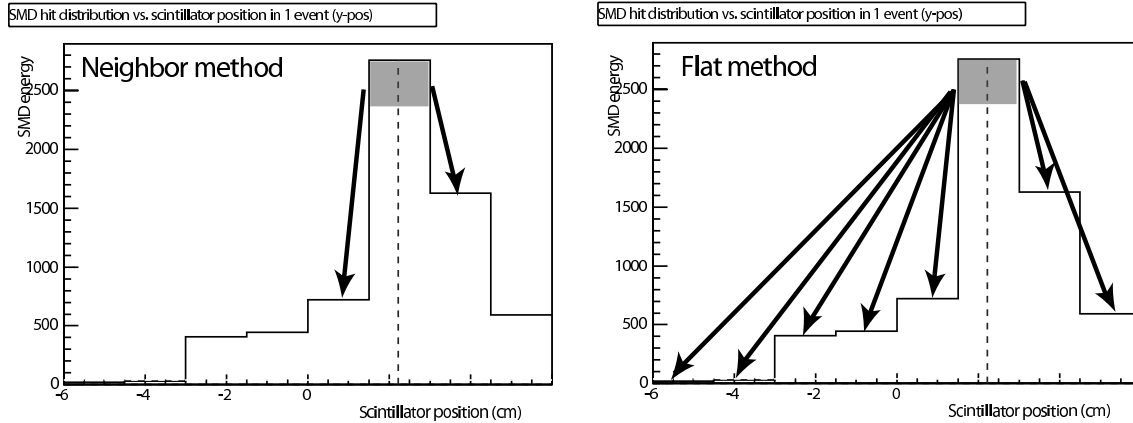


Figure 6.18: Schematic views of the smearing procedures for the neighboring method (left) and flat method (right) in case of y position (The number of scintillators = 8). (Left : neighboring method) A fraction, $f_{neighboring}$, of the charge in i -th scintillator is shared to neighbor two scintillators. (Right : flat method) A fraction, f_{flat} , of charge in the i -th scintillator is shared to all scintillators. Figures just show the smearing for one scintillator, and the smearing was applied to all scintillators above threshold so that the charge sum is conserved.

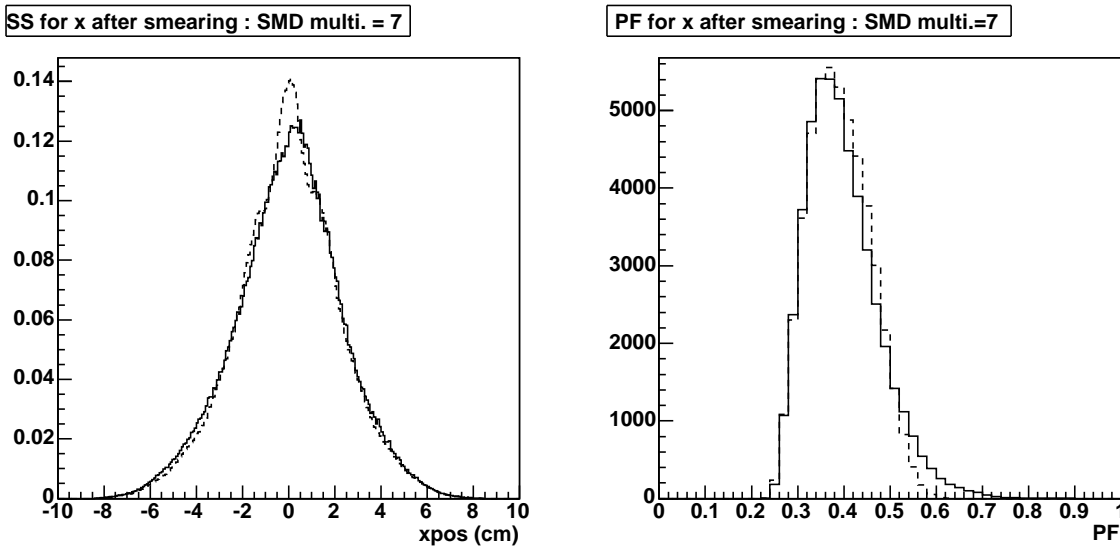


Figure 6.19: SS and PF shapes after the smearing for x position at the SMD multiplicity = 7. Solid and dashed lines show the shapes for the real and simulation data, respectively. For reproducing the real data, we determined the smearing parameters for the neighboring and flat methods as 0.28 and 0.05, respectively. The smearing parameter of neighboring method was decided by minimizing the χ^2 value of the histogram fit for PF shapes between the real and the simulation data. After the PF shape was matched, SS shape also reproduced that of the real data.

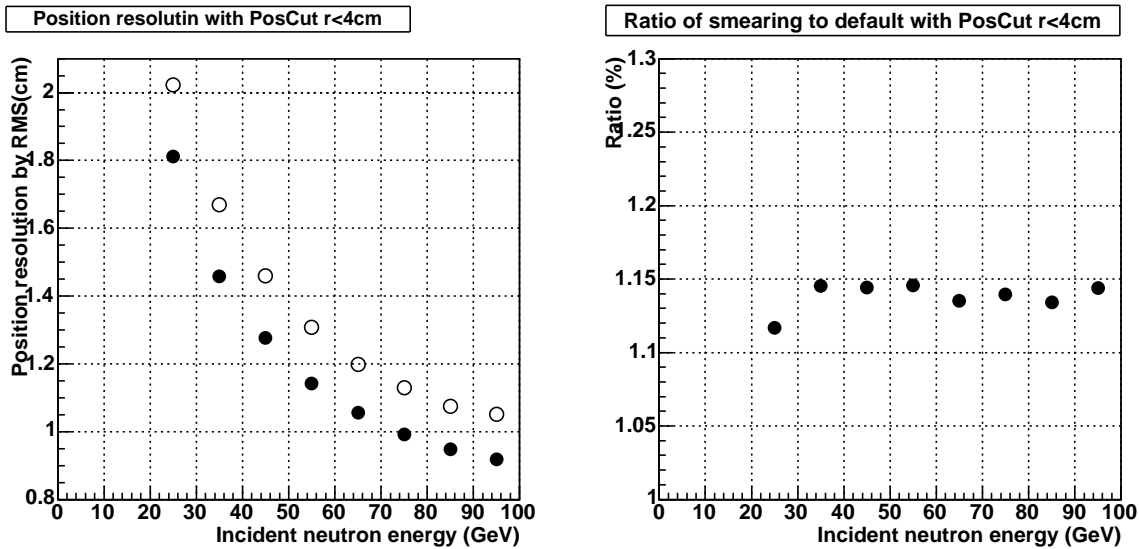


Figure 6.20: Left) The position resolution as a function of the incident neutron energy in $r < 4$ cm estimated by the simulation. Closed and open circles show the position resolutions without and with the smearing to match the SS and PF shapes respectively, and the ratio is shown in the right figure. It looks independent of the incident energy and the average value of 14.1% is considering as a maximum systematic error for the estimation of the position resolution.

GEANT3 and summarized in Table 6.1. Main particles detected with the ZDC are the photon, neutron and proton. Measured energy distributions for these three particles are plotted in Figure 6.21 right ³.

In the first expectation, only neutral particles, the photon and neutron, are detected with the ZDC since there is the DX magnet. However the proton has a chance to deposit its energy in the ZDC as follows. Figure 6.22 shows the event structures of protons for various incident energies. A bent low energy proton makes a particle shower by hitting the DX magnet or beam pipe, and particles from the shower can hit the ZDC. Such proton event can be removed by the charge veto counter.

Physics processes for major three particles estimated by PYTHIA are summarized in Table 6.2. Most of the photon and neutron are generated by a diffractive and a gluon scattering processes. ⁴ Protons are generated by the elastic and diffractive processes.

6.2.2 Neutron identification

As mentioned in the previous section, major backgrounds are photons and protons for the neutron measurement. They can be removed based on their behaviors as follows.

³High energy tail above 100 GeV is caused by the edge effect; the hadron shower hits fibers in the top region. Details are discussed in section 6.1.2.

⁴In PYTHIA hard process, the leading neutron is generated mainly from a string fragmentation ($\sim 65\%$) and the decay from $\Delta^0, \Delta^+, \Delta^-, \Lambda^0$. the forward photon is decayed from the π^0 ($\sim 91\%$) and η ($\sim 7\%$).

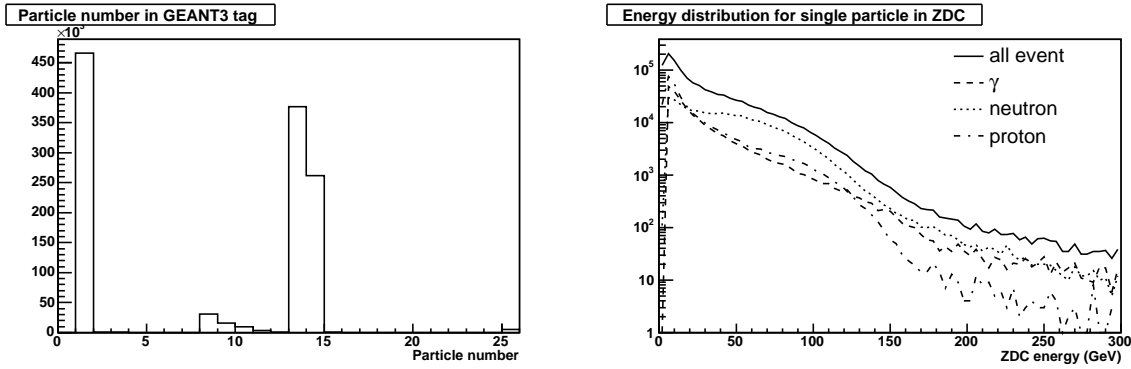


Figure 6.21: The event structure which is detected with the ZDC in pp collision at $\sqrt{s}=200$ GeV was studied by GEANT3 with PYTHIA simulation. The ZDC threshold has set to 5 GeV in the similar to the ZDCN|S trigger. Here, I show the event that one particle is detected with the ZDC in each pp collision (about 92%). The particle tag-number in GEANT3 (summarized in Table 6.1) is plotted in the left. Major particles, the photon, neutron and proton are shown as the tag-number = 1, 13 and 14, respectively. Measured energy distributions for these three particles with the ZDC are plotted in the right figure.

Tag-number	Particle	Tag-number	Particle
1	γ	10	K_L^0
2	e^+	11	K^+
3	e^-	12	K^-
5	μ^+	13	n
6	μ^-	14	p
8	π^+	15	\bar{n}
9	π^-	25	\bar{p}

Table 6.1: The tag-numbers for particles in GEANT3

Physics process	Neutron (μb)	γ (μb)	Proton (μb)
$qq \rightarrow qq$	35	46	14
$q\bar{q} \rightarrow q\bar{q}$	<1	<1	<1
$q\bar{q} \rightarrow gg$	<1	<1	<1
$qq \rightarrow qq$	268	358	95
$gg \rightarrow q\bar{q}$	9	12	3
$gg \rightarrow gg$	352	468	114
Elastic scattering	0	0	446
Single diffractive (XB)	<1	2	387
Single diffractive (AX)	462	527	107
Double diffractive	328	413	92
Low- p_T scattering	551	651	137
Total	2006	2479	1395

Table 6.2: Cross sections for major three particles detected with the ZDC in each physics process studied by GEANT3 with PYTHIA. Same energy threshold as ZDCN|S trigger, 5 GeV, was required.

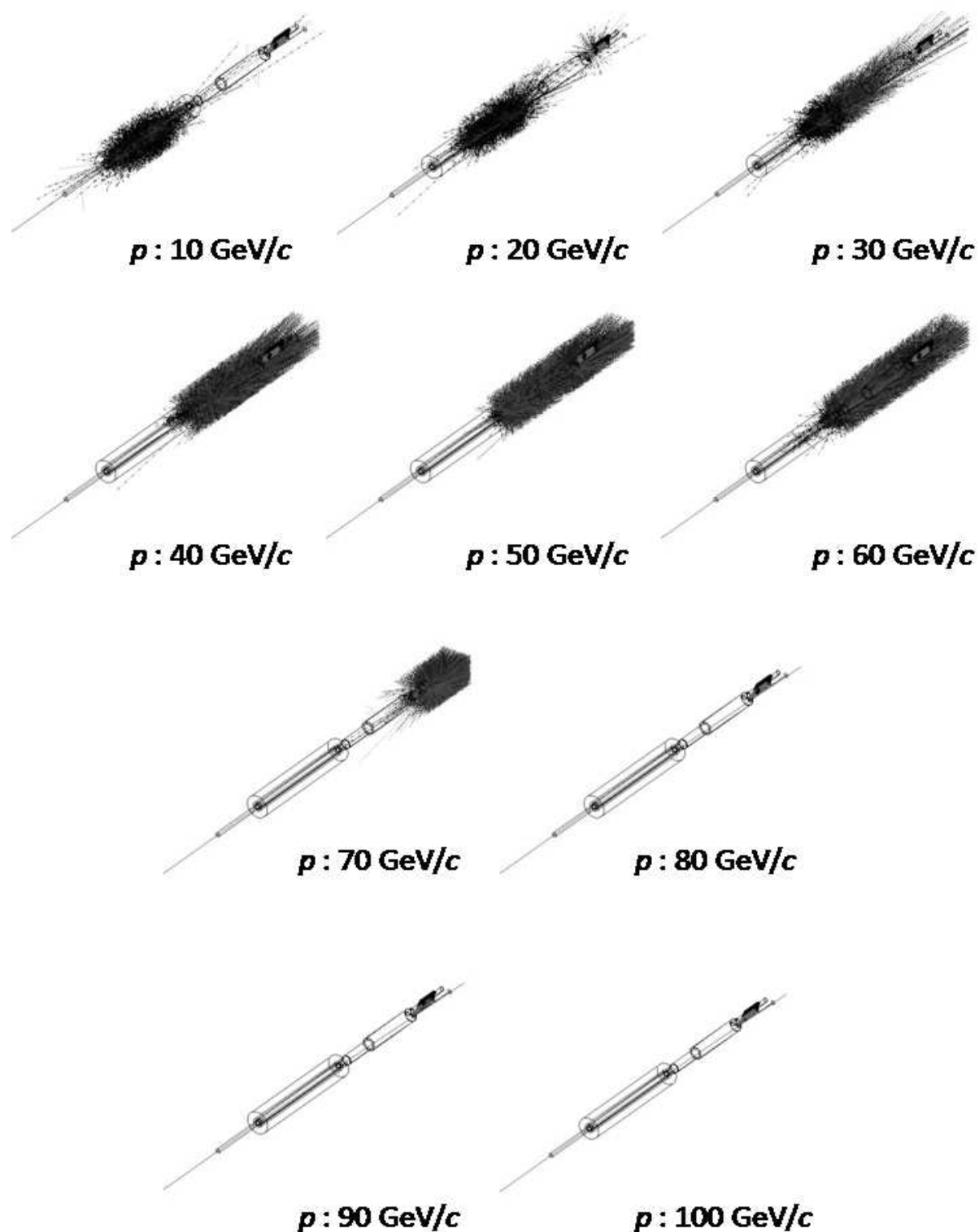


Figure 6.22: The event structure of the proton for various incident momenta. In case of the momentum below $70 \text{ GeV}/c$, the particle shower is generated by hitting the DX magnet or beam pipe and it can get into the ZDC acceptance.

- The behavior for both photons and protons : The deposit energy in the ZDC is distributed in the lower energy part, less than 20 GeV, as shown in Figure 6.21.
- The behavior for photons : Photons stop in the first ZDC module which has $51 X_0$. Thus, photons can be removed by requiring some energy deposit in the SMD or second ZDC.
- The behavior for protons : Charged particles in the proton shower are expected to deposit the energy in the charge veto counter. It can be removed by requiring charge veto cut.

The neutron energy above 20 GeV and the charge veto cut were required as a basic cut in this analysis and most of proton events were removed by this cut. There are two methods to remove the photon as follows

1. Using the SMD :

The requirement of SMD hits; more than one scintillator above threshold (the SMD multiplicity ≥ 2) for both x and y \rightarrow Neutron purity = $93.6 \pm 0.3\%$

2. Using the second ZDC module :

The second ZDC energy deposit above 20 GeV \rightarrow Neutron purity = $93.6 \pm 0.5\%$

Main backgrounds after the neutron identifications are the K^0 and proton. At the analyses of the cross section and the asymmetry, the SMD cut was applied automatically since the position information calculated by the SMD is necessary. The second ZDC cut was used to the estimation of the SMD cut efficiency which is discussed in section 7.5.

The purities which are described in this section were estimated for the neutron energy above 20 GeV. In the cross section and the asymmetry analyses, we required also the acceptance cut, $r < X$ cm and/or more higher energy cut. In these cases, the purities would become better and are estimated in each analysis section.

6.2.3 Background contamination after the neutron identification

Background contamination after the neutron identification estimated by GEANT3 with PYTHIA and their reliabilities are discussed in this section.

K^0 contamination

At the ISR experiment, the K^0 contamination to the neutron measurement were estimated from the K^\pm measurements [2]. Conclusions were 10 % at $x_F=0.2$ and less than 4 % at $x_F > 0.4$. Table 6.3 lists the fraction of the K^0 and proton contamination after the neutron identification with the acceptance cuts, $r < 3$ cm, in case of pp at $\sqrt{s}=200$ GeV estimated by the simulation. The fraction of the K^0 to the neutron in PYTHIA is consistent with the ISR result. It indicates the K^0 contamination estimated by PYTHIA is reasonable. However there is no measurement experimentally. Thus, we have included no correction for the K^0 contamination in this analysis as well as the IP12 analysis (section 3.2).

Proton contamination

The proton background is very sensitive to the materials around the ZDC and the magnet tuning in the accelerator. Systematics for the proton contamination estimated by the simulation were evaluated by a fraction of charged events in the charge veto counter.

Figure 6.23 shows the comparison of charge distributions in charge veto counters between the real and simulation data normalized by their statistics. Noise was estimated by the pedestal width of the real data and the width = 16.64 ch was incorporated into the simulation. For this analysis, photon events were removed by requiring the second ZDC module cut (section 6.2.2) since a converted photon in upstream materials hits the charge veto counter. A fraction of proton events can be evaluated as a fraction of charged candidates which is the events in one MIP or more. Their fractions were 0.424 and 0.279 for the real and simulation, respectively. Proton events for the real data were about 1.5 times higher than that of the simulation.

A threshold dependence of the selection of charged particle candidates was also studied. Typically we applied 50 channel to the threshold and checked the ratio of the proton fraction in the real and simulation for ± 10 channel (Table 6.4). Their fluctuation was less than 1% and the threshold dependence is negligibly small. Therefore, factor 1.5 was reasonable value for the fraction of charged candidates between the real and simulation data. It would be including the systematics of the proton generation in PYTHIA, the material tunes in GEANT3 and the magnet tuning in the accelerator.

Since it is just estimated by simulation, we have included no correction to the results, this is added as a systematic error. According to the study for the structure of the proton event in section 6.2.1, the proton event would be detected in the direction of beam bending which is negative x for the SOUTH ZDC. This behavior was confirmed by the real data as shown in Figure 6.24 which is a scatter plot of the x position determined by the SMD *vs.* the charge distribution in the charge veto counter. Most of charged candidates were distributed in negative x region. It indicates that the proton background was not related to the proton spin and we can assume the proton background A_N equals to zero. We added its systematic error by the dilution method discussed in Appendix A.4 with $A_N^{bg}=0$.

Multi-particles event

The event structure in pp collision has been studied as far as the one particle detection in one event. From PYTHIA study, the event which has two or more particles into the ZDC acceptance is about 8%, it depends on the acceptance cut. We have included this type of background into the systematic error.

x_F	K^0 (%)	proton (%)
0.1~0.2	13.91 ± 1.04	1.65 ± 0.34
0.2~0.3	6.61 ± 0.41	2.67 ± 0.26
0.3~0.4	2.77 ± 0.19	4.27 ± 0.23
0.4~0.5	1.71 ± 0.13	5.24 ± 0.23
0.5~0.6	1.13 ± 0.10	4.50 ± 0.20
0.6~0.7	0.61 ± 0.07	4.00 ± 0.19
0.7~0.8	0.48 ± 0.07	3.91 ± 0.21
0.8~0.9	0.18 ± 0.05	3.48 ± 0.22
0.9~1.0	0.005 ± 0.003	15.26 ± 0.53

Table 6.3: The background fraction of the K^0 and proton after the neutron identification in $r < 3$ cm estimated by GEANT3 with PYTHIA in pp collision at $\sqrt{s} = 200$ GeV.

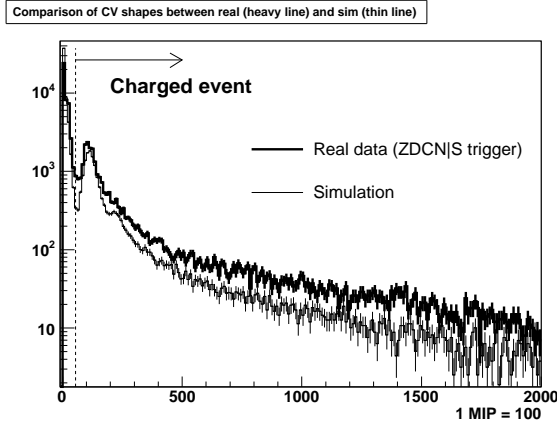


Figure 6.23: The comparison of charge distributions in charge veto counters between the real and simulation data with the second ZDC cut (photon veto).

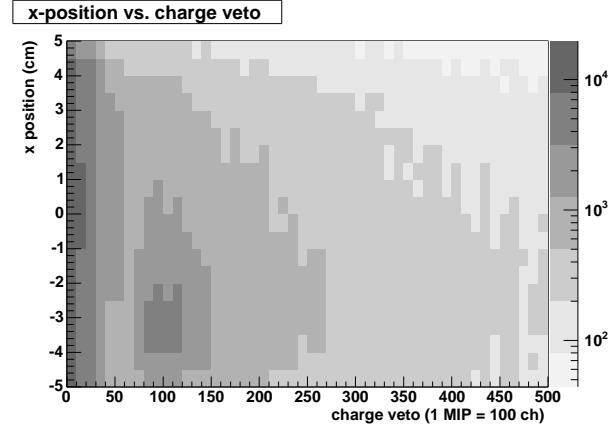


Figure 6.24: The x position calculated by the SMD *vs.* the charge distribution in the charge veto counter for the real data. Most of charged events were distributed in negative x region which is the direction of beam bending by the DX magnet.

Charge veto counter cut	Real	Sim	Ratio (Real/Sim)
40	0.461	0.302	1.525
50	0.424	0.279	1.519
60	0.408	0.270	1.510

Table 6.4: Fractions of charged candidates in the charge veto counter after requiring the photon veto. They were evaluated for three thresholds, 40, 50(default) and 60 ch, to check the threshold dependence. Ratios of them are also listed and they are threshold independent.

Chapter 7

Analysis for the cross section

7.1 Cross section calculation

7.1.1 Cross section at the PHENIX experiment

Since it is difficult to determine p_T by the PHENIX data alone, the cross section was estimated as a differential with respect to x_F as,

$$\frac{d\sigma}{dx_F} = \frac{N_{\text{neutron}}}{\mathcal{L}} \frac{1}{dx_F}, \quad (7.1)$$

where, N_{neutron} is counts for the neutron sample after the correction of cut efficiencies (section 7.5, 7.7) and the energy unfolding (section 7.6).

7.1.2 Cross section at the ISR experiment

Invariant cross sections measured at the ISR experiment were converted to differential cross sections for the comparison with the PHENIX data. The conversion formula to $d\sigma/dx_F$ is described with the approximation in the forward kinematics as,

$$E \frac{d^3\sigma}{d^3p} \approx \frac{1}{2\pi} \frac{x_F}{dx_F} \frac{d^2\sigma}{p_T dp_T} \rightarrow \frac{d\sigma}{dx_F} = \frac{2\pi}{x_F} \int_{Acc.} E \frac{d^3\sigma}{d^3p} p_T dp_T, \quad (7.2)$$

where *Acc.* means the p_T range for the PHENIX acceptance cut (for example, $0 < p_T < 0.11x_F$ GeV/ c for the $r < 2$ cm cut).

7.2 Energy distribution in the very forward kinematics

For the cross section analysis, 65 million events taken by the ZDCN|S trigger were used. The acceptance cut was decided as $r < 2$ cm to choose the similar kinematics of the ISR experiment; the detection angle is about 1 mrad. It is expected to be maximum $p_T \approx 0.11$ GeV/ c for the 100 GeV neutron by this cut. We assumed a beam axis on the ZDC geometry was same as the ZDC center in this analysis. However, it is a possible that the beam axis was shifted. The beam axis search on the ZDC geometry is shown in section 8.1 and the effect for the cross section is discussed in section 7.9.3.

Figure 7.1 shows the energy distribution measured with the ZDC after the neutron identification and the acceptance cut. A detailed discussion of the neutron identification are in section 6.2.2. The measured energy spectrum has a peak structure as shown in Figure 7.1.

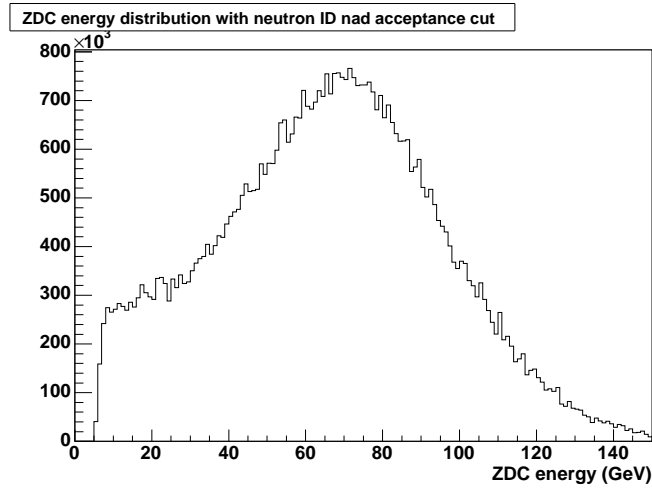


Figure 7.1: The energy distribution measured with the ZDC after the neutron identification and the acceptance cut ($r < 2$ cm, corresponds to $p_T < 0.11$ GeV/ c).

7.3 Stability

In this section, we discuss the stability checks we have made run-by-run for the neutron measurement.

7.3.1 Energy gain

If a gain of the ZDC was changed in the run period, it appears in a variation of peak positions. The stability of the energy gain can be evaluated by the fluctuation through the run period as shown in Figure 7.2. The energy gain was stable.

7.3.2 Neutron yield

The ratio of the neutron yield to the BBCLL1(NoVtxCut) counts through the run period give the stability of the cut condition for the neutron measurement. The ratio, R_N , was defined as,

$$R_N = \frac{N \text{ of counts with the neutron ID and the acceptance cut}}{N \text{ of BBCLL1(NoVtxCut) counts}}. \quad (7.3)$$

Figure 7.3 shows the ratio through run period with a constant fit result. The neutron yield was stable through the measurement.

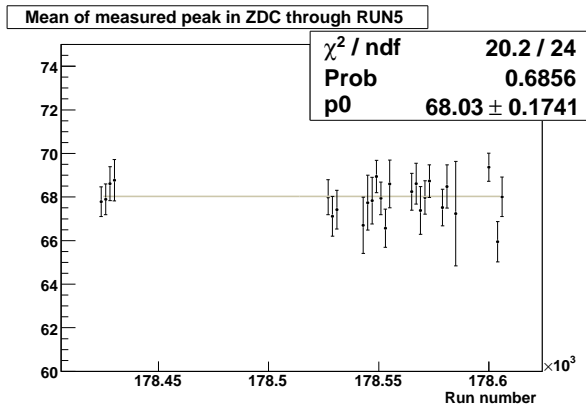


Figure 7.2: The peak value of the energy distribution through the run period.

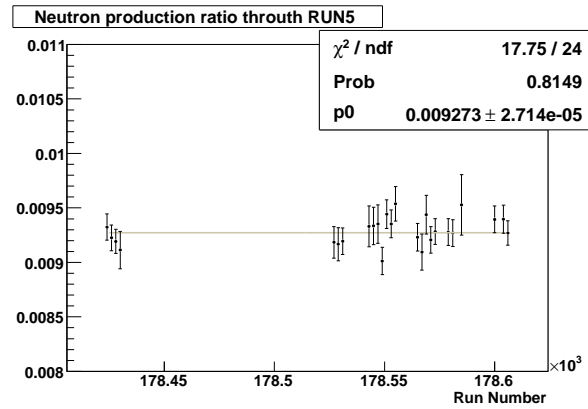


Figure 7.3: The ratio of the neutron yield to the BBCLL1(NoVtx) counts through the run period.

7.4 Study of the beam gas background

As one of the backgrounds, we need to consider a beam gas event which is the particle shower event occurred by an interaction between the proton beam and particles in the beam pipe. It is removed by the requirement of the collision vertex since most of beam gas events distribute in out of the collision time window. However, in case of the ZDC self trigger, we cannot distinguish the collision event and beam gas event. The amount of the beam gas event is estimated in this section.

As a RHIC operation in 2005 run, there were 9 abort bunches in each beam. In the PHENIX interaction point, abort bunches of one beam cross to the filled bunch of other beam. In these crossing, only the beam gas event can occur, whereas the collision can never. We can estimate the fraction of the beam gas background by the events in abort bunches assuming there is no differences of beam conditions in all bunches.

Figure 7.4 shows the event counts in each bunch crossing after the neutron identification and the acceptance cut. Abort bunch crossings are found as dashed areas in Figure 7.4. The fraction of the beam gas background was estimated to be 0.0062 ± 0.0004 in average. We conclude that it was negligibly small.

7.5 Relative efficiency to the SMD cut between the real and simulation data

The neutron hit position was calculated by the centroid method using the information of scintillator charges above the threshold (equation 5.1). In this analysis, same threshold, 40 ch, was applied to the real and simulation data and the efficiency of the acceptance cut using the SMD was estimated by the simulation in section 7.7. However, the SMD cut efficiency between the real and simulation data can be different since absolute calibration was not well known in the

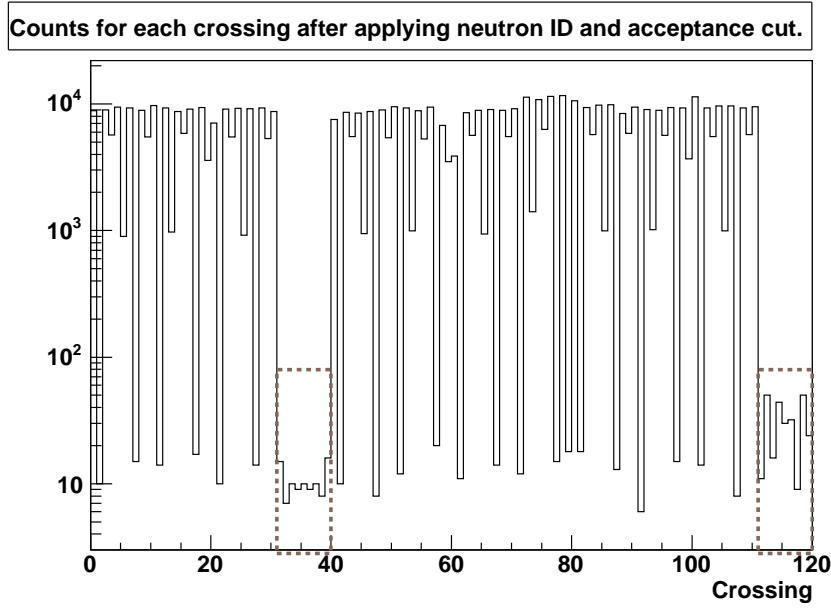


Figure 7.4: The event counts in each bunch crossing after the neutron identification and the acceptance cuts. Dashed areas show the events in the abort bunch crossings that only beam gas events occur. (31–39 : abort bunches in the Yellow beam and 111–120 : abort bunches in the Blue beam)

real data (section 5.2.1). These difference of efficiencies can be estimated using the nearly pure neutron sample by the neutron identification with the second ZDC cut (section 6.2.2). The SMD cut efficiency for the neutron measurement was evaluated by a following formula,

$$\epsilon_{SMD\ cut} = \frac{N\ of\ (Neutron\ ID\ with\ the\ second\ ZDC\ cut)\ \&\ (the\ SMD\ cut)}{N\ of\ (Neutron\ ID\ with\ the\ second\ ZDC\ cut)}. \quad (7.4)$$

The efficiencies for the real and simulation are shown in Figure 7.5 as a function of the measured energy. A relative efficiency as a ratio of the real and simulation data is shown in the left-bottom. It is nearly equal to one but it depends on the measured energy. The energy spectrum was corrected based on this result before the energy unfolding in section 7.6.

7.6 Energy Unfolding

The measured neutron energy with the ZDC is smeared by the energy resolution. For the extraction of an initial energy distribution, it is necessary to unfold the measured energy distribution. In this section, the energy unfolding [72] is discussed .

7.6.1 Unfolding method

We assume that the initial distribution $x(E)$ is smeared to the measured distribution $y(E')$ and this smearing is described by a linear combination. Their relation can be given by the matrix

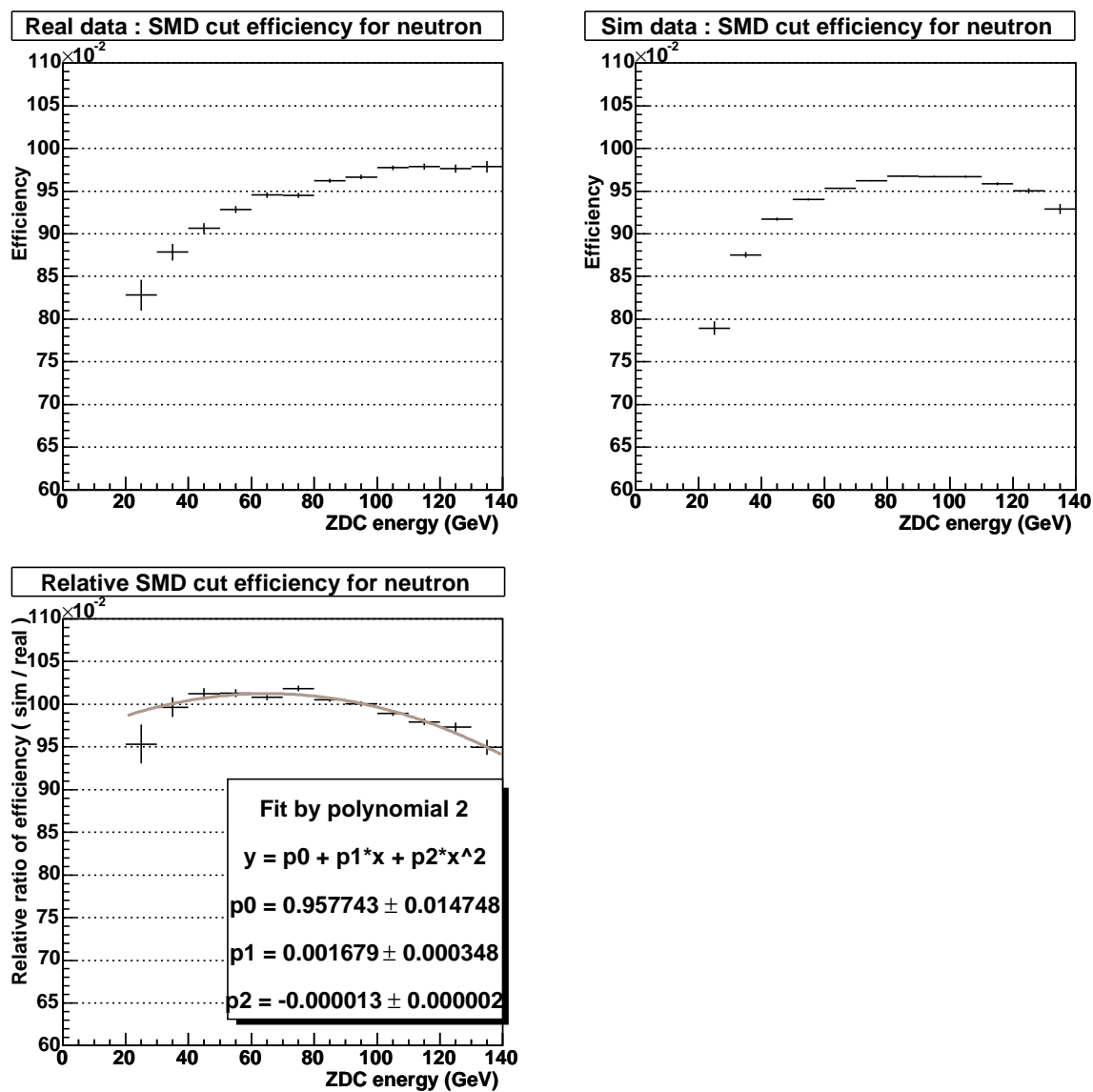


Figure 7.5: The SMD cut efficiencies for the real (Left) and simulation data (Right) in Top two figures. Bottom figure shows the ratio of the efficiencies for the simulation to the real data.

$A(E', E)$ which is a transition matrix for the energy smearing.

$$y(E') = A(E', E)x(E). \quad (7.5)$$

It can be represented as $\vec{y} = A\vec{x}$. The extraction of the initial distribution is possible with an inversion of the matrix A .

$$\vec{x} = A^{-1}\vec{y}, \quad V_x = A^{-1}V_y(A^{-1})^T, \quad (7.6)$$

where V_x and V_y are the error vectors for \vec{x} and \vec{y} , respectively.¹

If the smearing effect is large, the result looks terrible and is too sensitive to a small change of A . It can be discussed using an orthogonal decomposition. The matrix A is expressed by,

$$A = UDU^{-1}, \quad (7.7)$$

where U is a transform matrix and D is a diagonal matrix. The diagonal elements of the matrix D are the eigenvalue λ_j of the matrix A . Equation 7.6 is represented as,

$$\begin{aligned} \vec{y} &= A\vec{x} = UDU^{-1}\vec{x}, \\ U^{-1}\vec{y} &= DU^{-1}\vec{x} \quad \rightarrow \quad \vec{c} = D\vec{b}, \end{aligned} \quad (7.8)$$

where $\vec{c} = U^{-1}\vec{y}$ and $\vec{b} = U^{-1}\vec{x}$ are new vectors transformed from \vec{y} and \vec{x} , respectively. Each of the coefficients b_j and c_j in $\vec{c} = D\vec{b}$ is transformed independently of any other coefficient by using eigenvalue λ_j ,

$$c_j = \lambda_j \cdot b_j. \quad (7.9)$$

In order to perform the unfolding, the coefficients c_j have been influenced by statistical fluctuations of the elements of measured vector \vec{y} . The b_j which includes the information of initial vector x is obtained by $b_j = c_j/\lambda_j$. The statistical fluctuation of the c_j is delivered to the b_j as magnified values in case of small eigenvalue λ_j . It is the reason why the result is unsatisfactory. Reasonable result can be obtained by cutting the c_j which has a large statistical uncertainty.

7.6.2 Unfolding the data

Figure 7.6 shows the scatter plot of the initial and measured neutron energies estimated by the simulation. The transition matrix A was calculated by it. A binning is set to 20 GeV due to the 20% energy resolution for the 100 GeV neutron.

First, the coefficients c_j were calculated and shown in Figure 7.7. Three sets of the transition matrix A , which have the same energy resolution but different initial energy distributions², were

¹If \vec{x} and \vec{y} have different dimensions, A has zero-row or -column. In this case, we can not calculate A^{-1} since a determinant is zero. We need to calculate A^{-1} as a pseudo-inverse matrix, A^+ , which is a generalized inverse matrix. It still satisfies equation 7.6.

²Initial shapes are prepared to increase, be flat and decrease as a function of x_F . These shapes are close to the cross sections at $p_T \approx 0.0$ GeV/ c , 0.2 GeV/ c and 0.4 GeV/ c in the ISR results (Figure 1.5).

prepared to check the statistical error propagation of the c_j . Basically c_j distributions should be same since it depends on the energy resolution only, not on the initial distribution. However, if the c_j has large statistical uncertainty, its value is easily fluctuated by a small change of A . From Figure 7.7, the c_4 has a large statistical uncertainty and it is delivered to the b_4 magnified by the smallest eigenvalue λ_4 ³. The c_4 should be removed for the reasonable unfolding. The statistics was scaled for the reduction with the c_4 cut so that the statistics was conserved.

Energy spectra before and after the unfolding are plotted in Figure 7.8. Horizontal axis is changed to x_F by equation 1.3.

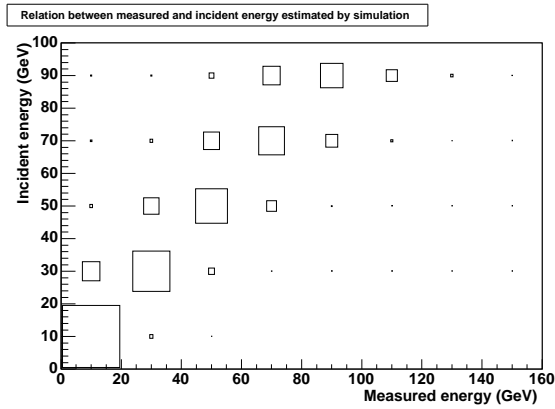


Figure 7.6: A relation between the initial and the measured neutron energies estimated by the simulation. z -axis was normalized as a sum of horizontal values in each vertical bin. The transition matrix A was calculated by this relation.

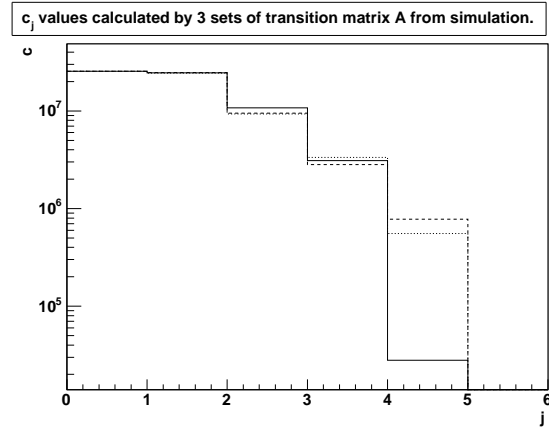


Figure 7.7: The values of the coefficients c_j calculated by three sets of the transition parameter A which have the same energy resolution, but different initial distributions. The c at $j=4$ has a large statistical uncertainty.

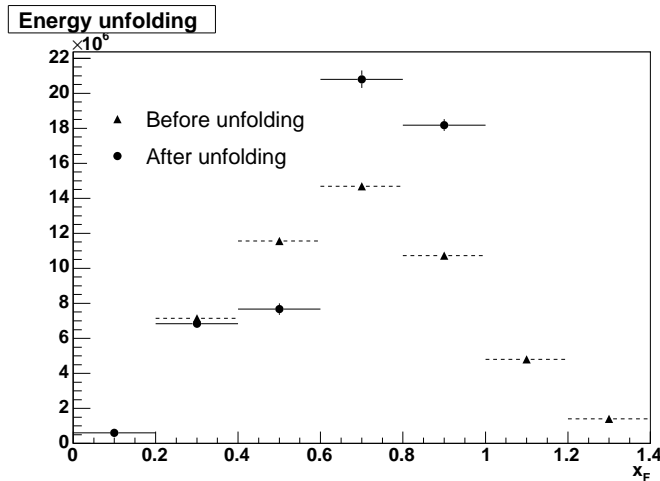


Figure 7.8: Energy distributions before and after the energy unfolding. The unfolding was performed so that statistics was conserved.

³Typical eigenvalue, λ_j , for the A being smaller starting at one with increasing j . For example, $\{\lambda_0, \lambda_1, \lambda_2, \lambda_3, \lambda_4\} = \{1.00, 0.82, 0.59, 0.37, 0.12\}$ in our case.

7.7 Estimation of the efficiency for the experimental cut

The efficiency of the experimental cut, including the neutron identification and the acceptance cut, for the unfolded x_F distribution was estimated by the simulation with the single neutron event generator. The efficiency was defined as follows.

$$\epsilon_{cut\ eff} = \frac{N\ of\ counts\ after\ the\ experimental\ cut\ with\ the\ detector\ resolution}{N\ of\ simulation\ inputs\ in\ the\ acceptance}. \quad (7.10)$$

In this analysis, the acceptance cut was performed by the radius, r , thus, the efficiency can be visualized by looking at the p_T distribution bin-by-bin based on the equation 1.4, $p_T = x_F \cdot E_p \cdot \theta_n \approx 0.056 \cdot x_F \cdot r$ GeV/ c .

Figure 7.9 shows the simulated p_T distributions (dashed line) in each x_F bin starting at 0.2 with 0.2 interval. Maximum p_T for the acceptance cut, $r < 2$ cm, in each x_F are given by $p_T^{Max} = 0.11 \cdot x_F$ GeV/ c shown as dot-dashed lines. Thus, the expected p_T distribution in the acceptance is below dot-dashed lines. However actual p_T distributions with the experimental cut were smeared due to the position resolution shown as solid lines. Ratio of their counts are the efficiency for the experimental cut as equation 7.10 and listed in table 7.1. The errors were derived from the uncertainty of the p_T shape obtained by the ISR experiment, $\exp(-4.8 \pm 0.3 p_T)$; the maximum variations of the efficiencies using $\exp(-4.5 p_T)$ and $\exp(-5.1 p_T)$ to that using $\exp(-4.8 p_T)$ are shown. These variations were added as a systematic error.

The solid curves also show the p_T resolution derived from the position resolution and the resolution seems to be insufficient to determine the p_T with present detectors. Mean values of simulated p_T distributions in each energy region are also listed in table 7.1.

Neutron x_F	Expected p_T region for $r < 2$ cm (GeV/ c)	Mean p_T with the experimental cut (GeV/ c)	Efficiency (Systematics derived from p_T shape)
0.2–0.4	0–0.033	0.050	0.707 ± 0.060 (8.5%)
0.4–0.6	0–0.056	0.071	0.777 ± 0.037 (4.8%)
0.6–0.8	0–0.078	0.087	0.735 ± 0.017 (2.3%)
0.8–1.0	0–0.100	0.099	0.658 ± 0.018 (2.7%)

Table 7.1: The expected p_T region, mean p_T value and the efficiency for the experimental cut estimated by the simulation (Figure 7.9). The errors for efficiencies are derived from the uncertainty of the p_T shape obtained from the ISR experiment, $\exp(-4.8 \pm 0.3 p_T)$.

7.8 Result

The cross section was obtained after the correction of the energy unfolding and the cut efficiency as shown in Figure 7.10. Error bars only show the statistical uncertainty derived from the unfolding. Before the physics discussion in chapter 9, systematic errors are discussed from next sections.

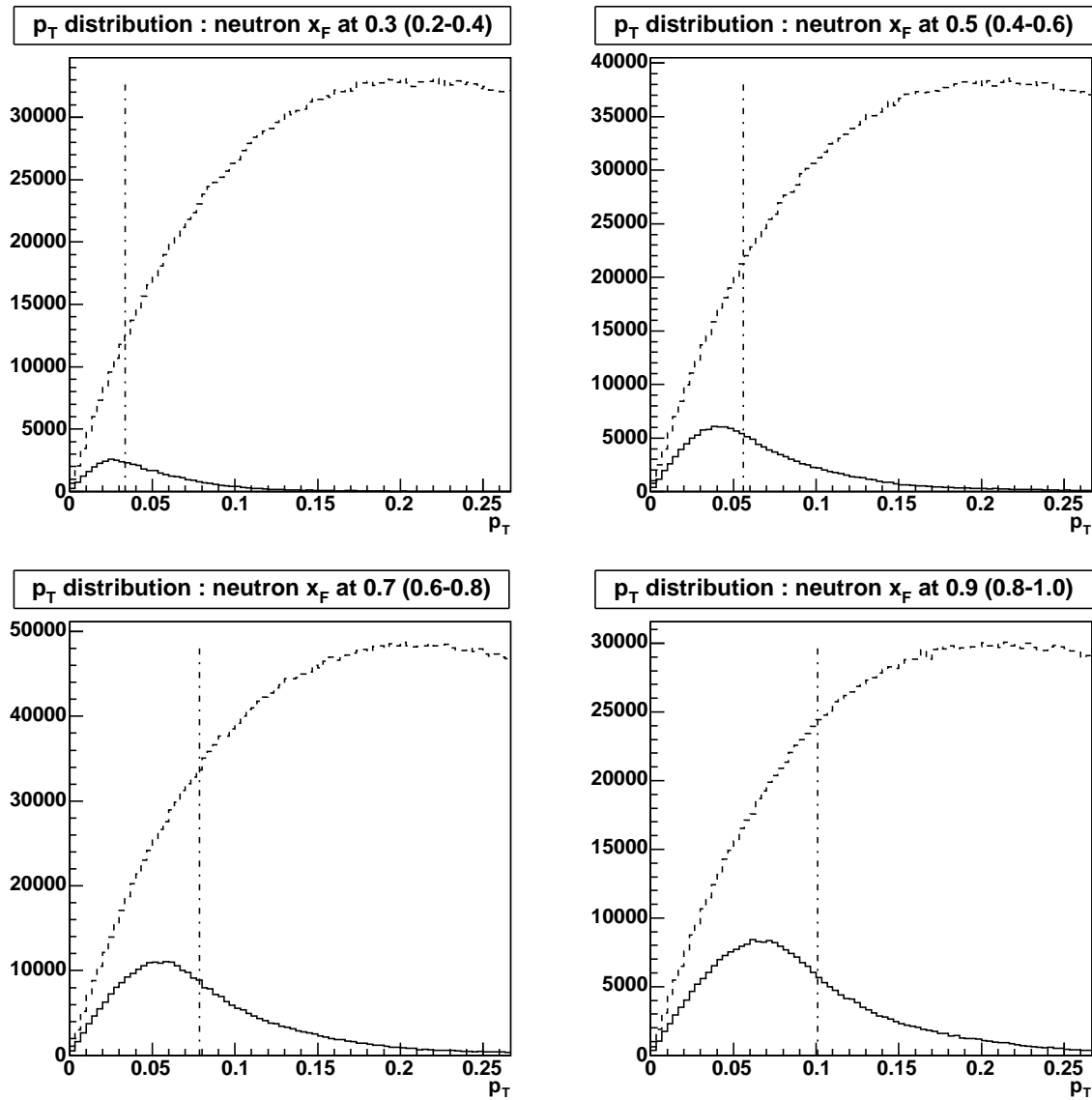


Figure 7.9: Simulated p_T distributions using the p_T shape measured at the ISR experiment. Initial p_T distributions are shown as dashed line in each x_F region. Expected p_T region for the acceptance, $r < 2$ cm, is below dot-dashed line which is the maximum p_T calculated as $\approx 0.11 \cdot x_F$ GeV/c. However actual p_T distributions with the experimental cut, including the neutron identification and the acceptance cut, were smeared as solid lines due to the position resolution. The ratio of a) Entries of p_T distribution in the experimental cut (solid line) to b) Entries in initial p_T shape below the dot-dash line are the efficiency for the experimental cut.

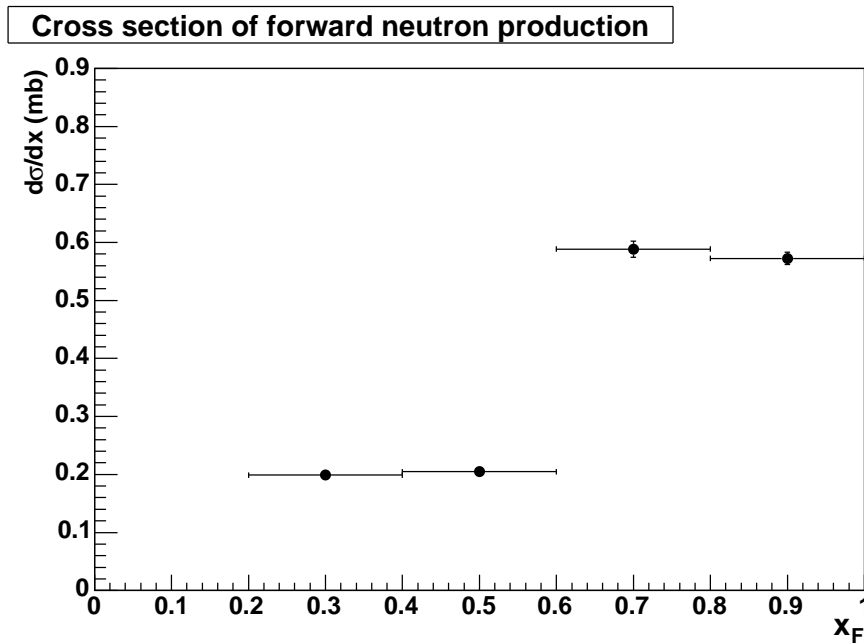


Figure 7.10: The cross section after the correction of the cut efficiency and the energy unfolding. Error bars only show the statistical uncertainties derived from the unfolding.

7.9 Systematic errors

Systematic errors for the cross section measurement are discussed in this section. Scaling errors are summarized in section 7.9.1 and bin-by-bin correlated systematics are discussed in section 7.9.2 or later. Only the bin-by-bin systematics for the cut efficiency were evaluated in section 7.7. All errors were estimated as the ratio of the variation to the final cross section values. Total errors were calculated by quadratic sum.

7.9.1 Scaling errors

- The background estimation by the simulation with PYTHIA event generator. (section 6.2.3).
 - Background contamination (in the measured neutron energy with the ZDC from 20 to 140 GeV for the acceptance cut of $r < 2$ cm)
 - * BG from the proton : 3.6% (Original value is 2.4%. the proton contamination estimated by the simulation should be 1.5 times as discussed in section 6.2.3)
 - * Multi particles detection in each collision : 7%
- Systematics for the luminosity estimation by BBC counts
 - 9.7% (22.9 ± 2.2 mb for the BBCLL1 trigger)
- In total : 12.5%

7.9.2 Systematics for the energy linearity

In section 6.1.1, the ZDC energy response for the neutron below 100 GeV was estimated by the simulation and it has the non-linearity. This non-linearity was corrected by the energy unfolding because its effect is included in the transition matrix A (section 7.6). Since the hadron interaction was just estimated by the simulation, systematics should be considered. We considered it as a variation of the cross section evaluated with a different matrix A with the linear response.

Figure 7.11 shows differential cross sections calculated with the transition matrix A for the non-linear (default) and linear energy responses. Table 7.2 lists the ratio of the variation to the final value which was calculated with the non-linear response in each x_F bin. They are added as a systematic error in each bin.

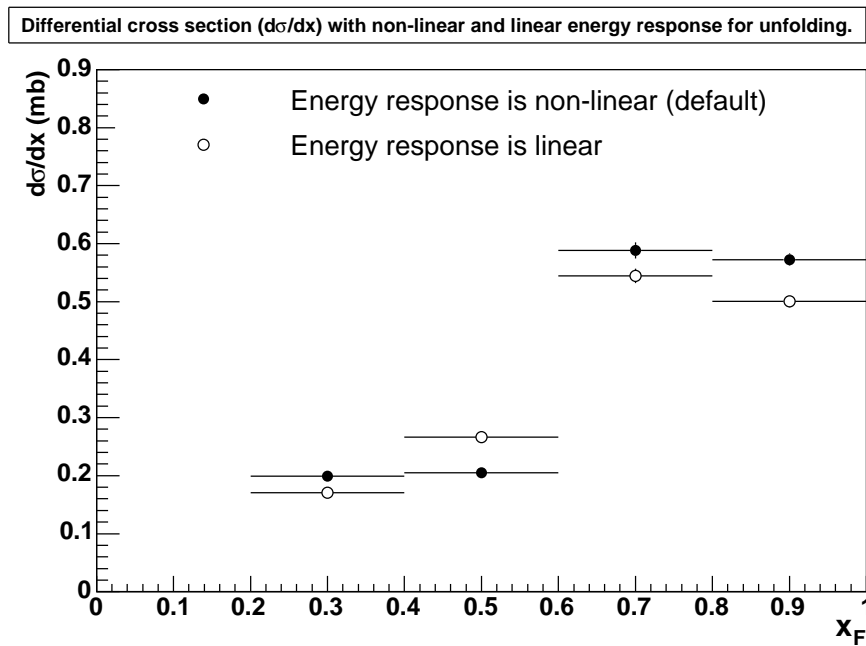


Figure 7.11: Differential cross sections calculated by the transition matrix A with the non-linear (default) and the linear energy responses.

x_F	Systematic error (%)
0.2~0.4	14.33
0.4~0.6	30.16
0.6~0.8	7.46
0.8~1.0	12.59

Table 7.2: Systematic errors for the energy response. Errors are shown as a ratio of the variation to the final cross section value.

7.9.3 Systematics for the determination of the beam axis on the ZDC geometry

In this analysis, we assumed that the beam axis points to the ZDC center. Searching for the beam axis on the ZDC geometry was performed by the position scan of the asymmetry in section 8.1. Results of the beam axis searches for x and y were $+0.46$ cm and -1.10 cm from the ZDC center, respectively.

The shift of the beam axis also appear in the position distributions at high SMD multiplicity event. Figure 7.12 shows the position distribution as a function of the SMD multiplicity for the real and simulation data. In the low multiplicity case, the real and simulation data agree well for both x and y . But at the high multiplicity events, the center for x and y are shifted and their tendencies are consistent with the results of the beam axis searches.

However the beam axis shifts were only shown in pp collision as discussed in section 8.1. We do not understand the reason why. In this analysis, we suffice them by the estimation of the effect to the cross section measurement as systematic error. For this estimation, cross sections were calculated in the different acceptances according to the result of the beam axis shift while keeping $r < 2$ cm and their variations were applied as systematic error. The results of cross sections are shown in Figure 7.13 and the ratio of the variations to the final values are listed in Table 7.3.

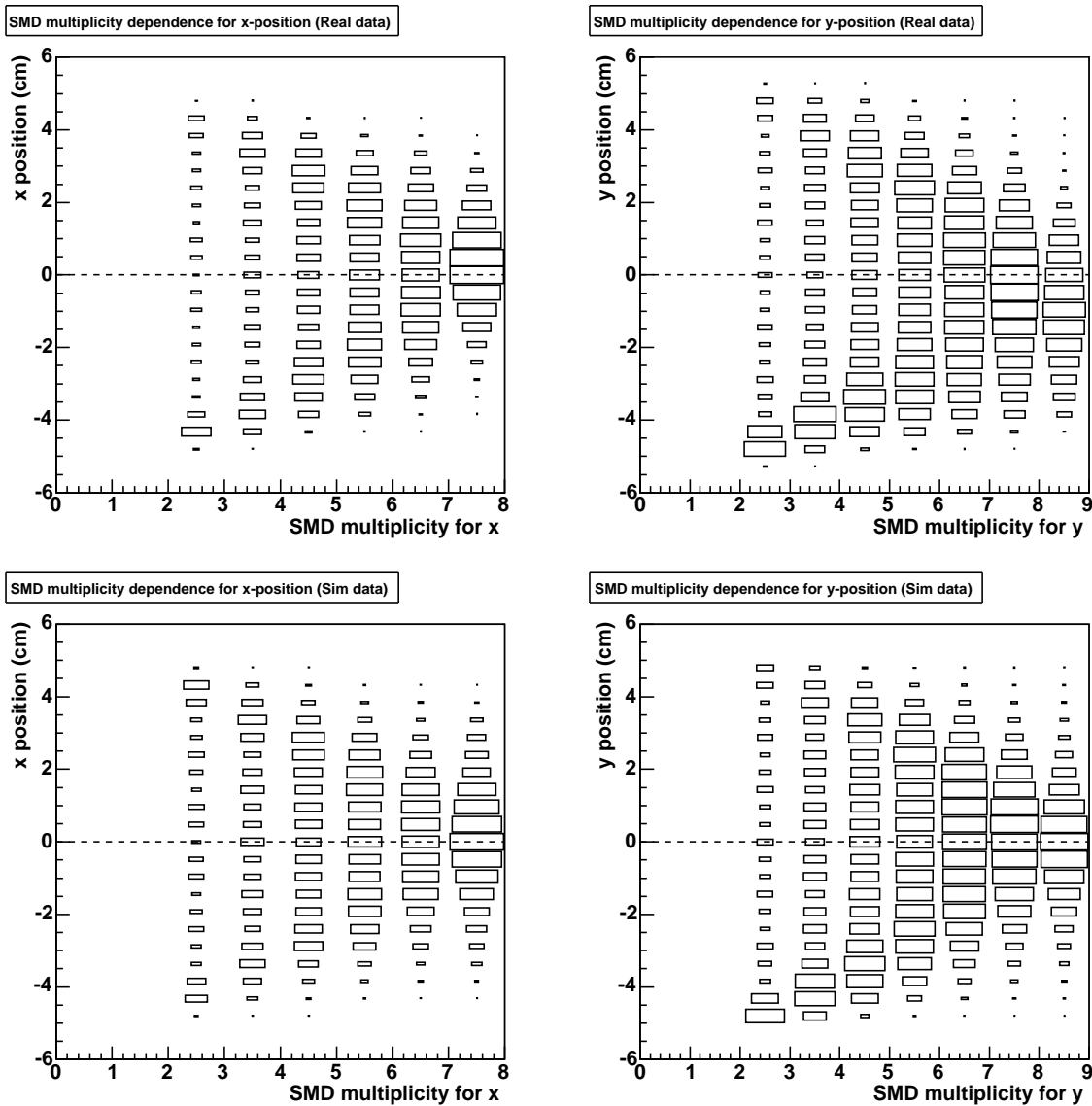


Figure 7.12: Position distributions for x (Left) and y (Right) as a function of the SMD multiplicity for the real (Top) and simulation data (Bottom). Asymmetric distribution for y at low SMD multiplicity was due to the different edge effect for the top and bottom regions (section 6.1.2). Center positions of the real data are shifted at high SMD multiplicity for both x and y and tendencies are consistent with the results of the beam axis searches in section 8.1. The beam axis shift can not be reproduced by the simulation, thus the shifts are not caused by the detector geometry.

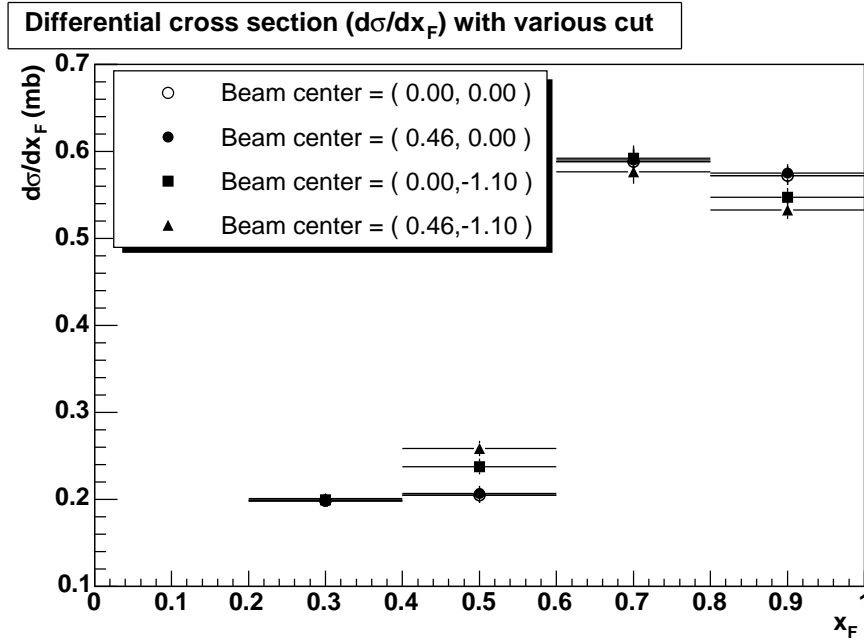


Figure 7.13: Cross sections were calculated in the different acceptances according to the result of the beam axis search. The centers of acceptances were $(x,y)=(0.00,0.00)$, $(0.46,0.00)$, $(0.00,-1.10)$ and $(0.46,-1.10)$ cm with keeping $r < 2$ cm.

x_F	$(x,y)=(0.46,0.00)$ (%)	$(x,y)=(0.00,-1.10)$ (%)	$(x,y)=(0.46,-1.10)$ (%)
0.2~0.4	0.32	0.38	1.03
0.4~0.6	1.03	16.04	26.27
0.6~0.8	0.34	0.69	2.04
0.8~1.0	0.46	4.34	6.94

Table 7.3: Differences of the cross section values by moving the acceptance center. Values were calculated as the ratio of variations to the final cross section value in each x_F bin. Maximum differences shown as bold characters were added as a systematic error.

Chapter 8

Analysis for the single transverse spin asymmetry

In this chapter, analyses for single spin asymmetries are shown. The definition of single transverse spin asymmetry (A_N) are written in Appendix A. The azimuthal angle and x_F dependencies of A_N are evaluated and shown in section 8.2 and 8.3, respectively.

8.1 The study of the beam axis on the detector geometry

The ZDC center was aligned to a beam axis at the beginning of 2003 run. Basically we assumed that the beam axis was on the ZDC center in this analysis. Moreover we can obtain the beam axis on the detector geometry by a position scan of the A_N which is calculated by the luminosity formula since A_N should be zero kinematically at the beam axis (Appendix A). Figure 8.1 shows schematic views of position scans. Scans went through x and y directions starting at negative region and we called the “horizontal scan” and “vertical scan”, respectively. At the vertically polarized pp collision, which is an usual setting in transverse run at RHIC, the A_N should appear in the horizontal scan only; the A_N is expected to be zero at the beam axis and distributed symmetric around it. The A_N for vertical scan should be zero in all region at that time. At the horizontally polarized pp collision, the A_N is expected to appear in the vertical scan only. We can extract beam axes for x and y by looking at intersections of zero-asymmetry in these scans.

Figure 8.2 and 8.3 show results of the position scans for the vertically and horizontally polarized pp collisions, respectively¹. We used BBCLL1&(ZDCN|S) data samples in this analysis. The A_N distributions for all scans give the consistent shapes as we expected. The beam axes for x and y were obtained as $+0.46\pm 0.08$ cm and -1.10 ± 0.14 cm for x and y , respectively.

However this estimation has some systematics. It appears in the vertical scan for horizontally polarized pp run in the forward kinematics as a systematic error for the relative luminosity, R ; The values of A_N should be zero for all bins, but the values were systematically shifted to the negative. Same R was used to the horizontal scan. Therefore, we cannot conclude the shift of the beam axis in x estimated by the A_N scan alone.

¹Horizontally polarized pp collision was performed at 2006 run.

For the beam axis in y , its shift is so large. According to the RHIC complex, the fluctuation of the beam axis should be a few mm. For more discussions, we checked position distributions in heavy ion data which was CuCu collision at 2005 run² and the result is Figure 8.4. We can also evaluate the beam axis by these distributions since 100 GeV neutrons from the heavy ion peripheral collision are emitted within a few cm diffusion at the ZDC transverse geometry [2]. The beam axis for x and y were obtained as 0.28 ± 0.01 cm and -0.07 ± 0.01 cm, respectively. There are inconsistencies between the pp and heavy ion data, especially in the y -axis. We do not understand the reason why.

The beam axis shift that we observed should be considered as systematic errors for the results. Systematics were defined as variations of the cross section and asymmetry results obtained by moving the center of acceptance while keeping same cut region (for example, $r < 2$ cm for the cross section analysis).

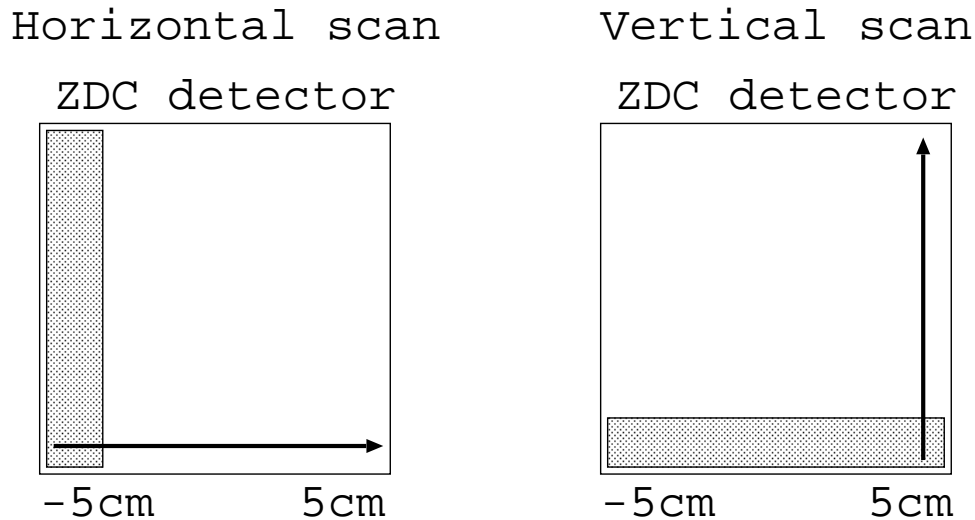


Figure 8.1: Schematic views of the position scans of A_N calculated by the luminosity formula for searching beam axes in x (Left) and y (Right). The gray region, 1×10 and 10×1 cm for the horizontal and vertical scans, respectively, is the acceptance of the A_N calculation in each bin in Figure 8.2 and 8.3.

²It was performed just before pp run period.

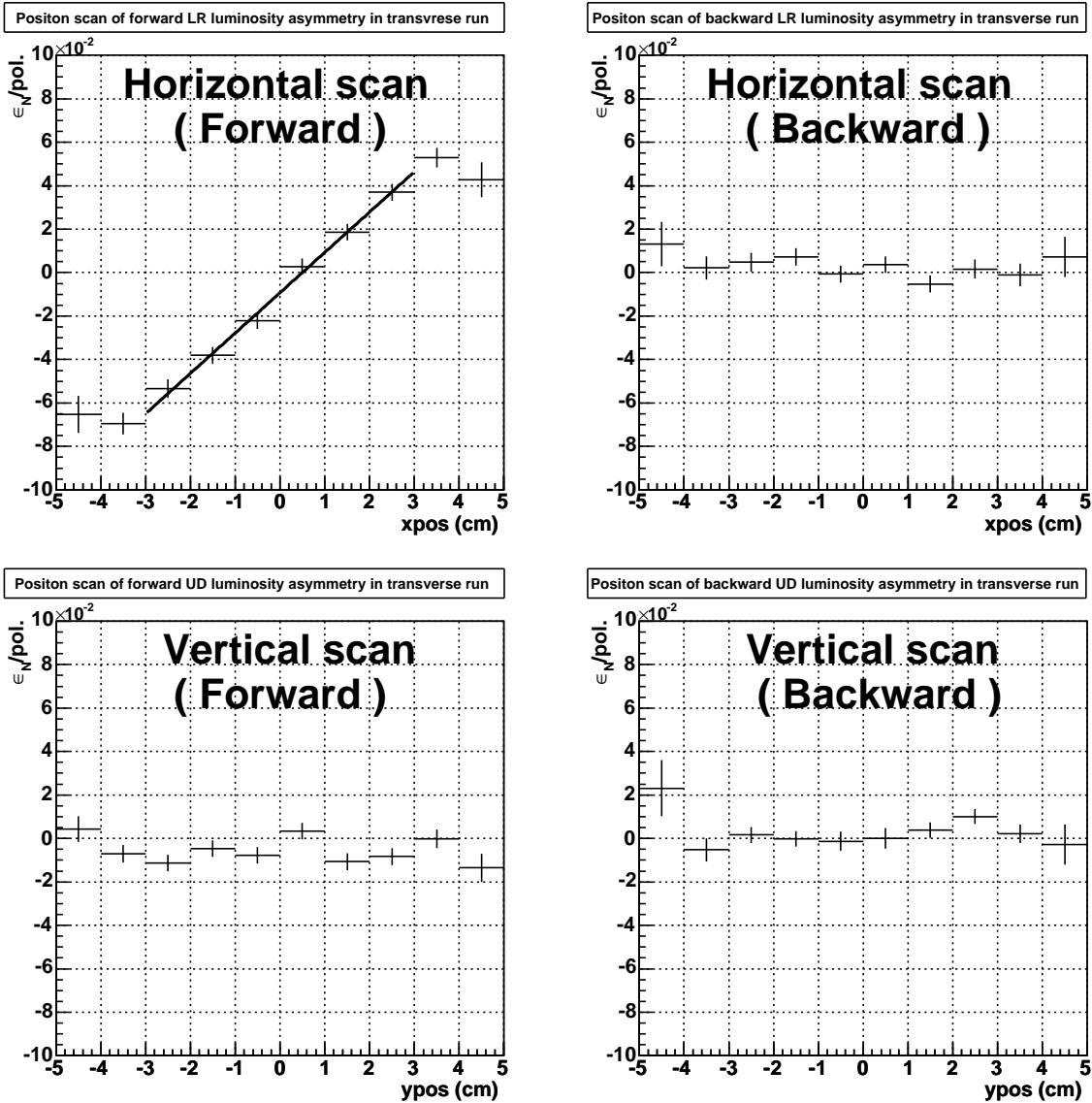


Figure 8.2: The position scan of ϵ_N calculated by the luminosity formula at the transversely polarized pp run. The finite asymmetry is seen at the horizontal scan in the forward kinematics and its intersection within $\epsilon_N=0$ should be the beam axis in x . Based on this result, the beam axis was obtained as $+0.46 \pm 0.08$ cm in x for the ZDC geometry.

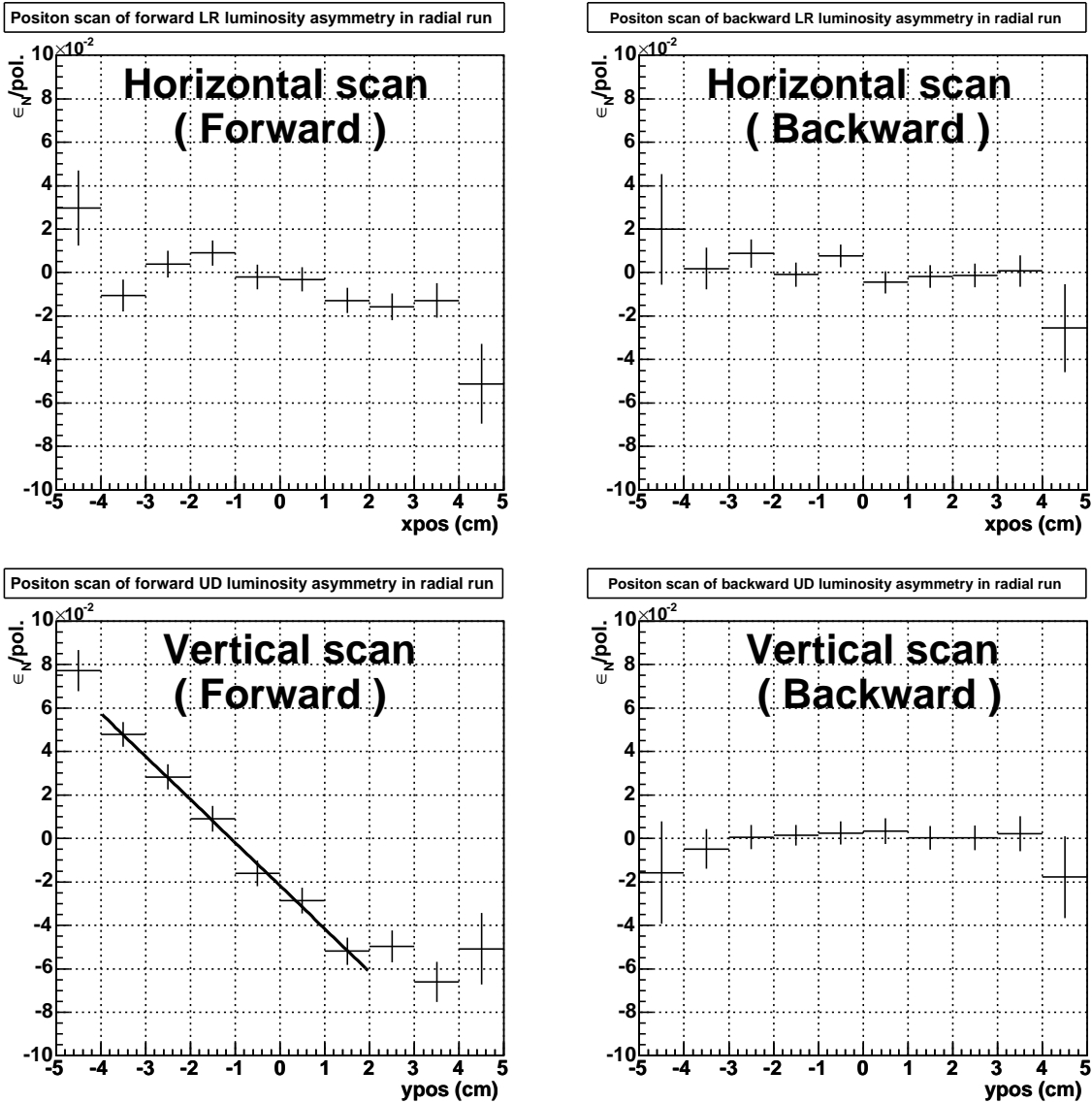


Figure 8.3: The position scan of ϵ_N calculated by the luminosity formula at the horizontally polarized pp run. The finite asymmetry is seen at the vertical scan in the forward kinematics and its intersection within $\epsilon_N=0$ should be the beam axis in y . Based on this result, the beam axis was obtained as -1.10 ± 0.14 cm in y for the ZDC geometry.

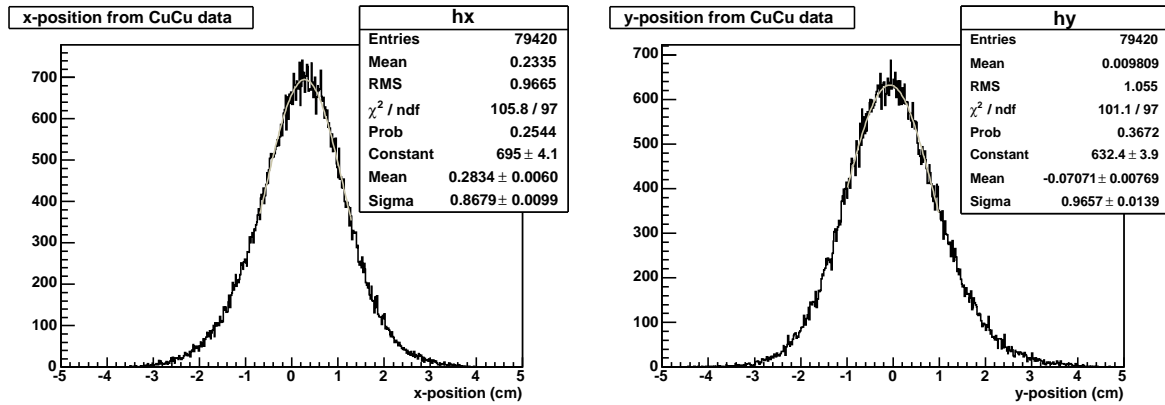


Figure 8.4: Position distributions for x and y for the CuCu data in 2005 run. Neutron energy was selected to be above 300 GeV, corresponds to three neutrons or more from the peripheral collision. Beam axes looks almost center in the ZDC geometry.

8.2 Azimuthal angle dependence of A_N

8.2.1 Asymmetry calculation

The acceptance definition for the azimuthal angle (ϕ) dependent asymmetry is shown in Figure 8.5. For the comparison with the previous measurement, the IP12 experiment (see part I), same acceptance cut, $0.5 < r < 4.0$ cm, was applied. The acceptance area was cut to 16 pieces in a radial pattern and asymmetry was calculated by the square root formula in the same way of the IP12 experiment. (section 3.4)³.

For this analysis, we used 6.5 million (3 fills) and 17.6 million (4 fills) events for the ZDCN|S and BBCLL1&(ZDCN|S) trigger samples, respectively. The energy cut was required to select 40–120 GeV in the measured energy with the ZDC. Before merging ϵ_N 's of all fills, they were divided by polarizations in each fill; the polarization can be fluctuated fill-by-fill due to a time dependence of the acceleration performance. The polarization in each fill is listed in Table 8.1. Merged ϵ_N divided by the polarization are plotted in Figure 8.6. Finite asymmetries are seen in the forward kinematics for both trigger samples and they can be fitted by the sine curve (equation 3.6) well.

8.2.2 Preparation of the simulation sets for each trigger

Measured energy distributions for two trigger samples after the experimental cut were different as shown in Figure 8.7. The neutron energy associated with charged particles was lower than that without the association. It is appropriate in the view of energy conservation.

We should prepare two sets of simulations for the estimations of the smearing parameters, $\epsilon_\phi^{\text{smearing}}$, which are correlated to the position resolution and the position resolution is correlated

³The definition of ϕ is different with the IP12 experiment. The $\phi=0$ at the PHENIX corresponds to the $\phi=-\pi/2$ at the IP12. To perform the ϕ dependence, both experiments calculated A_N in counterclockwise.

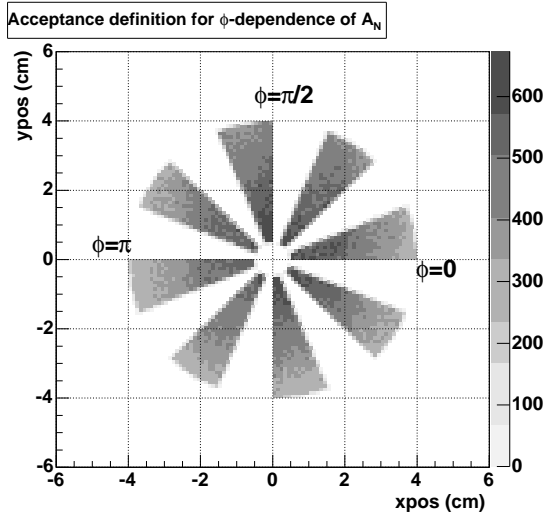


Figure 8.5: The acceptance definition for the ϕ dependence of A_N . The acceptance cut was required $0.5 < r < 4.0$ cm in the same way of the IP12 experiment. The acceptance was also divided to 16 pieces in a radial pattern and the asymmetry was calculated by the square root formula starting at $\phi=0$ to π in counterclockwise. In this figure, only even pieces are plotted.

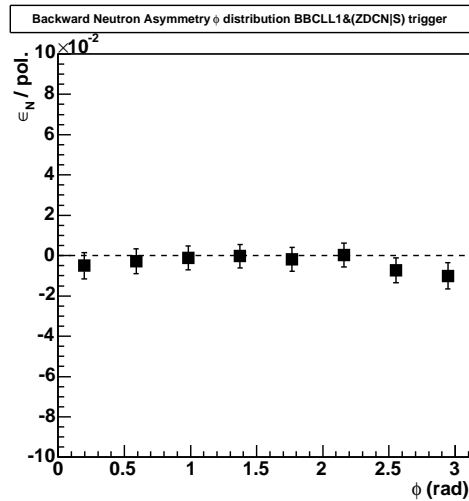
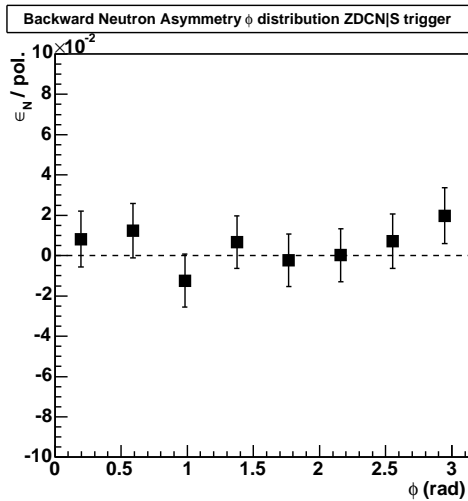
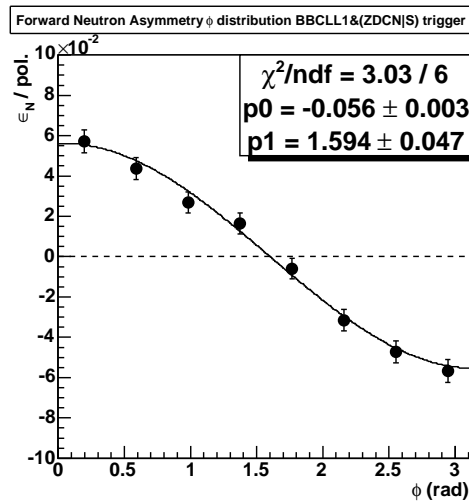
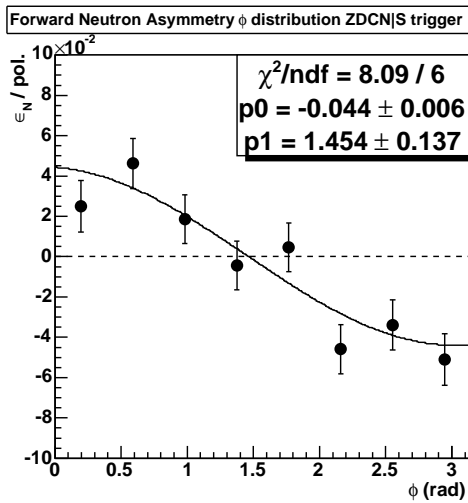


Figure 8.6: The ϕ dependence of ϵ_N divided by the polarization. Top and bottom figures show the asymmetries in the forward and backward kinematics, respectively. Left and right figures show them for the ZDCN|S and BBCLL1&(ZDCN|S) samples, respectively. Finite asymmetries are seen in the forward kinematics and can be fitted by the sine curve well. Backward asymmetries were consistent with zero for both samples.

Polarization

Fill number	Blue beam (%)	Yellow beam (%)
6931	43.06±2.94	52.25±3.50
7294	47.63±2.69	46.30±8.23
7295	47.70±2.45	50.67±3.25
7296	46.30±2.30	52.20±3.23

Table 8.1: The polarization value in each fill which was used for the asymmetry analysis. Fill#6931 had the BBCLL1&(ZDCN|S) data sample only. In the present analysis, we used the SOUTH ZDC only. Thus, asymmetries in the forward and backward kinematics were calculated by the Yellow and Blue polarizations, respectively. Systematic uncertainties of 6.2% and 5.9% for the Yellow and Blue beams are not included.

with the neutron energy (section 6.1.3). The energy distributions for the simulation inputs were determined in the same way of the cross section analysis (chapter 7). After some iterations by modifying the input shapes⁴, we obtained the simulations which well reproduce measured energy distributions above 40 GeV as shown in Figure 8.8. Same simulations were used for the analysis of the x_F dependence (Chapter 8.3).

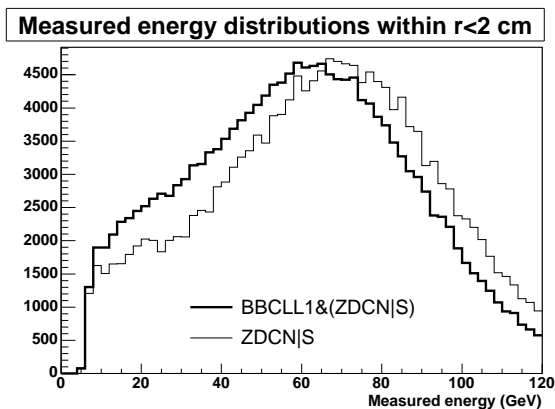


Figure 8.7: Measured energy distributions after the neutron identification and the acceptance cut for the ZDCN|S and BBCLL1&(ZDCN|S) samples.

8.2.3 Estimation of the smearing effect

The ϵ_N is smeared from the A_N by the wrong assignment of left and right due to the position resolution. It is called smearing effect and it was estimated by the simulation. From equation 3.5, the smearing parameter, $\epsilon_\phi^{smearing}$, can be evaluated by the simulation as,

$$\epsilon_\phi^{smearing} = \frac{A_N^{Output}}{A_N^{Input}}, \quad (8.1)$$

where, A_N^{Output} corresponds to the ϵ_N of the real data; it is including effects of the experimental cut and the position resolution. As A_N^{Input} , we generated neutrons with the sine modulated $A_N(\phi)$ as equation 3.6 with $A_N = -0.10$. The output is shown in Figure 8.9 in case of the

⁴In the cross section calculation, we cannot obtain the detail shape because we concluded it with only three points. The small iteration to reproduce the measured energy distribution is necessary.

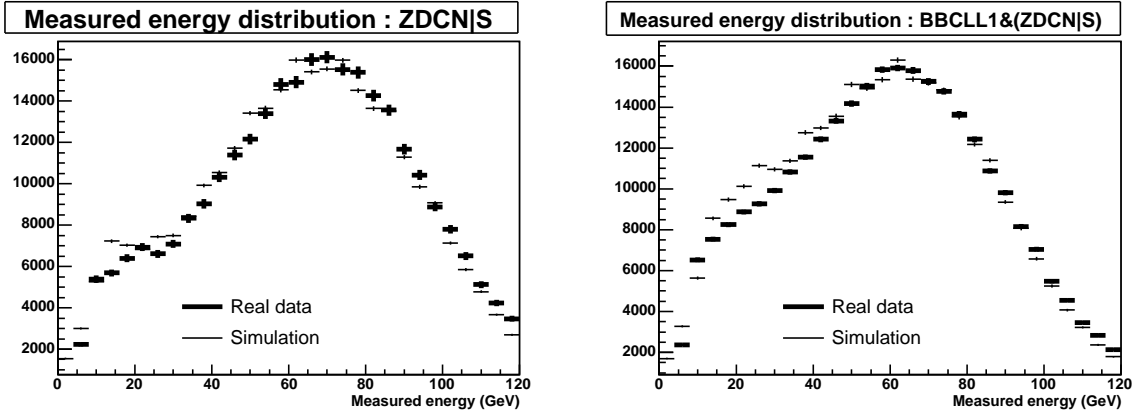


Figure 8.8: Measured energy distributions for the real and simulation data. Input shapes for the simulations were modified to reproduce the measured energy distributions above 40 GeV for the ZDCN|S and BBCLL1&(ZDCN|S) trigger samples.

ZDCN|S. Smearing amplitude was obtained as -0.076 and their ratio, 0.76 , is a correction factor of the smearing effect. We also estimated that for the BBCLL1&(ZDCN|S) by same procedure and obtain smearing parameters as follows.

- $\epsilon_{\phi}^{smearing}[\text{ZDCN|S}] : 0.760 \pm 0.015$
- $\epsilon_{\phi}^{smearing}[\text{BBCLL1\&(ZDCN|S)}] : 0.746 \pm 0.016$

They were not so different.

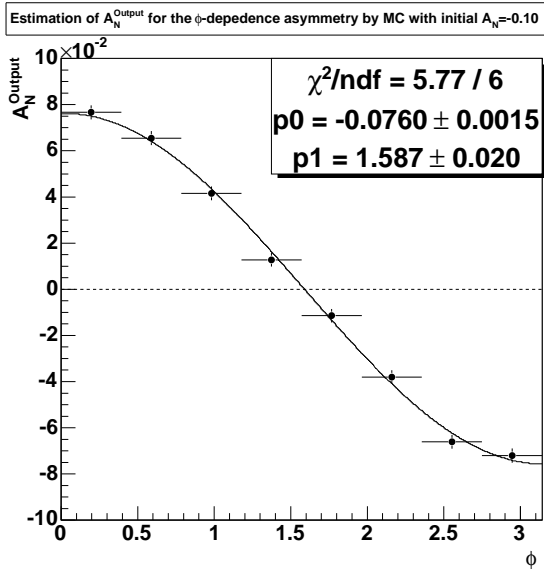


Figure 8.9: The output of the ϕ -dependent A_N from the simulation which was modified to the ZDCN|S sample. As a simulation input, $A_N(\phi) = A_N \sin(\phi - \pi/2)$ with $A_N = -0.10$ was used. The output amplitude was reduced to -0.076 and the ratio of them, 0.76 , is a correction factor of the smearing effect.

8.2.4 Systematic errors

Background contamination

The background contamination was studied by the simulation with PYTHIA event generator. After the neutron identification and the acceptance cut, the neutron purities were,

- Without BBC trigger, ZDCN|S : 0.975 ± 0.006
- With BBC trigger, BBCLL1&(ZDCN|S): 0.977 ± 0.010

Main background contributions were the K^0 and proton. According to the discussion in section 6.2.3, we added the systematic error contributed from the proton only. They were 1.4% and 1.0% for the ZDCN|S and BBCLL1& (ZDCN|S) triggers, respectively and should be increased 1.5 times. Increased values, 2.1% and 1.5% were added as systematic errors.

The background from the beam gas event was also discussed in the cross section study (section 7.4). It was 0.22% and negligible.

Systematics from the beam axis shift

The systematic error for the determination of the beam axis was discussed in this section. According to the results of beam axis searches, $A_N(\phi)$ were calculated with center positions as $(x,y) = (0.46, 0.00)$, $(0.00, -1.10)$ and $(0.46, -1.10)$ cm while keeping the acceptance cut, $0.5 < r < 4.0$ cm. Results fitted by the sine curve are shown in Figure 8.10. We cannot distinguish the best fit from χ^2 values. Thus, maximum variations to final values, which were calculated by $(x,y) = (0.00, 0.00)$ cm, are added as systematic errors. Table 8.2 lists asymmetry amplitudes and variations to final values.

ZDCN S		
Acceptance center in (x,y) cm	ϵ_N / pol.	Variation to the final value (%)
(0.00, 0.00)	0.0443 ± 0.0063	“This is the final value”
(0.46, 0.00)	0.0448 ± 0.0063	1.13
(0.00, -1.10)	0.0414 ± 0.0062	6.55
(0.46, -1.10)	0.0439 ± 0.0062	0.90
BBCLL1&(ZDCN S)		
Acceptance center in (x,y) cm	ϵ_N / pol.	Variation to the final value (%)
(0.00, 0.00)	0.0559 ± 0.0028	“This is the final value”
(0.46, 0.00)	0.0530 ± 0.0028	5.19
(0.00, -1.10)	0.0576 ± 0.0028	3.04
(0.46, -1.10)	0.0559 ± 0.0028	~ 0

Table 8.2: The ϵ_N calculated with various center positions of the acceptance. Variations to final values are also shown and maximum variations are displayed as bold characters. The maximum one is added as systematic errors.

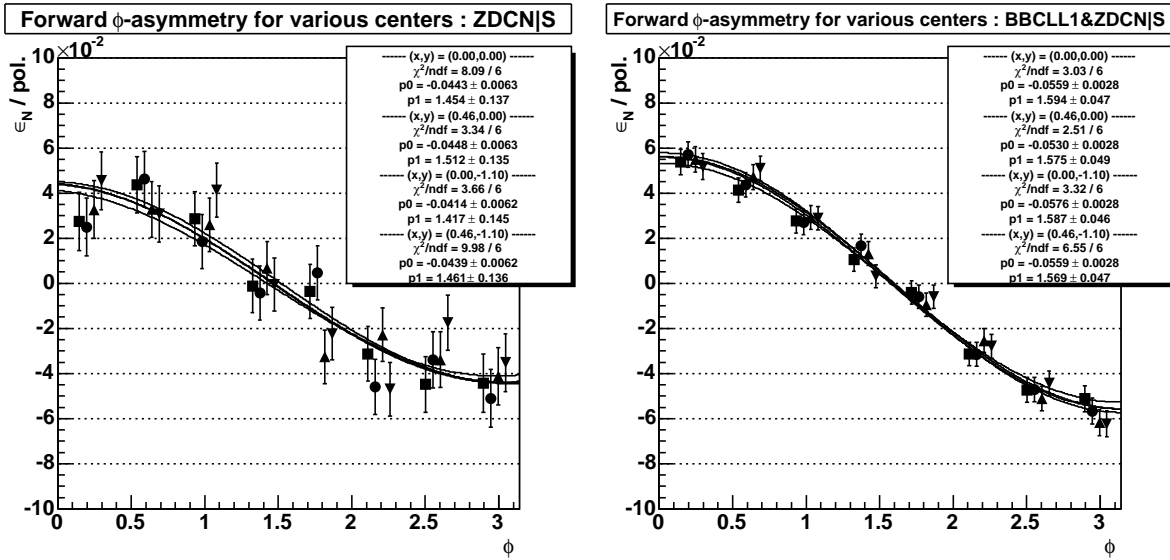


Figure 8.10: The ϕ dependence of ϵ_N calculated with various center positions of the acceptance as $(x,y) = (0.00, 0.00)$, $(0.46, 0.00)$, $(0.00, -1.10)$ and $(0.46, -1.10)$ cm are plotted as circle, square, triangle-up and triangle-down points, respectively. The horizontal value in each point was shifted to be easily viewable: only circle points show correct values.

Systematics for the correction of the smearing effect

Since the smearing effect is caused by the position resolution, systematic error of the position resolution, 14.1% (section 6.1.5), should be reflected to uncertainties for the result. It was estimated by a variation of the asymmetry value calculated with the 14.1% increased position resolution in the simulation. Figure 8.11 shows output asymmetries with the default position resolution and the 14.1% increased one. The asymmetry was more smeared with 4.2% reduction. The variation is assigned as a systematic error for the smearing correction.

Effect of the detector asymmetry

A detector asymmetry is defined as a difference of acceptance for left and right (Appendix A). The detector asymmetry is basically canceled out using the square root formula until third order. In this section, the cancellation of the detector asymmetry is shown.

Figure 8.12 shows detector asymmetries calculated by moving the x -center of the acceptance; x -centers were $-0.4, -0.2, 0.0, 0.2, 0.4$ cm. The detector asymmetry increased 0.25 by moving the x -center from -0.4 cm to 0.4 cm. However physics asymmetries which are also shown in Figure 8.12 did not change within 0.003. This result indicates the square root formula was correctly working for the cancellation of the detector asymmetry.

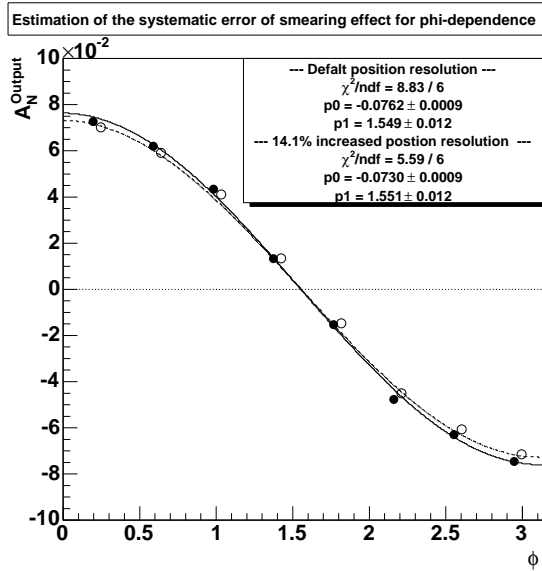


Figure 8.11: The ϕ dependence of A_N with the default and 14.1% increased position resolutions estimated by the simulation are plotted as closed and open circles, respectively. As a simulation input, $A_N(\phi) = A_N \sin(\phi - \pi/2)$ with $A_N = -0.10$ was generated. The variation of amplitudes was 4.2%.

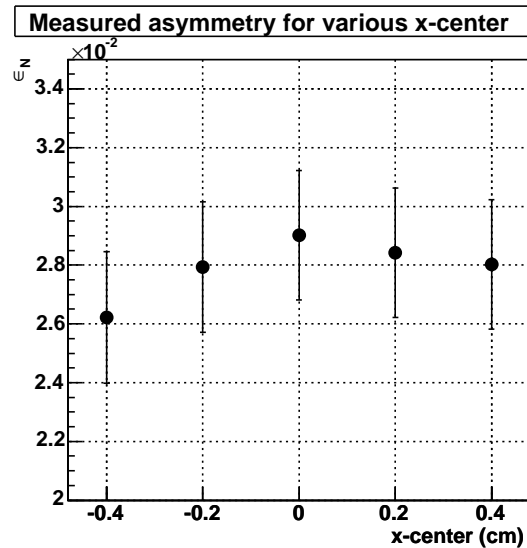
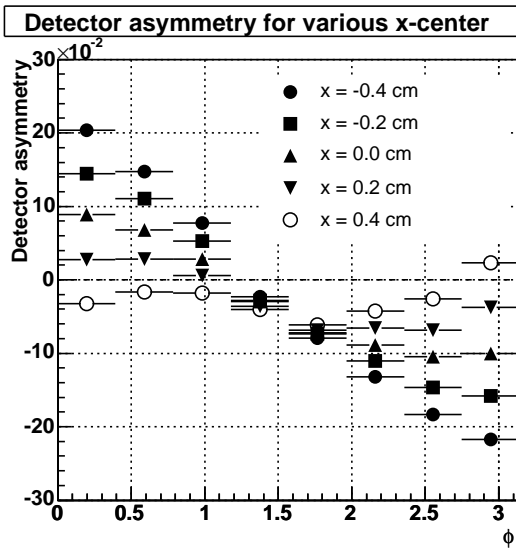


Figure 8.12: Left) Detector asymmetries as a function of ϕ for various x -centers ; x -center for $-0.4, -0.2, 0.0, 0.2, 0.4$ cm. Right) Physics asymmetries, ϵ_N , as function of the x -center.

Bunch shuffling

A technique called ‘‘bunch shuffling’’ can be utilized to check uncertainties in asymmetries due to the variation of beam characteristics bunch by bunch. The basic idea is the comparison of the asymmetry fluctuation to the statistical uncertainty by random assignments of spin patterns in each bunch, which is called a bunch shuffling. If there is no systematic uncertainty, the fluctuation of asymmetry with the bunch shuffling should be same as the statistical uncertainty. If there is, the fluctuation being larger than the statistical one.

Asymmetry calculations by the bunch shuffling were performed fill by fill and the results divided by polarizations were fitted through the run period in each shuffling. For example, results for 5 shuffles are shown in Figure 8.13. The χ^2 value of the constant fit is described in each shuffle with the assumption of the same $\epsilon_\phi^{smearing}$ in all fills as,

$$\chi^2 = \sum_f^n \frac{(A_N(f) - \langle A_N(f) \rangle)^2}{\sigma_{stat.}^2(f)}, \quad (8.2)$$

where f is the fill number with n being the total number of fills. Therefore, χ^2 distributions lead to the comparison of the asymmetry fluctuation, shown as numerator, to the statistical uncertainty, shown as denominator, through the run period. We can evaluate bunch-by-bunch systematics whether the χ^2/ndf is unit or not.

In this analysis, the bunch shuffling was performed 30,000 times. Figure 8.14 and 8.15 show χ^2/ndf distributions in each ϕ region for the ZDCN|S and BBCLL1&(ZDCN|S) samples, respectively. We found large χ^2/ndf values in the first and last bins. It is caused by the residual of the physics asymmetry which would affect as,

$$\begin{aligned} \Delta A_N^{Residual} &\sim A_N \sqrt{\frac{1}{n_{bunch}} \left[1 + \left(\frac{\Delta l}{\langle l \rangle} \right)^2 \right]}, \\ \Delta(\chi^2/ndf) &\sim \frac{(\Delta A_N^{Residual})^2}{\sigma_{stat}^2}, \end{aligned} \quad (8.3)$$

where n_{bunch} is total bunch number in all fill, $n_{bunch} = \sum_{fill} n_{bunch}^f$. $\langle l \rangle$ and Δl denote the mean value and the bunch-by-bunch fluctuation of luminosity. Detailed calculation of the residual asymmetry are shown in Appendix C.2. In the data sets, n_{bunch} for the ZDCN|S and BBCLL1&(ZDCN|S) were 195 and 245, respectively. For example, the value of $\Delta(\chi^2/ndf)$ for first and last bins were ≈ 0.42 with $\epsilon_N/pol. \approx 0.057$ for the BBCLL1&(ZDCN|S) trigger sample⁵. On the other hand, the χ^2/ndf value for bin#4 was almost unit since the $\epsilon_N/pol.$ was nearly zero in this bin (Figure 8.6); the residual asymmetry was negligible.

In addition, we should consider the fluctuation of χ^2/ndf value coming from the total bunch number. The χ^2/ndf can fluctuate as,

$$\Delta(\chi^2/ndf) \sim \left(1 \pm \frac{1}{\sqrt{(n_{bunch} - 1)}} \right)^2 - 1. \quad (8.4)$$

⁵Values of the $\Delta(\chi^2/ndf)$ for all bins are listed in Appendix C.2.

Details are shown in Appendix C.1. It means that we cannot ignore the fluctuation in case of small n_{bunch} . For our data samples, values of $\Delta(\chi^2/ndf)$ for the ZDCN|S and BBCLL1&(ZDCN|S) are about 0.15 and 0.13, respectively. Systematical fluctuations are $\sqrt{0.15} \cdot \sigma_{stat} = 0.39 \cdot \sigma_{stat}$ and $\sqrt{0.13} \cdot \sigma_{stat} = 0.36 \cdot \sigma_{stat}$ for ZDCN|S and BBCLL1&(ZDCN|S), respectively. The systematics estimated by the bunch shuffling is limited by this fluctuation.

Values of χ^2/ndf for all bins can be understood with the fluctuation caused by n_{bunch} and the residual asymmetry. We conclude the fake asymmetry from the bunch-by-bunch is less than $0.39\sigma_{stat}$ and $0.36\sigma_{stat}$ for the ZDCN|S and BBCLL1&(ZDCN|S), respectively. We did not include these uncertainties to the final systematics in A_N .

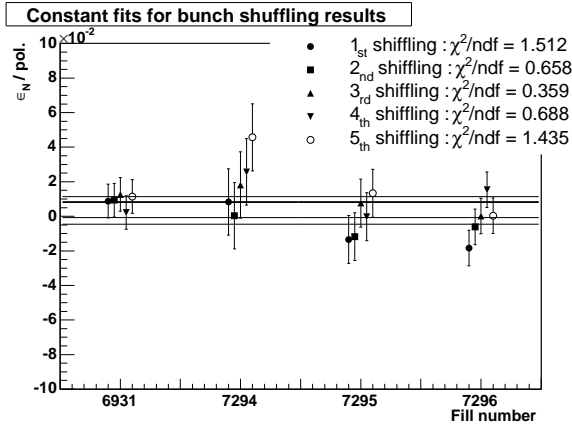


Figure 8.13: Asymmetries were calculated by the bunch shuffling and shown as a function of the fill. In this picture, the bunch shuffling was performed five times, for example. Results were fitted by constant through all fills and fit lines are shown as solid lines. Values χ^2/ndf of fit results are also shown.

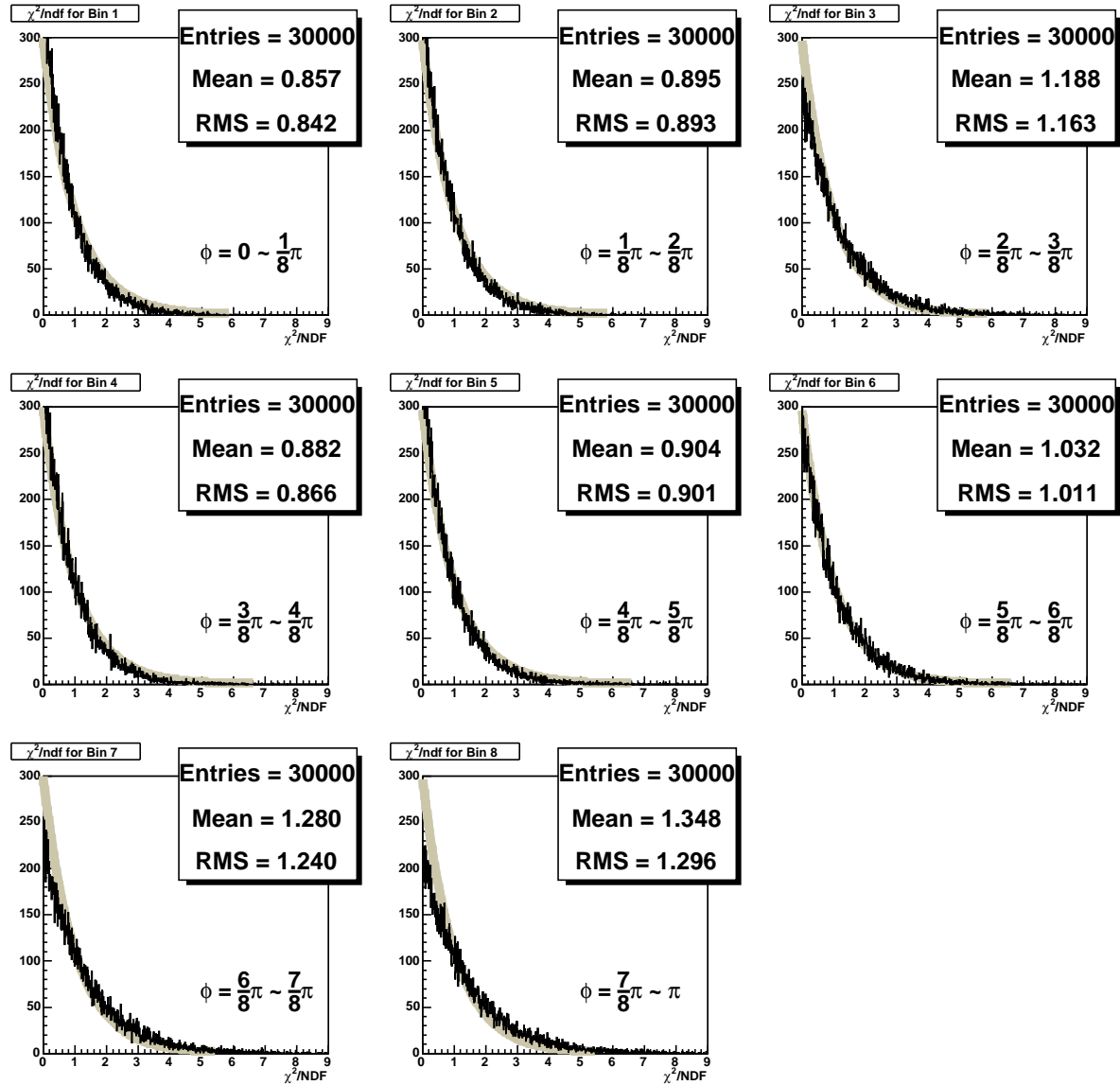


Figure 8.14: Distributions of χ^2/ndf obtained from the bunch shuffling for the ZDCN|S sample. Each histogram indicates each bin for the ϕ -dependent A_N . Solid gray line is the expected χ^2/ndf distribution for 3 fills ($ndf = 2$) so that the asymmetry fluctuation by the bunch shuffling equal to the statistical uncertainty.

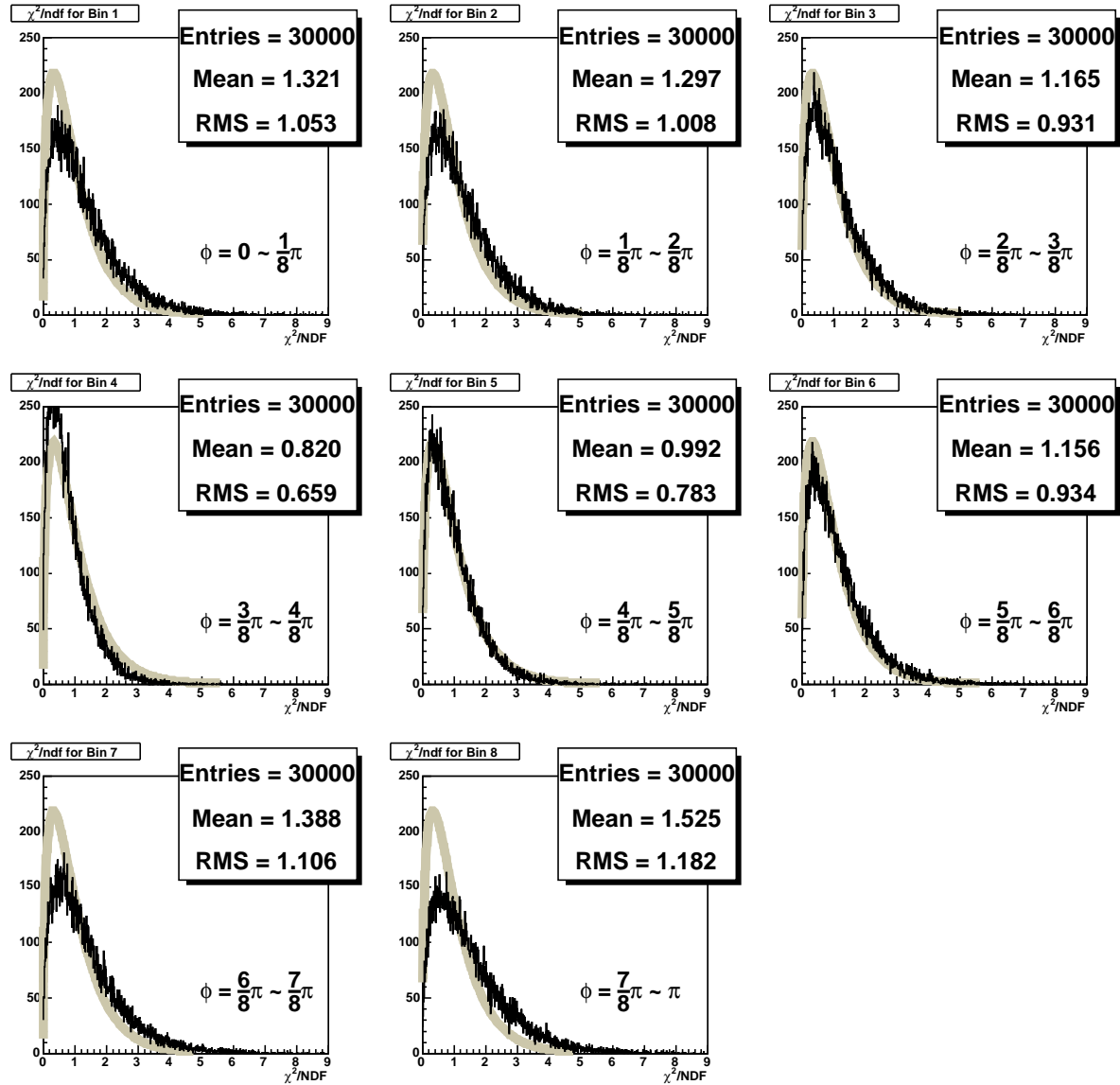


Figure 8.15: Distributions of χ^2/ndf obtained from the bunch shuffling for the BBCL1&(ZDCN|S) sample. Each histogram indicates each bin for the ϕ -dependent A_N . Solid gray line is the expected χ^2/ndf distribution for 4 fills ($ndf = 3$) so that the asymmetry fluctuation by the bunch shuffling equal to the statistical uncertainty.

Summary of systematic errors

Systematic errors are listed in this section. Values are presented as variations to final values. If there are differences between two trigger samples, the ZDCN|S value is written up in parentheses. Total uncertainties were calculated by quadratic sum.

- Estimation from the measurement : total 5.2% (6.6%)
 - Beam axis shift : 5.2% (6.6%)
 - Beam gas background for the ZDCN|S trigger : (<1%)
- Simulation uncertainty : total 7.4% (8.0%)
 - Background contamination : 1.5% (2.1%)
 - Smearing effect from the position resolution : 4.2%
 - Multiple hits in one event : 5.9% (6.5%)
- Total : 9.0% (10.4%)
- Polarization : 6.2% for the Yellow beam

8.3 x_F dependence of A_N

8.3.1 Asymmetry calculation

The acceptance definition for the x_F dependence of A_N is shown in Figure 8.16. It required $0.5 < r < 3.0$ cm, which is not same as the azimuthal angle dependence because we should not use the edge region to avoid the edge effect (section 6.1.2). The acceptance was also divided to the left and right sectors by the azimuthal angle cut which was determined to maximize the figure of merit according to the $\cos\phi$ dependence of A_N ,

$$\frac{S^2}{N} = \frac{(\int_{-\phi_0}^{\phi_0} \cos\phi d\phi)^2}{2\phi_0}, \quad (8.5)$$

and obtained as $\phi_0=66.8^\circ$. With this definition, the effective A_N of present analysis is expected to be

$$\frac{A_N^{eff}}{A_N} = \frac{\int_{-\phi_0}^{\phi_0} \cos\phi d\phi}{2\phi_0} \Bigg|_{\phi_0=66.8^\circ} = 0.788. \quad (8.6)$$

This effect is a part of the smearing effect which is estimated in section 8.3.2.

Asymmetry was calculated by the square root formula with the number of event in the left sector (N_L) and the right sector (N_R) in each measured energy (E) as,

$$\epsilon_N(E) = \frac{\sqrt{N_L^\uparrow(E)N_R^\downarrow(E)} - \sqrt{N_R^\uparrow(E)N_L^\downarrow(E)}}{\sqrt{N_L^\uparrow(E)N_R^\downarrow(E)} + \sqrt{N_R^\uparrow(E)N_L^\downarrow(E)}}. \quad (8.7)$$

After the correction of the polarization, P , and the smearing effect, $\epsilon_E^{smearing}$ which is discussed in next section, we obtain initial $A_N(E)$ as,

$$A_N(E) = \frac{1}{P} \frac{1}{\epsilon_E^{smearing}(E)} \epsilon_N(E). \quad (8.8)$$

We used same data samples as the ϕ dependence analysis (section 8.2.1). According to the 20% energy resolution at the 100 GeV neutron, we chose 20 GeV binning in the measured energy with the ZDC starting at 40 GeV and last bin was decided from 80 to 120 GeV due to the resolution.

The measured energy dependence of ϵ_N divided by the polarization are plotted in Figure 8.17. Finite asymmetry can be seen in the forward kinematics for both trigger samples and they look flat. The energy unfolding is a straight forward to extract the initial x_F from the measured energy in the same way of the cross section analysis, however, the correlated errors from the unfolding are so terrible and illusive⁶. For the estimation of the x_F dependence, the mean value of x_F in each bin was estimated by the simulations which were modified to reproduce the measured energy distributions for each trigger samples (section 8.2.2).

⁶In this case, the correlated error would be ~ 2.5 times higher than the statistics error before the unfolding. It means the unfolded error for the ZDCN|S sample would overlap with $A_N = 0$ in all bins. But it is not true. These errors are highly anti-correlated within the finite asymmetry which is seen obviously before the unfolding. Such errors would invite the misunderstanding.

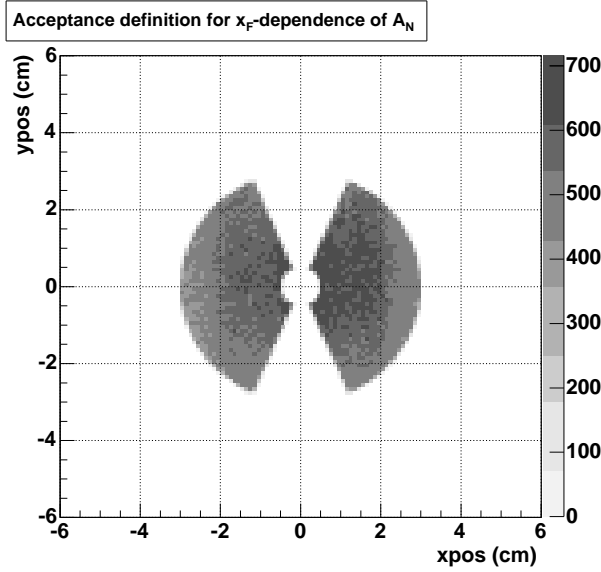


Figure 8.16: The acceptance definition for the x_F dependence of A_N . It required $0.5 < r < 3.0$ cm to avoid the edge effect. We divided the region in the left and right sectors by the azimuthal angle cut, $-66.8^\circ < \phi < 66.8^\circ$, to maximize the figure of merit according to the $\cos\phi$ dependence of A_N (equation 8.5).

8.3.2 Estimation of the smearing effect

The ϵ_N is smeared from A_N due to the position resolution discussed in section 8.2.3. The smearing effect was estimated by the simulation with the same acceptance cut and, then, included the smearing from the acceptance cut of equation 8.6. Figure 8.18 shows the output asymmetry as a function of the measured energy obtained by the simulation which was modified to the ZDCN|S sample (see section 8.2.2). As a simulation input, we generated neutrons with the sine modulated $A(\phi)$ with $A_N = -0.10$ in all x_F regions. The A_N^{Output} were obtained as (40–60, 60–80, 80–120(GeV)) = $(-0.050, -0.054, -0.055)$. Their variations to the initial amplitude as equation 8.1 are correction factors for the smearing effect. Same calculation was performed by the simulation which was modified to the BBCLL1& (ZDCN|S) sample, and we obtained $\epsilon_E^{smearing}(E)$ in each trigger sample as follows.

- ZDCN|S : (40–60, 60–80, 80–120(GeV)) = $(0.50 \pm 0.03, 0.54 \pm 0.03, 0.55 \pm 0.03)$
- BBCLL1&(ZDCN|S) : (40–60, 60–80, 80–120(GeV)) = $(0.50 \pm 0.02, 0.59 \pm 0.02, 0.55 \pm 0.02)$

8.3.3 Estimation of the mean x_F in each bin

After the correction of the smearing effect, we obtain the measured energy dependence of A_N . The mean values of x_F in each bin were estimated in this section.

The mean x_F values for the ZDCN|S and BBCLL1&(ZDCN|S) samples were estimated by the simulations. The x_F distribution in each energy bin is shown in Figure 8.19. Mean x_F values for three bins, (40–60, 60–80, 80–120(GeV)), are $\langle x_F \rangle = (0.57 \pm 0.13, 0.68 \pm 0.11, 0.78 \pm 0.09)$ and $(0.55 \pm 0.12, 0.66 \pm 0.10, 0.75 \pm 0.08)$ for the ZDCN|S and BBCLL1&(ZDCN|S) samples, respectively. Errors were obtained as RMS values.

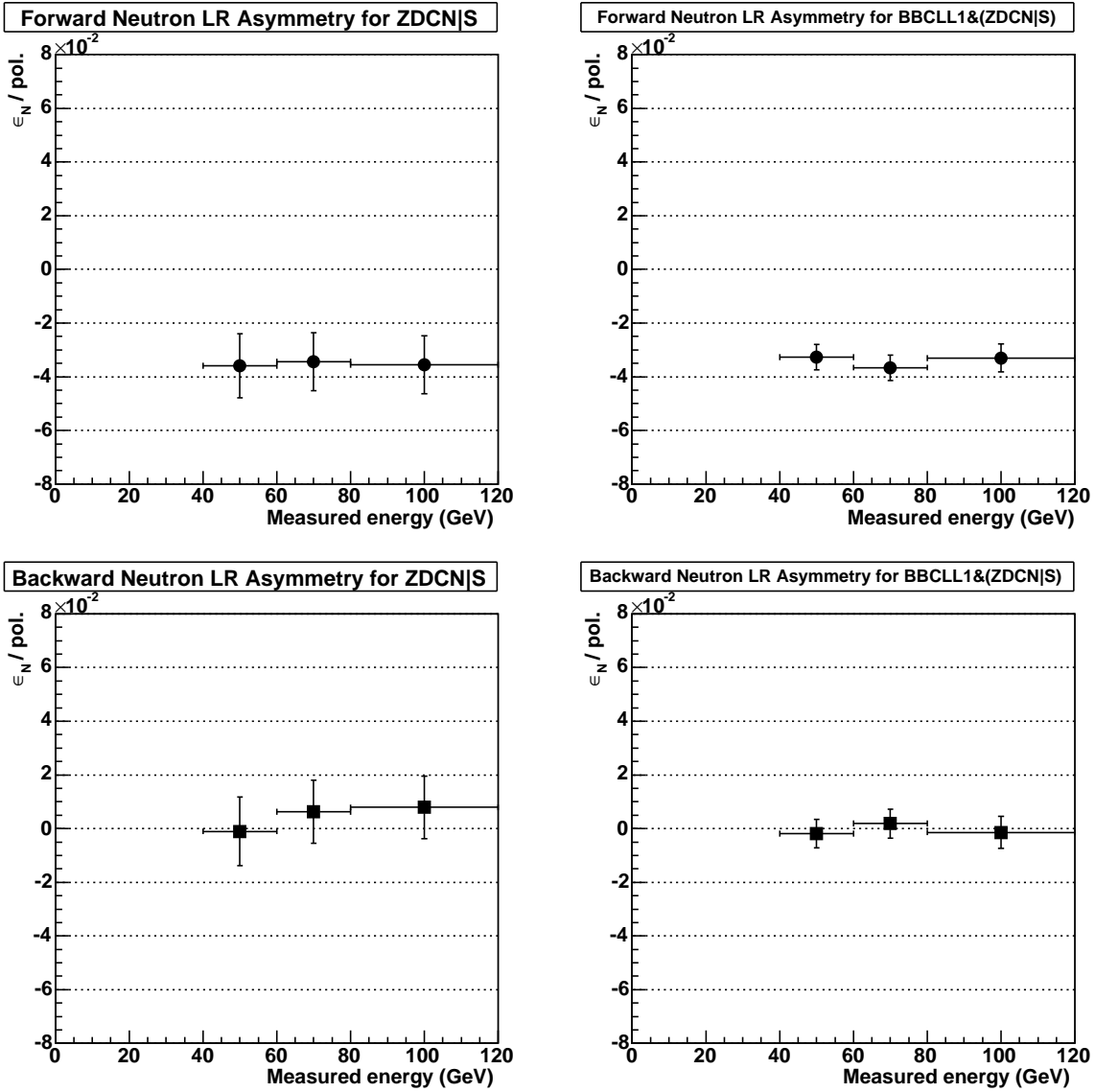


Figure 8.17: The measured energy dependent ϵ_N divided by polarizations. Top and bottom show results in the forward and backward kinematics, respectively. Left and right figures show these for the ZDCN|S and BBCLL1&(ZDCN|S) samples, respectively. Negative A_N can be seen in the forward region.

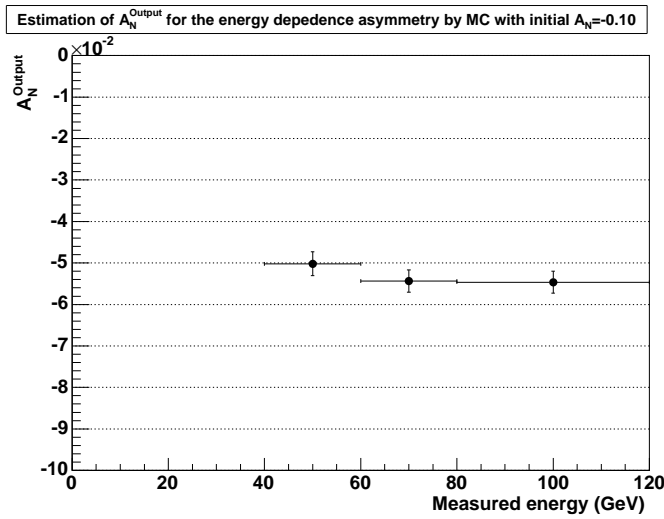


Figure 8.18: The A_N^{Output} as a function of the measured energy estimated by the simulation which was modified to the ZDCN|S sample. As an input, we generated $A(\phi)=A_N\sin(\phi - \pi/2)$ with $A_N=-0.10$ in all x_F region. The asymmetry was smeared to 50~55% due to the position resolution and the acceptance cut.

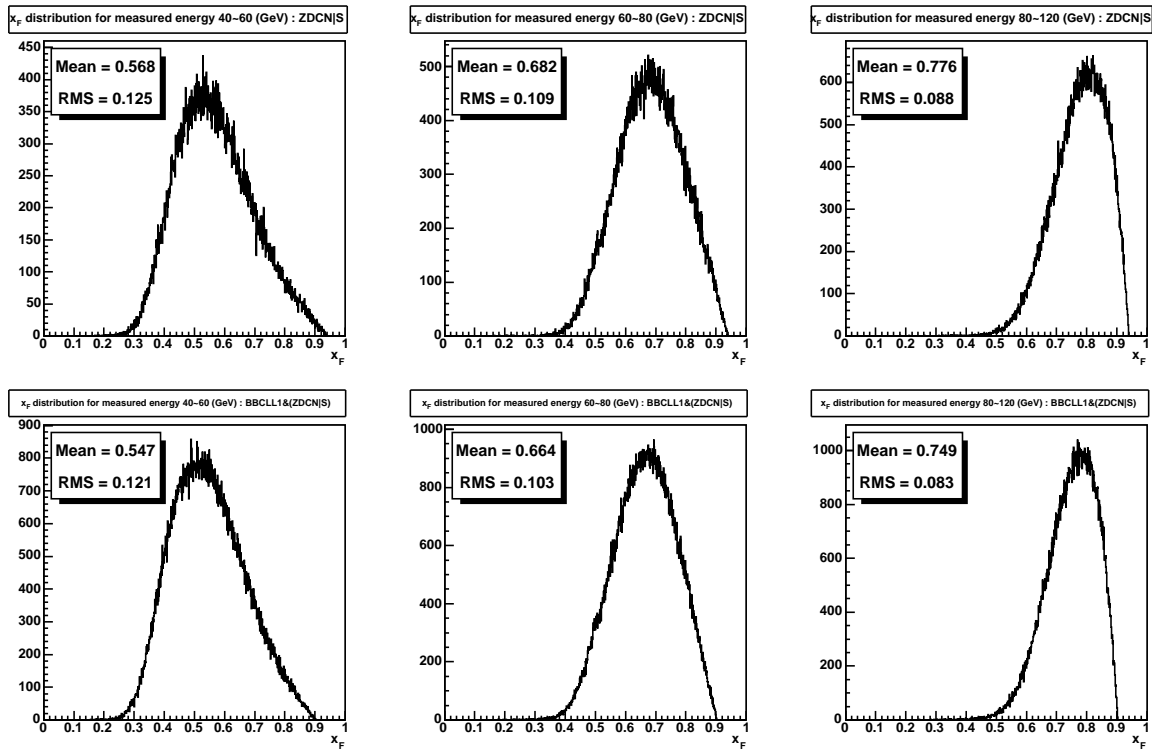


Figure 8.19: The simulated initial x_F distribution in each measured energy bin for Left) 40–60, Center) 60–80 and Right) 80–120 GeV. Top and bottom figures show these for the ZDCN|S and BBCLL1&(ZDCN|S) samples, respectively.

8.3.4 Systematic errors

The systematic errors for the x_F dependence are evaluated in this section. The methods are basically same as the ϕ -dependence analysis (section 8.2.4). We describe the results only.

Background contamination

After the neutron identification and the acceptance cut, the neutron purities were,

- Without BBC trigger, ZDCN|S : 0.976 ± 0.007
- With BBC trigger, BBCLL1&(ZDCN|S): 0.979 ± 0.014

The proton backgrounds were 1.3% and 0.9% for the ZDCN|S and BBCLL1& (ZDCN|S) samples, respectively and should be increased 1.5 times. Increased values, 2.0% and 1.4% were added as a systematic errors.

Systematics for the beam axis shift

According to results of beam axis searches, $A_N(E)$ were calculated with various center positions as $(x,y) = (0.46, 0.00)$, $(0.00, -1.10)$ and $(0.46, -1.10)$ cm while keeping the acceptance cut and results are shown in Figure 8.20. Table 8.3 lists asymmetry values and their variations to final values which were calculated by the center of $(x,y) = (0.00, 0.00)$ cm. Maximum variations to final values are added as a systematic errors.

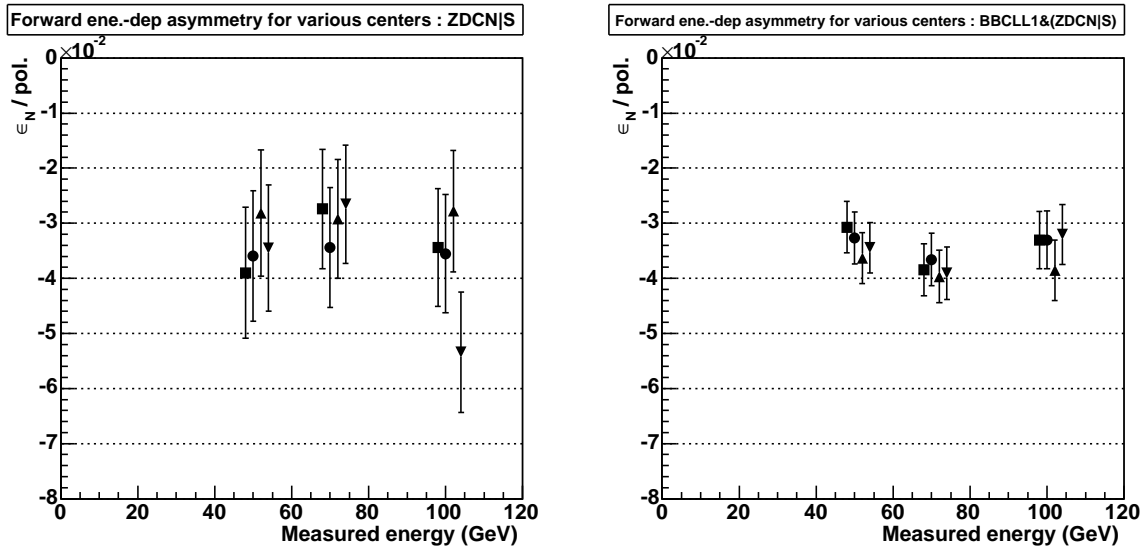


Figure 8.20: The measured energy dependence of ϵ_N divided by the polarization calculated with the acceptance center as $(x,y) = (0.00, 0.00)$, $(0.46, 0.00)$, $(0.00, -1.10)$ and $(0.46, -1.10)$ cm are plotted as circle, square, triangle-up and triangle-down points, respectively. Horizontal value in each point was shifted to be easily viewable; only circle points show correct values.

ZDCN S			
Acceptance center (x,y) cm	40~60 (GeV)	60~80 (GeV)	80~120 (GeV)
(0.00, 0.00)	-0.0359	-0.0344	-0.0355
(0.46, 0.00)	-0.0390 (8.6%)	-0.0274 (20.3%)	-0.0344 (3.2%)
(0.00, -1.10)	-0.0282 (21.6%)	-0.0292 (15.0%)	-0.0278 (21.7%)
(0.46, -1.10)	-0.0345 (4.0%)	-0.0265 (22.8%)	-0.0534 (50.4%)

BBCLL1&(ZDCN S)			
Acceptance center (x,y) cm	40~60 (GeV)	60~80 (GeV)	80~120 (GeV)
(0.00, 0.00)	-0.0326	-0.0366	-0.0330
(0.46, 0.00)	-0.0307 (5.9%)	-0.0384 (5.0%)	-0.0331 (0.1%)
(0.00, -1.10)	-0.0363 (11.2%)	-0.0397 (8.4%)	-0.0386 (16.8%)
(0.46, -1.10)	-0.0344 (5.4%)	-0.0391 (6.7%)	-0.0320 (3.0%)

Table 8.3: The ϵ_N divided by polarizations calculated with various centers of the acceptance in each measured energy bin. The variations to final values, which were calculated by the center of $(x,y)=(0,0)$ cm, are written in parentheses. Maximum variations are shown as bold characters and added as a systematic error.

Systematics for the estimation of the smearing effect

Figure 8.21 shows the A_N^{Output} with the default position resolution and 14.1% increased one. Asymmetry was more smeared with $\sim 6.5\%$ reduction. It was applied to systematic errors in A_N for the smearing correction.

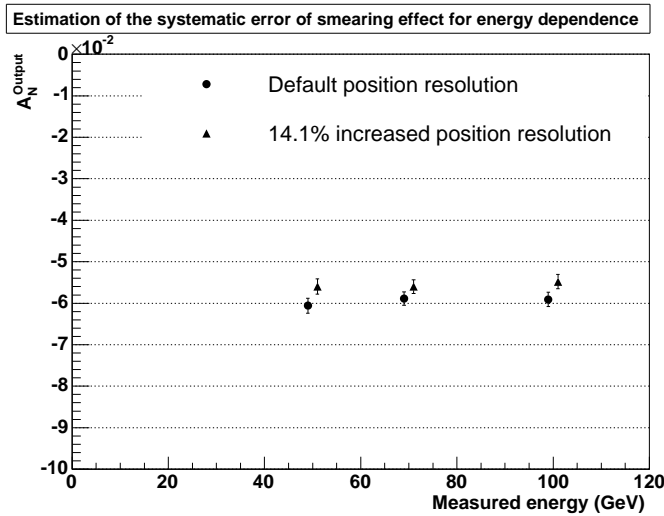


Figure 8.21: The measured energy dependence of A_N^{Output} with the default position resolution (Circle points) and 14.1% increased one (Triangle points) estimated by the simulation. As an input, we generated neutrons as $A(\phi)=A_N\sin(\phi - \pi/2)$ with $A_N=-0.10$. By increasing the position resolution, the smearing effects were also increased and variations were $\sim 6.5\%$.

Bunch shuffling

Details of the bunch shuffling are written in the ϕ dependence analysis (section 8.2.4). For the x_F dependence, the bunch shuffling was performed by an up-down asymmetry since it would be zero in the vertically polarized beam. Therefore, we can ignore the residual asymmetry from the finite A_N (Appendix C.2). The acceptance definition of the up-down asymmetry is shown

in Figure 8.22. It is obtained by rotating the acceptance of the left-right asymmetry 90 degrees.

Figure 8.23 shows results of the bunch shuffling. They were performed in each measured energy bin (40–60, 60–80 and 80–120 GeV). As discussed in section 8.2.4, the χ^2/ndf values can be fluctuated as 1.00 ± 0.15 and 1.00 ± 0.13 for the ZDCN|S and BBCLL1&(ZDCN|S) samples, respectively. Results of bunch shuffling consistent with the $\chi^2/ndf = 1$ within its uncertainty in all bins. We conclude the fake asymmetry from the bunch-by-bunch is less than $0.39\sigma_{stat}$ and $0.36\sigma_{stat}$ for the ZDCN|S and BBCLL1&(ZDCN|S), respectively. We did not include these errors to the final uncertainties in A_N .

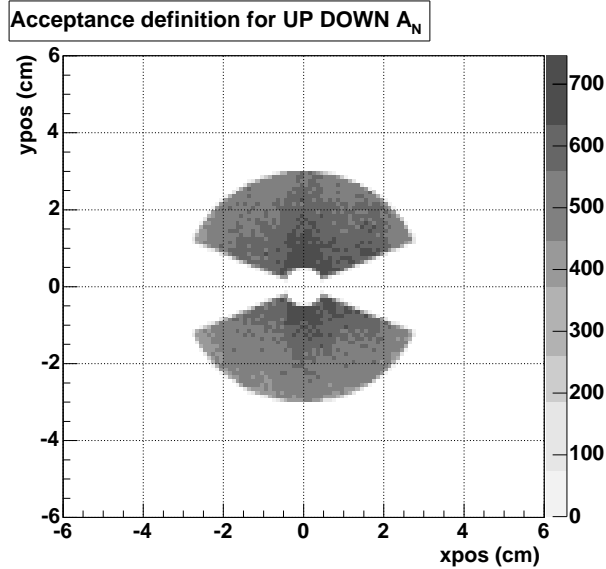


Figure 8.22: The acceptance definition for the up-down asymmetry for the x_F dependence. It is obtained by rotating the acceptance of the left-right asymmetry 90 degrees.

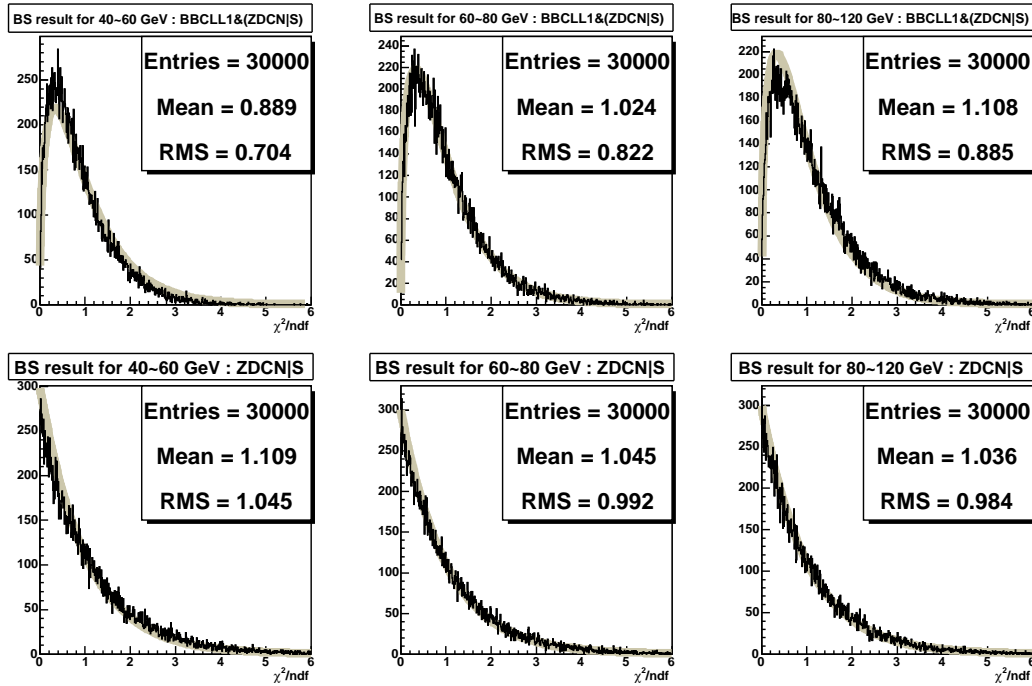


Figure 8.23: Results of the bunch shuffling performed by the up-down asymmetries in each measured energy bin, Left) 40–60, Center) 60–80 and Right) 80–120 GeV. Top and bottom figures show these for the BBCLL1&(ZDCN|S) and ZDCN|S samples, respectively.

Summary of systematic errors

Systematic errors are presented as variations to final values. If there are differences between two triggers, the value of the ZDCN|S is written in the parentheses. Total errors were calculated by quadratic sum. Correlated errors are shown as bold characters.

- Estimation from measurement
 - **Center shift** : 11.2, 8.4, 16.8 (**21.6, 22.8, 50.4**) %
 - Beam gas background for the ZDCN|S trigger : (<1%)
- Simulation uncertainty : total 9.0% (9.5%)
 - Background estimation : 1.4% (2.0%)
 - Smearing effect from the position resolution : 6.5%
 - Multi hits in one event : 6.1% (6.6%).
- Total scaling error : 9.0% (9.5%)
- Polarizations : 6.2% and 5.9% for the positive and negative x_F , respectively.

Chapter 9

Results of the PHENIX experiment

9.1 Cross section

The differential cross section, $d\sigma/dx_F$, for the leading neutron production in pp collision at $\sqrt{s}=200$ GeV was evaluated and listed in Table 9.1. We just show the result of x_F above 0.4 since the data at $x_F = 0.2$ would be affected by the energy cut off before the unfolding. The expected integrated p_T region in each bin is $0-0.11x_F$ GeV/ c as equation 1.3 with the acceptance cut of $r < 2$ cm. We have no correction for x_F bin in this analysis.

For the comparison with the ISR result, their differential cross sections with the same acceptance, it means same p_T region, were calculated from the invariant cross sections by equation 7.2. As a p_T shape, we used $\exp(-4.8p_T)$ which were obtained from $0.3 < x_F < 0.7$ region in the ISR energies (Figure 6.2). The shape should be more steep at large x_F by reading their results of Figure 1.5, however it is difficult to take correct shape from the figure. For the estimation of the differential cross section in the PHENIX data¹ and the ISR, we used $\exp(-4.8p_T)$ as p_T shape in all x_F regions². The cross section values for the ISR are listed in Table 9.2 and differential cross sections are plotted in Figure 9.1. ISR shapes are reproduced by a combination of polynomial 3 and gaussian well.

The comparison is shown in Figure 9.2. The absolute normalization errors for the PHENIX measurement, 12.5 %, is not included. The cross section is consistent with the ISR data. x_F scaling has no violation in higher center of mass energy. This result prefers the OPE model.

$d\sigma/dx_F(\text{mb}) : pp \text{ at } \sqrt{s} = 200 \text{ (GeV)}$	
x_F	$d\sigma/dx_F \text{ (mb)}$
0.50	$0.205 \pm 0.009 \pm 0.082$
0.70	$0.588 \pm 0.014 \pm 0.048$
0.90	$0.572 \pm 0.011 \pm 0.083$

Table 9.1: The result of the differential cross section for the leading neutron production in pp collision at $\sqrt{s}=200$ GeV. The first and second errors show the statistics after the unfolding and systematics. The absolute normalization error, 12.5 %, is not included.

¹ p_T shape was used to the simulation input.

²In the rough estimation, the p_T shape at $x_F = 0.8$ is $\exp(-6.6p_T)$ and it means the differential cross sections using $\exp(-4.8p_T)$ was over estimated; the values around $x_F = 0.8$ would be 10% reduction for both results.

9.2 Azimuthal angle dependence of A_N

The azimuthal angle dependence of A_N for the leading neutron production are plotted in Figure 9.3 and listed in Table 9.3. Results are shown in the forward kinematics only; these in the backward were consistent with zero as shown in Figure 8.6. The error bars are statistical only and the scaling errors from the measurement, 10.4% and 9.0% for the ZDCN|S and BBCLL1&(ZDCN|S) samples, are not included. Lines are fit results of the sine curve defined as equation 3.6. Results well satisfy the characteristics of A_N .

As a result, A_N is larger when BBC hits are required in this acceptance ($0.5 < r < 4$ cm). It may also consistent with the OPE picture; the asymmetry can be generated by the pion exchange which is spin-flip interaction and the BBC coincidentally detects the charged particles which are generated by proton-pion scattering. ³

As a comparison with the IP12 result, we compared the A_N of BBCLL1&(ZDCN|S) sample. Amplitudes of A_N measured at the PHENIX and the IP12 are $(-0.075 \pm 0.004 \pm 0.008) \times (1.00 \pm 0.09)$ and $(-0.090 \pm 0.006 \pm 0.009) \times (1.00^{+0.52}_{-0.25})$, respectively. Errors indicate the statistics, systematics and the scaling uncertainty from the polarization measurement. They are consistent within the errors including the scaling errors. ⁴

9.3 x_F dependence of A_N

The x_F dependence of A_N for the leading neutron production are plotted in Figure 9.4 and listed in Table 9.4. Positive and negative x_F points were obtained from the forward and backward asymmetries, respectively. Statistical uncertainties are shown as error bars and correlated systematic uncertainties are shown as brackets. Scaling errors from the measurement, 9.5% and 9.0% for the ZDCN|S and BBCLL1&(ZDCN|S) samples respectively, are not included. Scaling errors of the polarization measurement, 6.2% and 5.9% for the positive and negative x_F respectively, are not included too.

We can see the significant negative A_N in the positive x_F region and there is no energy dependence within the errors. On the basis of the OPE model, the asymmetry is expected to appear the interference of the pion exchange and the other Reggeon exchange which has spin non-flip amplitude. This result is expected to evaluate the other Reggeon contribution over x_F . We are waiting for the theoretical calculation to discuss in details.

³Actually the charged particles detected with the BBC associated with the leading neutron have interesting property; it also has a finite single transverse spin asymmetry. Details are in Appendix D.

⁴However the center values are not so consistent. One concern is the different detection coverages for the charged particles; $2.2 < |\eta| < 3.9$ in the horizontal and vertical directions for the IP12 experiment, and $3.0 < |\eta| < 3.9$ for the PHENIX experiment.

$Ed^3\sigma/dp^3(\text{mb} \cdot \text{GeV}^{-2} \cdot c^3)$				
x_F	$\sqrt{s} = 30.6$ (GeV)	$\sqrt{s}=44.9$ (GeV)	$\sqrt{s}=52.8$ (GeV)	$\sqrt{s} = 62.7$ (GeV)
0.150	-	13.7 ± 1.5	10.9 ± 1.4	9.5 ± 1.2
0.200	9.6 ± 1.6	12.8 ± 1.4	10.0 ± 1.3	8.5 ± 1.1
0.250	9.6 ± 1.4	12.2 ± 1.3	9.9 ± 1.2	8.2 ± 1.0
0.300	9.8 ± 1.3	11.9 ± 1.2	10.0 ± 1.2	8.5 ± 0.9
0.350	10.0 ± 1.3	11.9 ± 1.2	10.4 ± 1.1	8.7 ± 1.0
0.400	10.5 ± 1.3	12.3 ± 1.2	10.9 ± 1.1	9.1 ± 1.0
0.450	11.2 ± 1.3	12.7 ± 1.2	11.4 ± 1.0	9.8 ± 1.0
0.500	12.3 ± 1.2	13.6 ± 1.1	12.2 ± 1.0	11.1 ± 1.0
0.550	13.4 ± 1.2	14.8 ± 1.1	13.3 ± 1.1	12.5 ± 1.0
0.600	15.1 ± 1.2	16.4 ± 1.1	14.7 ± 1.1	14.0 ± 1.0
0.650	17.4 ± 1.3	18.2 ± 1.3	17.0 ± 1.3	15.7 ± 1.1
0.700	20.3 ± 1.3	21.0 ± 1.4	19.8 ± 1.4	17.9 ± 1.2
0.750	23.3 ± 1.6	25.5 ± 1.7	23.6 ± 1.6	21.6 ± 1.3
0.775	25.0 ± 1.7	27.8 ± 1.8	25.5 ± 1.6	23.5 ± 1.6
0.800	26.6 ± 1.8	29.1 ± 1.8	26.7 ± 1.6	25.2 ± 1.6
0.825	27.4 ± 1.8	29.2 ± 1.8	26.7 ± 1.6	26.4 ± 1.6
0.850	26.7 ± 1.9	28.0 ± 1.8	25.7 ± 1.7	26.6 ± 1.6
0.875	23.8 ± 2.5	25.3 ± 2.1	23.8 ± 1.8	25.8 ± 1.7
0.900	18.6 ± 3.0	20.9 ± 2.8	19.3 ± 2.6	23.4 ± 2.5
0.925	13.5 ± 3.0	14.9 ± 2.8	13.8 ± 2.6	16.3 ± 2.8
0.950	8.3 ± 3.0	8.3 ± 2.8	8.3 ± 2.6	9.1 ± 2.8
0.975	3.2 ± 3.0	1.8 ± 2.8	2.7 ± 2.6	1.8 ± 2.8
$d\sigma/dx_F$ (mb)				
0.150	0.000 ± 0.000	0.076 ± 0.008	0.060 ± 0.008	0.052 ± 0.007
0.200	0.069 ± 0.012	0.092 ± 0.010	0.072 ± 0.009	0.061 ± 0.008
0.250	0.085 ± 0.012	0.108 ± 0.012	0.088 ± 0.011	0.073 ± 0.009
0.300	0.103 ± 0.014	0.125 ± 0.013	0.105 ± 0.013	0.089 ± 0.009
0.350	0.120 ± 0.016	0.143 ± 0.014	0.125 ± 0.013	0.104 ± 0.012
0.400	0.141 ± 0.018	0.166 ± 0.016	0.147 ± 0.015	0.123 ± 0.013
0.450	0.167 ± 0.019	0.189 ± 0.018	0.170 ± 0.015	0.146 ± 0.015
0.500	0.200 ± 0.020	0.221 ± 0.018	0.198 ± 0.016	0.181 ± 0.016
0.550	0.236 ± 0.021	0.260 ± 0.019	0.234 ± 0.019	0.220 ± 0.018
0.600	0.285 ± 0.023	0.309 ± 0.021	0.277 ± 0.021	0.264 ± 0.019
0.650	0.349 ± 0.026	0.365 ± 0.026	0.341 ± 0.026	0.315 ± 0.022
0.700	0.431 ± 0.028	0.446 ± 0.030	0.421 ± 0.030	0.380 ± 0.025
0.750	0.521 ± 0.036	0.571 ± 0.038	0.528 ± 0.036	0.483 ± 0.029
0.775	0.573 ± 0.039	0.637 ± 0.041	0.585 ± 0.037	0.539 ± 0.037
0.800	0.624 ± 0.042	0.683 ± 0.042	0.626 ± 0.038	0.591 ± 0.038
0.825	0.657 ± 0.043	0.701 ± 0.043	0.641 ± 0.038	0.633 ± 0.038
0.850	0.654 ± 0.047	0.686 ± 0.044	0.630 ± 0.042	0.652 ± 0.039
0.875	0.595 ± 0.063	0.633 ± 0.053	0.595 ± 0.045	0.645 ± 0.043
0.900	0.474 ± 0.077	0.533 ± 0.071	0.492 ± 0.066	0.597 ± 0.064
0.925	0.351 ± 0.078	0.387 ± 0.073	0.359 ± 0.068	0.424 ± 0.073
0.950	0.220 ± 0.079	0.220 ± 0.074	0.220 ± 0.069	0.241 ± 0.074
0.975	0.086 ± 0.081	0.048 ± 0.075	0.073 ± 0.070	0.048 ± 0.075

Table 9.2: Top) Original values of invariant cross sections from the ISR. They were obtained from Reference [2]. Bottom) The converted values as a differential cross section, $d\sigma/dx_F$, from the invariant cross sections by equation 7.2. As a p_T shape, we used $\exp(-4.8p_T)$ and the integrated p_T region was $0-0.11x_F$ (GeV/c), corresponds to the acceptance cut of the PHENIX measurement.

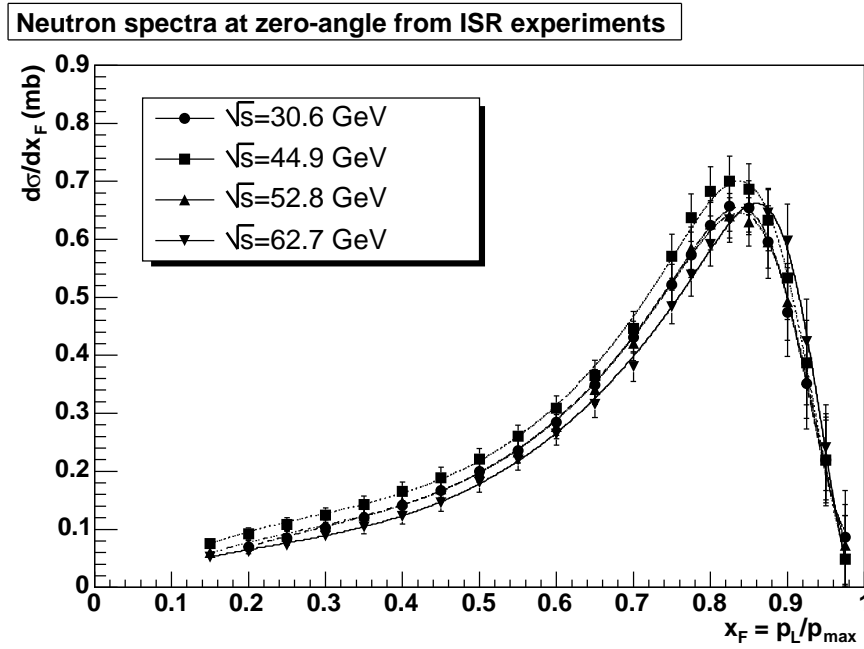


Figure 9.1: The differential cross sections converted from invariant cross sections from the ISR by equation 7.2. The values are listed in Table 9.2. They can be fitted by a combination of polynomial 3 and gaussian well.

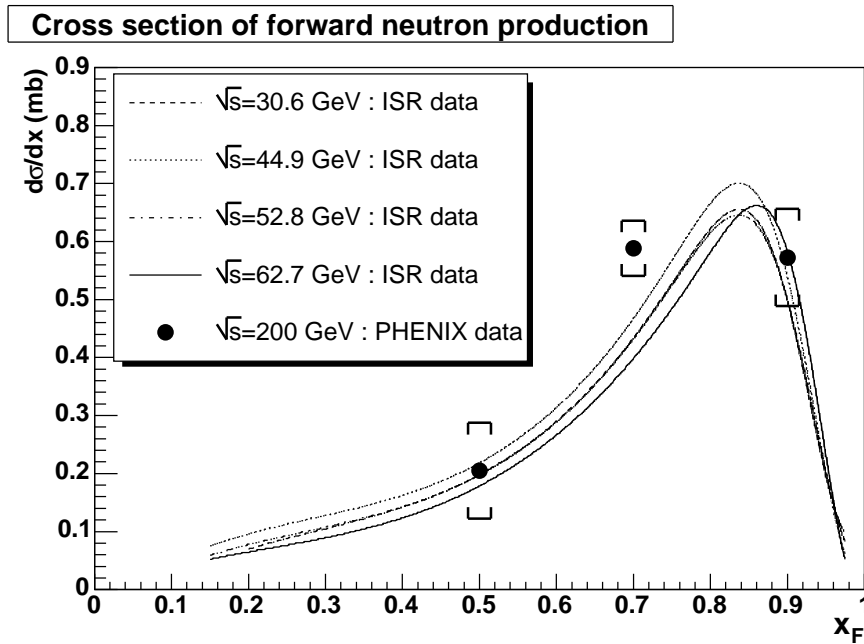


Figure 9.2: The cross section of the leading neutron production in pp collision at $\sqrt{s}=200$ GeV shown as circles. We have no correction for the x_F bin. Statistical errors are buried in each point and systematic errors are shown as brackets. The integrated p_T region in each bin is 0–0.11 x_F GeV/ c . Shapes of the ISR results, which are the fit results of Figure 9.1, are also shown. Absolute normalization errors for the PHENIX and ISR are 12.5% and 20%, respectively.

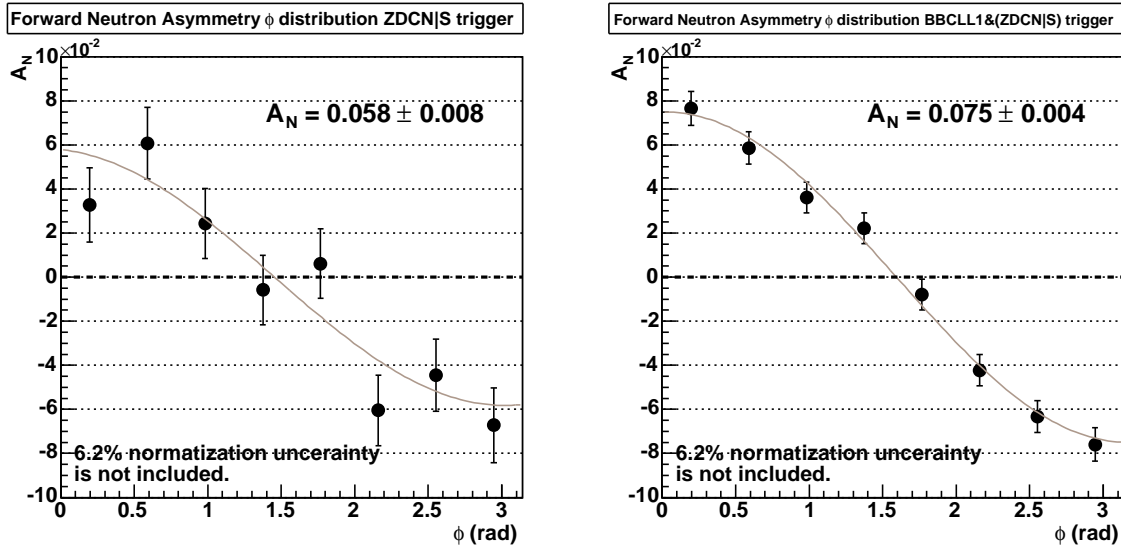


Figure 9.3: The azimuthal angle dependence of A_N for the leading neutron productions in the ZDCN|S (Left) and BBCLL1&(ZDCN|S) (Right) samples. The measured neutron energy was integrated from 40 to 120 GeV. We applied $0.5 < r < 4$ cm to the acceptance cut, or production angles 0.3 - 2.2 mrad in the same way of the IP12 experiment. The errors show statistics only. The scaling errors from the measurement, 10.4 and 9.0%, for the ZDCN|S and BBCLL1&(ZDCN|S) samples are not including. Scaling uncertainty from the beam polarization, 6.2%, is not included too.

$A_N (\times 10^{-2})$		
Azimuthal angle	ZDCN S	BBCLL1&(ZDCN S)
$0 < \phi < \pi/8$	3.28 ± 1.68	7.66 ± 0.76
$\pi/8 < \phi < 2\pi/8$	6.08 ± 1.63	5.86 ± 0.73
$2\pi/8 < \phi < 3\pi/8$	2.43 ± 1.59	3.61 ± 0.70
$3\pi/8 < \phi < 4\pi/8$	-0.58 ± 1.58	2.22 ± 0.69
$4\pi/8 < \phi < 5\pi/8$	0.61 ± 1.58	-0.80 ± 0.69
$5\pi/8 < \phi < 6\pi/8$	-6.04 ± 1.60	-4.23 ± 0.71
$6\pi/8 < \phi < 7\pi/8$	-4.46 ± 1.64	-6.32 ± 0.73
$7\pi/8 < \phi < \pi$	-6.72 ± 1.69	-7.59 ± 0.76

Table 9.3: The results of the azimuthal angle dependence of A_N for the leading neutron production in pp collision at $\sqrt{s}=200$ GeV. Errors show the statistics only. The scaling errors from the measurement, 10.4 and 9.0%, for the ZDCN|S and BBCLL1&(ZDCN|S) samples are not included. Scaling uncertainty from the beam polarization, 6.2%, is not included too.

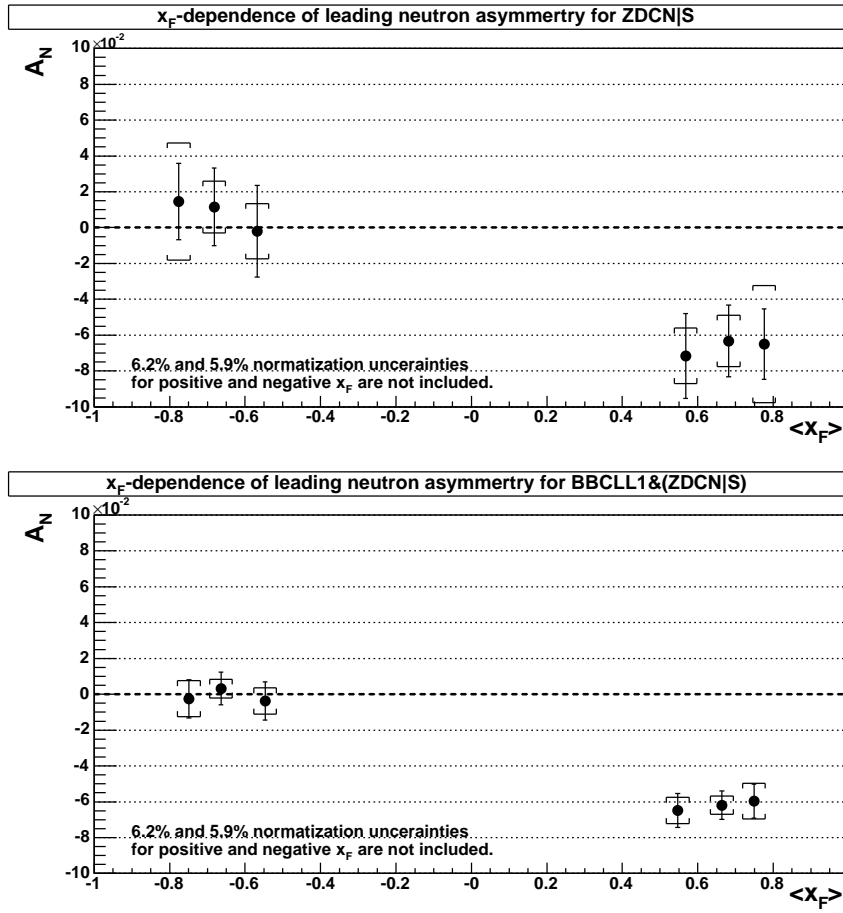


Figure 9.4: The x_F dependence of A_N for the leading neutron production in the ZDCN|S (Top) and BBCLL1&(ZDCN|S) (Bottom) samples. We applied $0.5 < r < 3.0$ cm to the acceptance cut, or production angles 0.3–1.6 mrad; it is not same as the azimuthal angle dependence to minimize the edge effect (section 6.1). According to the estimation of the mean x_F , section 8.3.3, x_F values were determined. The scaling errors from the measurement, 9.5 and 9.0%, for the ZDCN|S and BBCLL1&(ZDCN|S) triggers are not included. Scaling uncertainties from the polarizations, 6.2% and 5.9% for positive and negative x_F respectively, are not included too.

ZDCN S		BBCLL1&(ZDCN S)	
$\langle x_F \rangle$	$A_N (\times 10^{-2})$	$\langle x_F \rangle$	$A_N (\times 10^{-2})$
-0.776	$1.455 \pm 2.133 \pm 3.276$	-0.749	$-0.251 \pm 1.070 \pm 1.002$
-0.682	$1.155 \pm 2.171 \pm 1.442$	-0.664	$0.320 \pm 0.911 \pm 0.520$
-0.568	$-0.202 \pm 2.565 \pm 1.546$	-0.547	$-0.371 \pm 1.065 \pm 0.727$
0.568	$-7.158 \pm 2.365 \pm 1.546$	0.547	$-6.487 \pm 0.939 \pm 0.727$
0.682	$-6.325 \pm 1.999 \pm 1.442$	0.664	$-6.189 \pm 0.804 \pm 0.520$
0.776	$-6.500 \pm 1.962 \pm 3.276$	0.749	$-5.965 \pm 0.945 \pm 1.002$

Table 9.4: The results of the x_F dependence of A_N for the leading neutron production in pp collision at $\sqrt{s}=200$ GeV. First and second uncertainties show statistics and systematics, respectively. Scaling errors from the measurement, 9.5 and 9.0%, for the ZDCN|S and BBCLL1&(ZDCN|S) samples are not included. Scaling uncertainties from the beam polarizations, 6.2% and 5.9% for the positive and negative x_F respectively, are not included too.

Chapter 10

Discussion

In this thesis, we reported the discovery of the single spin asymmetry for the leading neutron production in pp collision at $\sqrt{s}=200$ GeV. The measurement of cross section for the leading neutron was performed as a further investigation and it is consistent with the x_F scaling claimed by the ISR experiment which is well described by the OPE model in Regge calculus (section 1.2.4). Therefore, the observed large asymmetry for the neutron production is considered to come from the interference between a spin-flip amplitude due to the pion exchange and non-flip amplitudes from other Reggeon exchange. So far our knowledge of Reggeon exchange components for the leading neutron is almost the pion. The asymmetry would have the sensitivity to the contribution of other spin non-flip Reggeon exchange even if it is small amplitude. The theoretical calculation is on going.

In addition, we want to discuss our results based on the meson-cloud model. This model gives a best description for the recent interesting result from the Drell-Yan experiment at FNAL E866.¹ The meson-cloud model was applied to the leading neutron production in the ISR experiment and successfully described with the pion cloud (section 1.2.5). It is interesting whether the meson-cloud model can describe the observed asymmetry or not. If it can, the asymmetry would be a new observable for the discussion of the hadronic structure of the nucleon based on the meson-cloud model. Clarification of the hadronic structure of the nucleon is important to the proton spin physics since such system can have an orbital angular momentum and we need to consider this contribution if the hadron structure is present. We are waiting for the theoretical calculation to discuss in details.

Future measurement in RHIC

We reported the x_F dependence of cross section and asymmetry on this thesis and so far our detector is insufficient for the measurement of p_T . Detector improvements are desired to measure more precise x_F and evaluate p_T , but improvements are difficult due to the acceptance limit. However polarized pp collision can be realized at various center of mass energies in RHIC.

¹In this model, Drell-Yan process is generated by the interaction between the d quark in one proton and the \bar{d} quark in the π^+ of $p \rightarrow n\pi^+$ state for other proton. At that time, neutron should be generated in very forward kinematics as the leading neutron. The coincidence of these measurements is interesting.

Already $\sqrt{s}=410$ GeV and 62 GeV runs were performed in 2005 and 2006 run, and significant asymmetries of the leading neutron were shown at online (Appendix E). In the near future, RHIC plans to accelerate the polarized proton to $\sqrt{s}=500$ GeV. We will be able to perform the cross section in such higher energy. For the asymmetry, we will study not only the x_F dependence but also p_T dependence which can be expected to be evaluated by the comparison of different center of mass energies with fixed x_F and measured angle, θ_n (p_T is approximately written as $p_T \sim x_F E_p \theta_n$ (GeV/c)).

Chapter 11

Conclusion

In 2001–2002 run period at RHIC, transversely polarized protons were accelerated to 100 GeV for the first time, with collisions at $\sqrt{s}=200$ GeV. The IP12 experiment searched for a production process with a single transverse spin asymmetry, A_N , based on a large pion asymmetry in forward kinematics from polarized pp collision at $\sqrt{s} = 19.4$ GeV. The experiment was designed to detect photons decayed from π^0 , but was also capable to detect neutrons in the very forward kinematics, ± 2.8 mrad. Detector was placed downstream of the RHIC Dx magnets, which bent out a proton beam and produced charged particles.

Observed asymmetries for photon and π^0 are consistent with zero within the statistics, whereas a significant asymmetry was observed for neutrons in forward kinematics, $A_N = (-0.090 \pm 0.006 \pm 0.009) \times (1.0^{+0.52}_{-0.25})$, where the first and the second errors in the parenthesis are of statistical and systematic, respectively. The scaling error originates the beam polarization uncertainty. The asymmetry in backward was zero. The asymmetry was confirmed by the hadron calorimeter as $A_N = (-0.126 \pm 0.017 \pm 0.045) \times (1.0^{+0.52}_{-0.26})$. It was unexpectedly large asymmetry in this low p_T range, the p_T range for the neutrons was limited by acceptance which gives $p_T < 0.22$ GeV, since polarization phenomena which have been observed so far seems to vanish in such low p_T (*cf.* pion A_N and Λ polarization).

For further investigation about this large asymmetry in the leading neutron production and its origin, we have measured the x_F dependence of A_N and cross section with the PHENIX detector in the similar kinematics region at $\sqrt{s}=200$ GeV. The observed asymmetries are consistent with the IP12 result within the error. We also performed the x_F dependence of A_N as mean x_F through $0.5 < x_F < 0.9$ with the resolution of ~ 0.1 in RMS. Asymmetry showed almost no x_F dependence. The measured cross section at $\sqrt{s}=200$ GeV has no violation of x_F scaling with the results from the ISR experiment. These cross sections for large x_F neutron production, as well as those in ep collisions by ZEUS, are mainly reproduced by a pion exchange. Therefore, the observed large asymmetry for the neutron production is considered to come from the interference between a spin-flip amplitude due to the pion exchange and non-flip amplitudes from other Reggeon exchange.

On the basis of OPE model, the discovered neutron A_N would have the sensitivity to the

contribution of other Reggeon exchange even if it is a small amplitude. It would be a new observable for the discussion of hadronic structure of the proton based on the meson cloud model. More precise measurement is expected to give a new knowledge in forward physics.

In the near future, RHIC plans to accelerate the polarized proton to $\sqrt{s}=500$ GeV. We will be able to perform the measurements at various x_F for the cross section in such higher energy. For the asymmetry, we will study not only x_F dependence but also p_T dependence which is expected to be evaluated by the comparison of different center of mass energies with fixed x_F and the measured angle, θ_n (p_T is approximately written as $p_T \sim x_F E_p \theta_n$ (GeV/c)).

Acknowledgments

First of all, I would like to express my gratitude to Prof. Ken'ichi Imai, who has been my supervisor. I appreciate him to give me interesting physics talk and continuous encouragement.

I am grateful to Prof. Naohito Saito who teach me wide range of physics interests. I have learned attitudes to the physics research as a physicist from him.

I would like to express my respect to Dr. Yuji Goto who preserves discussion and support at BNL. He has provided fruitful discussion for not only this thesis but also other physics. I could not complete this thesis without his support.

I would like to thank all the collaborators of the IP12 experiment group; Dr. Yoshinori Fukao, Dr. Alexander Bazilevsky, Dr. Leslie Bland, Dr. A. Bogdanov, Dr. Gerry Bunce, Dr. Hideto En'yo, Dr. Brendan Fox, Dr. Yuji Goto, Dr. John Haggerty, Prof. Ken Imai, Dr. William Lentz, Dr. D. von Lintig, Prof. Ming X. Liu, Dr. Yousef Makdisi, Dr. Muto Ryotaro, Dr. S.B. Nurushev, E. Pascuzzi, Dr. Martin Purschke, Prof. Naohito Saito, Dr. Fuminori Sakuma, Dr. Sean Stoll, Dr. Kiyoshi Tanida, Dr. Junji Tojo, Dr. Yasushi Watanabe and Dr. Craig Woody.

I would like to thank all the PHENIX collaborators and the staff of Collider-Accelerator Department at BNL. The experiment has not been done without their enormous efforts. I am deeply grateful to Dr. Gerry Bunce who has been supervisor at RIKEN BNL Research Center. With his support, I could polish the analysis and finish my thesis. I am obliged to Dr. Sebastian White who is supervisor of the ZDC detector group. He gave me many advice and suggestion about analysis using the ZDC detector. I appreciate to Dr. Alexei Denisov for his teaching and advice for the ZDC detector operation. I would like to thank Dr. Mickey Chiu. He has gave many advices and helps the ZDC operation at experimental running time. I can not complete the leading neutron analysis without support from ZDC group. I am grateful to all the members of RIKEN BNL Research Center for their support during my stay at BNL. I would like to thank Ms. Pam Esposito, Ms. Tammy Heinz, Ms. Jane Lysik, Ms. Taeko Ito, Ms. Chiharu Shimoyamada-Kawamura, Mr. Jun Nakamura and Mr. Ryouyusuke Maruyama for their administrative and secretarial support.

I am grateful to all members of Radiation Laboratory in RIKEN. I am deeply grateful to the Chief Scientist, Dr. Hideto En'yo. I am very impressed his leadership. He gave me many advices, suggestions, support and encouragements as an scientist with broader perspective. I appreciate to Dr. Yasuyuki Akiba. He gave me many techniques and procedures of the physics analysis. I

would like to express special thanks to Dr. Satoshi Yokkaichi. He gives useful comments and suggestion for my analysis. I would like to express my gratitude to Ms. Noriko Kiyama, Ms. Michiko Muroi and Ms. Karen Sakuma for their secretarial support and hospitality.

I would like to thank all members of “Experimental Nuclear and Hadronic Physics (NH)” group in Kyoto University. I am deeply grateful to Dr. Kiyoshi Tanida who has been one of my advisers. He helps me to finish thesis work with his wide knowledge. He also read throughout my thesis and give worthwhile comments. I am obliged to Mr. Masayuki Niiyama. Discussions with him have been very fruitful for me, especially for the introduction part of this thesis. I would like to express special thanks to Mr. Kazuya Aoki. I have enjoyed discussion with him about physics, analysis, etc. They are valuable time for me. I am grateful to Prof. Masanobu Nakamura, Prof. Haruhiko Funahashi, Prof. Tetsuya Murakami and Prof. Masaru Yosoi, for valuable discussions. I would like to express my thanks to Ms. Ayako Furumori-Nagaoka, Ms. Ayumi Nakao, Ms. Sonoko Chiaki and Ms. Shiori Yamamoto for their secretarial support and hospitality at NH group.

I would like to address my sincere thanks to all graduate students, especially in the same grade, Dr. Yoshinori Fukao, Dr. Koji Miwa, Mr. Terunao Nakura, Dr. Hiromi Okada, Mr. Shinsuke Ota and Mr. Satoru Terashima for their friendships and encouragements. I would like to also appreciate to Dr. Yoshinori Fukao and Dr. Hiromi Okada for their careful reading and extensive feedback for this thesis; the present version is greatly improved, thanks to beneficial comments.

Finally, I have to appreciate to my parents, Mr. Toshio Togawa and Ms. Mitsuru Togawa, and my brother, Mr. Makoto Togawa for their continuous support and encouragement.

Appendix A

Definition of the single transverse spin asymmetry

Spin asymmetry is defined as a difference of the cross sections with the different spin directions of the scattered particles . In case of single transverse spin asymmetry, it can be defined as,

$$A_N \equiv \frac{d\sigma^\uparrow - d\sigma^\downarrow}{d\sigma^\uparrow + d\sigma^\downarrow}. \quad (\text{A.1})$$

Superscripts of \uparrow and \downarrow indicate the polarization directions are vertically transverse in up and down. From the rotational and parity invariance, A_N should be zero at the $p_T=0$ GeV and the values in the detection at left and right toward the spin direction should be symmetric. Thus A_N is represented as,

$$A_N = \frac{\sigma_L^\uparrow - \sigma_L^\downarrow}{\sigma_L^\uparrow + \sigma_L^\downarrow} = -\frac{\sigma_R^\uparrow - \sigma_R^\downarrow}{\sigma_R^\uparrow + \sigma_R^\downarrow} = \frac{\sigma_L^\uparrow - \sigma_R^\uparrow}{\sigma_L^\uparrow + \sigma_R^\uparrow}. \quad (\text{A.2})$$

Subscripts for L and R mean left and right areas toward the polarization axis. Positive A_N is defined for the left detection as convention. By this description, A_N is called “left-right asymmetry” sometimes.

A_N can be represented to the useful expressions using the experimental yields and beam polarization, P , by formulas in section A.2.

A.1 Necessity to be finite A_N

The most convenient way to handle spin is to use the helicity formalism. Transverse spin state, $|\uparrow\rangle$ and $|\downarrow\rangle$, can be described by helicity spin state, $|+\rangle$ and $|-\rangle$, as

$$|\uparrow\rangle = \frac{1}{\sqrt{2}} (|+\rangle + i|-\rangle), \quad |\downarrow\rangle = \frac{1}{\sqrt{2}} (|+\rangle - i|-\rangle). \quad (\text{A.3})$$

The A_N for the inclusive production in Figure 1.11 can be represented as,

$$\begin{aligned} A_N = \frac{d\sigma^\uparrow - d\sigma^\downarrow}{d\sigma^\uparrow + d\sigma^\downarrow} &= \frac{\sum_X |\langle cX | T | \uparrow \rangle|^2 - \sum_X |\langle cX | T | \downarrow \rangle|^2}{\sum_X |\langle cX | T | \uparrow \rangle|^2 + \sum_X |\langle cX | T | \downarrow \rangle|^2} \\ &= \frac{2 \operatorname{Im} \sum_X \langle - | T^\dagger | cX \rangle \langle cX | T | + \rangle}{\sum_X |\langle cX | T | + \rangle|^2 + \sum_X |\langle cX | T | - \rangle|^2}. \end{aligned} \quad (\text{A.4})$$

Here, numerator is known as cross section. For the non-zero A_N , the helicity flip interaction as a denominator is necessary.

OPE model is one of possible candidates for the origin of the leading neutron A_N since pion exchange is the fully spin flip interaction.

A.2 Square root formula

Asymmetry can be calculated by the square root mean of experimental yields for the combinations of spin up and down in left and right detector regions; $N_L^\uparrow, N_L^\downarrow, N_R^\uparrow$ and N_R^\downarrow . Before the explanation of square root formula, we should define these variables as follows,

$$\begin{aligned}
 N_L^\uparrow &= \sigma_L^\uparrow \mathcal{L}^\uparrow \Omega_L \\
 N_L^\downarrow &= \sigma_L^\downarrow \mathcal{L}^\downarrow \Omega_L \\
 N_R^\uparrow &= \sigma_R^\uparrow \mathcal{L}^\uparrow \Omega_R \\
 N_R^\downarrow &= \sigma_R^\downarrow \mathcal{L}^\downarrow \Omega_R
 \end{aligned} \tag{A.5}$$

where,

- $\sigma^{\uparrow(\downarrow)}$: Cross section for spin up (down).
- $\mathcal{L}^{\uparrow(\downarrow)}$: Luminosity for spin up (down).
- $\Omega_{L(R)}$: Acceptance for left (right) geometry.

Equation A.5 can be represented by these variables of a spin average and spin asymmetry which are defined as,

Cross section for left and right

$$\begin{aligned}
 \sigma_L &\equiv \frac{\sigma_L^\uparrow + \sigma_L^\downarrow}{2}, & A_{NL} &\equiv \frac{\sigma_L^\uparrow - \sigma_L^\downarrow}{\sigma_L^\uparrow + \sigma_L^\downarrow} \\
 \sigma_R &\equiv \frac{\sigma_R^\uparrow + \sigma_R^\downarrow}{2}, & A_{NR} &\equiv \frac{\sigma_R^\uparrow - \sigma_R^\downarrow}{\sigma_R^\uparrow + \sigma_R^\downarrow} \\
 \sigma_0 &\equiv \sigma_L = \sigma_R \quad (\text{Rotational symmetry}).
 \end{aligned} \tag{A.6}$$

Luminosity

$$\mathcal{L} \equiv \frac{\mathcal{L}^\uparrow + \mathcal{L}^\downarrow}{2}, \quad \epsilon_{\mathcal{L}} \equiv \frac{\mathcal{L}^\uparrow - \mathcal{L}^\downarrow}{\mathcal{L}^\uparrow + \mathcal{L}^\downarrow}. \tag{A.7}$$

Acceptance

$$\Omega \equiv \frac{\Omega_L + \Omega_R}{2}, \quad \epsilon_{\Omega} \equiv \frac{\Omega_L - \Omega_R}{\Omega_L + \Omega_R}. \tag{A.8}$$

Basically A_{NL} and A_{NR} in equation A.6 are same by rotational symmetry, however we should consider the systematic uncertainty if $A_{NL} \neq A_{NR}$ due to the some reasons which cannot be studied. A_N and its systematic uncertainty, ϵ_A , can be defined as,

$$A_N \equiv \frac{A_{NL} + A_{NR}}{2}, \quad \epsilon_A \equiv \frac{A_{NL} - A_{NR}}{A_{NL} + A_{NR}}. \tag{A.9}$$

It is assumed that the values of ϵ_A is small, $|\epsilon_A| \ll 1$.

Finally, equation A.5 can be represented as,

$$\begin{aligned}
 N_L^\uparrow &= \sigma_0 \mathcal{L} \Omega (1 + \epsilon_{\mathcal{L}}) (1 + \epsilon_{\Omega}) [1 + (1 + \epsilon_P)(1 + \epsilon_A) P A_N] \\
 N_L^\downarrow &= \sigma_0 \mathcal{L} \Omega (1 - \epsilon_{\mathcal{L}}) (1 + \epsilon_{\Omega}) [1 - (1 - \epsilon_P)(1 + \epsilon_A) P A_N] \\
 N_R^\uparrow &= \sigma_0 \mathcal{L} \Omega (1 + \epsilon_{\mathcal{L}}) (1 - \epsilon_{\Omega}) [1 - (1 + \epsilon_P)(1 - \epsilon_A) P A_N] \\
 N_R^\downarrow &= \sigma_0 \mathcal{L} \Omega (1 - \epsilon_{\mathcal{L}}) (1 - \epsilon_{\Omega}) [1 + (1 - \epsilon_P)(1 - \epsilon_A) P A_N].
 \end{aligned} \tag{A.10}$$

A.2.1 Physics asymmetry

Physics asymmetry, which is shown as ϵ_N on this thesis, is defined as,

$$\begin{aligned}
 \epsilon_{Phys} &\equiv \frac{\sqrt{N_L^\uparrow N_R^\downarrow} - \sqrt{N_L^\downarrow N_R^\uparrow}}{\sqrt{N_L^\uparrow N_R^\downarrow} + \sqrt{N_L^\downarrow N_R^\uparrow}} \\
 &\sim P A_N [1 - 2\epsilon_A \epsilon_P (P A_N) + (\epsilon_A^2 + \epsilon_P^2)(P A_N)^2 + O(\epsilon^5)] \\
 &\sim P A_N,
 \end{aligned} \tag{A.11}$$

where N is the experimental yield and its sub(super)scripts are same as equation A.2. For the last approximation, we assume that $P A_N$, ϵ_A , ϵ_P , $\epsilon_{\mathcal{L}}$ and ϵ_{Ω} are small (These five small quantities are represented as ϵ). This approximation is also applied to a detector and a luminosity asymmetries which are explained in next sections. The contribution of the systematic uncertainties to A_N is canceled out until the third order of ϵ by using square root formula.

Statistical uncertainty is obtained as,

$$\begin{aligned}
 \delta\epsilon_{Phys} &= \frac{\sqrt{N_L^\uparrow N_L^\downarrow N_R^\uparrow N_R^\downarrow}}{\left(\sqrt{N_L^\uparrow N_R^\downarrow} + \sqrt{N_L^\downarrow N_R^\uparrow}\right)^2} \sqrt{\frac{1}{N_L^\uparrow} + \frac{1}{N_L^\downarrow} + \frac{1}{N_R^\uparrow} + \frac{1}{N_R^\downarrow}} \\
 &\sim \frac{1}{\sqrt{N}} \text{ for } N_L^\uparrow \sim N_L^\downarrow \sim N_R^\uparrow \sim N_R^\downarrow,
 \end{aligned} \tag{A.12}$$

where N is total number of yield; $N = N_L^\uparrow + N_L^\downarrow + N_R^\uparrow + N_R^\downarrow$.

A.2.2 Detector asymmetry

Detector asymmetry is defined as,

$$\begin{aligned}
 \epsilon_{Det} &\equiv \frac{\sqrt{N_L^\uparrow N_L^\downarrow} - \sqrt{N_R^\uparrow N_R^\downarrow}}{\sqrt{N_L^\uparrow N_L^\downarrow} + \sqrt{N_R^\uparrow N_R^\downarrow}} \\
 &\sim \epsilon_{\Omega} + \epsilon_P (P A_N) - \epsilon_A (P A_N)^2 + O(\epsilon^4) \\
 &\sim \epsilon_{\Omega}.
 \end{aligned} \tag{A.13}$$

The uncertainty is obtained by equation A.12 with changing $\sqrt{N_L^\uparrow N_R^\downarrow} + \sqrt{N_L^\downarrow N_R^\uparrow}$ to $\sqrt{N_L^\uparrow N_L^\downarrow} + \sqrt{N_R^\uparrow N_R^\downarrow}$.

A.2.3 Luminosity asymmetry

Luminosity asymmetry is defined as,

$$\begin{aligned}
\epsilon_{Lumi} &\equiv \frac{\sqrt{N_L^\uparrow N_R^\uparrow} - \sqrt{N_L^\downarrow N_R^\downarrow}}{\sqrt{N_L^\uparrow N_R^\uparrow} + \sqrt{N_L^\downarrow N_R^\downarrow}} \\
&\sim \epsilon_{\mathcal{L}} + \epsilon_A(PA_N) - \epsilon_P(PA_N)^2 + O(\epsilon^4) \\
&\sim \epsilon_{\mathcal{L}}.
\end{aligned} \tag{A.14}$$

The uncertainty is obtained by equation A.12 with changing $\sqrt{N_L^\uparrow N_R^\downarrow} + \sqrt{N_L^\downarrow N_R^\uparrow}$ to $\sqrt{N_L^\uparrow N_R^\uparrow} + \sqrt{N_L^\downarrow N_R^\downarrow}$.

A.3 Luminosity formula

Physics asymmetry also can be calculated by using beam luminosity in the fixed detector region.

In case of the usage of left region, equation A.2 is represented as,

$$\epsilon_{Phys}(L) \equiv \frac{N_L^\uparrow - RN_L^\downarrow}{N_L^\uparrow + RN_L^\downarrow}, \quad R \equiv \frac{\mathcal{L}^\uparrow}{\mathcal{L}^\downarrow}, \tag{A.15}$$

where N and L are the experimental yield and integrated luminosity. Superscripts are same as equation A.2. R is called Relative Luminosity, defined as the ratio of luminosities for spin up and down. In this analysis, BBCLL1 count is used for the luminosity calculation. N^\uparrow and N^\downarrow can be described as ,

$$\begin{aligned}
N_L^\uparrow &\sim \sigma_0 \mathcal{L}^\uparrow \Omega_L [1 + (1 + \epsilon_P)A_N P] \\
N_L^\downarrow &\sim \sigma_0 \mathcal{L}^\downarrow \Omega_L [1 - (1 - \epsilon_P)A_N P].
\end{aligned} \tag{A.16}$$

Equation A.15 can be same representation as equation A.11 by square root formula. In this formula, there is no contribution of the detector asymmetry, but the factor of the luminosity remains as $R = (\mathcal{L}^\uparrow/\mathcal{L}^\downarrow) = (1 + \epsilon_{\mathcal{L}})/(1 - \epsilon_{\mathcal{L}})$.

Statistical uncertainty is obtained as,

$$\begin{aligned}
\delta\epsilon_{Phys}(L) &= 2R \frac{\sqrt{N_L^\uparrow N_L^\downarrow (N_L^\uparrow + N_L^\downarrow)}}{(N_L^\uparrow + RN_L^\downarrow)^2} \\
&\sim \frac{1}{\sqrt{N_L}} \text{ at } N_L^\uparrow \sim N_L^\downarrow,
\end{aligned} \tag{A.17}$$

where N_L is total number of yield detected in left region; $N_L = N_L^\uparrow + N_L^\downarrow$.

We can obtain the asymmetry in right detection, $\epsilon_{Phys}(R)$, by same way. By rotational and parity invariance, amplitude of $\epsilon_{Phys}(L)$ is equal to that of $\epsilon_{Phys}(R)$. If there are some systematics due to the some reasons which cannot be studied, it would appear as $\epsilon_{Phys}(L) \neq \epsilon_{Phys}(R)$.

Since A_N must be zero at the beam center ($p_T=0$ GeV), the beam center can be extracted by the scanning of A_N values calculated by the luminosity formula (it is used in section 8.1).

A.4 Background contamination

We should concern the effect of background contamination to the asymmetry measurement. With the assumption of the very small $\epsilon_{\mathcal{L}}, \epsilon_{\Omega}, \epsilon_A$ and ϵ_P in equation A.10, the number of yields with background contamination can be described as,

$$\begin{aligned}
 N_L^\uparrow &= \sigma_0 \mathcal{L} d\Omega \left[(1-r)(1 + PA_N^S) + r(1 + PA_N^{bg}) \right] \\
 N_L^\downarrow &= \sigma_0 \mathcal{L} d\Omega \left[(1-r)(1 - PA_N^S) + r(1 - PA_N^{bg}) \right] \\
 N_R^\uparrow &= \sigma_0 \mathcal{L} d\Omega \left[(1-r)(1 - PA_N^S) + r(1 - PA_N^{bg}) \right] \\
 N_R^\downarrow &= \sigma_0 \mathcal{L} d\Omega \left[(1-r)(1 + PA_N^S) + r(1 + PA_N^{bg}) \right], \tag{A.18}
 \end{aligned}$$

where A_N^S is the asymmetry of signal. r and A_N^{bg} are defined as a fraction of background contamination and its asymmetry respectively. Measured asymmetry by square root formula is,

$$\epsilon_{Phys} = P \left[(1-r)A_N^S + rA_N^{bg} \right]. \tag{A.19}$$

We can extract A_N^S by measured asymmetry, $A_N^{S+bg} = \epsilon_{Phys}/P$, and its uncertainty as,

$$A_N^S = \frac{A_N^{S+bg} - rA_N^{bg}}{1-r}, \quad \delta A_N^S = \frac{\sqrt{(\delta A_N^{S+bg})^2 + r^2(\delta A_N^{bg})^2}}{1-r}. \tag{A.20}$$

It is same result for luminosity formula.

Appendix B

Local Polarimeter

B.1 Introduction

Extracting the spin state of partons in the polarized nucleon is one of main purposes at RHIC which is the first and unique polarized proton collider in the world. Especially, the study of the parton polarization has been performed by measuring A_{LL} which is defined as a differences of the cross sections for different helicity combination with the longitudinally polarized collisions ,

$$A_{LL} \equiv \frac{\sigma^{++} - \sigma^{+-}}{\sigma^{++} + \sigma^{+-}}, \quad (\text{B.1})$$

where $+(-)$ indicates that helicity state of the proton beam.

In the RHIC ring, proton polarization are keeping as vertically transverse. Absolute and fill-by-fill polarizations have been measured by the pp - and pC -CNI polarimeters, respectively. A spin rotators which are installed up and downstream of the collision points at PHENIX and STAR enables us to take the longitudinal beams by rotating the proton spin from vertical to longitudinal at upstream and restore to vertical at downstream.

If the polarization direction is diagonal with finite polar angle after the rotation, measured A_{LL} has transverse component as,

$$P^B P^Y A_{LL}^{Measured} \approx P_T^B P_T^Y A_{TT} + P_L^B P_L^Y A_{LL}, \quad (\text{B.2})$$

where, A_{TT} is defined in the same way of A_{LL} for the transverse polarization as,

$$A_{TT} \equiv \frac{\sigma^{\uparrow\uparrow} - \sigma^{\uparrow\downarrow}}{\sigma^{\uparrow\uparrow} + \sigma^{\uparrow\downarrow}}. \quad (\text{B.3})$$

P^B and P^Y are beam polarizations for Blue and Yellow beams, respectively. Subscripts, T and L , indicate transverse and longitudinal components of polarization as $P^2 = P_T^2 + P_L^2$. For the extraction of A_{LL} from $P^B P^Y A_{LL}^{Measured}$, it is necessary to know P_T , P_L and A_{TT} . A_{TT} should be measured by the transversely polarized pp collisions. P_T and P_L for both beams can be obtained by the measurement of leading neutron A_N as follows.

A_N is governed with the sine modulation to the transverse spin component. Thus, expected shapes of the azimuthal angle dependence of measured A_N for $A(\phi) = -0.10 \times \sin(\phi + \phi_0)$

with various spin directions of the proton are shown in Figure B.1. We obtained shape (a) with the vertically polarized pp collision at the spin rotator OFF. After the spin rotator is ON, the proton spin is rotated to any direction and the azimuthal dependence of A_N is changed based on its spin direction at the collision point. Rotation in ϕ and θ angles affect to ϕ_0 as shape (b) and amplitude as shape (c), respectively. As shown in shape (c), we can check the longitudinal direction by measuring A_N being zero after the spin rotator is ON¹. Even if the transverse component is remaining shown as (d), its amount can be evaluated by comparing the amplitude with shape (a). Details procedures are shown in next section. Since the extraction of P_T and P_L are performed at the PHENIX collision point locally, it is called ‘‘Local Polarimeter’’.

We have collected the data by BBCLL1&(ZDCN|S) trigger for the local polarimeter analysis to know P_T and P_L in the PHENIX minimum bias samples (section 5.2.4). At the commissioning period for the spin rotator tuning, we take the data with full PHENIX DAQ bandwidth². We check the spin direction within 1 hour and feedback the result to the accelerator to minimize the transverse component, P_T . Through the physics run period, the data have been collected with 100–200 Hz. We have estimated the transverse and longitudinal components through the run by offline analysis.

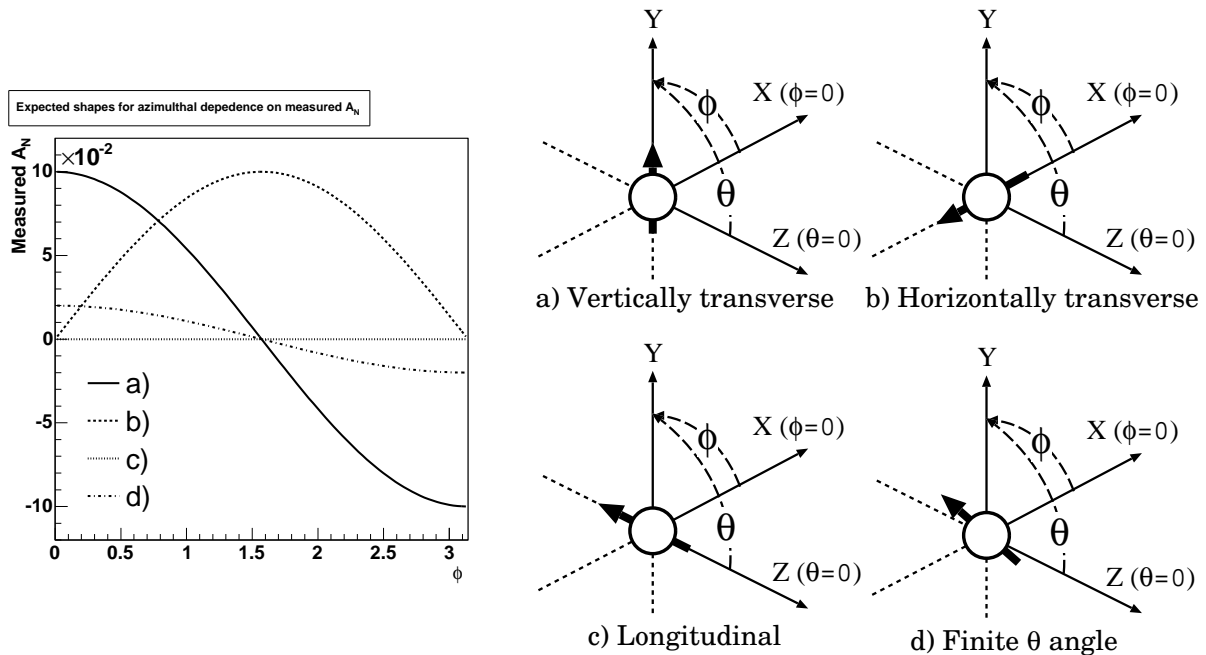


Figure B.1: Expected shapes for the azimuthal dependence of measured A_N for $A(\phi) = -0.10 \times \sin(\phi + \phi_0)$ in case of various spin direction of the proton beam. Collision point is $(x,y,z) = (0,0,0)$ cm.

¹This measurement has no sensitivity for the helicity sign since amplitudes being zero in both signs.

²Full DAQ bandwidth are $\sim 1, 2$ and 5 kHz for 2003, 2004 and 2005 year runs respectively.

B.2 Procedure

As we mentioned in introduction, The spin direction at the collision point is evaluated by the comparison of the measured A_N amplitude at longitudinal run period, $A_N^{Longitudinal}$, and that at transverse run period, $A_N^{Transverse}$. We extract the longitudinal and transverse components of the polarization direction at longitudinal period as,

$$\frac{P_L}{P} = \sqrt{1 - \left(\frac{P_T}{P}\right)^2}, \quad \frac{P_T}{P} = \frac{A_N^{Longitudinal}}{A_N^{Transverse}}. \quad (\text{B.4})$$

Since it is possible that the transverse component is diagonal after the spin rotation, comparison should be performed by not only the amplitude but also the phase of azimuthal dependence. However, it is difficult to obtain correct values from the fit results of sine modulation in case of nearly zero asymmetry since the amplitude and phase are complicated; fit result is labile. For the stable operation. The comparison has been performed with the LR asymmetry, $A_{LR}^{Longitudinal}$, and UD asymmetry, $A_{UD}^{Longitudinal}$. P_T/P can be represented as,

$$\frac{P_T}{P} = \sqrt{\kappa_{LR}^2 + \kappa_{UD}^2}, \quad \text{where, } \kappa_{LR} \equiv \left(\frac{A_{LR}^{Longitudinal}}{A_N^{Transverse}}\right), \kappa_{UD} \equiv \left(\frac{A_{UD}^{Longitudinal}}{A_N^{Transverse}}\right). \quad (\text{B.5})$$

Here, measured parameters κ_{LR} and κ_{UD} are obtained as the average amplitude through the run period and the relation of them is included the phase information.

B.3 Measurement

In this note, I introduce the measurement of 2005 year run. Acceptances for the measurements of LR and UD asymmetries were defined as Figure B.2. ϵ_N has been calculated by the square root formula with neutron yields. For the local polarimeter analysis, we can ignore the smearing effect from the position resolution by taking the ratio of $A_N^{Transverse}$ and $A_N^{Longitudinal}$ assuming the smearing effect has no time dependence. Neutron identifications were applied by the SMD cut and no requirement of the forward scintillator; sample may include proton shower events³. However the contamination is no matter for the local polarimeter work since it is canceled by taking ratio as well as the smearing effect. Since polarization would be changed fill by fill, we calculated ϵ_N divided by the polarization in each fill.

B.3.1 $A_N^{Transverse}$

Results of forward $A_{LR}^{Transverse}$ and $A_{UD}^{Transverse}$ as function of measured energies are shown in Figure B.3. In both beams, significant asymmetries can be seen in the LR and not in the UD. It indicates that both beams were completely polarized in vertical and we can use $A_{LR}^{Transverse}$ results as $A_N^{Transverse}$ in equation B.5. We obtained $A_N^{Transverse}$ value as an average in the measured energy from 20 to 120 GeV. Their values are 0.044 ± 0.002 and 0.042 ± 0.002 for the Blue and Yellow beams, respectively.

³At that time, proton shower event was not well studied.

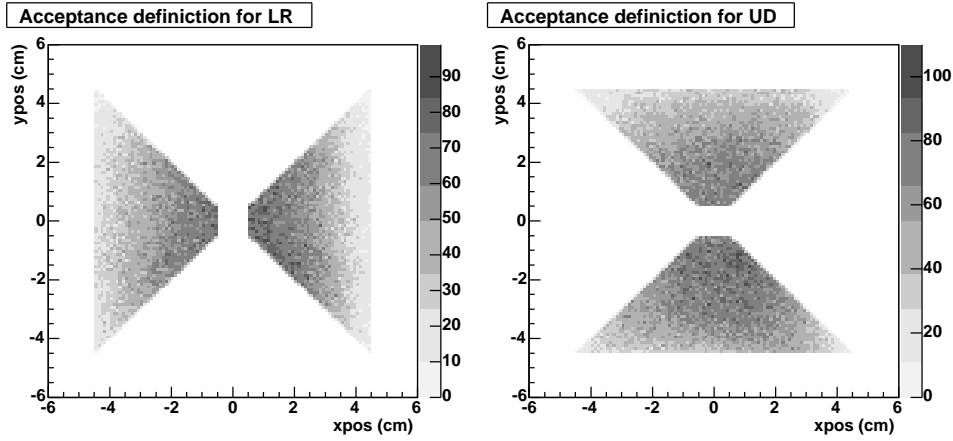


Figure B.2: Acceptance definitions for Left-Right and Up-Down asymmetries (A_{LR} , A_{UD}).

B.3.2 $A_{LR}^{Longitudinal}$ and $A_{UD}^{Longitudinal}$

Results of forward $\epsilon_{LR}^{Longitudinal}$ and $\epsilon_{UD}^{Longitudinal}$ divided by polarizations as $A_{LR}^{Longitudinal}$ and $A_{UD}^{Longitudinal}$ were calculated fill by fill shown as Figure B.4. The values were calculated as an average in the measured energy from 20 to 120 GeV in the same way of $A_N^{Transverse}$. The average values through 2005 year period were obtained by constant fit. We obtained κ_{LR} and κ_{UD} from equation B.5 (see Table B.1). Significant transverse components were remaining for both beams.

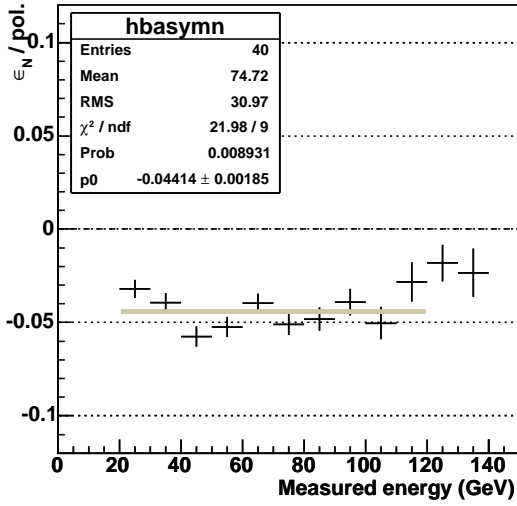
For the confirmation of this measurement, backward $\epsilon_{LR}^{Longitudinal}$ and $\epsilon_{UD}^{Longitudinal}$ divided by polarizations were performed as Figure B.5. Values were completely zero. It is consistent with the zero-asymmetry in the backward region (negative- x_F) and confirms the small amount of asymmetries observed in the forward were not fake asymmetries.

B.4 Estimation of P_L/P

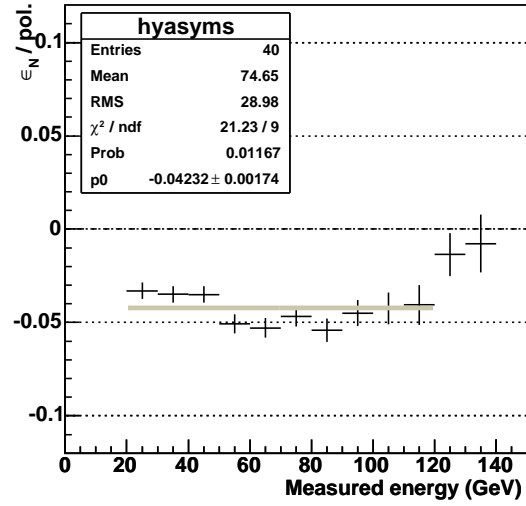
We measured κ_{LR} and κ_{UD} so far. As a next step, P_T/P and P_L/P are calculated by equation B.4 and B.5 but we should be careful to treat a boundary condition of these equations; P_T/P and P_L/P can not exceed 1 and lower than 0 from the relation of unit circle. From equation B.5, we can easily imagine that this problem appears as an asymmetric error of P_T/P when κ_{LR} and κ_{UD} are nearly equal to zero with the same magnitude of statistical errors. Usual gaussian error propagation is wrong at that case. Unfortunately, this situation is pretty match to longitudinal run period.

For the estimation of P_L/P distribution, we calculated P_L/P by equation B.4 through B.5 with the random gaussian generation of κ_{LR} and κ_{UD} values based on their errors many times. P_L/P distributions for 2003 and 2005 year runs are shown in Figure B.6. In 2003 year run, distribution is completely asymmetric due to the reason mentioned above. In this case, we obtained the center value of P_L/P as most probable value. Statistics errors were evaluated as

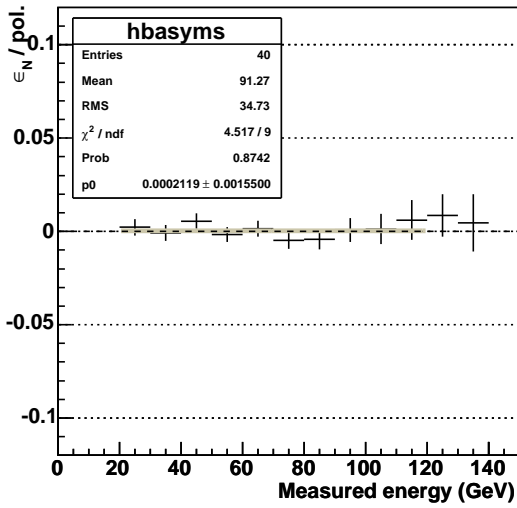
Forward LR asymmetry for BLUE beam



Forward LR asymmetry for YELLOW beam



Forward UD asymmetry for BLUE beam



Forward UD asymmetry for YELLOW beam

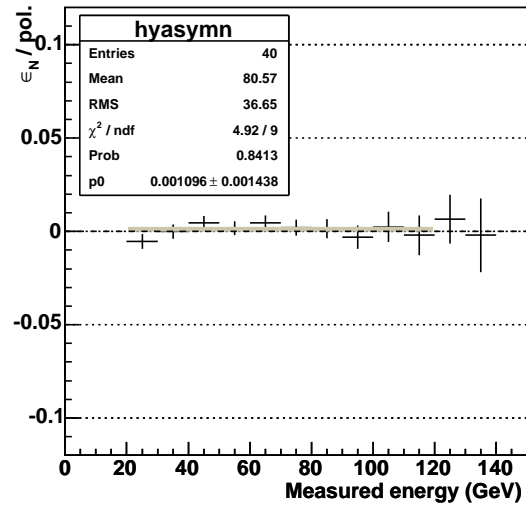


Figure B.3: Results of forward ϵ_N^{LR} and ϵ_N^{UD} divided by polarizations for Blue and Yellow beams at transverse run period. They are plotted as function of the measured energy.

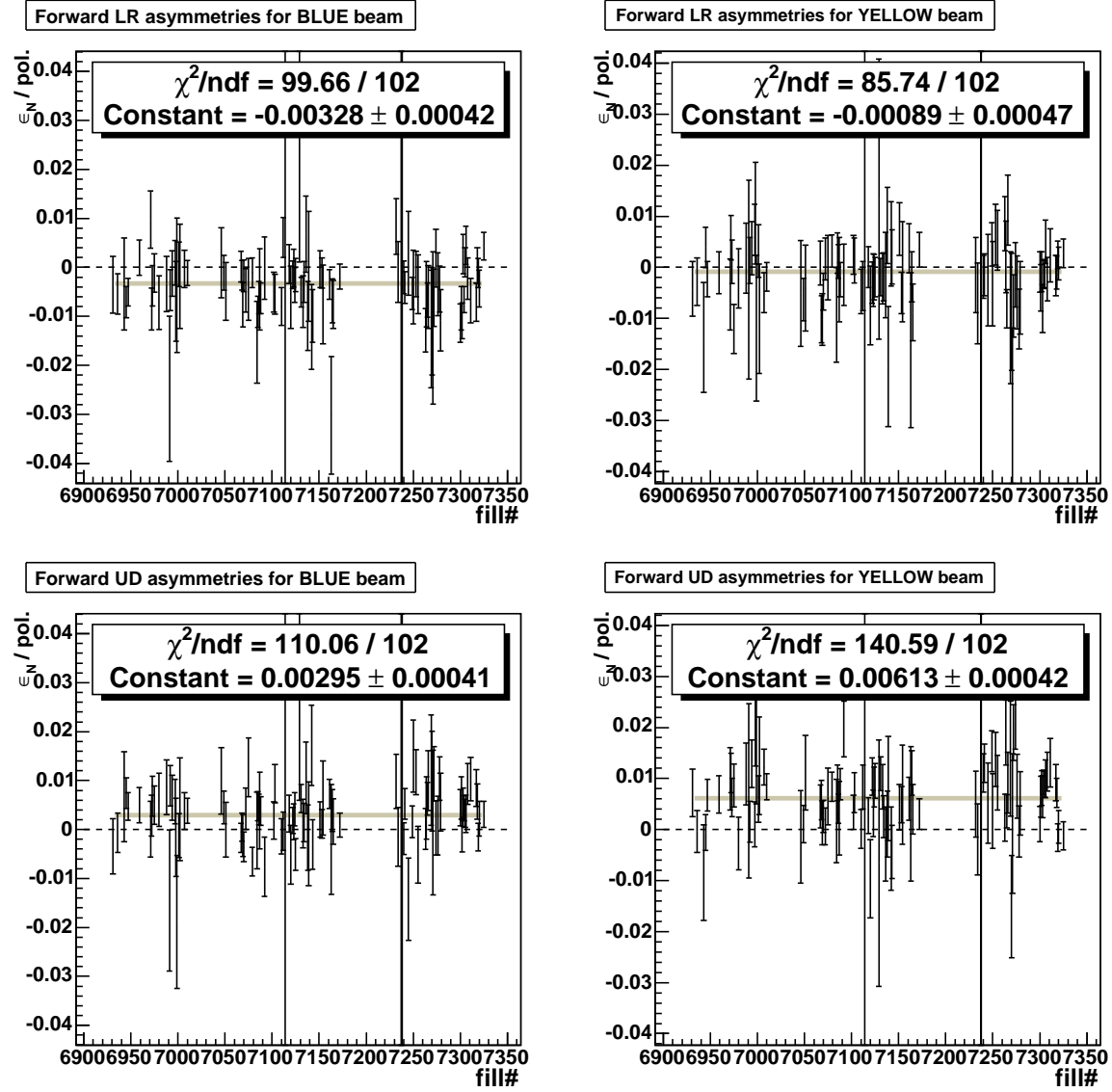


Figure B.4: Results of forward ϵ_N^{LR} and ϵ_N^{UD} divided by polarizations for Blue and Yellow beams as function of fill number, through longitudinal run period. Energy region was used from 20 to 120 GeV in the measured energy in the same way of $A_N^{Transverse}$. Maximum and minimum for vertical axes are set to the values of $\epsilon_N^{Transverse}$ divided by the polarization.

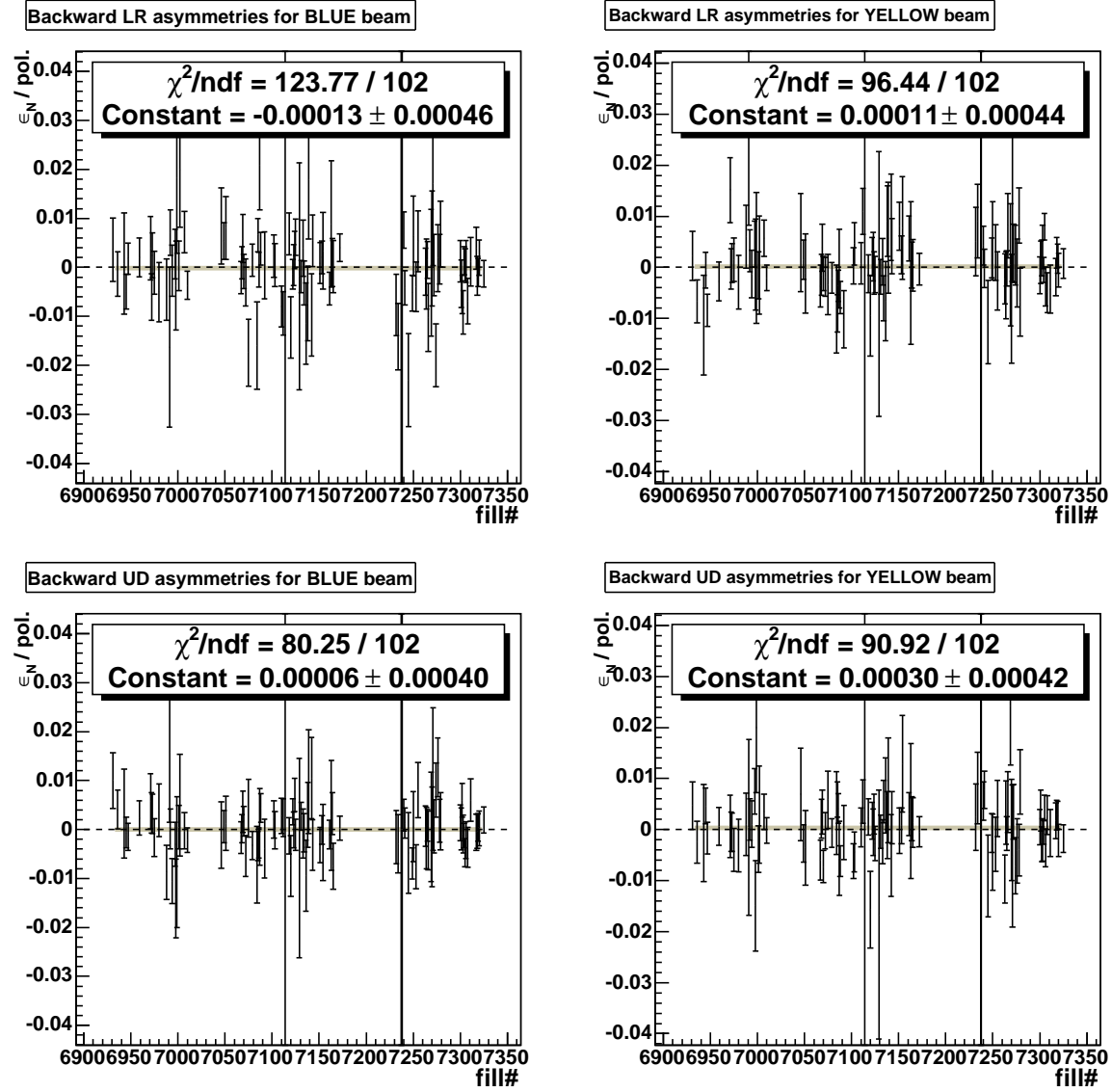


Figure B.5: Results of backward ϵ_N^{LR} and ϵ_N^{UD} divided by polarizations for Blue and Yellow beams as function of fill number, through longitudinal run period. Energy region was used from 20 to 120 GeV in the measured energy in the same way of $A_N^{Transverse}$. Maximum and minimum for vertical axes are set to the values of $\epsilon_N^{Transverse}$ divided by the polarization.

the region including 68.3% counts from center value for positive and negative regions. In 2005 year run, the distribution looks gaussian with the high statistics measurement. It indicates usual gaussian error propagation would work in case of 2005 year statistics. These values are summarized in section B.5.

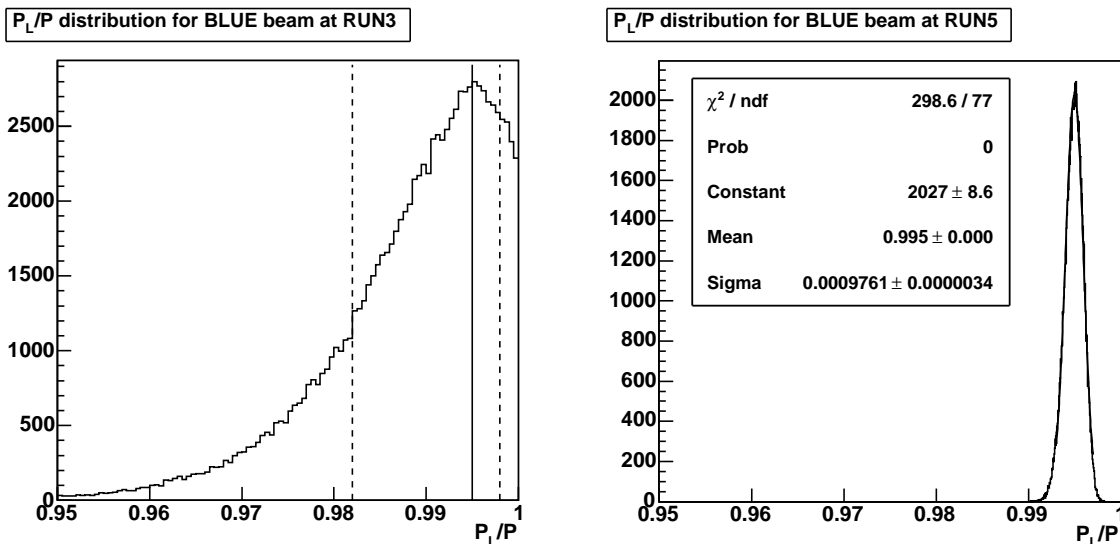


Figure B.6: P_L/P distributions for 2003 (Left) and 2005 year (Right) runs. In 2003 year run, distribution is completely asymmetric and we obtained the center value of P_L/P as most probable value (solid line). Statistics errors were evaluated as the region including 68.3% counts from center value for positive and negative regions (dashed line). In 2005 year run, distribution looks gaussian with the high statistics measurement.

B.5 Summary table

Transverse and longitudinal components of the beam polarization at longitudinal run period have been extracted by the local polarimeter analysis. Table B.1 shows the summary of results from 2003 to 2005 year runs. Systematic errors have been evaluated by bunch shuffling (section 8.2.4) and they are basically small.

Directions of beam polarizations were almost longitudinal for all longitudinal run period.

Year	BLUE beam			YELLOW beam		
	κ_{LR}	κ_{UD}	P_L/P	κ_{LR}	κ_{UD}	P_L/P
2003	0.027 ± 0.069	0.116 ± 0.067	$0.995^{+0.003}_{-0.013}$	0.213 ± 0.066	0.077 ± 0.050	$0.975^{+0.012}_{-0.019}$
2004	0.084 ± 0.047	0.042 ± 0.046	$0.997^{+0.002}_{-0.007}$	-0.008 ± 0.056	-0.074 ± 0.045	$0.998^{+0.002}_{-0.008}$
2005	0.074 ± 0.010	0.067 ± 0.010	0.995 ± 0.001	0.021 ± 0.011	0.145 ± 0.012	0.989 ± 0.002

Table B.1: Summary table of κ_{LR} , κ_{UD} and P_L/P in longitudinal run period from 2003 to 2005 year runs. Errors show statistics only.

Appendix C

Uncertainty in bunch shuffling

C.1 Uncertainty from the bunch number

Assuming the same luminosities for all bunches (bunch number n), asymmetry can be calculated as,

$$A = \frac{\sigma^\uparrow - \sigma^\downarrow}{\sigma^\uparrow + \sigma^\downarrow} \sim \frac{N^\uparrow - N^\downarrow}{N^\uparrow + N^\downarrow}, \quad (\text{C.1})$$

where N^\uparrow and N^\downarrow are the number of yield for spin \uparrow and \downarrow , respectively. The uncertainty of asymmetry can be calculated with the assumption of that yield N_i is distributed with the mean μ and σ as,

$$\begin{aligned} (\Delta A)^2 &= \frac{4 [(N^\uparrow)^2 (\Delta N^\downarrow)^2 + (N^\downarrow)^2 (\Delta N^\uparrow)^2]}{(N^\uparrow + N^\downarrow)^4} \\ &= \frac{1}{n} \left(\frac{\sigma}{\mu} \right)^2 = \frac{(\Delta \mu)^2}{\mu^2}, \end{aligned} \quad (\text{C.2})$$

where $\Delta \mu$ is the uncertainty for the mean which is described as $(\Delta \mu)^2 = \sigma^2/n$. The uncertainty of error depends on the uncertainty of μ . With the approximation of the gaussian distribution for N_i as μ_0 and σ_0 , $\mu_0 \sim \sigma_0^2$,

$$\Delta A_N \sim \frac{1}{\sqrt{n\mu_0}} = \frac{1}{\sqrt{N}}, \quad (\text{C.3})$$

where N is the total yield, $N = \sum_n N_i$. This is usually used as a statistics error.

By the way, the unbiased variance of mean value μ , S_n , is written by,

$$S_n^2 = \frac{1}{n(n-1)} \sum_n (N_i - \mu)^2. \quad (\text{C.4})$$

When the bunch number n is higher, $S_n^2 = (\Delta \mu)^2|_{n \rightarrow \infty}$.

It must estimate the uncertainty of S_n if n is small number and $\Delta \mu \rightarrow \Delta \mu \pm \Delta S_n$ in equation C.2. The uncertainty of S_n is calculated as,

$$\begin{aligned} (2S_n \Delta S_n)^2 = \Delta(S_n^2)^2 &= \frac{4}{n^2(n-1)^2} \sum_n (N_i - \mu)^2 (\Delta N_i)^2 \\ &\sim \frac{4}{n(n-1)^2} \sigma^4. \end{aligned} \quad (\text{C.5})$$

Here, the approximation of gaussian distribution of N_i in each bunch, $(N_i - \mu)^2 = (\Delta N_i)^2 = \sigma_i^2$ and $\sigma = \sigma_1 = \sigma_2 = \dots = \sigma_n$ are used. And S_n^2 in the left hand side can be written as $\sim \sigma^2/(n-1)$. So, ΔS_n is,

$$\begin{aligned} (\Delta S_n)^2 &\sim \frac{\sigma^2}{n(n-1)} \\ &= \frac{(\Delta\mu)^2}{n-1} \quad \rightarrow \quad \Delta S_n = \frac{\Delta\mu}{\sqrt{n-1}}. \end{aligned} \quad (\text{C.6})$$

ΔA can be represented as,

$$\Delta A_N \rightarrow \frac{\Delta\mu}{\mu} \left(1 \pm \frac{\Delta S_n}{\Delta\mu}\right) \sim \frac{1}{\sqrt{N}} \left(1 \pm \frac{1}{\sqrt{n-1}}\right). \quad (\text{C.7})$$

It indicates A can be fluctuated as a relative value to ΔA which depends on bunch number n .

For example, $n = 245$ and 195 for BBCLL1&(ZDCN|S) and ZDCN|S triggers respectively. It means the relative uncertainty to the errors for them are 6.4% and 7.2%. In case of bunch shuffling, it is affected to the χ^2 values as follows,

$$\begin{aligned} \chi^2/ndf &= \frac{1}{n-1} \sum_i^n \frac{(N_i - \mu)^2}{\sigma_i^2} \\ &\sim \frac{[(1 \pm 1/\sqrt{n-1})\sigma]^2}{\sigma^2} = \left(1 \pm \frac{1}{\sqrt{n-1}}\right)^2. \\ \Delta(\chi^2/ndf) &\sim \left(1 \pm \frac{1}{\sqrt{n-1}}\right)^2 - 1. \end{aligned} \quad (\text{C.8})$$

χ^2/ndf values for BBCLL1&(ZDCN|S) and ZDCN|S can be fluctuated $1_{-0.12}^{+0.13}$ and $1_{-0.14}^{+0.15}$ respectively.

C.2 Residual asymmetry in bunch shuffling

After the bunch shuffling, some bunches are unchanged their spin direction and others are changed to opposite. Starting at the number of yield of initial polarization direction \uparrow , N_\uparrow , the number of yields for un-changing and changing the spin direction are written as N_\uparrow^\uparrow and N_\uparrow^\downarrow respectively. Its description is also applied for luminosity as L_\uparrow^\uparrow and L_\uparrow^\downarrow . These variables have following relations.

$$\begin{aligned} N_\uparrow &= N_\uparrow^\uparrow + N_\uparrow^\downarrow & L_\uparrow &= L_\uparrow^\uparrow + L_\uparrow^\downarrow \\ N_\downarrow &= N_\downarrow^\uparrow + N_\downarrow^\downarrow & L_\downarrow &= L_\downarrow^\uparrow + L_\downarrow^\downarrow. \end{aligned} \quad (\text{C.9})$$

Asymmetry after the bunch shuffling, $A^{shuffle}$, can be calculated by these variables as follows.

$$\begin{aligned} A^{shuffle} &= \frac{\sigma^\uparrow - \sigma^\downarrow}{\sigma^\uparrow + \sigma^\downarrow} \\ &= \frac{\frac{N_\uparrow^\uparrow + N_\downarrow^\uparrow}{L_\uparrow^\uparrow + L_\downarrow^\uparrow} - \frac{N_\uparrow^\downarrow + N_\downarrow^\downarrow}{L_\uparrow^\downarrow + L_\downarrow^\downarrow}}{\frac{N_\uparrow^\uparrow + N_\downarrow^\uparrow}{L_\uparrow^\uparrow + L_\downarrow^\uparrow} + \frac{N_\uparrow^\downarrow + N_\downarrow^\downarrow}{L_\uparrow^\downarrow + L_\downarrow^\downarrow}} \end{aligned}$$

$$\begin{aligned}
&= \frac{A \left(\frac{L_{\uparrow}^{\uparrow} - L_{\downarrow}^{\uparrow}}{L_{\uparrow}^{\uparrow} + L_{\downarrow}^{\uparrow}} - \frac{L_{\uparrow}^{\downarrow} - L_{\downarrow}^{\downarrow}}{L_{\uparrow}^{\downarrow} + L_{\downarrow}^{\downarrow}} \right)}{2 + A \left(\frac{L_{\uparrow}^{\uparrow} - L_{\downarrow}^{\uparrow}}{L_{\uparrow}^{\uparrow} + L_{\downarrow}^{\uparrow}} + \frac{L_{\uparrow}^{\downarrow} - L_{\downarrow}^{\downarrow}}{L_{\uparrow}^{\downarrow} + L_{\downarrow}^{\downarrow}} \right)} \\
&\sim \frac{1}{2} A \left(\frac{L_{\uparrow}^{\uparrow} - L_{\downarrow}^{\uparrow}}{L_{\uparrow}^{\uparrow} + L_{\downarrow}^{\uparrow}} - \frac{L_{\uparrow}^{\downarrow} - L_{\downarrow}^{\downarrow}}{L_{\uparrow}^{\downarrow} + L_{\downarrow}^{\downarrow}} \right) \\
&= A \frac{L_{\uparrow}^{\uparrow} L_{\downarrow}^{\downarrow} - L_{\uparrow}^{\downarrow} L_{\downarrow}^{\uparrow}}{(L_{\uparrow}^{\uparrow} + L_{\downarrow}^{\uparrow})(L_{\uparrow}^{\downarrow} + L_{\downarrow}^{\downarrow})} \\
&= A \frac{L_{\uparrow}^{\uparrow} L_{\downarrow} - L_{\downarrow}^{\uparrow} L_{\uparrow}}{(L_{\uparrow}^{\uparrow} + L_{\downarrow}^{\uparrow})(L_{\uparrow} + L_{\downarrow}) + (L_{\uparrow}^{\uparrow} + L_{\downarrow}^{\uparrow})^2} \\
&= AB_{lum}. \tag{C.10}
\end{aligned}$$

From second to third equation a relation of $N_{\uparrow}^{\uparrow(\downarrow)} = CL_{\uparrow}^{\uparrow(\downarrow)}(1 + A)$ and $N_{\downarrow}^{\uparrow(\downarrow)} = CL_{\downarrow}^{\uparrow(\downarrow)}(1 - A)$ with the asymmetry value A are used. From third to fourth equation, approximation $A \ll 1$ is applied and equation C.9 is used from fourth to fifth.

This equation means the $A^{shufffle}$ is depends on the asymmetry with the fluctuation of luminosity if asymmetry is finite value. The mean value of $A^{shufffle}$ should be zero since the mean values of each luminosity is $L/4$ with the total integrated luminosity, $L \equiv L_{\uparrow}^{\uparrow} + L_{\uparrow}^{\downarrow} + L_{\downarrow}^{\uparrow} + L_{\downarrow}^{\downarrow}$. The fluctuation affects to the results of the bunch shuffling and it is estimated in next section.

The fluctuation of B_{lum} is written as follows.

$$\Delta B_{lum} = \sqrt{\left(\frac{\partial B_{lum}}{\partial L_{\uparrow}^{\uparrow}} \right)^2 (\Delta L_{\uparrow}^{\uparrow})^2 + \left(\frac{\partial B_{lum}}{\partial L_{\downarrow}^{\uparrow}} \right)^2 (\Delta L_{\downarrow}^{\uparrow})^2}. \tag{C.11}$$

In case of L_{\uparrow}^{\uparrow} , differential part is,

$$\frac{\partial B_{lum}}{\partial L_{\uparrow}^{\uparrow}} = \frac{L_{\downarrow} \left[(L_{\uparrow}^{\uparrow} + L_{\downarrow}^{\uparrow})(L_{\uparrow} + L_{\downarrow}) + (L_{\uparrow}^{\uparrow} + L_{\downarrow}^{\uparrow})^2 \right] - \left[(L_{\uparrow} + L_{\downarrow}) - 2(L_{\uparrow}^{\uparrow} + L_{\downarrow}^{\uparrow}) \right] (L_{\uparrow}^{\uparrow} L_{\downarrow} - L_{\downarrow}^{\uparrow} L_{\uparrow})}{\left[(L_{\uparrow}^{\uparrow} + L_{\downarrow}^{\uparrow})(L_{\uparrow} + L_{\downarrow}) + (L_{\uparrow}^{\uparrow} + L_{\downarrow}^{\uparrow})^2 \right]^2} \tag{C.12}$$

The mean value of it would be $2/L$ at $L_{\uparrow}^{\uparrow} = L_{\downarrow}^{\uparrow} = L_{\uparrow}^{\downarrow} = L_{\downarrow}^{\downarrow} = L/4$ and $L_{\uparrow} = L_{\downarrow} = L/2$. And ΔL part is,

$$\begin{aligned}
L_{\uparrow}^{\uparrow} &= n_{\uparrow}^{\uparrow} \langle l \rangle \\
(\Delta L_{\uparrow}^{\uparrow})^2 &= (\Delta n_{\uparrow}^{\uparrow})^2 \langle l \rangle^2 + (n_{\uparrow}^{\uparrow})^2 (\Delta \langle l \rangle)^2 \\
&= (\Delta n_{\uparrow}^{\uparrow})^2 \langle l \rangle^2 + (n_{\uparrow}^{\uparrow}) (\Delta l)^2, \tag{C.13}
\end{aligned}$$

where l is the integrated luminosity for each bunch crossing. $\langle l \rangle$ and Δl correspond to mean and fluctuation for l . n_{\uparrow}^{\uparrow} is the number of bunches which are unchanged spin direction from \uparrow as same notation as L_{\uparrow}^{\uparrow} . It has the relation of $n = n_{\uparrow}^{\uparrow} + n_{\downarrow}^{\uparrow} + n_{\uparrow}^{\downarrow} + n_{\downarrow}^{\downarrow}$. The mean value of n is represented with the approximation of $n_{\uparrow}^{\uparrow} = n_{\downarrow}^{\uparrow} = n_{\uparrow}^{\downarrow} = n_{\downarrow}^{\downarrow} = n/4$ as,

$$\langle n_{\uparrow}^{\uparrow} \rangle \sim \frac{n}{4}$$

$$(\Delta n_{\uparrow}^{\dagger})^2 = (n_{\uparrow}^{\dagger} + n_{\downarrow}^{\dagger}) \frac{1}{2} \left(1 - \frac{1}{2}\right) \sim \frac{n}{8}. \quad (\text{C.14})$$

In second equation, binomial distribution is considered. Equation C.13 is represented by $L = n\langle l \rangle$ as,

$$(\Delta L_{\uparrow}^{\dagger})^2 = \frac{L^2}{8n} \left[1 + 2 \left(\frac{\Delta l}{\langle l \rangle}\right)^2\right]. \quad (\text{C.15})$$

L_{\downarrow}^{\dagger} leads to be same results.

Equation C.11 is represented as,

$$\Delta B_{lum} \sim \sqrt{\frac{1}{n} \left[1 + 2 \left(\frac{\Delta l}{\langle l \rangle}\right)^2\right]}. \quad (\text{C.16})$$

The fluctuation of B_{lum} times asymmetry as shown in equation C.10 would appear in the result of the bunch shuffling. For the χ^2/ndf distribution, the fluctuation of the data, denominator in equation 8.2, would change to $\sigma_{stat.}^2 + (A\Delta B_{lum})^2$. Thus, allowable χ^2/ndf value of bunch shuffling result with finite asymmetry is,

$$\begin{aligned} \chi^2/ndf \text{ (with finite asymmetry)} &= \frac{\sigma_{stat.}^2 + (A\Delta B_{lum})^2}{\sigma_{stat.}^2}. \\ \Delta(\chi^2/ndf) &= \chi^2/ndf - 1 = \frac{(A\Delta B_{lum})^2}{\sigma_{stat.}^2}. \end{aligned} \quad (\text{C.17})$$

C.2.1 Expected $A^{shuffle}$ values for ϕ -dependence asymmetry

Expected bunch shuffling results for our ϕ -dependence asymmetries are summarized as follows.

Bin#	A_N^{eff}	$\sigma_{stat.}$	$A_N B_{lum}$	$\Delta(\chi^2/ndf)$
0 ($0 < \phi < \pi/8$)	0.0571	0.0057	0.0037	0.430
1 ($\pi/8 < \phi < 2\pi/8$)	0.0437	0.0054	0.0029	0.275
2 ($2\pi/8 < \phi < 3\pi/8$)	0.0269	0.0052	0.0018	0.113
3 ($3\pi/8 < \phi < 4\pi/8$)	0.0165	0.0052	0.0011	0.044
4 ($4\pi/8 < \phi < 5\pi/8$)	-0.0060	0.0052	-0.0004	0.005
5 ($5\pi/8 < \phi < 6\pi/8$)	-0.0315	0.0053	-0.0021	0.153
6 ($6\pi/8 < \phi < 7\pi/8$)	-0.0472	0.0054	-0.0031	0.320
7 ($7\pi/8 < \phi < \pi$)	-0.0567	0.0057	-0.0037	0.422

Table C.1: Expected $A^{shuffle}$ values for BBCLL1&(ZDCN|S) trigger.

Bin#	A_N^{eff}	$\sigma_{stat.}$	$A_N B_{lum}$	$\Delta(\chi^2/ndf)$
0 ($0 < \phi < \pi/8$)	0.0249	0.0128	0.0018	0.020
1 ($\pi/8 < \phi < 2\pi/8$)	0.0462	0.0124	0.0034	0.073
2 ($2\pi/8 < \phi < 3\pi/8$)	0.0185	0.0121	0.0013	0.012
3 ($3\pi/8 < \phi < 4\pi/8$)	-0.0044	0.0120	-0.0003	0.001
4 ($4\pi/8 < \phi < 5\pi/8$)	0.0047	0.0120	0.0003	0.001
5 ($5\pi/8 < \phi < 6\pi/8$)	-0.0459	0.0121	-0.0033	0.076
6 ($6\pi/8 < \phi < 7\pi/8$)	-0.0339	0.0124	-0.0025	0.039
7 ($7\pi/8 < \phi < \pi$)	-0.0511	0.0128	-0.0037	0.084

Table C.2: Expected $A^{shuffle}$ values for ZDCN|S trigger.

Appendix D

Charged particles at BBC associated with leading neutron

So far we investigated neutron measurement in forward kinematics. In addition, charged particles associated with the leading neutron indicates interesting behaviors.

D.1 Multiplicity distribution

The multiplicity distribution observed by the BBCs are shown in Figure D.1 In case of the sample collected by requiring BBC self trigger, multiplicities of both BBCs are same distributions (Left figure). However their distributions are changed in the neutron tagged sample; multiplicity of forward BBC is lower than that of backward (Right figure). Same behavior appeared at IP12 experiment (see section 3.7).

This result may be explained by OPE model. In the OPE framework, charged particles will be generated by the proton-pion scattering. Since energy of pion is lower than that of proton, multiplicity of charged particles in the neutron direction may be lower.

D.2 Single transverse spin asymmetry

The polarized phenomena were also observed in the charged particles for the sample of the neutron association; we can observe significant left-right asymmetries, especially in same direction as neutron.

- Forward BBC (same direction as neutron) : $-4.50 \pm 0.50 \pm 0.22\%$
- Backward BBC (opposite direction as neutron) : $2.28 \pm 0.55 \pm 0.10 \%$

Without the neutron association, their asymmetries are consistent with 0.

In focus on the the asymmetry for same direction as neutron, its sign is negative as well as neutron asymmetry. One consideration is that the information of polarization is delivered to the proton-pion scattering directly. In this case, charged particle from the scattering themselves can have asymmetry, but we may not know its sign. It is necessary to discuss with the theoretical calculation.

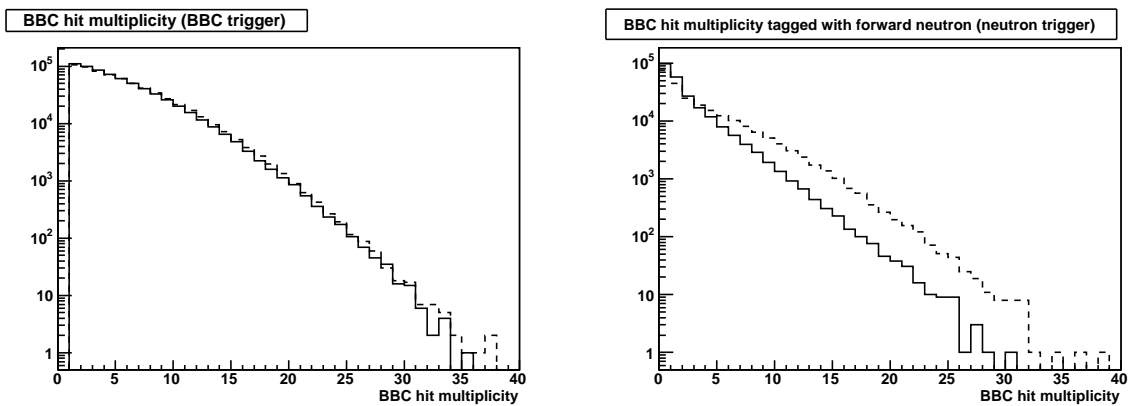


Figure D.1: The Multiplicity distributions of charged particles in BBC. Left) sample of the BBC self trigger (require at least 1 hit for both BBCs). Right) sample of the neutron tagged trigger by SOUTH ZDC. The solid line shows that for forward BBC in the neutron detection (SOUTH) and the dashed line shows that for backward BBC (NORTH).

Appendix E

Leading neutron asymmetries at various center of mass energies

In the RHIC, pp collisions at $\sqrt{s} = 62.4$ and 410 GeV were already performed. At that time, asymmetry studies were also performed as shown Figure E.1. We can see the significant asymmetries in the forward kinematics in both energies as well as $\sqrt{s}=200$ GeV.

In case of $\sqrt{s}=410$ GeV, it was the test acceleration to the next pp phase, at $\sqrt{s}=500$ GeV. They were successfully accelerated with keeping polarization. Leading neutron production keeps its large asymmetry to such higher energies and we expect to see finite asymmetry at $\sqrt{s}=500$ GeV. It means the local polarimeter work in Appendix B will be able to do with the same procedure at $\sqrt{s}=500$ GeV.

Unfortunately, we do not have proper polarization values from CNI polarimeter at $\sqrt{s}=410$ GeV since it was test. It is not possible to extract physics statement from the data. We are waiting the next high energy polarized pp collision, at $\sqrt{s} = 500$ GeV.

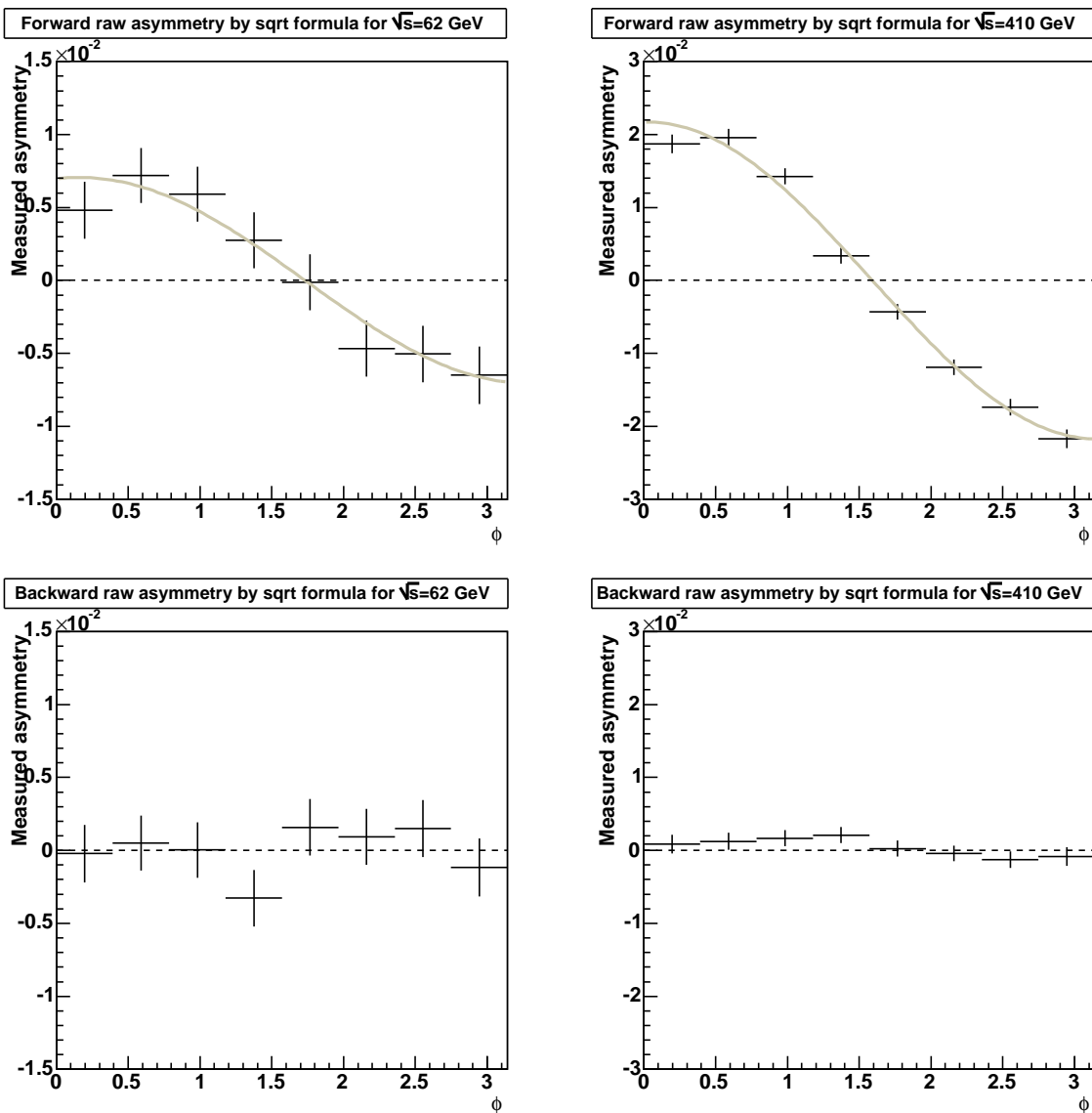


Figure E.1: The azimuthal angle dependence of single transverse spin asymmetries for various center of mass energies. Asymmetry is calculated by square root formula and no corrections such as polarization are applied. Left and right indicate $\sqrt{s}=62.4$ and 410 GeV, respectively. Top and bottom shows forward and backward asymmetries, respectively.

Appendix F

Polarization of inclusive Λ^0 production

Inclusive Λ^0 productions from pp and pA reactions are polarized in perpendicular to the production plane automatically. The polarization can be measured through the decay of $\Lambda^0 \rightarrow p + \pi^-$; decayed proton distribution in the rest frame is given by,

$$dN/d\Omega \propto (1 + \alpha P \cos\theta), \quad (\text{F.1})$$

where θ is the angle between proton momentum and Λ^0 spin direction. α is 0.647 ± 0.013 [73]. The magnitude of polarization, P , can be extracted by measuring θ dependence of proton distribution.

Λ^0 polarization was first discovered by $p\text{Be}$ reaction in 1976 at Fermilab [74] and has been observed in the range of 12 to 2000 GeV/ c (equivalent proton energy on fixed target) [75]-[82]¹. We introduce results from the R608 experiment at ISR, pp at $\sqrt{s}=31\text{--}62$ GeV, which is similar to the RHIC experiment, pp at $\sqrt{s}=200$ GeV. Figure F.1, F.2 and F.3 indicate \sqrt{s} , p_T and x_F dependences of Λ^0 polarizations in the range of $0.2 < x_F < 0.8$ and $0.4 < p_T < 1.3$ GeV/ c . Λ^0 polarization is negative, there is no obvious \sqrt{s} dependence and grows with increasing x_F . Λ^0 polarization also grows with increasing p_T up to ~ 1 GeV/ c and being flat in p_T above 1 GeV/ c .

Some mechanisms, Lynde semi-classical fragmentation model [90], Recombination model [91] and Fragmentation from high-spin baryon resonance [92] are discussed. They can explain polarization sign but not for large magnitude². Recently, OPE model suggests the description of Λ polarization [94]. In this model, it is assumed a diagram shown in Figure F.4, which is binary reaction $\pi p \rightarrow K\Lambda$ and the total πp cross section connected by the exchange of an off-shell Reggeized pion, dominates for the inclusive Λ production in the fragmentation region. Λ polarization is related to the binary reaction $\pi p \rightarrow K\Lambda$ which was measured by [95]-[98] and it successfully describes not only polarization sign but also large amplitude.

¹Polarization of roughly the same magnitude has been observed in the production by protons of every other hyperon [83]-[89].

²Apparently, the attempt of fragmentation from high-spin baryon resonance leads to a reasonable quantitative understanding of experimental situation [93].

It is very interesting suggestion for our leading neutron measurement; this model can also explain the large cross section of leading neutron production at pp and ep collisions (section 1.2). We would consider discovered neutron A_N with polarized phenomena of the exchanged pion.

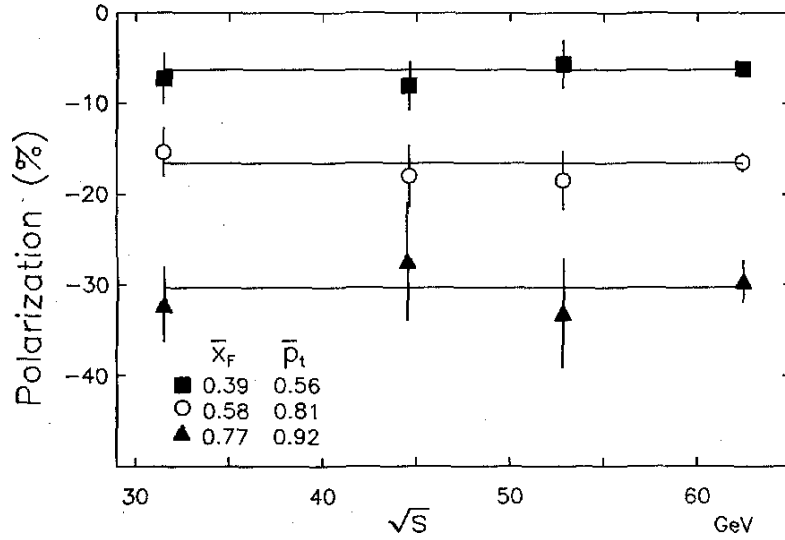


Figure F.1: Λ^0 polarization *vs.* center of mass energy for three x_F - p_T bins from pp collision. Horizontal lines are drawn as average polarization values for each bins. [82]

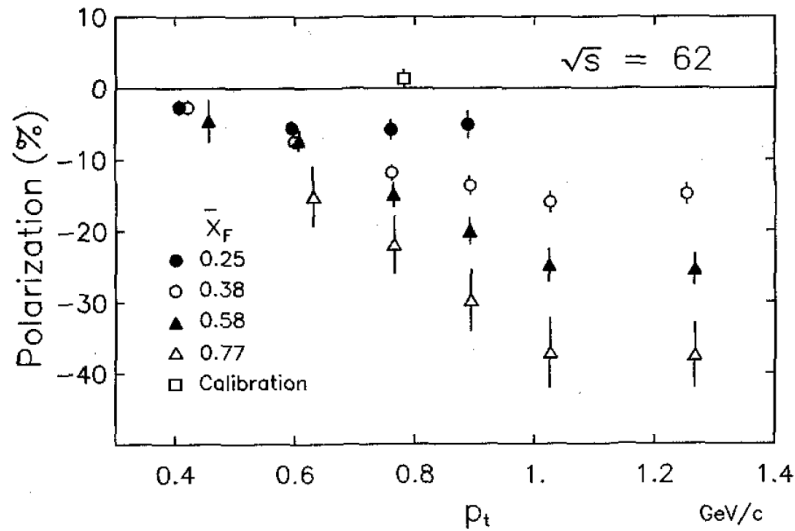


Figure F.2: Λ^0 polarization *vs.* p_T for fixed x_F from pp collision in $\sqrt{s}=62$ GeV. As explained in the text, the calibration point, $(1.3 \pm 1.3)\%$, is calculated using $p\pi^-$ pairs which do not arise from Λ^0 . [82]

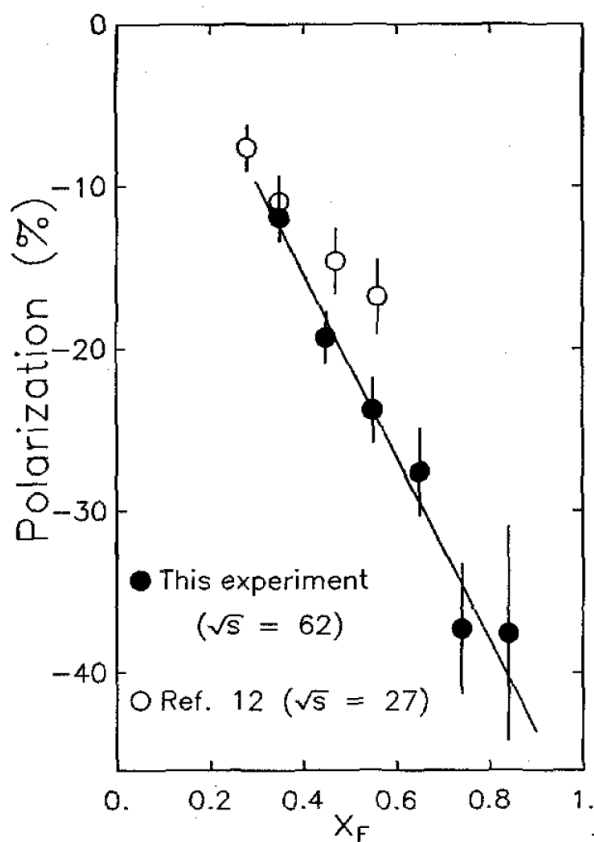


Figure F.3: Λ^0 polarization *vs.* x_F in $p_T > 0.96$ GeV/ c from pp collision in $\sqrt{s} = 62$ GeV (Average p_T is 1.14 GeV/ c) [82]. The open circles are the results from Fermilab in $p_T > 0.95$ GeV/ c [80].

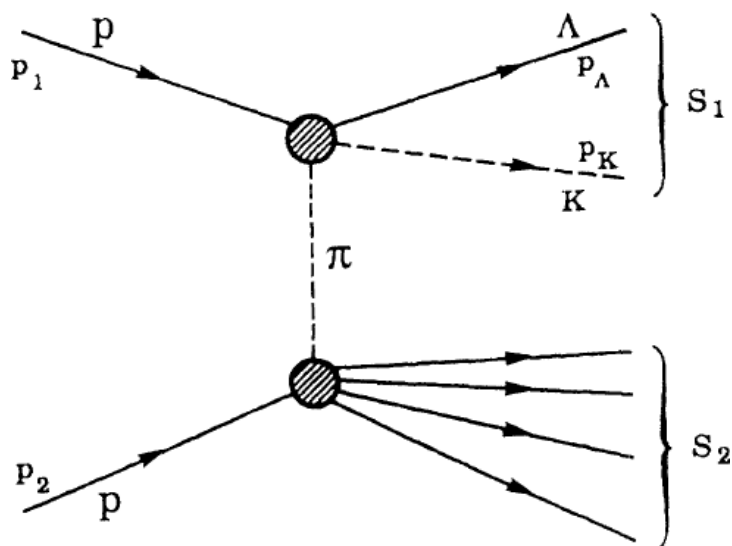


Figure F.4: Single-pion exchange diagram for the process $pp \rightarrow \Lambda K X$. [94]

Bibliography

- [1] G. Altarelli, N. Cabibbo, L. Maiani, and R. Petronzio, Nucl. Phys. **B69**, 531 (1974).
- [2] W. Flauger et al., Nucl. Phys. **B109**, 347 (1976).
- [3] J. Engler et al., Nucl. Phys. **B84**, 70 (1975).
- [4] C. Adloff et al. [H1 Collaboration], Eur. Phys. J. **C6**, 587 (1999).
- [5] S. Chekanov et al. [ZEUS Collaboration], Nucl. Phys. **B637**, 3 (2002).
- [6] S. Chekanov et al. [ZEUS Collaboration], Phys. Lett. **B610**, 199 (2005).
- [7] S. Chekanov et al. [ZEUS Collaboration], Phys. Lett. **B590**, 143 (2004).
- [8] S. Chekanov et al. [ZEUS Collaboration], Nucl. Phys. **B596**, 3 (2001).
- [9] A. Aktas et al. [H1 Collaboration], Eur. Phys. J. **C41**, 273 (2005).
- [10] N. N. Nikolaev, J. Speth and B. G. Zakharov [arXiv:hep-ph/9708290].
- [11] B. Kopeliovich, B. Povh and I. Potashnikova, Z. Phys. **C73**, 125 (1996).
- [12] A. Bunyatyan and Bogdan Povh, Eur. Phys. J. **A27**, 359 (2006).
- [13] A. B. Kaidalov et. al., Eur. Phys. J. **C47** 385 (2006).
- [14] A. Capella et al., Nucl. Phys. **B97**, 493 (1975).
- [15] N.N. Nikolaev et al., Phys. Rev. **D60**, 014004 (1999).
- [16] U. D'Alesio and H.J. Pirner, Eur. Phys. J. **A7**, 109, (2000).
- [17] G. L. Kane, J. Pumplin, and W. Repko, Phys. Rev. Lett. **41**, 1689 (1978).
- [18] J. Adams et al., Phys. Rev. Lett. **92**, 171801 (2004).
- [19] J. Hun Lee et al., *Proceedings for 5th International Workshop on Deep-Inelastic Scattering and Related Subjects (DIS2007)*.
- [20] M. Chiu et al., *Proceedings of 17th International Spin Physics Symposium (SPIN06)*.

- [21] D. W. Sivers., Phys. Rev. **D41**, 83 (1990).
- [22] M. Burkardt and D. S. Hwang. Phys. Rev., **D69**, 074032 (2004).
- [23] J. C. Collins., Nucl. Phys. **B396**, 161182 (1993).
- [24] J.-W. Qiu and G. Sterman., Phys. Rev. **D59**, 014004 (1999).
- [25] Y. Kanazawa and Y. Koike., Phys. Lett. **B478**, 121126 (2000).
- [26] D.L. Adams et al., Zeit. Phys. **C56**, 181 (1992).
- [27] D. L. Adams et al., Phys. Lett. **B264** 462 (1991).
- [28] A. Bravar, et al., Phys. Rev. Lett. **77** 2626 (1996).
- [29] A. Braver et al., Phys. Rev. Lett. **75**, 3073 (1995).
- [30] H. Jung, Comput. Phys. Commun. **86** (1995) 147.
- [31] M. Glück, E. Reya and A. Vogt, Z. Phys. **C53** (1992) 651.
M. Glück, E. Reya and A. Vogt, Z. Phys. **C53** (1992) 127.
M. Glück, E. Reya and A. Vogt, Z. Phys. **C67** (1995) 433.
- [32] H. Yukawa, Proc. Phys. Math. Soc. Japan **17** 48 (1935).
- [33] *Pomeron Physics and QCD*; Cambridge university press (2002).
- [34] *Particle Data Group database*; Data files and plots of cross sections and related quantities.
- [35] V. Stocks, R. Timmermans and J.J. de Swart, Phys. Rev. **C47** 512 (1993)
- [36] B.Robinson et al., Phys. Rev. Lett. **34** 1475 (1975)
- [37] M.Bishari, Phys. Lett. **B38** 510 (1972)
- [38] S. J. Brodsky, C. Peterson and N. Sakai, Phys. Rev. **D23**, 2745 (1981).
- [39] M. Franz, Maxim V. Polyakov and K. Goeke, Phys. Rev. **D62**, 074024 (2000).
- [40] G.F. Chew and F.E. Low, Phys. Rev. **113** 1640 (1959).
- [41] E.A. Hawker et al., Phys. Rev. Lett. **80** 3715 (1998).
- [42] G. Holtzwarth and R. Machleidt, Phys. Rev. **C55** 1088 (1998).
- [43] R.J. Fries abd A. Schäfer, *hep-ph/9801358*.
- [44] G. Bunce, N. Saito, J. Soffer and W. Vogelsang, Ann. Rev. Nucl. Part. Sci. **50** 525 (2000);
hep-ph/0007218.

- [45] K. Adcox et al., Nucl. Phys. **A757**, 184 (2005).
- [46] K. Adcox et al., Nucl. Instrum. Meth. **A499**, 469 (2003).
- [47] I. Alekseev et al., Nucl. Instrum. Meth. **A499**, 392 (2003).
- [48] I. Alekseev et al., *Configuration Manual Polarized Proton Collider Collider at RHIC* (2001).
<http://www.agsrhichome.bnl.gov/RHIC/Spin/design/CMan/CMan.pdf> (Updated at 2006)
- [49] T. Kohe et al., Part. Accel. **6**, 213 (1975).
- [50] H. Sato et al., Nucl. Instrum. Meth. **A272**, 617 (1988).
- [51] F.Z. Khurai et al., Phys. Rev. D **D39**, 45 (1989).
- [52] M. Bai et al., Phys. Rev. Lett. **96**, 174801 (2006).
- [53] A.N. Zelenski et al., Nucl. Inst, Meth. **A402** 185 (1998).
- [54] P.G. Sona, Energ. Nucl. 14, 295 (1967).
- [55] L.H. Thomas, Philos, Mag. **3** 1 (1927).
- [56] M. Froissart and R. Stora, Nucl. Inst. Meth. **1**, 297 (1960).
- [57] M. Bai, et al, Phys. Rev. Lett. **80** 4673 (1998).
- [58] M. Anerella, et al., Nucl. Instr. Meth. **A499** 280 (2003).
- [59] W.W. MacKay, et al., Superconducting Helical Snake Magnets: Design and Construction, DESY-PROC-1999-03, p. 163.
- [60] J. Tojo et al., Phys. Rev. Lett. **89** 052302 (2002)
- [61] T.L. Trueman, *arXiv:hep-ph/0305085*.
- [62] H. Okada et al., Phys. Lett. **B638** 450 (2006).
- [63] O.Jinnouchi et al., Proc. 16th International Spin Physics Symposium SPIN2004, 515 (2004).
- [64] T.C.Awes et al., Nucl. Instrum. Meth. **A311**, 130 (1992).
- [65] Detector Description and Simulation Tool, <http://wwwasd.web.cern.ch/wwwasd/geant>
- [66] C. Adler et al., Nucl. Instr. Meth. **A470**, 488 (2001).
- [67] M. Allen et al., Nucl. Instr. Meth. **A499**, 549 (2003).
- [68] S.S. Adler et al., Nucl. Instr. Meth. **A499**, 560 (2003).
- [69] S.S. Adler et al., Nucl. Instr. Meth. **A499**, 593 (2003).

- [70] K. Boyle et al., PHENIX analysis note, **an567**.
- [71] T. Sjostrand, *Comput. Phys. Commun.* **135**, 238 (2001).
- [72] Volker Blobel, arXiv:hep-ex/0208022.
- [73] O. Overseth et al., *Phys. Rev. Lett.* **19**, 319 (1967).
- [74] G. Bunce et al., *Phys. Rev. Lett.* **36**, 1113 (1976).
- [75] K. Heller et al., *Phys. Lett.* **B68**, 480 (1977).
- [76] K. Heller et al., *Phys. Rev. Lett.* **41**, 607 (1978).
- [77] F. Lomanno et al. *Phys. Rev. Lett.* **43**, 1905 (1979).
- [78] S. Erhan et al., *Phys. Lett.* **B82**, 301 (1979).
- [79] F. Abe et al., *Phys. Rev. Lett.* **50**, 1102 (1983); *J. Phys. Soc. Jpn.* **52**, 4107 (1983).
- [80] L.G. Pondrom et al., *Phys. Rep.* **122**, 57 (1985).
- [81] B. Lundberg et al., *Phys. Rev.* **D40**, 3557 (1989).
- [82] A. M. Smith et al., *Phys. Lett.* **B185**, 209 (1987).
- [83] P. T. Cox et al., *Phys. Rev., Lett.* **46**, 877 (1981).
- [84] C. Wilkinson et al., *Phys. Rev., Lett.* **46**, 803 (1981).
- [85] C. Ankenbrandt et al., *Phys. Rev., Lett.* **51**, 863 (1983).
- [86] L. Deck et al., *Phys. Rev.* **D28**, 1 (1983).
- [87] R. Rameika et al., *Phys. Rev. Lett.* **52**, 581 (1984).
- [88] Y. W. Wah et al., *Phys. Rev. Lett.* **55**, 2551 (1985).
- [89] G. Zapalac et al., *Phys. Rev. Lett.* **57**, 1526 (1986).
- [90] B. Anderson, G. Gustafson, G. Ingelman and T. Sjöstrand, *Phys. Rev. Lett.* **57**, 1526 (1986).
- [91] T. De Grand, J. Markkanen and H. Miettinen, *Phys. Rev.* **D32**, 2445 (1985).
- [92] G. Preoarata, *Proceedinds of the 1980 International Symposium on High Energy Physics with Polarized Beams abd Targets*.
- [93] Ph. Ratcliff, *Proceedinds of Polarized Colider Woerkshop*.
- [94] J. Soffer and N. A. Törnqvist, *Phys. Rev. Lett.* **68** 907 (1992).

- [95] R. D. Baker et al., Nucl. Phys. **B141** 29 (1978).
- [96] D. H. Saxon et al., Nucl. Phys. **B162** 522 (1980).
- [97] C. W. Ward et al., Phys. Lett. **B48** 471 (1974).
- [98] A. Snyder et al., Phys. Rev. **D21** 599 (1980).